PHYSICS AND APPLICATIONS OF OPTICAL LORENTZ FORCE

Mahdy Rahman Chowdhury

(*B.S.C, BUET, EEE, Bangladesh*)

A THESIS SUBMITTED FOR THE DEGREE OF DOCTOR OF PHILOSOPHY

DEPARTMENT OF ELECTRICAL AND COMPUTER ENGINEERING

NATIONAL UNIVERSITY OF SINGAPORE

April 2017

DECLARATION

I hereby declare that the thesis is my original work and it has been written by me in its entirety. I have duly acknowledged all the sources of information which have been used in the thesis.

This thesis has also not been submitted for any degree in any university previously.

Sign: 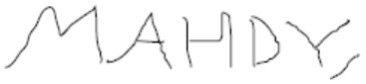

MAHDY RAHMAN CHOWDHURY

December 2016

“He prayeth best, who loveth best

All things both great and small;

For the dear God who loveth us,

He made and loveth all.”

- Samuel Taylor Coleridge

  (The Ancient Mariner, Lyrical Ballads).

This PhD thesis is dedicated to my beloved little sister.

‘Love is the master key to solve all the problems’

Acknowledgements

I would like to express my deepest appreciation to my supervisor Prof. Qiu Cheng Wei, who has the attitude and element of a genius. He continuously conveyed an enthusiasm in regard to my full theoretical work. I should also add that: he is not only a good supervisor but also a very kind and helpful person. Without his proper guidance and persistent help this dissertation would not have been possible.

I would like to thank my co-supervisor, Prof. Chen Zhi Ning, our collaborators such as Prof. Manuel Nieto Vesperinas and Porf. Weiqiang Ding, who gave me great confidence by showing strong trust and faith in me. They have always encouraged me to work harder and smarter and provided me full freedom to explore my research work while focusing on the final goal. I am grateful to them for helping and guiding me to reach the ultimate final conclusions of this thesis, without which it would not have been possible to finish this thesis. My special thanks to Prof. Qiu Cheng Wei, Prof. Weiqiang Ding, Prof. Golam Dastegir Al Quaderi (Dhaka University, Physics Dept.) and Mr. Arif Shahriar who have spent their valuable time to read my PhD thesis. Without their kind suggestions and timely advice, it would be really tough for me to reach the final version of this thesis.

I would like to express my gratitude to all the past and present members in the Microwave Lab of the National University of Singapore and the researchers under the supervision of my supervisor, for their appreciated help and friendship. Special thanks go to Dr. Qasim Mehmood, Mr. Tianhang Zhang, Dr. Mohammaed Danesh, Dr. Zhao Jiajun, Dr. Dongliang Gao, Mr. Amin Kianinejad, Mr. Mei Shengtao, Ms. Srien sithara and Mr. Ashraf Adam for their help throughout the thesis. It has been a real joy working with them, chatting with them and having meals together. I would like to thank all my friends and specially my housemates in Singapore.

Lastly, I would like to thank my great parents who always gave me their support. I would like to take this opportunity to tell you all that I love you all so much and I will always be in debt to everything you have done for me in my life. I also want to thank my beloved wife, Nabila (Samantha) Alam. You spent much time accompanying me (even not staying with me in Singapore) and waiting for me to complete my research works. Specially, you almost alone handled my little baby for almost two years during my PhD program. I also thank my mother (also my father) and my mother in law (also my father in law) who took care and looked after my little baby. My special gratitude to my father who was a source of inspiration to me. At the beginning of my PhD program, my one and only little sister passed away. I decided not to carry on this PhD program. It was my father who inspired me to earn this PhD and then to go back my Country, Bangladesh. The higher education system of Bangladesh is just developing. My father advised me to finish my PhD with proper learning so that after coming back to Bangladesh, I shall contribute significantly in such a developing education system as a true academician. I also love my country very much and always dream to contribute in the area of theoretical research, especially in physics. These things have always inspired me to work hard during my whole thesis and also made me understood that: 'Love is the master key to solve all the problems'. Lastly, I am thankful to the creator. If my son, Arham Chowdhury Isa, were not born by the middle of this PhD program, it would never be possible for me to work with mental peace and to finish my thesis so smoothly.

Abstract

In 1918 Albert Einstein wrote in a letter to Walter Dällenbach against his own theory of optical force: *"It has long been known that the values I had derived with Laub at the time are wrong; Abraham, in particular, was the one who presented this in a thorough paper. The correct strain tensor has incidentally already been pointed out by Minkowski"*. Unfortunately after almost 100 years, it is still not clear why Einstein wrote so regarding the theory of optical/electromagnetic force (the optical stress tensor (ST)) associated with Lorentz force. The electromagnetic force is one of the four fundamental interactions (other three: the strong interaction, the weak interaction and gravitation) in nature. In spite of experiencing much progress from 1970, research on optical/electromagnetic forces has so far revealed only the partial nature of light-matter interaction. For example, inside a material media an appropriate description of photon momenta (i.e. the Abraham-Minkowski dilemma) and an appropriate description of stress tensors along with Lorentz /volumetric forces (known as Minkowski, Abraham, Chu, Einstein-Laub and Ampere/Nelson forces) are still matters of great controversy.

In this thesis, physics and applications of Lorentz force along with stress tensors and photon momenta have been investigated in details with special interest in tractor beam effect, plasmonic objects, chiral objects and the objects embedded in a generic material medium.

At first, we have considered simpler case: application of Lorentz force for the objects placed in air. Specifically we demonstrate how the mechanism of Lorentz force can be used in a tractor beam-like effect for pulling multiple Rayleigh particles placed outside a dielectric hollow core waveguide and coupler. We also represent the Lorentz force analysis for plasmonic off-axis and on-axis spherical heterodimers and it is shown that the reversal of longitudinal binding force can be easily controlled by forced symmetry breaking. Though it is commonly believed that plasmonic forces

mostly arise from the surface force and Fano resonance can be a promising way to achieve binding force reversal, our study based on Lorentz force dynamics suggests notably opposite proposals for the case of plasmonic spherical heterodimers.

Next, we have also considered objects those are embedded in a material medium. The fundamental results/proposals of this thesis are presented afterwards. We have shown that the well-known Lorentz force leads to inconsistent result (pushing force) instead of the experimentally observed optical pulling force as observed in interfacial tractor beam experiments. As one of the major contributions of this thesis, we identify the 'exact' reasons why the well-known distinct Lorentz/volumetric forces fail not only for interfacial tractor beam experiment but also for several other major radiation pressure experiments performed up to date. Later, we demonstrate that it is still possible to establish different equivalent time-averaged Lorentz / volumetric force formulas based on the fulfilment of just two 'consistency conditions'. Based on those proposed 'consistency conditions', finally, we demonstrate that by modifying the Einstein-Laub or Chu formulation; time-averaged STs and volume forces are obtainable, which can overcome the aforementioned inconsistencies. For example- these modified formulations can yield the 'correct' time averaged force similar to Minkowski's force for almost all the previous real experiments. Specially, our proposed modified Einstein-Laub ST can be considered as an efficient mathematical toolkit, an alternative of time and memory consuming volumetric forces, to yield the internal bulk force of a chiral or achiral object embedded in complex material backgrounds (i.e. homogeneous, heterogeneous, bounded etc.). Later, we have also shown an interesting application of modified Lorentz force to control the reversal of optical binding force of plasmonic cubes placed over plasmonic substrate due to strong Fano resonance.

Finally, based on our proposals throughout the thesis, at the end of this thesis we propose a new hypothesis named as the 'existence domain'. '*Existence domain*' is the region either outside of a scattering body taking only its exterior fields into account,

or in its interior considering only the inside fields. Though almost all the time averaged distinct STs and volumetric force laws are restricted to the idea of 'existence domain', we demonstrate that the stress tensor, volumetric force and photon momentum of Minkowski are free from such and other restrictions both in instantaneous and time averaged situations. After almost 100 years of Einstein's prediction, this thesis, most probably, finally answers why only Minkowski's theory of optical force and photon momentum remains consistent in all circumstances.

Proposals presented in this thesis can be very effective for resolving not only the dilemma of distinct stress tensors and optical Lorentz/ volumetric forces but also for settling the controversy of Abraham-Minkowski photon momenta. This thesis may also open a new window for optical pulling force/tractor beams along with the novel manipulation process of plasmonic dimers.

Table of Contents

Chapter 1

Chapter 2

Chapter 3

Chapter 4

Chapter 5

Modification of Lorentz Force for embedded chiral and achiral objects

Chapter 6

Modified Lorentz Force and Plasmonic Cube Dimers over Substrate: Binding Force Reversal 104

Chapter 7

Consistency of Minkowski's Theory: Some Final Proposals 123

Chapter 8

List of Figures

List of Tables

List of Acronyms (in Alphabetic Order)

3D	three dimensional
APM	Abraham photon momentum
BR	big rotate
CP	circularly polarized
DD	dipole dipole
DQ	dipole quadrupole
DWTB	dielectric waveguide tractor beam
EL	Einstein-Laub
FDTD	Finite difference time domain
ITB	interfacial tractor beam
LP	linearly polarized
LSP	localized surface plasmon
MEL	modified Einstein-Laub
MPM	Minkowski photon momentum
NOF	negative optical force
OM	optical manipulation

QD quadrupole dipole

QQ quadrupole quadrupole

ST stress tensor

SR small rotate

SPP surface plasmon polariton

List of Publications, Patents and Conferences

Publications in Peer-reviewed International Journals

†=Equal Contribution, *=Corresponding author.

1. Qiu, C.-W. †*, Ding, W. †, **Mahdy, M. R. C.**, Gao, D., Zhang, T., Cheong, F. C., Dogariu, A., Wang, Z. & Lim, C. T. Photon Momentum Transfer in Inhomogeneous Dielectric Mixtures and Induced Tractor Beam. *Light: Science and Applications* **4**, e278 (2015)**.** [Nature Publishing Group]

2. Rahman, M. M., Sayem, A. A., **Mahdy, M. R. C. ***, Haque, M. E., Islam, R., Chowdhury, S. T. R. & Matin, M. A., Tractor beam for fully immersed multiple objects: Long distance pulling, trapping, and rotation with a single optical set-up, Annalen der Physik **527**, 777 (2015). [Cover page and cover story of December 2015 issue of Annalen Der Physik]

3. Zhu, T. †, **Mahdy, M. R. C.** †, Cao, Y., Lv, H., Sun, F., Jiang, Z. & Ding, W. *, Optical pulling using evanescent mode in sub-wavelength channels. Opt. Express. **24**, 18436 (2016).

4. **M.R.C. Mahdy**†*, M. Q. Mehmood† , Weiqiang Ding, Tianhang Zhang, Zhi Ning Chen, Lorentz Force and the Optical Pulling of Multiple Rayleigh Particles outside the Dielectric Cylindrical Waveguides , Annalen der Physik 529, 1600213 (2017).

5. **M.R.C. Mahdy**[†*], Tianhang Zhang[†], Weiqiang Ding[*], Amin Kianinejad, Manuel Nieto-Vesperinas, Consistency of time averaged optical force laws for embedded chiral and achiral objects. *arXiv preprint arXiv:1704.00334* (2017).
   [Submitted version in journal: **M.R.C. Mahdy**[†*], Tianhang Zhang[†], Weiqiang Ding[*], Amin Kianinejad, Manuel Nieto-Vesperinas, A solution to the problem: time averaged total optical force.]

6. Dongliang Gao, Weiqiang Ding, Manuel Nieto-Vesperinas, Xumin Ding, **Mahdy Rahman**, Tianhang Zhang, Chwee Teck Lim and Cheng-Wei Qiu[*], Optical Manipulation from Microscale to Nanoscale: Fundamentals, Advances, and Prospects. *Light: Science and Applications* **6**, e17039 (2017)**.** [Nature Publishing Group]

7. Tianhang Zhang, **M.R.C. Mahdy**, Yongmin Liu, Jinghua Teng, Lim Chwee Teck, Zheng Wang and Cheng-Wei Qiu*, All-Optical Chirality-sensitive Sorting via Reversible Lateral Forces in Interference Fields. *ACS Nano* (2017).

8. **M.R.C. Mahdy**, Md. Danesh, Tianhang Zhang, Weiqiang Ding, Cheng-Wei Qiu*, Lorentz Force and Plasmonic on-axis and off-axis Spherical Heterodimers: Reversal of Optical Binding Force as the Effect of Symmetry Breaking. (will be submitted in journal soon)

9. **M.R.C. Mahdy**, Tianhang Zhang, Md. Danesh, Weiqiang Ding, Cheng-Wei Qiu*, Plasmonic Cube Dimers over Substrate: A Flexible Approach of Binding Force Reversal Induced by Fano Resonance. (will be submitted in journal soon)

10. **M.R.C. Mahdy**, GD Al-Quaderi, Tianhang Zhang, Weiqiang Ding, Manuel Nieto-Vesperinas, Cheng-Wei Qiu* , An investigation on the consistency of optical forces and photon momenta for instantaneous and time averaged scenario (under preparation) [a small part of the article already discussed in: Mahdy, M. R. C., Dongliang Gao, Weiqiang Ding, M. Q. Mehmood, Manuel Nieto-Vesperinas, and Cheng-Wei Qiu, arXiv:1509.06971 (2015)]

Chapter 1

Introduction and Literature Review

1.1 Introduction

The electromagnetic force is one of the four fundamental interactions (commonly called forces) in nature. The other three fundamental interactions are the weak interaction, the strong interaction, and gravitation. By utilizing the optical/electromagnetic force, optical manipulation (OM) [such as optical cooling [1], trapping [2], binding [3-5], sorting and transporting [6-8]] have experienced an intensive development in the past 40 years [9-11]. OM is now considered as one of the most important tools in many scientific areas, including optics [9], atomic physics [12,13], biological science [14] , and chemistry [15]. Traditionally, the configuration of a small dielectric sphere in the focus is usually investigated by considering the scattering of the fundamental mode of a Gaussian beam [1,2]. According to the theory of electrostatics state, small Rayleigh particles develop an electric dipole moment in response to the electric field of the light and the induced dipole is then drawn by the field intensity gradients; this phenomenon results in a force called Optical Gradient Force [16]. Again, due to the transfer of momentum from the photons to an object, another optical force namely Optical Scattering Force, comes into action. Optical Scattering Force is the combination of radiation pressure and spin curl component [16]. Recently, OM has gone beyond this scenario, and more complex configurations have been investigated.

For example, OM resolution has been increased beyond the Rayleigh limit by extending it to the near-field, thus taking advantage of non-radiative forces [17,18]. The manipulated objects can be generic Mie or bigger sized objects [rather than a

single and small dielectric medium] such as magnetodielectric [16], chiral [19-21], plasmonic [22,23] or multilayered coating [24]. For such cases, the common way to yield the total optical force is to apply the well-known Maxwell stress tensor (ST) method [25] instead of the approximate force calculation method of dipolar force [16] (i.e. gradient, scattering and spin curl force). In contrast, the Lorentz/volumetric force is applied to compute the force density throughout the particles, which demonstrates regions of compression and tension within the medium [26]. Most importantly, Lorentz force also describes how the volumetric force on a generic object is distributed [27], which is described as Lorentz volumetric force distribution. This information cannot be retrieved from the optical stress tensor based [25] force calculation. The process of yielding the total force become more complex when the embedding background is considered material media [28] instead of air or vacuum.

The aim of this chapter is to present an introductory picture of OM (i.e. literature review); from fundamental photon momentum transfer, dilemma, existing problems and advances toward future prospects on nanoscale and microscale objects and structures, which have recently attracted considerable attention [17, 28, 29]. At first, in the next section, we have reviewed very shortly how to calculate the optical force on an object placed in air. After that, the Lorentz/volumetric force and its connection with stress tensor have been reviewed for simple case: object placed in air. However, when an object is placed in material media instead of the air background, optical force calculations require more appropriate and accurate description of photon momenta and forces. This ‘appropriate and accurate description’ is still quite controversial [28]. As a result, dilemma on distinct photon momenta and electromagnetic stress tensors [27], which are connected with different Lorentz/volumetric force densities inside matter, are reviewed in the later part in this chapter. Almost half part of this thesis has tried to cover and solve such controversial but fundamental issues on optical stress tensors, Lorentz /volumetric forces and the

photon momenta inside material medium. The other half part of this thesis mainly focuses on the novel applications of the Lorentz and proposed modified Lorentz force on plasmonic dimers and counter-intuitive tractor beam effect.

Though previously OM was restricted mainly on Gaussian beams or simple backgrounds, recently the incident light is also constituted by special wave fields such as non-diffraction Bessel beams, multiple beam interference, or complex backgrounds. A representative example is the recently proposed optical tractor beams [30-36], which can exert a negative non-conservative force on a body pulling it opposite to its propagation direction [37]. In addition, when the objects are resonant with the incident light (i.e. plasmonic object [38]), the optical force may be greatly enhanced. Recently force on plasmonic objects has achieved considerable attention due to some unusual behavior of plasmonic objects connected with Fano resonance [39], super scattering [40], localized surface plasmon [41] and surface plasmon propagation [42]. As a result, just before the end of this chapter, two very special applications of optical force such as counter-intuitive optical pulling force with tractor beams and the reversal of near field optical binding force due to plasmonic objects have also been discussed. In fact, the applications of Lorentz force dynamics is still not investigated in details for such exciting cases of optical manipulations: tractor beams and plasmonic dimers. Almost half part of this thesis has tried to cover such issues based on Lorentz and proposed modified Lorentz force.

Finally, at the end of this chapter, a detail outline of the thesis has been presented in the last section.

1.2 The Simplest Case of Optical Force Calculation: Object placed in air

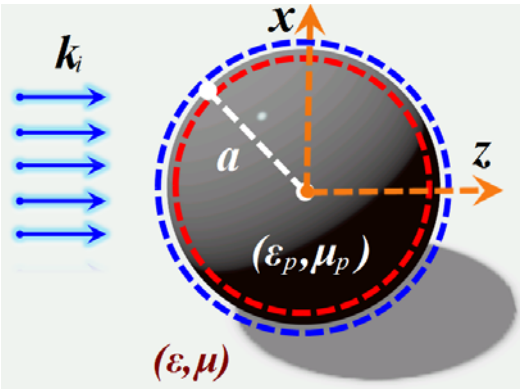

Fig. 1.1 Optical momentum transfers from an incident plane wave of propagating vector k_i to a spherical particle with permittivity ε_p and permeability μ_p. The total force calculated using the Stress Tensor (ST) is: F_{out} when the time-averaged ST is evaluated from fields outside the particle, through a surface of radius $r = a^+ = 1.001a$ (blue lines), and F_{in} when the time-averaged ST is evaluated from the inside of the particle through a surface of radius $r = a^- = 0.999a$ (red lines).

We specify that throughout this thesis we refer to 'exterior' or 'outside' forces as those evaluated outside the volume of the macroscopic particles, while ‘interior’ or 'inside' refer to those quantities inside this object volume. To determine the optical force experienced by a particle, we refer to Fig. 1.1. If we set a boundary very close to the particle from outside, i.e., radius $r = a^+$, (a is the particle radius, assuming it spherical (in three dimensions) or cylindrical (in two dimensions)), and calculate the time-averaged force using only exterior fields, this will be considered as the outside force. On the other hand, if we set a boundary very close to the particle from inside, i.e. at $r = a^-$, and calculate the time averaged force using only interior fields, this will be the inside force.

Usually the ‘outside optical force’ [35, 43] is calculated by the integration of time averaged Minkowski [35, 43] stress tensor at $r = 1.01a = a^+$ (It means we are selecting a spherical surface with a radius slightly larger than the object, on which the

integration of stress tensor $\overline{\overline{\boldsymbol{T}}}$ is calculated for the total optical force) employing the background fields of the scatterer of radius a:

$$\left\langle \boldsymbol{F}_{\text{Total}}^{\text{Out}} \right\rangle = \oint \left\langle \overline{\overline{\boldsymbol{T}}}^{\text{out}} \right\rangle \cdot d\boldsymbol{s}$$
$$\left\langle \overline{\overline{\boldsymbol{T}}}^{\text{out}} \right\rangle = \frac{1}{2}\text{Re}[\boldsymbol{D}_{\text{out}}\boldsymbol{E}_{\text{out}}^{*} + \boldsymbol{B}_{\text{out}}\boldsymbol{H}_{\text{out}}^{*} - \frac{1}{2}\overline{\overline{\boldsymbol{I}}}(\boldsymbol{E}_{\text{out}}^{*} \cdot \boldsymbol{D}_{\text{out}} + \boldsymbol{H}_{\text{out}}^{*} \cdot \boldsymbol{B}_{\text{out}})] \quad (1.1)$$

Where 'out' represents the exterior total field (i.e. incident plus the scattered field) of the scatterer; $\boldsymbol{E}$, $\boldsymbol{D}$, $\boldsymbol{H}$ and $\boldsymbol{B}$ are the electric field, displacement vector, magnetic field, and induction vectors, respectively, while $\langle\ \rangle$ represents the time average and $\overline{\overline{\boldsymbol{I}}}$ the unity tensor. On the other hand, if Eq (1.1) is applied at $r = 0.999a = a^{-}$ [43, 44] by employing the internal field of the scatterer placed in air, it leads to zero force [44] for lossless scatterers. As a result, the usual way is to determine the total force is the 'outside force' based on Eq (1.1). But a question arises: what is the connection of Eq (1.1) with optical volumetric/Lorentz force? Answer of this last question is discussed in details in the next section.

1.3 Optical Force Calculation by Volumetric Force

Answer of the last question, connection of Lorentz force with stress tensor, comes from the linear momentum conservation equation [17]. According to linear momentum conservation equation, the total transferred momentum to an object should be written as [17]:

$$\nabla \cdot \overline{\overline{\boldsymbol{T}}} = \boldsymbol{f} + \frac{\partial}{\partial t}\boldsymbol{G} \quad (1.2a)$$

$\boldsymbol{G}$ is the electromagnetic momentum density and $\boldsymbol{f}$ is the volumetric force density. Eq (1.2a) is considered as one of the main pillars of classical

electrodynamics along with Maxwell's equations. Eq (1.2a) can also be described in an alternative approach [17]: $\boldsymbol{p}_{\text{Total}} = \boldsymbol{p}_{\text{Mech.}} + \boldsymbol{p}_{\text{Non-Mech.}}$ Here $\boldsymbol{p}$ represents momentum. Ultimately in the time average form, Eq (1.2a) turns into the force equation:

$$\oint \left\langle \bar{\bar{\boldsymbol{T}}} \right\rangle \cdot d\boldsymbol{s} = \left\langle \boldsymbol{F} \right\rangle = \int \boldsymbol{f}\, dv \tag{1.2b}$$

It should be noted that $\frac{\partial}{\partial t}\boldsymbol{G}$ term vanishes due to time average. We have already discussed regarding the left side of Eq (1.2b), the surface integral of optical stress tensor, in the previous section. The right side of Eq (1.2b) is volume integral. Now a problem arises. Though the background is air, the Lorentz /volumetric force, $\boldsymbol{f}$, is connected with the idea of optical force distribution inside the object. As a result, though the left side of Eq (1.2a) [i.e. total momentum] is a single conserved quantity, in the right side of Eq (1.2) the form of $\boldsymbol{G}$ or $\boldsymbol{f}$ is not unique. In Eq (1.2a), the $\partial\boldsymbol{G}/\partial$t term is connected with photon momentum, $\boldsymbol{p}_{\text{Non-Mech.}}$; where $\boldsymbol{p}_{\text{Non-Mech.}} = \int \boldsymbol{G}\, dV$ and $\boldsymbol{G}$ is the electromagnetic momentum density. Inside matter, two different definition of photon momenta are considered, which is known as the Abraham-Minkowski controversy [27]. This controversy will be discussed shortly in a forthcoming sub-section. However, the usual common/generic 'compact' form of the time averaged Lorentz volumetric force is written as [45]:

$$\boldsymbol{f} = \rho_{\text{total}}\boldsymbol{E} + \boldsymbol{J}_{\text{total}} \times \boldsymbol{B} \tag{1.3}$$

ρ_{total} is the total volumetric charge, $\boldsymbol{J}_{\text{total}}$ contains the densities of free as well as bound currents arising from polarization and magnetization densities and $\boldsymbol{B}$ is the magnetic induction [45]. Surprisingly, there are five different 'elaborate' forms of volumetric force [27,28] and their corresponding stress tensors as shown in Table-1.1.

It is still a matter of debate which volumetric Lorentz force is more appropriate than the other one [27,28,46].

Interestingly, when the background of an embedded object is air or vacuum, all the Lorentz volumetric forces shown in Table-1.1 leads to exactly same time averaged total force according to Eq (1.2b). So, when the background of an object is air, for the calculation of time averaged total force, there is no problem. But the problem arises from the idea of volumetric force distribution process. This matter is discussed in the next section.

Table-1.1: Previous macroscopic tress tensors, electromagnetic momentum densities and force density laws

	Stress tensor, $\overline{\overline{\boldsymbol{T}}}$, and force density, $\boldsymbol{f}$	Electromagnetic momentum density, $\boldsymbol{G}$
Minkowski	$\overline{\overline{\boldsymbol{T}}} = \boldsymbol{DE} + \boldsymbol{BH} - \frac{1}{2}\left(\boldsymbol{B}\cdot\boldsymbol{H} + \boldsymbol{D}\cdot\boldsymbol{E}\right)\overline{\overline{\boldsymbol{I}}}$ $\boldsymbol{f} = -\frac{1}{2}\boldsymbol{E}^2\Delta\varepsilon - \frac{1}{2}\boldsymbol{H}^2\Delta\mu$	$\boldsymbol{D}\times\boldsymbol{B}$
Abraham	$\overline{\overline{\boldsymbol{T}}} = \frac{1}{2}\left[\boldsymbol{DE} + \boldsymbol{ED} + \boldsymbol{BH} + \boldsymbol{HB} - \left(\boldsymbol{B}\cdot\boldsymbol{H} + \boldsymbol{D}\cdot\boldsymbol{E}\right)\overline{\overline{\boldsymbol{I}}}\right]$ $\boldsymbol{f} = \left(-\frac{1}{2}\boldsymbol{E}^2\Delta\varepsilon - \frac{1}{2}\boldsymbol{H}^2\Delta\mu\right) + \mathbf{f}^{\mathbf{A}};$ $\mathbf{f}_A = \left(n^2-1\right)\frac{\partial}{\partial t}\left(\frac{\boldsymbol{E}\times\boldsymbol{H}}{c^2}\right)$	$\frac{\boldsymbol{E}\times\boldsymbol{H}}{c^2}$
Einstein-Laub	$\overline{\overline{\boldsymbol{T}}} = \boldsymbol{DE} + \boldsymbol{BH} - \frac{1}{2}(\mu_o\boldsymbol{H}\cdot\boldsymbol{H} + \varepsilon_0\boldsymbol{E}\cdot\boldsymbol{E})\overline{\overline{\boldsymbol{I}}}$ $\boldsymbol{f} = (\boldsymbol{P}\cdot\nabla)\boldsymbol{E} + (\boldsymbol{M}\cdot\nabla)\boldsymbol{H} + \frac{\partial\boldsymbol{P}}{\partial t}\times\mu_o\boldsymbol{H} - \frac{\partial\boldsymbol{M}}{\partial t}\times\varepsilon_0\boldsymbol{E}$	$\frac{\boldsymbol{E}\times\boldsymbol{H}}{c^2}$
Chu	$\overline{\overline{\boldsymbol{T}}} = \varepsilon_0\boldsymbol{EE} + \mu_0\boldsymbol{HH} - \frac{1}{2}(\mu_o\boldsymbol{H}\cdot\boldsymbol{H} + \varepsilon_0\boldsymbol{E}\cdot\boldsymbol{E})\overline{\overline{\boldsymbol{I}}}$ $\boldsymbol{f} = -(\nabla\cdot\boldsymbol{P})\boldsymbol{E} - (\nabla\cdot\boldsymbol{M})\boldsymbol{H} + \frac{\partial\boldsymbol{P}}{\partial t}\times\mu_0\boldsymbol{H} - \frac{\partial\boldsymbol{M}}{\partial t}\times\varepsilon_0\boldsymbol{E}$	$\frac{\boldsymbol{E}\times\boldsymbol{H}}{c^2}$
Ampere/ Nelson	$\overline{\overline{\boldsymbol{T}}} = \varepsilon_0\boldsymbol{EE} + \mu_0^{-1}\boldsymbol{BB} - \frac{1}{2}\left(\mu_0^{-1}\boldsymbol{B}^2 + \varepsilon_0\boldsymbol{E}^2\right)\overline{\overline{\boldsymbol{I}}}$ $\boldsymbol{f} = -(\nabla\cdot\boldsymbol{P})\boldsymbol{E} + \frac{\partial\boldsymbol{P}}{\partial t}\times\boldsymbol{B} + (\nabla\times\boldsymbol{M})\times\boldsymbol{B}$	$\varepsilon_0\boldsymbol{E}\times\boldsymbol{B}$

Polarization, $\boldsymbol{P}$; magnetization, $\boldsymbol{M}$.

1.4 Different Volumetric Force Laws: Problem of Force Distribution

One remarkable example on the inconsistency of optical volumetric force distribution is the famous Ashkin–Dziedzic experiment in ref. [47]. A two-dimensional fluid dynamic simulations of the Ashkin–Dziedzic experiment has been conducted in ref. [28] as shown in Fig. 1.2. In Fig. 1.2, the lower fluid (blue) represents water (n = 1.33) and the upper fluid (white) represents air (n = 1). In [28], the air–water interface is excited by a 60 ns-long and 530-nm-wavelength pulse at normal incidence. The time-averaged force density distributions exerted by the pulse are calculated using the Minkowski, Abraham, Einstein–Laub, Chu, and Ampere formulations, which are shown next to the resulting velocity field (blue arrows) of the deformed interface [28] in Fig. 1.2. The Abraham, Minkowski, and Einstein–Laub formulations predict an upward bulge for TE and TM polarizations for both illumination directions [consistent with experimental observations [47]]. The Ampere and Chu formulations predict an upward and downward bulge for TM and TE polarizations, respectively [inconsistent with experimental observations [47]].

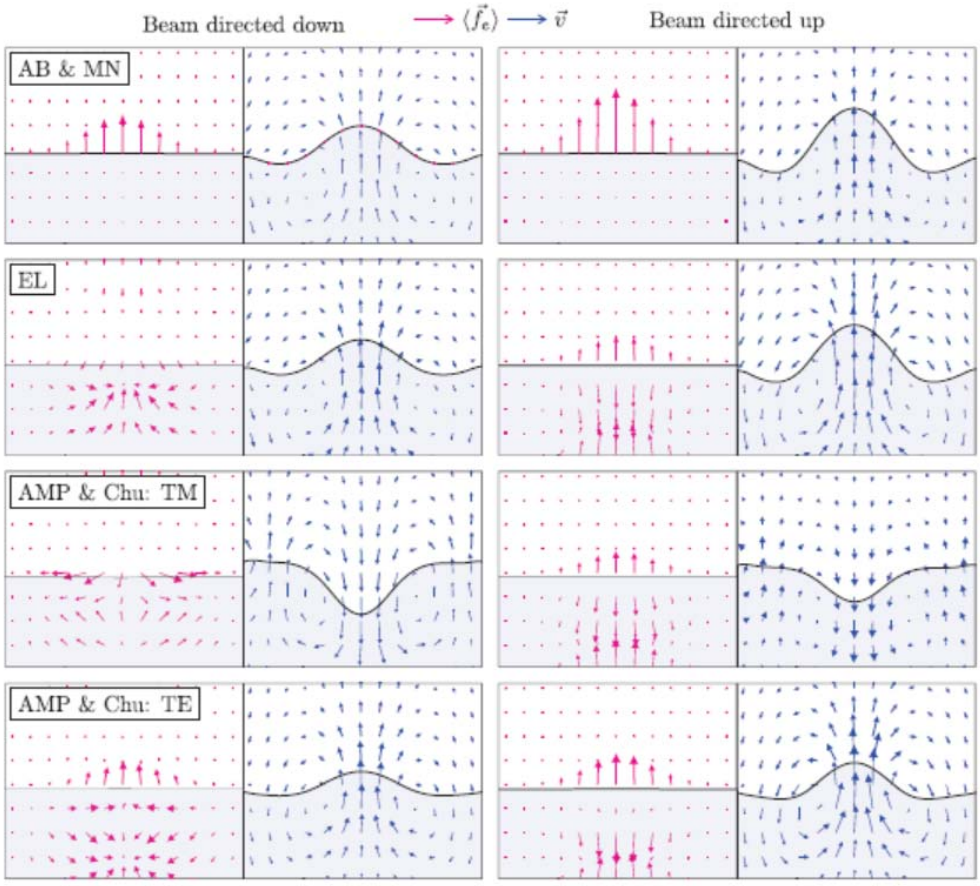

Fig. 1.2: Volumetric force distribution for different force laws according to [28] for the Ashkin–Dziedzic experiment [47]. The Abraham, Minkowski, and Einstein–Laub formulations predict an upward bulge for TE and TM polarizations for both illumination directions [consistent with experimental observations [47]]. The Ampere and Chu formulations predict an upward and downward bulge for TM and TE polarizations, respectively [inconsistent with experimental observations [47]].Figures adapted and reproduced with permission from ref. [28], © 2015, Institute of Physics (IOP) publishing.

1.5 Problem with Optical Force Calculation: Object Embedded in Material Background

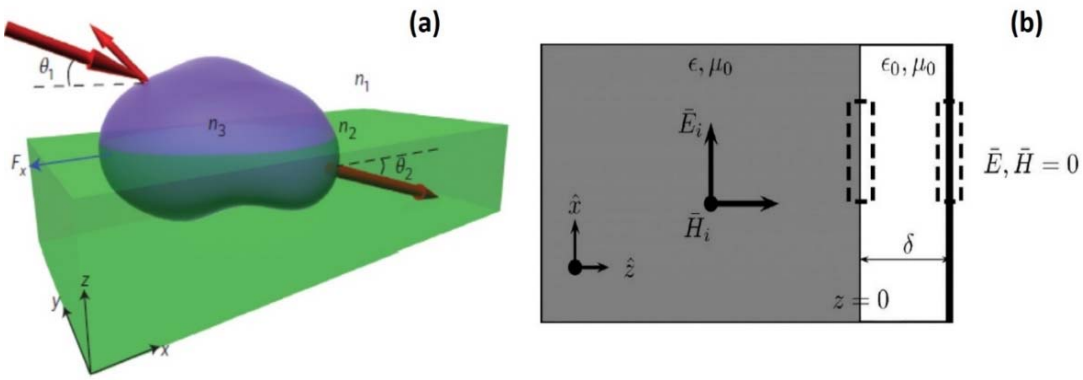

Fig. 1.3: Though the calculation of time averaged optical force by different volumetric/Lorentz forces lead to same result for the case of air background, this fact does not remain valid for the case of material background. (a) The prototype of the interfacial tractor beam experiment reported in [35]. So far two different independent works ([28] and [43]) have investigated that same experiment reported in [35]. Different volumetric force laws lead to distinct results; especially Chu and Ampere forces lead to inconsistent pushing force. (b) Another famous example of such disagreements [53]: the 1954 Jones–Richards experiment [55] and the 1978 Jones–Leslie experiment [56]. It is observed that only Minkowski and Abraham formulations always predict the time averaged results which are consistent to the real experimental observations in [55] and [56] according to [28]. Figures adapted and reproduced with permission from (a) ref. [35], © 2013, Nature publishing group and (b) ref. [53], © 2011, Optical Society of America (OSA).

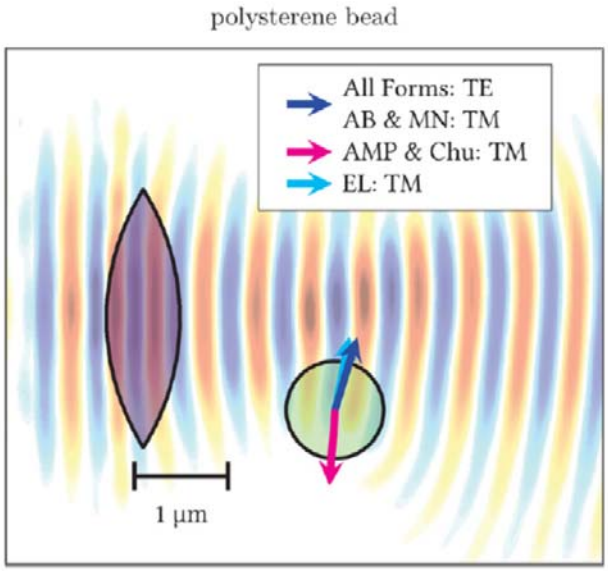

Fig. 1.4: Simulated radiation pressure on a polystyrene bead (green) [28] placed at the edge of the focal point of a continuous-wave beam (λ_0= 532 nm) in a background medium of water (n = 1.33). The polystyrene bead (n = 1.58) has a diameter of 820 nm and the force acting on it has been determined in [28] under the rigid body assumption by integrating the force density distribution within the bead calculated using the Minkowski, Abraham, Einstein–Laub (EL), Chu, and Ampere/Nelson formulations. These formulations predict distinct magnitudes of total force in [28] and lead to inconsistent result (direction of total force) with Chu and Ampere formulations for TM polarization. Figures adapted and reproduced with permission from ref. [28], © 2015, Institute of Physics (IOP) publishing.

The calculation process of total optical force on a body embedded in a medium has different versions [27,28] [cf. Table- 1.1]. But this force is usually derived by integrating the momentum flux over any closed surface surrounding this object [cf. Fig. 1.1]. For example- initially, Minkowski [48] suggested that a field energy-momentum tensor should preserve its form in all Lorentz frames. According to his suggestion, the stress tensor should be:

$$\overline{\overline{T}}_{\mathrm{M}} = \boldsymbol{DE} + \boldsymbol{BH} - \frac{1}{2}(\boldsymbol{B}\cdot\boldsymbol{H} + \boldsymbol{D}\cdot\boldsymbol{E})\overline{\overline{I}} \tag{1.4}$$

The volumetric force density of Minkowski's stress tensor is known as Helmholtz force density:

$$\boldsymbol{f}_{\mathrm{H}} = -\frac{1}{2}\boldsymbol{E}^2\Delta\varepsilon - \frac{1}{2}\boldsymbol{H}^2\Delta\mu\,. \tag{1.5}$$

Major radiation pressure experiments have always supported Minkowski's theory [27,28, 35, 46, 49,50].

Alternatively, Abraham suggested that the symmetric electro-magnetic stress tensor and force density in matter as [51,52]:

$$\overline{\overline{\boldsymbol{T}}}_{A} = \frac{1}{2}[\boldsymbol{DE} + \boldsymbol{ED} + \boldsymbol{BH} + \boldsymbol{HB} - (\boldsymbol{B}\cdot\boldsymbol{H} + \boldsymbol{D}\cdot\boldsymbol{E})\overline{\overline{\boldsymbol{I}}}\,], \tag{1.6}$$

$$\boldsymbol{f}_{\mathrm{A}} = \left(-\frac{1}{2}\boldsymbol{E}^2\Delta\varepsilon - \frac{1}{2}\boldsymbol{H}^2\Delta\mu\right) + \mathbf{f}^{\mathbf{A}} \tag{1.7}$$

where $\mathbf{f}^{A}$ is the extra "Abraham force" density [46,50]. Experiments in favour of Abraham formulation will be found in detailed in Refs. [28,46,49,50]. However, it should be remarked that in most configurations, dealing with time-averaged forces of an object embedded in any material medium, both theories yield the same time-averaged optical force [28, 46, 49, 50]. In fact, the difference between Minkowski's

force and Abraham's force arises only in the instantaneous force [46, 50] mainly due to the extra "Abraham force". It is remarkable that, like the Minkowski's formulation, Abraham's theory does not separate the momentum into the sum of field and material components. It describes $\boldsymbol{D}$ and $\boldsymbol{B}$ as a single quantity so that the polarization $\boldsymbol{P}$ and magnetization $\boldsymbol{M}$ are not separately formulated [cf. Table-1.1].

There are also three major stress tensors and volume forces other than that of Abraham or Minkowski formulations [27, 28, 46]. Those stress tensors and volume forces are: Einstein-Laub, Chu and Nelson/ Ampere stress tensor as shown in Table-1.1 along with their corresponding Lorentz volumetric force density. But when the background is considered as a material medium rather than air or vacuum, those different volumetric force formulations given in Table-1.1 predict distinct magnitudes and directions of the time-averaged force on an embedded scatterer in several experiments [28,46] [cf. Fig. 1.3 and 1.4].

The notable fact is that the time averaged total force based on Eq (1.4) or (1.6) is usually considered as 'outside total force' [35,43] [which is calculated at r=1.01a = a^+ employing the exterior background fields of the embedded scatterer]. On the other hand, whether Einstein-Laub, Chu and Nelson/ Ampere formulations should be applied as 'outside force' or 'inside force' (which is calculated at r= 0.999a=a^- employing the interior fields of the embedded scatterer) is still not properly understood. The time averaged total forces significantly differ for different volumetric formulations according to [28] and [46] for real experiments conducted so far [2,35,43,53-56] considering background as a material medium and few other cases [cf. Fig. 1.3 and 1.4]. Hence it is still a quite ambiguous task to determine which volumetric force and its associated ST are more appropriate when the background is material media instead of air or vacuum. The controversies in the area of optical force calculation would be resolved if the corresponding ranges of validity of the optical force formulations are clearly identified. This issue has been investigated in some major parts of this thesis.

However, it should be noted that: As Minkowski's (or Abraham's) time averaged formulations have always led to the correct time averaged total force for almost all major radiation pressure experiments, the formulations of Minkowski (or Abraham) is yet considered the most reliable approach [50] for the time-averaged force on objects of any size or shape.

1.6 Abraham-Minkowski Controversy: Photon Momentum inside Matter

Generally speaking, the force is a consequence of the change of momentum carried by photons [1,2,35,43,47,53]. Interestingly, there is a long-standing debate over the determination of the momentum of photons in media, which may now be synthesized as the Minkowski-Abraham controversy [27, 57]. A century has now passed pertaining to the correct form of optical momentum in media. Both Experiments and theories have been applied at classical and quantum levels in attempt to resolve this problem. The ensuing debate on photon momentum, **p**, in matter is essentially known as the Abraham-Minkowski (AM) or related controversies [58] in electrodynamics, i.e., whether one should write:

$$p_{Min} = \frac{n\hbar\omega}{c}, \quad \text{or} \quad p_{Abr} = \frac{\hbar\omega}{nc}\ , \tag{1.8}$$

where $\hbar$ is the reduced Planck's constant, ω represents the angular frequency of light, c is its speed in vacuum, and n denotes the refractive index of the medium. In terms of $\boldsymbol{G}$ inside a medium, Eqs in (1.8) are written as [58]:

$$\boldsymbol{p}_{\mathrm{Abr}} = \int dV \frac{\boldsymbol{E}\times\boldsymbol{H}}{c^2} \quad \text{and} \quad \boldsymbol{p}_{\mathrm{Min}} = \int dV \boldsymbol{D}\times\boldsymbol{B}\,. \tag{1.9}$$

The Abraham MD is $\boldsymbol{G}_{Abr} = (\boldsymbol{E} \times \boldsymbol{H}) / c^2$, whereas the Minkowski momentum density is characterized by $\boldsymbol{G}_{Mink.} = \boldsymbol{D} \times \boldsymbol{B}$. Though there are insightful arguments in favour of both momentum densities, the real issue is which one is measurable in a particular event, rather than the fact of which one is correct.

Although it is believed that the idea of Abraham photon momentum as kinetic momentum of photon and Minkowski photon momentum as canonical momentum of photon resolves the conceptual complexity regarding these two rivalry momenta [58], their connections with the rivalry stress tensors and Lorentz/volumetric force formulas are still not clear. This issue has been investigated in some parts of this thesis.

1.7 Optical Tractor Beams

Manipulation of objects with laser beams has always been a hot topic in scientific fields and science fiction. In the latest decade, "tractor beams" which drag trapped objects towards the light source, have attracted much attention [25,30-36,59-64].

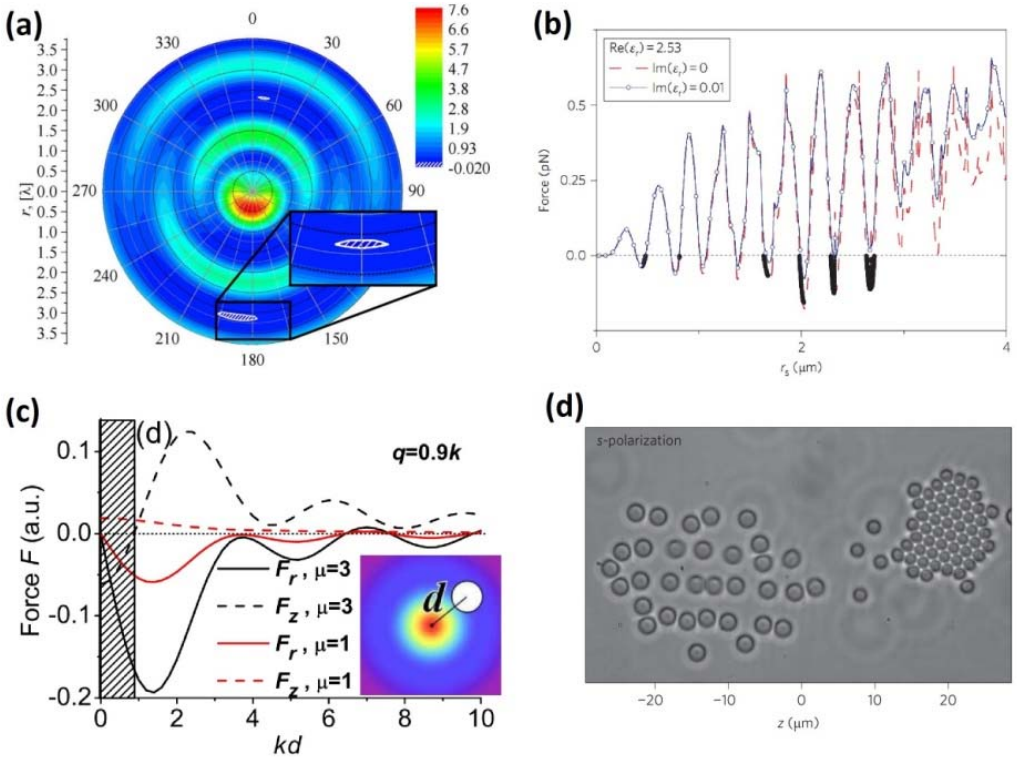

Fig.1.5 Different examples of tractor beams. (a) Distribution of optical force along the wave axis on a silver nanoparticle at the wavelength of 400 nm. The inset shows the region of negative optical force (NOF). (b) the optical force on a polystyrene sphere by a Bessel beam. It shows that optical pulling force is possible for different radii of polystyrene particles. (c) the longitudinal forces F_z and radial forces F_r as a function of radial distance between the particle and beam axis. The shaded region represents stable pulling effect due to $F_z<0$ and $F_r<0$. Objects near the axis are confined by gradient force and transported in propagation direction by scattering force. (d) polystyrene particles with radii of 800 nm and 1000 nm are separated by s-polarized beam. Figure reproduced with permission from: (a) ref. [32]; © 2010, Optical Society of America (OSA), (b) ref. [59]; © 2011, Nature publishing group, (c), ref.[25]; © 2011, American Physical Society (APS), (d) ref.[36]; © 2013, Nature publishing group.

A tractor beam is a traveling wave which exerts a negative scattering force to a scatterer and pulls it opposite to the propagation direction of light. Most beams of light do not act as tractor beams because radiation pressure tends to drive illuminated objects down-stream. A tractor beam pulls and transports an object over a long

distance, whereas an optical tweezers cannot be termed as a tractor beam because of its inherently limited range and due to the use of gradient force.

Previous works regarding optical pulling using tractor beams can be divided into well-defined procedures. For example: (a) It has been demonstrated [32] that there is a region of negative optical force (NOF) for a class of designed optical beams [Fig. 1.5(a)]. However, the regions of NOF are small compared to the incident wavelength. Thus a nondiffraction beam constituted by 24 plane waves with the same k_z component was used in Ref. [31], (b) generating a negative force by exciting multipoles inside a scatterer [59], (c) the use of a single non-paraxial Bessel beam [Fig.1.5(c)] [25, 30], (d) A tractor beam generated by the interference of a single Gaussian beam and its reflection by a dielectric mirror also demonstrated the pulling effect [36]. This kind of tractor beam can sort different sizes of particles by switching between s- and p-polarized beams [Fig.1.5 (d)]. (e) Building a standing wave named the optical conveyor-belt [60, 61], (f) employing gain [62] or metamaterial [63] background media, (g) placing the particle between two different media to make linearly polarized light [35,43] to act as a tractor beam and (h) introducing the optical conveyor [33] as a travelling wave with two super-imposed zeroth ordered Bessel beams and later the all-rounder beam with two super-imposed higher order Bessel beams with frequency difference between them [34] as shown in Fig. 1.6 (a) and (b). However, most of the times optical pulling effects have been discussed from the point of view of quasi static analysis based on the external dipole force methods [30,34,62]; without considering much analysis on full electrodynamic calculation or the Lorentz force [27,28,65]. What is the physical connection of optical pulling force with Lorentz volumetric force? Answers of these questions are investigated later in this thesis.

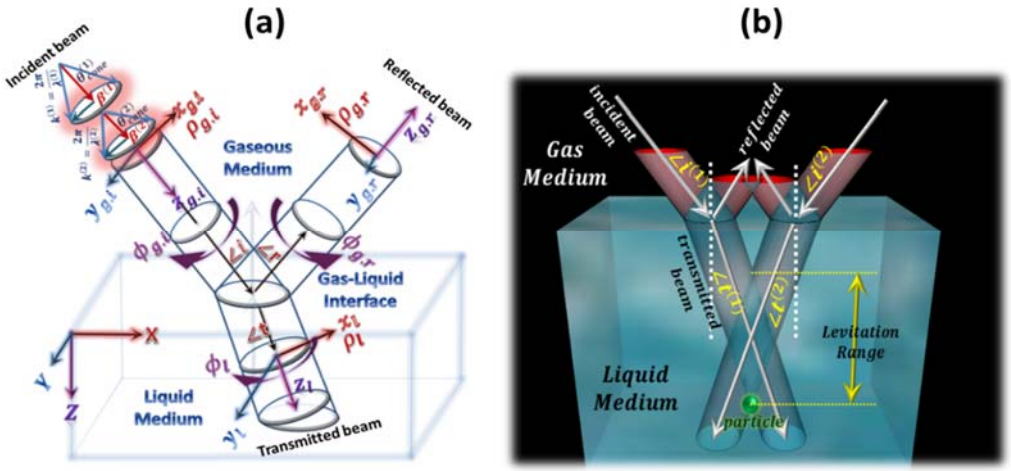

Fig.1.6: Continuous and three dimensional stable manipulations of fully immersed particles by using the optical gradient force generated by superimposing [34]: (a) coaxial pair of Bessel beams of reversed orders and different frequencies and (b) Non coaxial setup for a tractor beam with two Bessel beams of different helical nature. Only the particles located within a certain spatial range can be levitated using this latter beam set-up. Figures adapted and reproduced with permission from ref. [34], © 2015, WILEY-VCH Verlag GmbH & Co. KGaA, Weinheim.

1.8 Reversal of Near Field Optical Binding Force

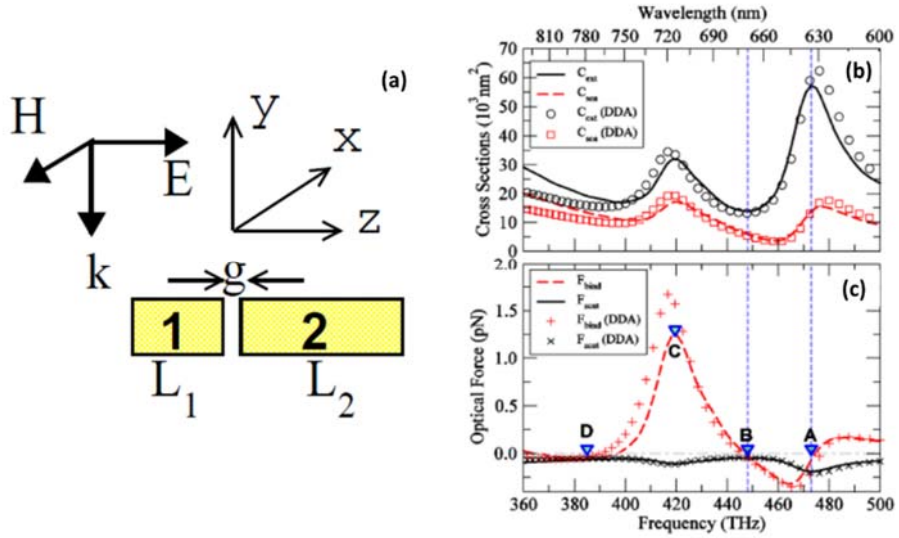

Fig.1.7: An example of binding force reversal due to Fano resonance. (a) The geometry of the system and the incoming light configuration. The plasmonic dimer consists of two nanorods with L_1 = 100 nm, L_2 = 280 nm, and gap g = 10 nm [22]. The diameter of the nanorods is d = 40 nm. (b) Optical features associated with the Dipole-Quadrupole Fano resonance. Optical extinction cross sections and optical scattering cross sections [22]. (c) Optical forces between the two nanorods and along the **k**-direction [22]. Figures adapted and reproduced with permission from ref. [22], © 2013, Optical Society of America (OSA).

In addition to the optical forces directly from light-matter interaction, optical binding forces can emerge from the momentum exchange between multiple particles. Light-mediated optical binding offers a new way for self-assembly, organization, and cell sorting [3,4, 66-68]. The spheroidal nanoparticles could arrange themselves into clusters, chains, photonic lattices and linear lines by optical binding [69,70]. Alternately, computer-generated holographic tweezers could also be used to organize particles into such nanostructures in three dimensions [71,72]. Especially optical binding forces of metallic nanoparticles have been found to be over 20 times larger than the gradient force [73] and they decayed slower than the gradient force, [74] which enables extremely stable nanometer manipulation.

Recently the reversal of near field optical binding force has achieved much attention [22,23,38,75,76]. However, such reversal of near field binding force is mostly connected with the plasmonic dimers [22, 23, 38, 75]. Based on Fano resonance, the reversal of near field optical binding force has been reported in [22] and [23] for nanorod structures [22] and for disk along with a ring structure [23] as shown in Figs. 1.7 and 1.8. 'Whether such Fano resonance (raised from heterodimer interaction) is a universal process of achieving binding force reversal?'- Answer of this question is still unknown. In addition, though Lorentz force analysis has been applied previously in [65,77-80] to understand the mechanism of chirality induced force, Luneburg lenses, mechanical interaction between light and graded index media, cloaking effect, background effect on radiation pressure; such analysis has never been applied to understand the plasmonic effects and plasmonic binding force. How the optical force distributes itself and which part of the total force is mainly responsible for plasmonic binding force reversals will be discussed based on the Lorentz force dynamics in this thesis.

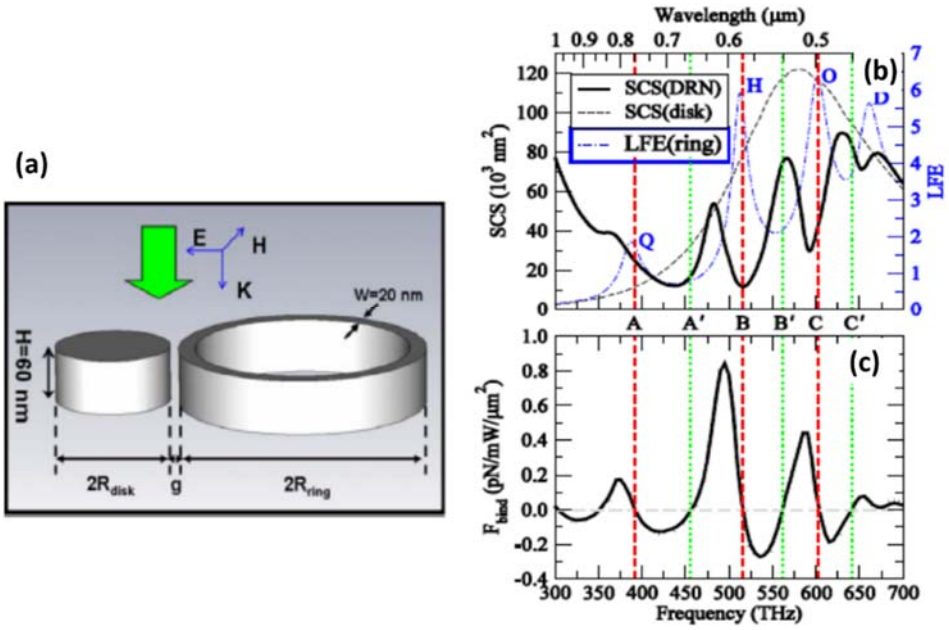

Fig. 1.8: Another example of binding force reversal due to Fano resonance. (a) disk-ring structure and the incident light [23]. (b) Scattering cross section of the disk-ring structure (black-solid line) and the individual nanodisk (black-dashed line) [23]. The local field enhancement of the individual nanoring (blue dash-dotted line) is also plotted. (c) Optical binding force spectrum of the disk-ring structure. The reversal points are marked with A, B, and C with respect to the vertical dashed lines, and the other reversal points are marked with A', B', and C' according to the vertical dotted lines [23]. Figures adapted and reproduced with permission from ref. [23], © 2013, Optical Society of America (OSA).

1.9 Thesis Outline

One of the main goals of this thesis is to investigate the problems/dilemmas of optical volumetric/Lorentz forces specially observed in real radiation pressure experiments performed up to date [cf. sections 1.4 to 1.6]. Moreover, Lorentz force based analysis is so far restricted to simple cases. In literature, Lorentz force analysis for optical pulling force (tractor beams) and the reversal of near field optical binding force (i.e. for plasmonic objects) have not been investigated in details [cf. sections 1.7 and 1.8]. As a result, in this thesis, physics and applications of Lorentz force have

been investigated in details with special interest in tractor beam effect, plasmonic objects, chiral objects and the objects embedded in a generic material medium.

At the beginning part of this thesis, in chapter 2 and 3, we have considered comparatively simple cases such as objects placed in air. Time averaged total force calculated by well-known Lorentz force and the external stress tensor method are found in full agreement for those two chapters. More specifically, chapter 2 demonstrates the Lorentz force analysis for tractor beam like effect. At the end of section 1.7 of this chapter, we have already discussed shortly that the stimulating connection of optical Lorentz force with counterintuitive tractor beam effect has not been investigated in details so far. Chapter 2 attempts to do so. It is shown based on Lorentz force analysis that the bound surface charges of Rayleigh scatterer experience backward force, which overcomes the positive bulk force and ultimately results in the net pulling of the scatterer for several spatial regions outside the two dielectric hollow core cylindrical waveguide. Later, this idea of 'dielectric waveguide tractor beam' has been extended for dielectric coupler set-ups.

At the end of section 1.8 of this chapter, we have discussed shortly that the connection of optical Lorentz force dynamics with plasmonics and specially the reversal of optical binding force have not been investigated in details so far. Chapter 3 demonstrates the Lorentz force analysis for plasmonic off-axis and on-axis spherical heterodimers. It is shown that the reversal of longitudinal binding force can be easily controlled due to forced symmetry breaking. Though it is commonly believed that plasmonic forces mostly arise from the surface force and Fano resonance can be a promising way to achieve binding force reversal, our study based on Lorentz force dynamics suggests notably opposite proposals for the case of plasmonic spherical heterodimers.

In contrast, in chapters 4, 5 and 6, we have considered a little bit complicated cases such as objects those are embedded in material medium. Specially chapters 4

and 5 deal with very fundamental topics of optical force: consistency of stress tensors, volumetric forces and photon momenta inside matter. The controversies and the problems related with such topics have already been discussed shortly in sections 1.4, 1.5 and 1.6 of this chapter. In chapter 4 it is shown that the well-known Lorentz force leads to inconsistent result (pushing force) instead of the experimentally observed optical pulling force for interfacial tractor beam experiment. Our suggested interpretation in chapter 4 supports the Minkowski approach only for the purpose of optical momentum transfer to the embedded scatterer for the interfacial tractor beam experiment [35] rejecting Peierls' and Abraham's approach, although the momentum of photon in the continuous background medium should be considered as the type of Abraham for the calculation of the bulk part of Lorentz volumetric force distribution.

Later chapter 5 discusses in details why well-known Lorentz forces fail not only in interfacial tractor beam experiment but also for several other real experiments. It is demonstrated that at the boundary of an object, the difference of the external Minkowski ST and internal ST of Chu (and Einstein-Laub) is found in agreement with the surface force yielded by Chu (and Einstein-Laub) volumetric force only when the background is air rather than a material. We identify this as one of the main reasons of the disagreements observed in the major radiation pressure experiments which include material medium as background. Some other notable reasons of such disagreements have also been identified and discussed in that chapter. We also demonstrate that it is still possible to establish different equivalent time-averaged Lorentz/volumetric force formulas based on the fulfilment of just two 'consistency conditions'. Based on those proposed 'consistency conditions', finally, we show that by modifying the Einstein-Laub or Chu formulation; time-averaged STs and volume forces are obtainable, which can overcome the aforementioned inconsistencies and yield the 'correct' force similar to Minkowski's force for almost all the previous real experiments. Specially, our proposed modified Einstein-Laub ST can be considered

as an efficient mathematical toolkit, an alternative of time and memory consuming volumetric forces, to yield the internal bulk force of a chiral or achiral object embedded in complex material backgrounds (i.e. homogeneous, heterogeneous, bounded etc.).

The behavior of Fano resonance and the reversal of near field optical binding force of dimers over different substrates have not been studied so far. This matter is investigated in details in chapter 6. In chapter 5, it has been discussed in details why Lorentz force should be modified when the embedding background is material one instead of air. In chapter 6, we have shown an interesting application of modified Lorentz force [i.e. modified Chu force] to control the reversal of optical binding force of plasmonic cubes placed over plasmonic substrate due to strong Fano resonance.

Last but not least, based on our proposals in chapter 5, at the end of this thesis (chapter 7) we propose a new hypothesis named as ‘existence domain’. ‘Existence domain’ is the region either outside a scattering body taking only its exterior fields into account, or in its interior considering only the inside fields. Though almost all the time averaged distinct STs and volumetric force laws are restricted to the idea of ‘existence domain’, we demonstrate that the time averaged stress tensor and volumetric force law of Minkowski are free from such restrictions. In addition, we have also discussed in details the differences between time averaged and instantaneous force laws for different formulations. Notably only Minkowski’s theory remains valid for all circumstances without any modification. After almost 100 years of Einstein’s prediction, this thesis, (most probably) finally answers why Minkowski’s theory remains valid everywhere in space (both in instantaneous and time averaged scenario) and can be considered as the base of a unified theory of optical force and photon momentum.

Proposals presented in this thesis can be very effective to resolve not only the dilemma of distinct stress tensors and optical Lorentz forces but also the controversy

of Abraham-Minkowski photon momenta. Our proposals may also open a new window of optical pulling force/tractor beams due to the exclusion of conventional structured tractor beams along with the artificial exotic matters. Last but not least, the proposed ideas for the reversal of near field optical binding force may also be useful for the future applications of plasmonic dimers in the areas of improved plasmonic sensors, particle clustering and aggregation.

Chapter 2

Lorentz Force and Its Application on Tractor Beam like Effect

2.0 Summary of chapter 2

The stimulating connection between the counter-intuitive optical pulling effects and the Lorentz force has not been investigated in literature. This chapter demonstrates that multiple absorbing or non-absorbing dielectric Rayleigh objects can be pulled locally with gradientless travelling waves outside a finite-sized cylindrical nano or micro waveguide, if it is made up of a hollow core along with the cladding of at least two different dielectrics of appropriate refractive indices. Lorentz force analysis reveals that the bound surface charges of Rayleigh scatterer experience backward force, which overcomes the positive bulk force and ultimately results in the net pulling of the scatterer for several spatial regions outside the waveguide. Finally, in order to control the pulling of multiple Rayleigh particles based on scattering force and binding force, we have proposed a possible cylindrical coupler set-up. The work presented in this chapter may open a new window of optical pulling force due to the exclusion of conventional structured tractor beams along with the artificial exotic matters.

2.1 Introduction

Controlling the optical force at nanoscale has important applications in emerging technological developments [81, 82]. In order to control the optical force at nanoscale, nano-opto mechanical systems are of great interest nowadays for different novel optical manipulations [83-89]. For example, a way to create optical pulling effect for Rayleigh particles is an evanescent wave [83, 84], which is conventionally applied in nano-opto mechanical systems for particle manipulation. A slot waveguide is reported in [85], which proposes a way of possible long distance transportation by pushing the particles along the slot and also trapping the particles in a two-dimension way. Later, the trapping and transport of polystyrene nano particles and DNA molecules have been demonstrated using such slotted silicon waveguides [86]. Nano-fiber can also be used for trapping or pushing atoms [87]. Instead of optical pulling, the light driven transport of nano particle against the fluidic flow has been experimentally demonstrated in presence of micro-meter sized fiber [88]. Using two oppositely directed beams from two ends of a 10-μm dielectric waveguide, trapping and pulling of nano particles have also been predicted [89]. However, a conventional dielectric micro-waveguide (cf. Ref. [89]) with the aid of only forward travelling fields has not been used to pull non-resonating conventional dielectric nano particles outside the fiber or waveguide, which can be considered as the tractor beam like effect. In contrast to the conventional beams with pushing force, a tractor beam is a customized travelling light beam which pulls any scatterer opposite to the propagation direction of light [25, 30, 33,34,35, 36, 62, 90, 91], which are distinct from the aforementioned opto-mechanical systems.

In this chapter, we demonstrate a possible scheme of three dimensional (3D) nano-opto-mechanical system to create local tractor beam effect for multiple non-

resonating Rayleigh particles (Silicon) outside the proposed finite-sized nano or micro waveguides with non-structured light and dielectric materials. The proposed pulling method does not require sophisticated control of structured light or exotic materials or the complicated background [25, 30, 33, 34, 35, 36, 62, 90, 91]. Only a waveguide or a coupler with a hollow air core along with the cladding of two different conventional dielectrics with appropriate permittivity is needed, which can be excited by simple non-structured source of light. We name our setup as "Dielectric Waveguide Tractor Beam" (DWTB), in which a forward propagating wave can drive multiple Rayleigh particles locally in a backward direction outside the finite-sized waveguide in absence of any backward propagating wave [91]. Based on the interaction between the scattering force [92] and optical binding force [3], we also propose a local pulling mechanism created by a cylindrical waveguide coupler. Due to the presence of additional controllable parameters, probably the manipulation of small nano particles [93, 94] (i.e. Rayleigh particles) will be flexible outside the proposed coupler setups.

However, most of the times optical pulling effects have been discussed from the point of view of quasi static analysis based on the external dipole force methods [30, 34, 62, 92]; without considering much analysis on full electrodynamic calculation or the Lorentz force [44,65,77,78,95,96]. Though Lorentz force analysis has been applied previously in [65, 77, 78, 96] to understand the mechanism of chirality induced force, Luneburg lenses, mechanical interaction between light and graded index media, cloaking effect, background effect on radiation pressure; such analysis has never been applied to understand the tractor beam like effect. Our verifications on the consistency between the full electrodynamic analysis based external stress tensor and volume/Lorentz force method in three dimensional (3D) environment may open a new window to understand the physical mechanism [65, 77, 96] of optical force not only for optical pulling but also for more complicated set-ups reported in [38, 97-99] (where dipolar force [92] does not lead to the consistent result). Though in this work

we have limited our discussion on non-resonating dielectric Rayleigh particles (both non-absorbing and absorbing), we believe that our proposed DWTB based pulling can also be applicable for resonating and plasmonic Rayleigh objects [38] due to the dominance of the identical part of the Lorentz force.

2.2 Single Rayleigh particle outside the waveguide: Force calculation

We specify that throughout this thesis we refer to 'exterior' or 'outside' forces as those evaluated outside the volume of the macroscopic particles, while ‘interior’ or 'inside' refer to those quantities inside this object volume. In order to consider the realistic effects, in this chapter we have done all the numerical calculations /full wave simulations in 3D structures [100].

The proposed simplest setup is illustrated in Fig. 2.1(a). The Silicon scatterer (with refractive index of n_s=3.5) is placed at the outside of the finite-sized nano or micro waveguide, which is made up of a hollow core and two different dielectric layers of cladding [i.e. Glass and Potassium Niobet ($KNbO_3$); where the refractive index of the second clad should be higher than the first one]. The ‘outside optical force’ [35, 43] is calculated by the integration of time averaged Minkowski [35, 43] stress tensor at r= 1.01a = a^+ [It means we are selecting a spherical surface with a radius slightly larger

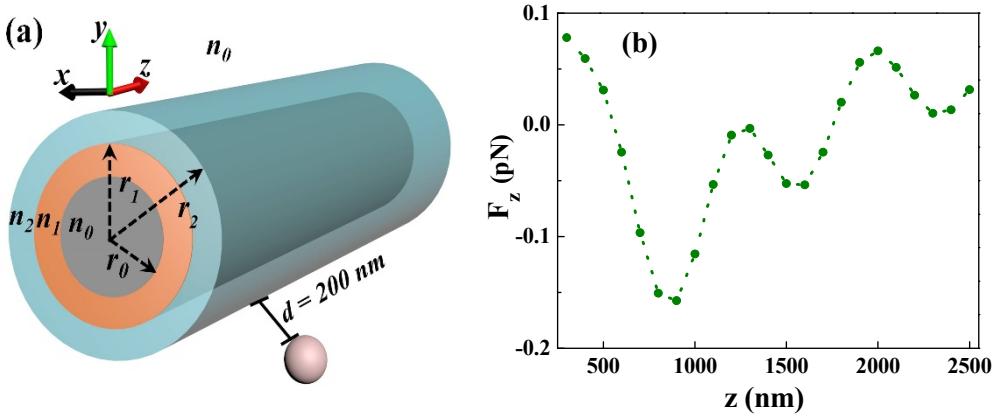

Fig. 2.1: Illustration of optical pulling force for a single Silicon particle (refractive index 3.5 and radius of 30 nm) placed at different *z*-positions outside a 3D cylindrical waveguide. Dotted (….) lines represent the possible time averaged force on the particle at different *z*-positions based on the actual force on the particle indicated by '.' marked points. (a) A 10 μm sized (this specific length has been considered according to Ref. [89]) three dimensional (3D) waveguide is excited by a plane wave source of wavelength 1500 nm. The radius are r_0=500 nm, r_1=600 nm, and r_2=700 nm. The refractive indexes are n_0=1.0, n_1=1.5 and n_2=2.25. A single silicon particle of radius 30 nm and refractive index of 3.5 is placed at different *z*-distances outside the waveguide. The radial-directed distance, *d*, is fixed at 200 nm for different *z*-distances/positions of the particle. (b) F_z (in pico Newton) on the single Rayleigh scatterer. Figures adapted and reproduced with permission from the work: Mahdy et al., Annalen der Physik, doi: 10.1002/andp.201600213 © 2016, WILEY-VCH Verlag GmbH & Co. KGaA, Weinheim.

than the object, on which the integration of Stress tensor is calculated for the total optical force (for details cf. Fig. 1.1 in chapter 1)] employing the background fields of the scatterer of radius *a*:

$$\left\langle \boldsymbol{F}_{\text{Total}}^{\text{Out}} \right\rangle = \oint \left\langle \overline{\overline{\boldsymbol{T}}}^{\text{out}} \right\rangle \cdot d\boldsymbol{s}$$
$$\left\langle \overline{\overline{\boldsymbol{T}}}^{\text{out}} \right\rangle = \frac{1}{2}\text{Re}[\boldsymbol{D}_{\text{out}}\boldsymbol{E}_{\text{out}}^{*} + \boldsymbol{B}_{\text{out}}\boldsymbol{H}_{\text{out}}^{*} - \frac{1}{2}\overline{\overline{\boldsymbol{I}}}(\boldsymbol{E}_{\text{out}}^{*} \cdot \boldsymbol{D}_{\text{out}} + \boldsymbol{H}_{\text{out}}^{*} \cdot \boldsymbol{B}_{\text{out}})] \quad . \qquad (2.1)$$

Where 'out' represents the exterior total field [i.e. incident plus the scattered field] of the scatterer; $\boldsymbol{E}$, $\boldsymbol{D}$, $\boldsymbol{H}$ and $\boldsymbol{B}$ are the electric field, electric displacement field, magnetic field, and magnetic induction field, respectively, while $\langle\ \rangle$ represents the time average and $\overline{\overline{\boldsymbol{I}}}$ the unity tensor.

On the other hand, based on the Lorentz force, the total force including the surface force and the bulk force [65,77,78]) can be written as:

$$\left\langle \boldsymbol{F}_{\text{Total}} \right\rangle = \left\langle \boldsymbol{F}_{\text{Volume}} \right\rangle = \left\langle \boldsymbol{F}_{\text{Bulk}} \right\rangle + \left\langle \boldsymbol{F}_{\text{Surf}} \right\rangle = \int \left\langle \boldsymbol{f}_{\text{Bulk}} \right\rangle dv + \int \left\langle \boldsymbol{f}_{\text{Surface}} \right\rangle ds \tag{2.2}$$

Where

$$\begin{aligned} \left\langle \boldsymbol{f}_{\text{Surface}} \right\rangle &= [\sigma_e \boldsymbol{E}^*_{avg} + \sigma_m \boldsymbol{H}^*_{avg}]_{\text{at } r=a} \\ &= \{\epsilon_o (\boldsymbol{E}_{\text{out}} - \boldsymbol{E}_{\text{in}}) \cdot \hat{\boldsymbol{n}}\} \left(\frac{\boldsymbol{E}_{\text{out}} + \boldsymbol{E}_{\text{in}}}{2} \right)^*_{\text{at } r=a} + \{\mu_0 (\boldsymbol{H}_{\text{out}} - \boldsymbol{H}_{\text{in}}) \cdot \hat{\boldsymbol{n}}\} \left(\frac{\boldsymbol{H}_{\text{out}} + \boldsymbol{H}_{\text{in}}}{2} \right)^*_{\text{at } r=a}, \end{aligned} \tag{2.3}$$

$\boldsymbol{f}_{\text{Surface}}$ is the surface force density (the force which is felt by the bound electric and magnetic surface charges of a scatterer), which is calculated just at the boundary of a scatterer [65,77,78]. 'in' represents the interior fields of the scatterer; 'avg' represents the mathematical average of the fields just at the boundary [i.e. exactly at r=a]. σ_e and σ_m are the bound electric and magnetic surface charge densities of the scatterer, respectively. The unit vector $\hat{\boldsymbol{n}}$ is an outward pointing normal to the surface. On the other hand, the time averaged bulk force density can be expressed as [65,77,78]:

$$\left\langle \boldsymbol{f}_{\text{Bulk}} \right\rangle = \frac{1}{2} \text{Re}[\varepsilon_0 (\nabla \cdot \boldsymbol{E}_{\text{in}}) \boldsymbol{E}^*_{\text{in}} + \mu_0 (\nabla \cdot \boldsymbol{H}_{\text{in}}) \boldsymbol{H}^*_{\text{in}}] - \frac{1}{2} \text{Re}[i\omega(\varepsilon_s - \varepsilon_0)\{\boldsymbol{E}_{\text{in}} \times \boldsymbol{B}^*_{\text{in}}\} + i\omega(\mu_s - \mu_0)\{\boldsymbol{D}^*_{\text{in}} \times \boldsymbol{H}_{\text{in}}\}] \tag{2.4}$$

$\boldsymbol{f}_{\text{Bulk}}$ is the bulk force density, which is calculated from the interior of the scatterer by employing the inside field [65,77,78]. ε_s is the permittivity and μ_s the permeability of the scatterer. It is important to note that the quasi static analysis based on 'external dipolar force' [38,92], which has also been described as the Lorentz force in [38] is quite different from the full electrodynamic analysis based on the Lorentz force defined in Eqs (2.2) - (2.4).

2.3 Detailed analysis of set-up

2.3.1 Electromagnetic fields and modes in a cylindrical waveguide

The primary source is a simple *x*-polarized plane wave $E_x = E_0 e^{i\beta z}$ and E_0 has been set to $1\,\mathrm{V/m}$ in the simulation model. This source [which is placed at around z=0 (the starting length of the waveguide) in the full wave simulation model; cf. Fig.2.1 (a)] is used to excite the conventional/modified Bessel fields inside/outside our finite-sized cylindrical waveguide [101, 102]. This intrinsic wave-fields can be calculated by a transfer matrix method [101, 102]. Throughout this work three different sized (length) 3D cylindrical waveguides have been considered: 10 μm (this specific size has been considered according to Ref. [89]), 15 μm and 20 μm. In each uniform cylindrical cladding of our waveguides, the four field components (E_z, H_φ, H_z, E_φ) can be expressed as a linear combination of any two types of Bessel functions [102]. Our waveguide has two dielectric claddings, where the guiding modes are leaky as the confinement is not perfect (i.e. the higher refractive index of the second clad). Just outside the waveguide (i.e., in the air background), there will be no incoming waves for the idealistic case [102]. It should be noted that the fields (E_z, H_φ, H_z, E_φ) calculated in [102] are the intrinsic fields *in absence of a scatterer*. Due to the finite structure of our waveguide and the presence of the scatterer, the intrinsic fields in [102] should be modified near a scatterer; and this has been managed by the full wave simulation based techniques applied in this work.

2.3.2 Behavior of external wave-field of a single scatterer placed outside proposed waveguides

In Fig.2.1 (b), it is shown that when a single scatterer is placed around our proposed waveguide at different *z*-distances, the scatterer experiences a net optical

pulling force towards the source in several spatial regions. Calculations have been done based on the outside stress tensor and also volume force density formula, respectively. They are in quite good agreement. Though in [103] the optical pulling outside a dielectric waveguide slab has been explained based on the modal conversion and resonant coupling of the scatterer, optical pulling force in our set-ups is not due to resonant coupling. We also find that a 3D cylindrical waveguide with hollow core along with *a single dielectric clad* is not capable of pulling the Rayleigh scatterer in continuous spatial position (which is in agreement with refs. in [104] where quasi static analysis has been emphasized to explain the time averaged total force). In case of optical pulling with our two-layered hollow core waveguide, the scatterer (which is a generic Rayleigh particle) is not in resonance at all [also cf. the introduction of ref. [97], the trapping of non-resonant particles]. Ultimately, the additional second clad along with the presence of a weak standing wave in it assists the pulling effect and alters the spin-orbit interaction [105] in presence of the particle. The effect of altered electrodynamic interaction (i.e. the pulling force of non-resonating particle), due to the addition of the suitable second clad for our setups, cannot be included in a simple manner in the quasi static force formula: such as external dipolar force in ref. [92]. As a result, a full electrodynamic analysis will be discussed in the next section.

In order to investigate the connection of our observed pulling force with the Poynting vector distribution [92], the total Poynting vector distribution of the waveguide is examined via full wave simulation [cf. Fig. 2.2 (a), (b) and (c)]. It is interesting to note that the real part of E_z is found in opposite phase after each 500-nm z-distance. Another interesting fact is that the Poynting vector direction at z=1000 nm plane is negative for the air core, which is discussed in detailed in [106]. However, it is not the generic reason of optical pulling force outside the waveguide [104]. For example- at z=1500 nm, the force is still negative but the total Poynting vector is

positive everywhere just like at z=500 nm where the force is positive. So, the conclusion is that: negative Poynting vector [106] is not responsible for such optical pulling force [104] in general.

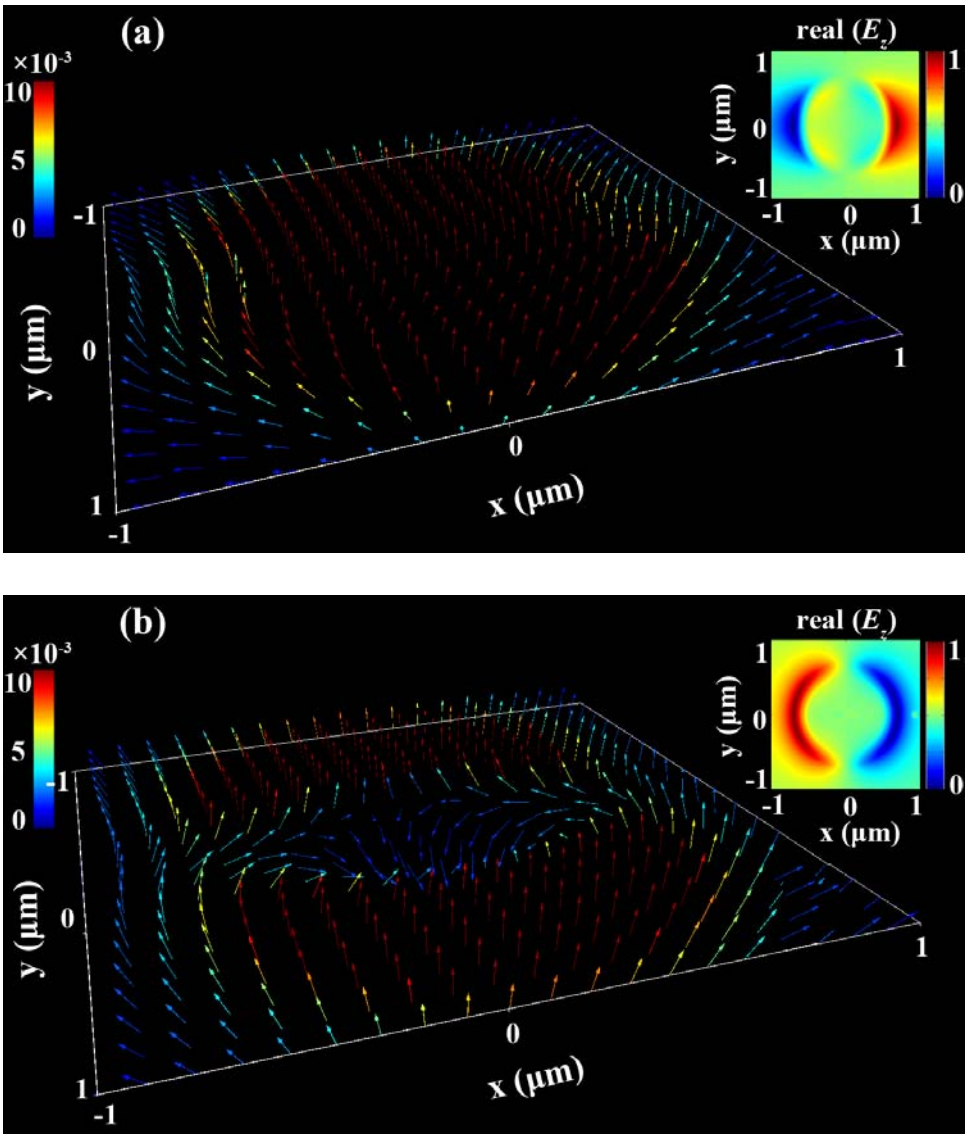

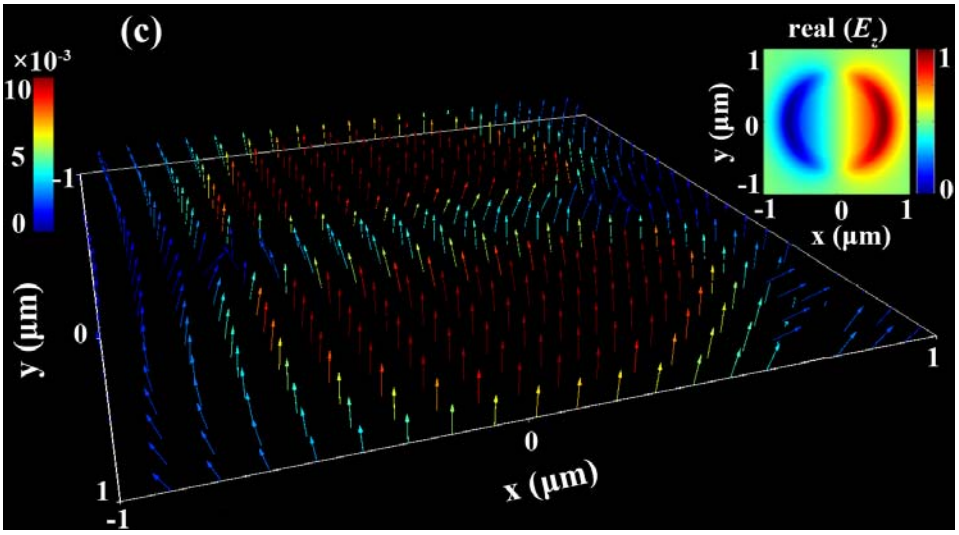

Fig. 2.2: Total Poynting vector distribution at the planes of z=500 nm (a), 1000 nm (b) and 1500 nm (c). The insets show the responding Re(E_z). It is observed that at z=1000 nm plane when optical pulling force occurs [cf. Fig. 2.1(b)] outside the cylindrical waveguide of Fig.2.1 (a), negative Poynting vector [cf. Fig. 2.2(b)] takes place. At the same time, inset of Fig. 2.2(b) represents opposite phase shift of the Real (E_z) with respect to Fig. 2.2(a). However, neither the negative Poynting vector nor the phase shift of Real (E_z) is the generic reason of the pulling effect. For example, Fig. 2.2(c) and in its inset: the total Poynting vector is positive and the Real (E_z) does not experience any opposite phase in comparison with the Real (E_z) given in the inset of Fig. 2.2(a). In Fig. 2.1(b) it is observed that the particle experiences local pulling force at z=1500 nm but it experiences pushing force at z=500 nm. Figures adapted and reproduced with permission from the work: Mahdy et al., Annalen der Physik, doi: 10.1002/andp.201600213 © 2016, WILEY-VCH Verlag GmbH & Co. KGaA, Weinheim.

2.4 Single or multiple Rayleigh particles outside the waveguides: Lorentz force Dynamics

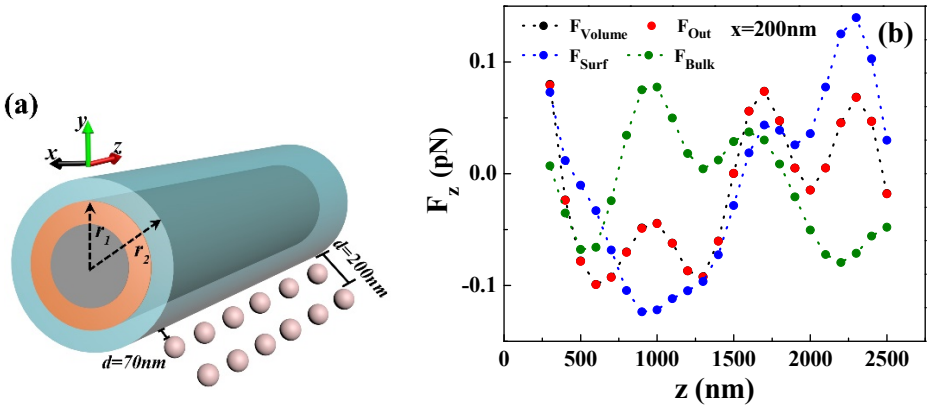

Fig. 2.3: (a) Possible Illustration of optical pulling force for multiple Silicon particles (all with refractive index 3.5 and radius 30 nm) placed outside the 3D waveguide with a length of 15 μm; light wavelength 1500 nm. For clarity, it does not represent the actual number of particles. In actual simulation set-up, due to time and computer memory restriction, we have placed total 46 particles (two different rows; each contains 23 particles) covering up to 2.5 μm of the total 15 μm sized waveguide. The *z*-direction center-to-center separations between the particles is 50 nm, and the separations of them to the waveguide are d=70 nm and d=200 nm, respectively. (b) Dotted (….) lines represent the possible time averaged force on the particle at different *z*-positions based on the actual force on different particles indicated by '.' marked points. F_z for particles at x=200 nm. $\langle \boldsymbol{F}_{\text{out}} \rangle$ is obtained using the time-averaged ST, whereas the force $\langle \boldsymbol{F}_{\text{Volume}} \rangle$ is calculated by Eq (2.2) from fields inside the object, and $\langle \boldsymbol{F}_{\text{Surf}} \rangle$ just from the surface. It is observed that the negative force is mainly the ultimate result of negative surface force for each scatterer, which overcomes the positive bulk force. In fact the time averaged total force follows the trend of surface force almost in all spatial positions. Figures adapted and reproduced with permission from the work: Mahdy et al., Annalen der Physik, doi: 10.1002/andp.201600213 © 2016, WILEY-VCH Verlag GmbH & Co. KGaA, Weinheim.

When several dielectric Rayleigh objects are placed outside the waveguide in Fig. 2.3(a), we have shown that optical pulling force remains valid as shown in Fig. 2.3(b). However, the magnitudes of the forces change in comparison with the single particle case due to the presence of binding force [3].

The explanation of the observed pulling force does not remain simple for this set-up because the idea of conventional conservative forces like gradient, scattering and curl force or the total external dipolar force cannot be applied even for object radius $a \ll \lambda$

[38, 97-99]; where: (i) the modification of modes due to interaction with the Rayleigh scatterers significantly alters [98] the properties of the force of an intrinsic dipole [92,107] and (ii) multipoles [38] are excited along with the retardation effect. For such cases, Lorentz force analysis [44,65,77,78,95,96] (which is a full electrodynamic analysis) can be an alternative, accurate and physically insightful way to explain complex setups like ours, though so far no attempt has been taken based on the Lorentz force to explain the tractor beam effects [25, 30, 33,34,35, 36, 62, 90, 91] or complex situations reported in refs [38, 97-99,104,107].

From the numerically calculated results in Fig. 2.3(b), it can be explained that the bound charges in the surface of the scatterer experience backward surface force $\langle \boldsymbol{F}_{\text{Surf}} \rangle$ and it overcomes the positive value of the bulk force $\langle \boldsymbol{F}_{\text{Bulk}} \rangle$ caused by the interaction between magnetic induction and induced polarization current (i.e. bound current [78]). Hence, the resultant force ultimately becomes negative and the dielectric Rayleigh particle experiences local backward pulling in some continuous spatial positions outside our proposed waveguide structure. In presence of external electric field, bound charges can oscillate around a mean position [108]. In this work, we are also observing a case where optical pulling force is arising mainly due to dominant negative surface force, while previous tractor beam works [25, 30, 33, 34, 35, 36, 62, 90, 91] have not investigated based on the idea of surface force and bulk force. Although such dominance of surface /polarization charges (that should lead to the dominance of surface force) is common for plasmonic structures [109] due to local field enhancement, the dominance of surface force for dielectric scatterers with positive permittivity is a little bit unusual and highly dependent on the shape of the scatterer (cf. the force on crescent shaped object in [78]).

Although it is sometimes considered that the bound charges and currents are merely computational tools for calculating electric and magnetic fields in matter, yet these

charges and currents are no less real than free charges and currents and can be measured experimentally [110,111]. According to ref. [110] [cf. Eq (10) given in [110]], within a linear, homogeneous, isotropic dielectric, in regions where there are no (free) volumetrically distributed charges, there are also no bound volumetric charges. This leads to an interesting conclusion that: in case of optical force, electrons that are more or less free to roam around the lattice may be said to act as free electrons and can be modelled as bound charges [95]. For the force exerted by the *E*-field is $-(\nabla\cdot\boldsymbol{P})\boldsymbol{E}$ [95] or $\varepsilon_0(\nabla\cdot\boldsymbol{E})\boldsymbol{E}$, as shown in our Eq (2.4). Here, $\boldsymbol{P}$ is the polarization vector**.** Though this force due to volume charge density vanishes inside an isotropic and homogeneous object [65,77,78], the net effect is that surface bound charges contribute to the total force as shown in Eq (2.3).

We have examined several other setups with placing multiple particles outside the proposed cylindrical waveguides. For all the set-ups with finite-sized cylindrical waveguides or couplers, the common reason of optical pulling effect is observed from the dominance of the negative surface force due to bound surface charges of the Rayleigh particles. I.e. in Fig. 2.1(b), nearly at z=1000 nm, the magnitude of optical pulling force on a single scatterer reaches local minima (negative maxima) due to strong negative surface force on the bound charges of the scatterer. This conclusion on surface force remains valid even for the surface force on a particle placed with multiple other particles in Fig. 2.3(b) for the 15-μm waveguide. However, in Fig. 2.3(b), due to multiple scattering and binding force [3], the bulk force changes significantly in comparison with the case of a single scatterer. As a result, though the total force on a single scatterer reaches the local minima (negative maxima) value nearly at *z*=1000 nm in Fig. 2.1 (b) along with strong surface force, total force on the scatterer in presence of multiple scatterers do not reach the local minima (negative maxima) value at *z*=1000 nm even with the presence of strong surface force, as shown in Fig. 2.3(b).

2.5 Robustness of pulling force to absorption, wavelength and waveguide length

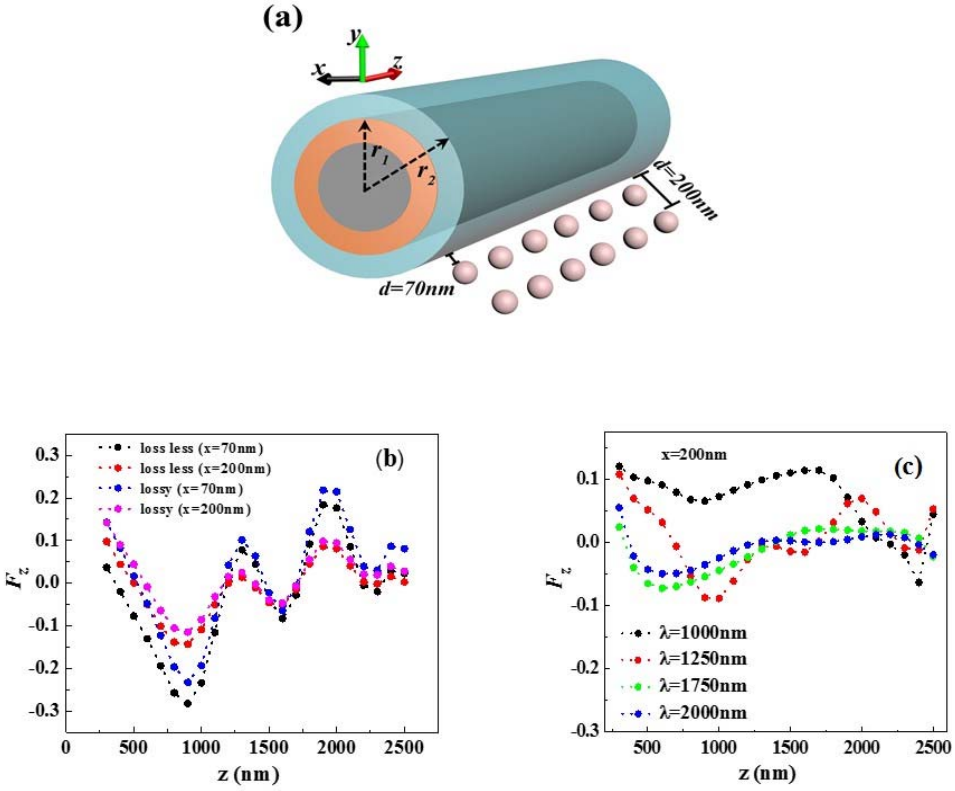

Fig. 2.4: Robustness test. (a) Same configuration of Fig. 2.3(a). But the length of the waveguide is 10 μm. (b) Dotted (….) lines represent the possible time averaged force on the particles at different *z*-positions based on the actual force on different particles (total 46 particles; 23 in each row) indicated by '.' marked points [also cf. Fig. 2.3]. Moderate loss (n= 3.5+0.5i) is introduced to all the particles placed outside the 10 μm waveguide. The magnitude of the pulling force is decreased very slightly and still pulling force is quite possible in presence of moderate absorption. It proves the robustness of our scheme. (c) The effect of the change of incident wavelength is shown for lossless particles at x=200 (total 46 particles; 23 in each row). If wavelength of the light source is changed for the set-up of Fig. (a) [i.e. 1000, 1250, 1750 and 2000 nm] but the particle size remains fixed; the force magnitudes have been dramatically varied for different wavelengths of the source. In lower wavelengths (i.e. 1000 nm wavelength) pulling force is greatly reduced, which indicates that the proposed idea of DWTB is applicable only for Rayleigh particles. Figures adapted and reproduced with permission from the work: Mahdy et al., Annalen der Physik, doi: 10.1002/andp.201600213 © 2016, WILEY-VCH Verlag GmbH & Co. KGaA, Weinheim.

In order to examine the robustness of our proposed set-ups, we have varied different key parameters. For example- at first we have introduced moderate loss (n_s=3.5+0.5i) to all the particles placed outside the waveguide [cf. Fig. 2.4(a) and (b)]. For absorbing scatterers, Eq (2.4) gets two different parts known as the bound force and conduction force [44]:

$$\left\langle \boldsymbol{F}_{\text{Bulk}} \right\rangle = \left\langle \boldsymbol{F}_b \right\rangle + \left\langle \boldsymbol{F}_c \right\rangle \tag{2.5a}$$

Currents arise in materials when there is a non-uniform distribution of charge. In dielectric materials, there is a current density corresponding to the net movement of electric dipole moments per unit volume, i.e. the polarization $\boldsymbol{P}$. When the polarization density changes with time, the time-dependent bound-charge density creates *polarization current density* (bound current [78], [110]). This bound current interacting with magnetic induction causes the bound force part of total bulk force. Here, the bound force $\langle \boldsymbol{F}_b \rangle$ can be written as [44]:

$$\left\langle \boldsymbol{F}_b \right\rangle = \int \left\langle \boldsymbol{f}_b \right\rangle dv \simeq -\frac{1}{2}\text{Re}[i\omega(\text{Re}[\varepsilon_s]-\varepsilon_0)\{\boldsymbol{E}_{\text{in}} \times \boldsymbol{B}_{\text{in}}^*\} + i\omega(\text{Re}[\mu_s]-\mu_0)\{\boldsymbol{D}_{\text{in}}^* \times \boldsymbol{H}_{\text{in}}\}] \tag{2.5b}$$

On the other hand, the time averaged conduction force $\langle \boldsymbol{F}_c \rangle$ (which is an additional interior force that arises due to the free currents inside the scatterer) takes the value [44]:

$$\left\langle \boldsymbol{F}_c \right\rangle = \int \left\langle \boldsymbol{f}_c \right\rangle dv = \int \frac{1}{2}\text{Re}\left[\omega\varepsilon_I \boldsymbol{E}_{\text{in}} \times \boldsymbol{B}_{\text{in}}^* - \omega\mu_I \boldsymbol{H}_{\text{in}} \times \boldsymbol{D}_{\text{in}}^*\right] dv \tag{2.5c}$$

Here ε_I and μ_I are the imaginary parts of the permittivity and permeability of a scatterer, respectively. It is observed that even if multiple absorbing scatterers are placed outside our waveguide, still optical pulling force occurs very similar to non-absorbing case as shown in Fig. 2.4 (b).

Next, we have varied the wavelength of light source in Fig. 2.4(c). We conclude that our proposed pulling effects work only for the Rayleigh limit of the particles (for both absorbing and non-absorbing). If the primary source wavelength is decreased too much (or by increasing the particle size; which is connected with the electrical size = $k_s a$; where k_s is the wave number 'inside' the material of scatterer), only few particles at random positions experience optical pulling force [cf. Fig. 2.4(c)]. However, as long as the Rayleigh limit (electrical size) is maintained, local pulling effect is observed for different wavelengths of the primary source. Finally, the overall length of our waveguide structures has also been varied, from 10 μm to 20 μm, and we have found that all the proposals introduced so far still remain valid.

2.6 Multiple Rayleigh particles outside the coupler

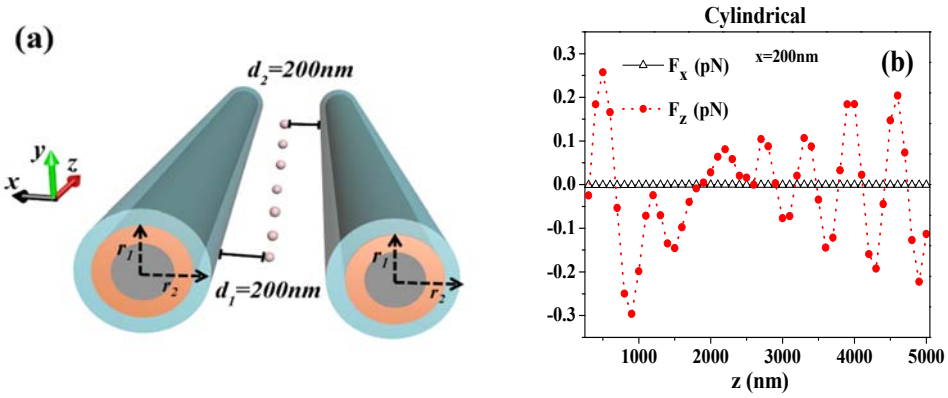

Fig. 2.5: Possible Illustration of optical pulling force for multiple Silicon particles placed outside two identical 10 μm sized (length) 3D cylindrical waveguides (a directional coupler). (a) The 'possible' set-up of 3D particles placed together at different z-distances at d=200 nm apart from each waveguide. Material and the configuration of the waveguides and particles are the same as those used in Fig. 2. 3. (b) Fig. (a) does not represent the actual number of particles. In actual simulation set-up due to time and computer memory restriction, we have placed total 48 particles in one row covering up to 5 μm of the total 10 μm sized waveguides. The forces (F_z and F_x) on an individual Rayleigh scatterer placed at different z-distances outside the waveguide (at fixed d=200 nm). Dotted (….) lines represent the possible time averaged force on the particle at different z-positions based on the actual force on different particles indicated by '.' marked points. The two identical waveguides are excited by a plane wave source of wavelength 1500 nm. We verified that the pulling

force due to cylindrical waveguide in Fig. 2.5(b) is also originated from negative surface force $\langle \boldsymbol{F}_{\text{Surf}} \rangle$ (not shown). Figures adapted and reproduced with permission from the work: Mahdy et al., Annalen der Physik, doi: 10.1002/andp.201600213 © 2016, WILEY-VCH Verlag GmbH & Co. KGaA, Weinheim.

Based on the interaction between the scattering force [92] and optical binding force [3], we have also proposed a local pulling mechanism created by a cylindrical waveguide coupler as shown in Fig. 2.5. Importantly, (i) by changing the phase of the guided modes in the two waveguides [76] or (ii) by differing the intensity (input power) of primary light source [89] or (iii) by increasing the intensity (input power) of primary light source [88], it may be possible to achieve a flexible way of multiple particle manipulation based on the model system of coupler set-up proposed in Fig. 2.5.

In Fig. 2.5, it is also observed that optical pulling force on multiple particle towards -*z* direction exists with moderate magnitude not only at the starting length but also at the later parts of the waveguide. However, the surface force part of the Lorentz force, $\langle \boldsymbol{F}_{\text{Surf}} \rangle$, (not shown) on the scatterer has also been observed negative and dominant for that set-up. It should be noted that the coupler set-up is just a possible model system [also cf. ref. [112]]. If we consider the lines of multiple Rayleigh particles from different distances from the two waveguides [i.e. different fixed *x*-positions, particle aligned in *z*-direction]; particles, which are almost at the same distance from both the waveguides, should experience smaller lateral gradient force in comparison with the single waveguide system.

2.7 Conclusion

In summary, we have demonstrated a possible way of achieving the local pulling force for multiple non-resonating Rayleigh objects considering both the exterior and

interior dynamics behaviors of optical force. The robustness of our proposed scheme, local pulling force of multiple particles in presence of a structured cylindrical waveguide or a coupler, has also been tested by varying several key parameters. Probably the space dependent local optical forces can be adjusted (positive or negative) for multiple nano particles outside the finite-sized nano or micro waveguides/couplers based on the ideas presented here. The consistency between the Lorentz force method and external stress tensor (i.e. full electrodynamic calculation [113] instead of the approximate quasi static analysis) has been demonstrated in details for complex 3D set-ups. The work presented in this chapter has provided not only a novel way to realize opto-mechanical tractor beam effect with the simple light source and material but also a physical insight on the observed effects considering the Lorentz force dynamics of both absorbing and non-absorbing scatterers. Though we have restricted our discussion for non-resonating dielectric Rayleigh particles (both non-absorbing and absorbing), we believe that our proposed DWTB based pulling can also be applicable for resonating and plasmonic Rayleigh objects [38,114] due to the very high dominance of surface force [114] part of the Lorentz force. For very recent trend of metamaterial cladded hollow core cylindrical waveguides [115, 116], this work may also open a new way of future investigations: i.e. an alternative mechanism of optical pulling force on the particles placed inside or outside the core of such cylindrical [115, 116] waveguides.

Chapter 3

Lorentz Force on Plasmonic Spherical Heterodimers: Reversal of Binding Force

3.0 Summary of chapter 3

In previous chapter the connection between Lorentz force and tractor beam effect has been investigated. In this chapter, the stimulating connection between the reversal of plasmonic binding force and Lorentz force dynamics has been investigated. As both bonding and anti-bonding modes are present in the visible spectra of well-known spherical plasmonic heterodimer sets, binding force reversal is commonly believed to occur for all such heterodimers. But this chapter suggests a very different proposal. We demonstrate that for the symmetry broken heterodimer configurations: reversal of lateral (for on-axis heterodimers) and longitudinal (for off-axis heterodimers: end-fire and nearly end-fire configurations) binding force follow fully distinct mechanisms. Interestingly, the reversal of longitudinal binding force can be easily controlled just by changing the direction of light propagation or just their relative orientation. Though it is commonly believed that plasmonic forces mostly arise from the surface force, and Fano resonance can be a promising way to achieve binding force reversal, our study based on Lorentz force dynamics suggests notably opposite proposals for the case of plasmonic spherical heterodimers.

3.1 INTRODUCTION

Fano resonances, super-scattering and plasmonic hybridization in nanostructures [39-41], [117] have received substantial attention in the area of plasmonics. The promising applications of plasmonic hybridization, super-scattering and Fano resonances have been investigated in improved sensitivity of the resonance [118], bio sensing [119], surface-enhanced Raman scattering [120,121], photonic propagation and wave guiding [122,123], plasmon-induced transparency [124] to super scattering [125] and many others [126,127]. In contrast, less attention is dedicated on near field optical force due to Fano resonance and plasmonic hybridization; especially for plasmonic dimers. When two metal nanoparticles are placed very closely to each other, the properties of their surface plasmons are dramatically modified. This configuration of nanoparticles is known as a "dimer". Different behaviors (other than optical force) of such dimers have been studied in refs. [39,41,117,128-132]. Among the dimers, specially heterodimers show remarkable properties: Fano resonances [41,130], avoided crossing behavior [41] and optical nanodiode effect [41]. But the behavior of near field optical force for such heterodimers have not been studied in details. So far only two works [38, 133], as per our knowledge, have studied the behavior of binding force for *on-axis spherical heterodimers*.

Though the behavior and reversal of near field optical binding force for spherical plasmonic on-axis *homodimers* [134- 136] (due to bonding and anti-bonding modes without plasmonic substrate) have been studied in details, such detail studies lack for the on-axis [38, 133] and *off-axis spherical heterodimers*. Here off-axis means end-fire [38] and nearly end-fire configuration [cf. Fig. 3.1 when the rotation angle, φ, of

the particle is between 60 to 120 degrees]. Considering the heterodimer cases, based on Fano resonance, the reversal of near field optical binding force has been reported in [22] and [23] for nanorod structures [22] and for disk along with a *ring* structure [23]. 'Whether such Fano resonance (raised from heterodimer interaction) is a universal process of achieving binding force reversal?'- Answer of this question is still unknown.

A plasmonic spherical "heterodimer" set-up supports both bonding and antibonding plasmon modes at the same time due to its broken symmetry [117]. Hence it is expected that binding force reversal should occur almost for all the spherical heterodimer structures. But our work in this chapter suggests that reversal of lateral (for on-axis heterodimers) and longitudinal (for off-axis heterodimers) binding force of symmetry broken heterodimers follow fully different key parameters/mechanisms; i.e. later one depends on relative orientation and constructive dipole-quadrupole resonance (though not super-scattering mode [40]) but the former one on light polarization and the induced electric resonance. Most importantly, the reversal of longitudinal binding force can be easily controlled due to forced symmetry breaking just by changing the direction of wave propagation for a specific set-up of off-axis heterodimers or by changing their relative orientation. Interestingly, though reversal of optical binding force occurs for nano rods or other shapes due to Fano resonance [22, 23], we have demonstrated that Fano resonance [39, 41] does not contribute to binding force reversal for spherical heterodimers. These observations are quite different than the homo-dimer cases reported in [113,134-137].

Though Lorentz force analysis has been applied previously in [65,77,79,96] to understand the mechanism of chirality induced force, Luneburg lenses, mechanical interaction between light and graded index media, cloaking effect, background effect on radiation pressure; such analysis has never been applied in details to understand

the plasmonic effects and plasmonic binding force. Although it is commonly believed that plasmonic forces mostly arise from the surface force/polarization induced charges [109,114], our study suggests a notably different proposal especially for the off-axis heterodimers. In addition, how the optical force distributes itself and which part of the total force is mainly responsible for plasmonic binding force reversals have also been discussed based on the Lorentz force dynamics without applying any approximate method.

Table-3.1 of this chapter (given below) represents a very short overview of our overall investigation throughout this chapter. Observations of this work should be very useful for the future plasmonic applications of the heterodimers in the areas of improved sensors [39, 118,119], particle clustering and aggregation [113,134,135].

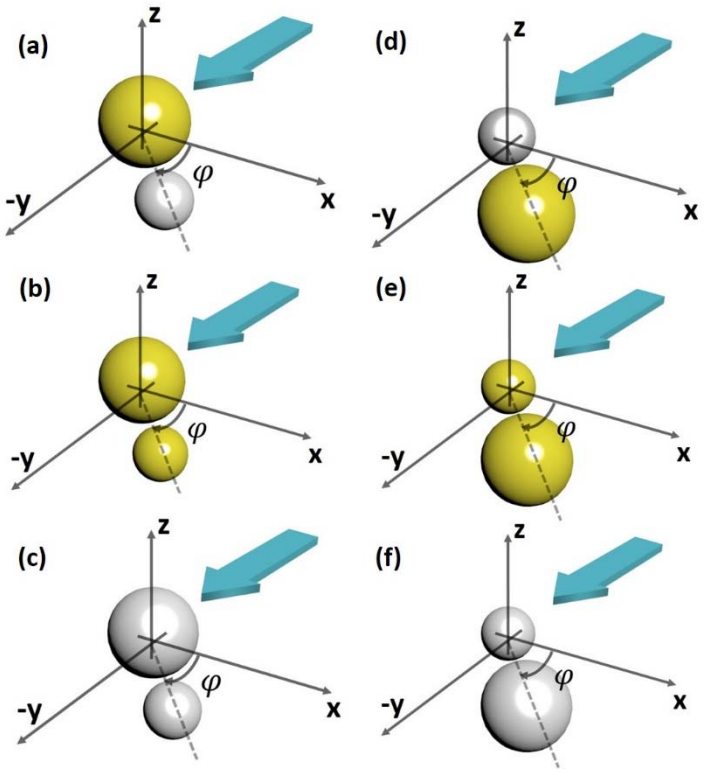

Fig. 3.1: Two particles of radii 100 and 50 nm are placed with inter particle distance from surface to surface '*d*'; *d*= 20 nm throughout this chapter. One particle centered at $(0,0,0)$ and the other centered at $(R\cos\varphi,-R\sin\varphi,0)$ with $R = d + r_1 + r_2$=170 nm the center-to-center distance of the two object. The angular displacement is 'φ' which is considered 0 degree when the dimers are on-axis in *x* direction. And the angular displacement is considered +90 degree [end fire configuration] when the dimers are on-axis in *–y* direction. This 'φ' should not be mixed up with the azimuthal angle of spherical co-ordinate system. Two different polarized light sources are applied propagating towards *–y* direction [in order to break the symmetry; light is shined from a specific side]: (i) For parallel polarization: *x*-polarized plane wave $E_x = E_0 e^{-i\beta y}$ (ii) For perpendicular polarization: *z*-polarized plane wave $E_z = E_0 e^{-i\beta y}$. Yellow color represents Au and Silver color represents Ag: (a) Au-Ag (b) Au-Au (c) Ag-Ag (d) Ag-Au (e) Au-Au and (f) Ag-Ag.

Table-3.1: An overview on the behavior of binding force for on and off-axis heterodimers

Hetero dimer Set	Number in Fig. 3.1	On-axis [φ=0]	Off-Axis [φ=60 to 120 deg.]	Pol.	Binding Force reversal: (i)Lateral (ii)Longitudinal	Comment (a) Inter-particle edge to edge gap, d, is always fixed 20 nm. (b) Heterodimer radii are fixed: 50 nm and 100 nm.
Ag-Au	(a) [=(d)]	Yes		⊥	(i)Yes	Lateral binding force reverses only for perpendicular polarization. For higher wavelength region: Reversal of force occurs due to zero surface and bulk Lorentz force at a specific wavelength near bonding (attractive force) resonance. For lower wavelength region: such force reversal can be recognized from the reversal of electric dipole moment of the smaller object. In fact, such reversals (repulsive to attractive) occur due to induced electric resonance near the bonding resonance mode.
Au-Au	(b) [=(e)]	Yes		⊥	(i)Yes	
Ag-Ag	(c) [=(f)]	Yes		⊥	(i)Yes	
Ag-Au	(a) [=(d)]	Yes		∥	(i)No	
Au-Au	(b) [=(e)]	Yes		∥	(i)No	
Ag-Ag	(c) [=(f)]	Yes		∥	(i)No	
Ag-Au	(a)		Yes	⊥ and ∥	(ii) No	Longitudinal binding force reverses [for only Ag-Au and Ag-Ag case] only when the bigger particle rotates and the light is perturbed by the fixed smaller object at first. This reversal occurs due to the constructive dipole-quadrupole resonance and due to the dominance of the bulk Lorentz force. However, for all heterodimer sets attractive and repulsive force can be very easily controlled by changing the light propagation direction or changing the relative orientation of the dimers. Such control is not possible with the spherical homo-dimers.
Au-Au	(b)		Yes	⊥ and ∥	(ii) No	
Ag-Ag	(c)		Yes	⊥ and ∥	(ii) No	
Ag-Au	(d)		Yes	⊥ and ∥	(ii) Yes	
Au-Au	(e)		Yes	⊥ and ∥	(ii) No	
Ag-Ag	(f)		Yes	⊥ and ∥	(ii) Yes	

3.1 Optical Force calculation

We again specify that throughout this thesis we refer to 'exterior' or 'outside' forces as those evaluated outside the volume of the macroscopic particles, while ‘interior’ or 'inside' refer to those quantities inside this object volume. In order to consider the realistic effects, in this chapter we have done all the numerical calculations /full wave simulations [100] in three dimensional (3D) structures.

The proposed simplest set-up is illustrated in Fig. 3.1. The Gold (Silver) and Silver (Gold) particles are placed near to each other. The real and imaginary part of the permittivity of Gold is taken from the standard CRC data [100, 138]; but for Silver it is taken from standard Palik data [100,139] (the criteria is the best agreement with the FDTD fitting model in [100] for full wave simulation). Inter particle distance is ‘d’. Suppose the source is a simple *x*-polarized plane wave $E_x = E_0 e^{-i\beta y}$ propagating towards *–y* direction. This set-up is a forced symmetry broken system which later plays a vital role for the reversal of binding force. If the heterodimer set-up is shined from the top, such ‘forced symmetry breaking’ is not possible. The ‘outside optical force’ [43, 84] is calculated by the integration of time averaged Minkowski [43,84] stress tensor at r=a^+ employing the background fields of the scatterer of radius *a*:

$$\begin{aligned} \left\langle \boldsymbol{F}_{\text{Total}}^{\text{Out}} \right\rangle &= \oint \left\langle \overline{\overline{\boldsymbol{T}}}^{\text{out}} \right\rangle \cdot d\boldsymbol{s} \\ \left\langle \overline{\overline{\boldsymbol{T}}}^{\text{out}} \right\rangle &= \frac{1}{2}\text{Re}[\boldsymbol{D}_{\text{out}}\boldsymbol{E}_{\text{out}}^{*} + \boldsymbol{B}_{\text{out}}\boldsymbol{H}_{\text{out}}^{*} - \frac{1}{2}\overline{\overline{\boldsymbol{I}}}(\boldsymbol{E}_{\text{out}}^{*}\cdot\boldsymbol{D}_{\text{out}} + \boldsymbol{H}_{\text{out}}^{*}\cdot\boldsymbol{B}_{\text{out}})] \end{aligned} . \quad (3.1)$$

Where 'out' represents the exterior total field of the scatterer; $\boldsymbol{E}$, $\boldsymbol{D}$, $\boldsymbol{H}$ and $\boldsymbol{B}$ are the electric field, displacement vector, magnetic field and induction vectors respectively, $\langle\ \rangle$ represents the time average and $\bar{\bar{\boldsymbol{I}}}$ is the unity tensor.

On the other hand, based on the Lorentz force, the total force (surface force and the bulk force [65,77,79,96]) can be written as:

$$\left\langle \boldsymbol{F}_{\text{Total}} \right\rangle = \left\langle \boldsymbol{F}_{\text{Volume}} \right\rangle = \left\langle \boldsymbol{F}_{\text{Bulk}} \right\rangle + \left\langle \boldsymbol{F}_{\text{Surf}} \right\rangle = \int \left\langle \boldsymbol{f}_{\text{Bulk}} \right\rangle dv + \int \left\langle \boldsymbol{f}_{\text{Surface}} \right\rangle ds \tag{3.2}$$

Where

$$\begin{aligned} \left\langle \boldsymbol{f}_{\text{Surface}} \right\rangle &= \sigma_e \boldsymbol{E}^*_{avg} + \sigma_m \boldsymbol{H}^*_{avg} \\ &= \left\{ \epsilon_o (\boldsymbol{E}_{\text{out}} - \boldsymbol{E}_{\text{in}}) \cdot \hat{\boldsymbol{n}} \right\} \left(\frac{\boldsymbol{E}_{\text{out}} + \boldsymbol{E}_{\text{in}}}{2} \right)^* + \left\{ \mu_0 (\boldsymbol{H}_{\text{out}} - \boldsymbol{H}_{\text{in}}) \cdot \hat{\boldsymbol{n}} \right\} \left(\frac{\boldsymbol{H}_{\text{out}} + \boldsymbol{H}_{\text{in}}}{2} \right)^*, \end{aligned} \tag{3.3}$$

$$\left\langle \boldsymbol{f}_{\text{Bulk}} \right\rangle = \frac{1}{2} \text{Re}[\varepsilon_0 (\nabla \cdot \boldsymbol{E}_{\text{in}}) \boldsymbol{E}^*_{\text{in}} + \mu_0 (\nabla \cdot \boldsymbol{H}) \boldsymbol{H}^*_{\text{in}}] - \frac{1}{2} \text{Re}[i\omega(\varepsilon_s - \varepsilon_0)\{\boldsymbol{E}_{\text{in}} \times \boldsymbol{B}^*_{\text{in}}\} + i\omega(\mu_s - \mu_0)\{\boldsymbol{D}^*_{\text{in}} \times \boldsymbol{H}_{\text{in}}\}] \tag{3.4}$$

$\boldsymbol{f}_{\text{Surface}}$ is the surface force density (the force which is felt by the bound electric and magnetic surface charges of a scatterer), which is calculated just at the boundary of a scatterer [65,77,79,96]. $\boldsymbol{f}_{\text{Bulk}}$ is the bulk force density, which is calculated from the interior of the scatterer by employing the inside field [65,77,79,96]. 'in' represents the interior fields of the scatterer; 'avg' represents the average of the field. σ_e and σ_m are the bound electric and magnetic surface charge densities of the scatterer respectively. ε_s is permittivity and μ_s is permeability of the scatterer. The unit vector $\hat{\boldsymbol{n}}$ is an outward pointing normal to the surface. As per we know, the Lorentz force dynamics of plasmonic particles and especially heterodimers have not been discussed previously. It is notable that the 'external dipolar force' [43, 84] (which has also been described as Lorentz force in [38]) is quite different than the Lorentz force defined in

our Eqs (3.2) - (3.4). Even if the quasi static analysis (i.e. dipolar force [40,41]) leads to wrong conclusion (for example- in refs [38, 97-99]); the agreement of Lorentz volume force [65,77,79,96] and external ST method based on full electrodynamic analysis, which is considered for all the force calculations in this work, should lead to the consistent result for realistic experiments.

3.3 Lateral binding force: On-Axis Spherical Heterodimers

Behavior of optical binding force for on-axis spherical heterodimers has been studied in [38] considering the inter particle edge to edge gap of only 2nm. In addition, the size of the spherical objects has been considered only 10 nm and another one maximum 40 nm in [38]. However, we have observed that if the inter particle gap is increased (i.e. 20 nm instead of 2 nm), the reversal of optical binding force dies out for both polarizations of light. However, a more generic way of the reversal of binding force has been investigated and demonstrated in the next sub-sections. Such an investigation is also important to find the answer of the question: 'Whether Fano resonance (raised from heterodimer interaction) is a universal process of achieving binding force reversal?'.

3.3.1 Parallel Polarization: No reversal of lateral binding force for Au-Ag, Au-Au and Ag-Ag on-axis heterodimers

It is observed in full wave simulation that for Ag-Au, Au-Au and Ag-Ag heterodimer configurations, the reversal of lateral binding force [$F_{Bind\ (x)} = (F_{B\ (x)}\text{-}F_{S\ (x)})$] does not occur for the light polarized parallel to the dimer axis. Here $F_{B(x)}$ and $F_{S(x)}$ are the $+x$ directed time averaged force on big and small particle respectively [cf. Figs in 3.1].

According to our several full wave simulation results, the important conclusion is that: although reversal of optical binding force occurs for nano rods or other shapes due to Fano resonance [22, 23], Fano resonance is in general not the reason of the reversal of optical binding force.

3.3.2 Perpendicular Polarization: Reversal of lateral binding force for Au-Ag, Au-Au and Ag-Ag on-axis heterodimers

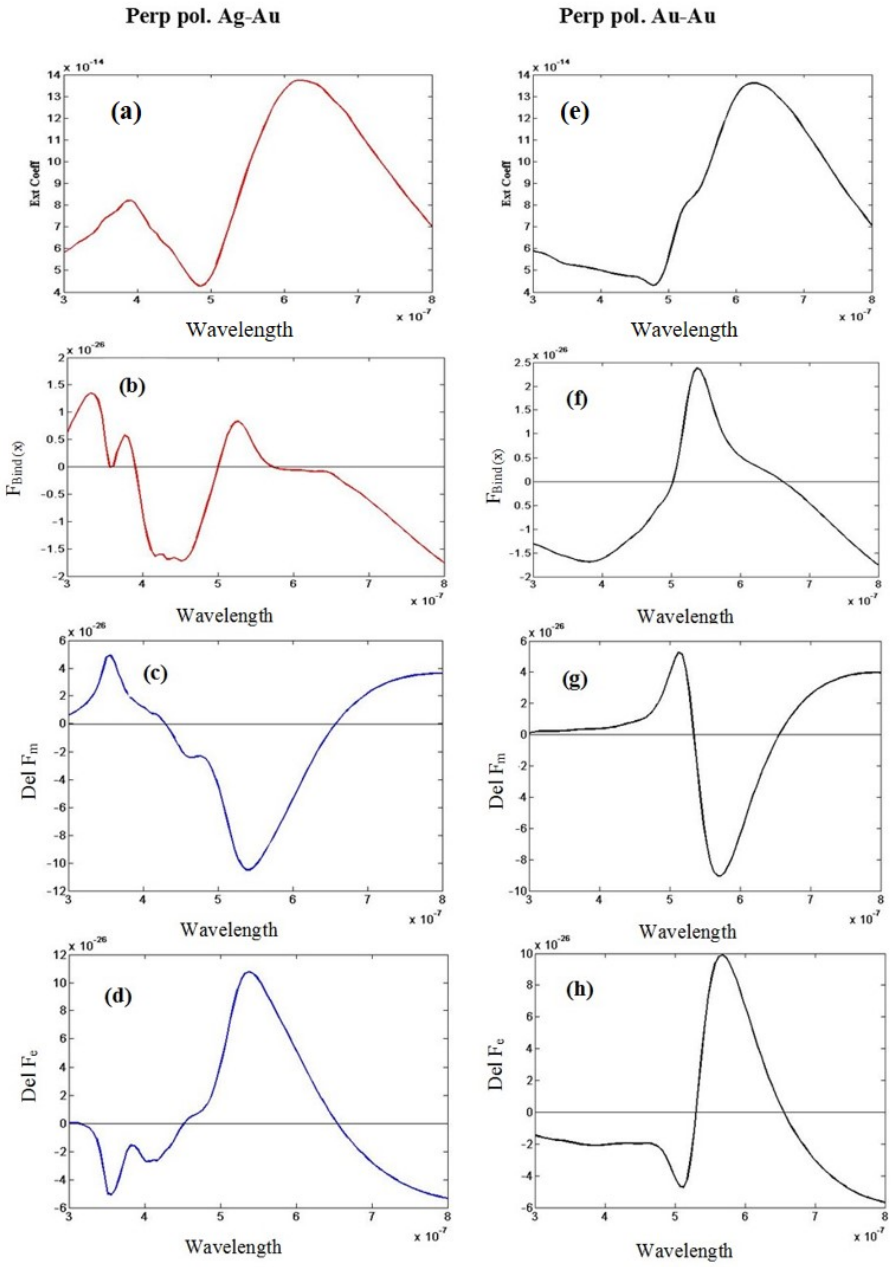

Fig.3.2: Considering perpendicular polarized light for the configuration of Fig.3.1 (a) and 'φ' = 0 degree [on axis Ag-Au]: (a) Extinction co-efficient. (b) The binding force $F_{Bind\,(x)} = (F_{B\,(x)}\text{-}F_{S\,(x)})$. (c) Difference of bulk Lorentz force. (d) Difference of surface

force. Considering same polarization of light for the configuration of Fig.3.1 (b) and 'φ' = 0 degree [on axis Au-Au]: (e) Extinction co-efficient (f) The binding force $F_{Bind\ (x)}$ = ($F_{B\ (x)}$-$F_{S\ (x)}$) (g) Difference of Lorentz bulk force for x components. (h) Difference of Lorentz surface force for x components.

We consider two on-axis Ag-Au, Au-Au and Ag-Ag particles of 100 and 50 nm with inter particle distance (edge to edge distance) of 20 nm [cf. Figs. 3.1 (a), (b) and (c)] and perpendicular polarized light.

(1) The difference of the bulk part of the total Lorentz force on a plasmonic object [also cf. Eq (3.4)] should describe the relative bulk force experienced by the optical molecule:

$$\text{Del } F_{Bulk} = \text{Del } F_{m} = \int [\langle \boldsymbol{f}_{\text{Bulk}\,(B)} \rangle dv_{(B)}] - \int [\langle \boldsymbol{f}_{\text{Bulk}\,(S)} \rangle dv_{(S)}] \quad (3.5)$$

Here; (B) and (S) represent: bigger and smaller object respectively. At the same time the difference of the surface part [which originates from induced surface charges; cf. Eq (3.3)] of the total Lorentz force on a plasmonic object should describe the relative surface force experienced by the optical molecule:

$$\text{Del } F_{Surf} = \text{Del } F_{e} = \int [\langle \boldsymbol{f}_{\text{Surface}\,(B)} \rangle ds_{(B)}] - \int [\langle \boldsymbol{f}_{\text{Surface}\,(S)} \rangle ds_{(S)}] \quad (3.6)$$

It should be noted that:

$F_{Bind\ (x)} = \left(F_{B\ (x)} - F_{S\ (x)}\right) = \text{Del } F_{\text{Bulk}(x)} + \text{Del } F_{\text{Surf}(x)}$. Subscript (x) represents the force in +x direction. It is observed that near the bonding resonance mode reversal of the optical binding force (negative to positive) occurs at wavelength 646 nm [cf. Fig. 3.2(a), (b) for Ag-Au and Fig. 3.2 (e), (f) for Au-Au]. Reversal of optical binding force occurs at that specific wavelength mainly due to the individual zero surface ($\text{Del } F_{\text{Surf}(x)} = 0$) and bulk (

$\mathrm{Del}\,F_{\mathrm{Bulk}(x)} = 0$) Lorentz force [cf. Fig. 3.2 (c), (d) for Ag-Au and Fig. 3.2(g), (h) for Au-Au].

(2) We now consider a different idea: the electric dipole moment p of the objects to explain the reversal of binding force based on same and opposite electric charges. This idea of electric dipole moment p should be a more generalized idea than the electric polarizability (discussed in ref. [38]), as the overall size of the dimer set-up is higher than the dipolar limit in this work. The real part of electric dipole moment of an object is defined as:

$$p = \mathrm{Re}\int [i\omega(\varepsilon_s - \varepsilon_0)\boldsymbol{E}_{\mathrm{in}}]dv \tag{3.7}$$

It is also demonstrated that whenever the 2nd reversal (positive to negative) of the lateral binding force occurs for transverse/perpendicular polarization near the wavelength 500 nm [cf. Fig. 3.2(a), (b) for Ag-Au and Fig. 3.2 (e), (f)], the real part of the induced electric dipole moment reverses its sign near the resonance of the smaller object in Fig. 3.3 (a) and (c).This does not occur for parallel polarized case as shown in Fig. 3.3(b) and (d). So, the reversal of lateral binding force near this specific wavelength can better be explained based on the idea of induced same or opposite electric charges similar to the idea (reversal of the electric polarizability near resonance) proposed in ref. [38]. Results of on-axis Ag-Ag heterodimers are similar to Ag-Au and Au-Au cases; which have been observed (but not shown here) in our full wave simulations.

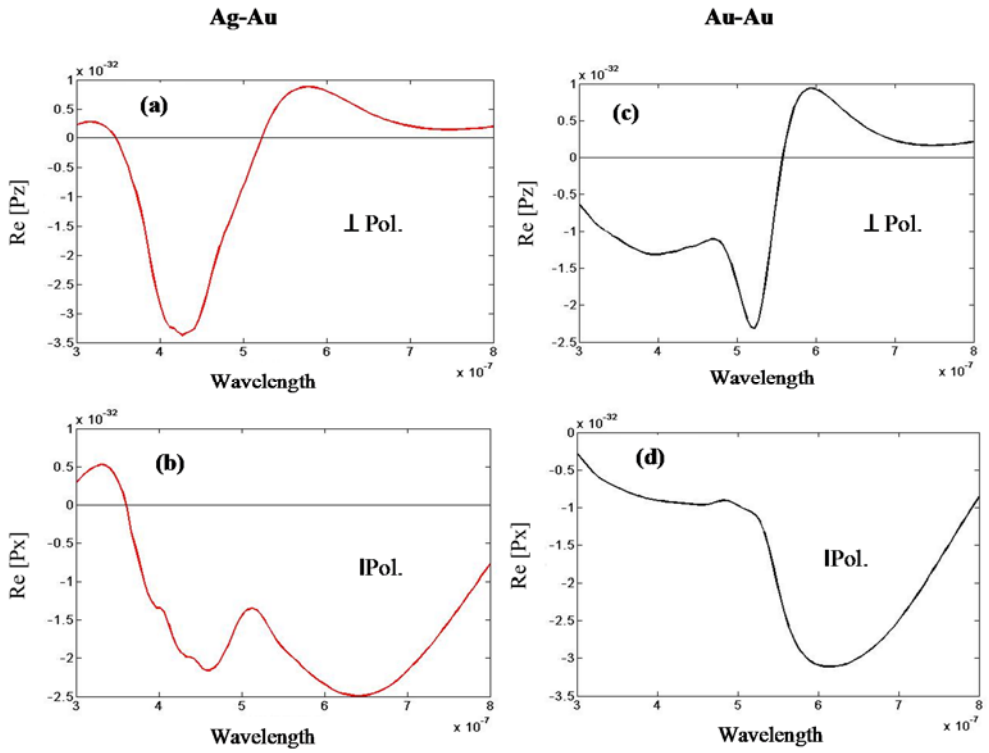

Fig. 3.3: For both polarizations, electric dipole moment of Ag-Au heterodimers [for configuration of Fig. 3.1 (a)] and Au-Au heterodimers [for configuration of Fig. 3.1 (b)].

3.4 Longitudinal binding force for Off-Axis Plasmonic Heterodimers: end-fire and near end-fire configuration

In this section we mainly focus on the Ag-Au heterodimers to explain the behaviour of the off-axis heterodimers. Reversal of the optical longitudinal binding force has been observed for only Ag-Au and Au-Au off-axis heterodimers (only when the smaller object perturbs the propagating light at first) and this issue is connected with the presence of constructive interference of dipole-quadrupole mode. Another notable point is that: mutual attraction and repulsion of all the off-axis heterodimers can be very easily controlled by changing the direction of propagating light or by changing

the relative orientation of the particles. All the conclusions of the forthcoming sections have been noted very shortly in Table-3.1.

3.4.1 Au-Ag off-axis heterodimers: Longitudinal binding force for both polarizations

Now, we consider Au-Ag particles of 100 and 50 nm respectively with inter particle distance of 20 nm [cf. Fig.3.1 (a) and (d)] but considering rotation angle, φ, of the particle is between 60 to 120 degrees [i.e. end fire or nearly end fire configuration [38]]. The light source is same. We start to create angular displacement from the x-axis considering two cases: (A) Rotating the smaller object keeping the bigger one fixed [cf. Fig. 3.1(a)] and (B) Rotating the bigger object keeping the smaller one fixed[cf. Fig. 3.1(d)]. Now the question arises: 'Should there be any difference on longitudinal optical binding force for these two cases- (A) and (B)?'. The notable observation of this work: the behavior of longitudinal binding forces are quite different for these two cases due to the forced breaking of symmetry by placing the light source at one side of the dimer configuration instead of at the top of the set-up. If the light source were placed at the top of the set-up, such difference should not arise. According to our forthcoming observations, forced symmetry breaking is detected as one of the key ways to control the inter-particle attraction and repulsion. Some previous symmetry broken set-ups have been discussed in [140, 141] (but not for optical force), which are different than our case.

However, for both cases- (A) and (B), the extinction cross sections reveal that bonding mode resonance blue shifts for increasing angular displacement in Fig. 3. 4(a), (c), (e), (g) for aforementioned both the cases. We have observed that this is also true for Au-Au heterodimers. It appears that an 'angular ruler' may also be possible similar to previously defined 'inter-particle gap ruler' in ref. [142].

For the off-axis heterodimers, the attractive force can be defined as the positive value of the optical binding force $F_{Bind\,(y)}(SR)= (F_{S\,(y)}-F_{B\,(y)})$ and $F_{Bind\,(y)}(BR)= (F_{B\,(y)}-F_{S\,(y)})$ [here SR means small rotating and BR means big rotating], considering two important facts: (a) the angular displacement angles should be much higher and φ should be as close as 90 degree [i.e. $60< \varphi <120$] and (b) x directed lateral force $F_{(x)}$ is at least ten times smaller than y directed force $F_{(y)}$ (which is usually satisfied, as the y directed/longitudinal scattering force is usually much higher than the x directed lateral force for plasmonic spherical heterodimers). It should also be noted that the scattering force of the bigger object is always pushing force [negative value of $F_{B\,(y)}$], which is one of the key issues to control the reversal of the y directed binding force (this will be explained next).

3.4.1.1 Au-Ag off-axis heterodimers: Rotating the smaller particle keeping the big one fixed

At first we consider the rotation of the smaller object [case (A); cf. Fig. 3.1(a)] for both perpendicular and parallel polarizations of light. For φ =60 to 90 degrees, it is observed that only the scattering force of the smaller object experiences the reversal at bonding resonance region. On the other hand, scattering force of the bigger object ($F_{B\,(y)}$) is always pushing force. But the most important fact is that $\left|F_{S\,(y)}\right| < \left|F_{B\,(y)}\right|$; always. As a result, $F_{Bind\,(y)}(SR) = (F_{S\,(y)}-F_{B\,(y)})$ is always positive [attractive force as shown in Fig. 3.4(b) and (f)]. Importantly, the real part of electric dipole moment of the smaller object reverses its sign near the bonding resonance [not shown] but $F_{Bind\,(y)}(SR)$ always remains attractive with no reversal of sign. In fact, the difference of the particle radius of both the particles plays a vital role. When one of the particles in the heterodimer is much larger than the other one and the propagating light is perturbed by the bigger object at first, the scattered field from the large particle becomes much larger compared to the incident field. When the field enhancement is quite high at the inter particle gap position, this enhanced field forces the dipole on

the small particle to oscillate in phase. Accordingly, with larger radius of bigger particle, the optical force between the particles becomes always attractive.

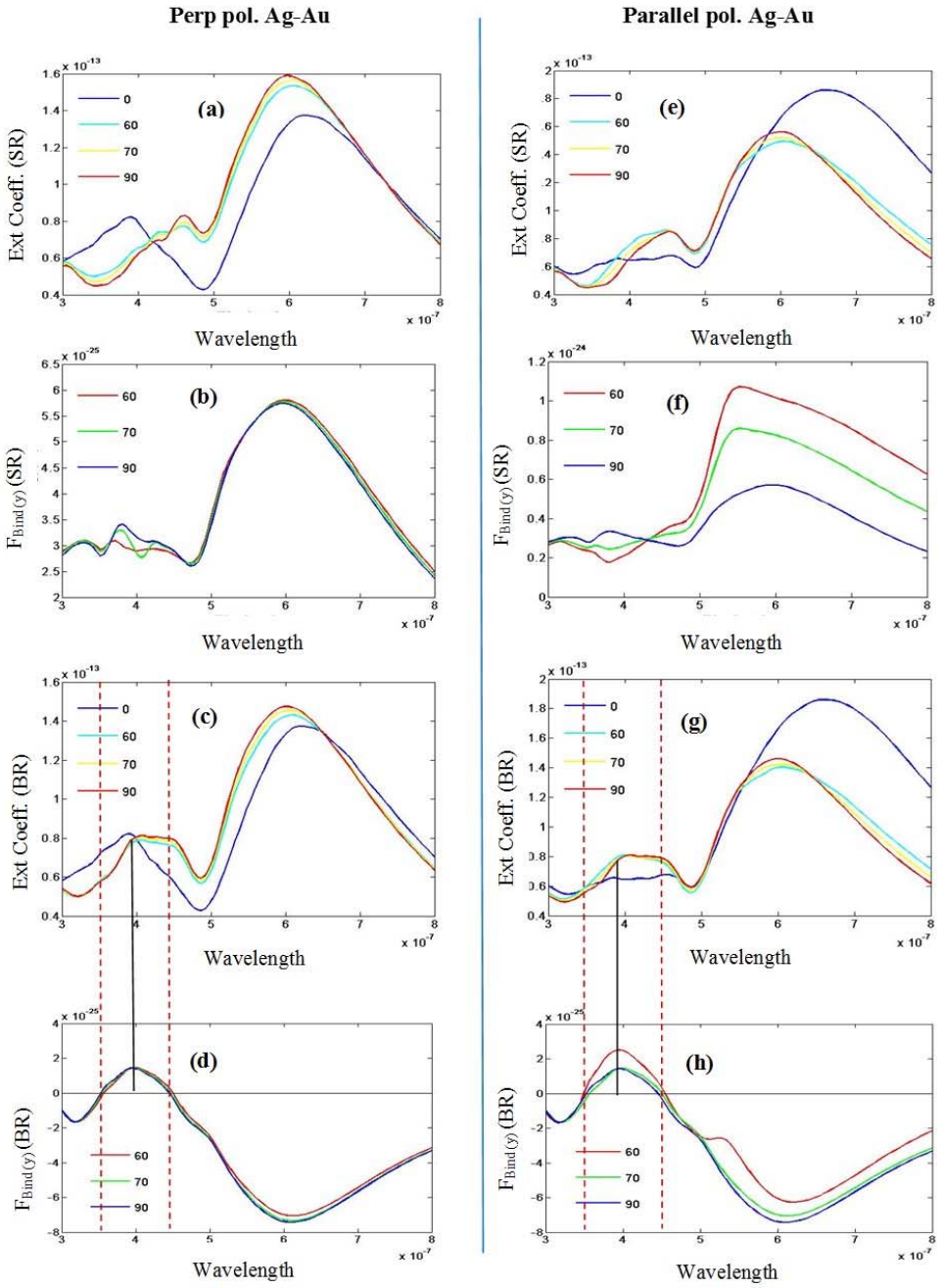

Fig.3.4: SR and BR represent 'small rotate' and 'big rotate' respectively and 'φ' = 60, 70 and 90 degree [off axis Ag-Au]. Considering perpendicular polarized light- for the configuration of Fig.3.1 (a): (a) Extinction co-efficient (SR) (b) The binding force $F_{Bind\,(y)}$ (SR); and for the configuration of Fig.3.1 (d): (c) Extinction co-efficient (BR) (d) the binding force $F_{Bind\,(y)}$ (BR). Considering parallel polarized light: for the configuration of Fig.3.1 (a): (e) Extinction co-efficient (SR) (f) The binding force $F_{Bind\,(y)}$ (SR); and for the configuration of Fig.3.1 (d): (g) Extinction co-efficient (BR) (h) The binding force $F_{Bind\,(y)}$ (BR).

3.4.1.2 Au-Ag off-axis heterodimers: Rotating the bigger particle keeping the small one fixed

Now, we shall consider the alternate orientation [case (B); cf. Fig. 3.1 (d)] by rotating the bigger object and keeping the smaller object fixed. If the bigger object is rotated remaining the smaller one fixed, $F_{Bind(y)}$ (BR) reverses during the antibonding type resonance mode and near spectral dip position. This is explained next.

When the smaller object was rotated and the propagating light was perturbed by the bigger object at first, the scattering force on the bigger object (always pushing) was always higher than the smaller one. But when the bigger object is rotating and the propagating light is perturbed by the smaller object at first, there are some chances to find some wavelength regions when the longitudinal/scattering force on the smaller object becomes higher than the bigger object. In this way the binding force $F_{Bind\ (y)}$ (BR)= ($F_{B\ (y)}$-$F_{S\ (y)}$) can be observed attractive in those wavelength regions. This is what exactly happens during the anti-bonding type resonance modes as shown in Fig. 3.3 (c), (d) and (g), (h); which is quite different than the conventional idea of optical binding force with homodimers [113]. For homodimers, according to the quasi-static approximation limit [113]: the bonding modes and antibonding modes have positive and negative definite slopes, respectively. As a result, consequently they must, respectively, induce attraction and repulsion. But we clearly observe the opposite scenario for the longitudinal binding force of heterodimer set (at a fixed edge to edge distance of 20 nm) when the light is perturbed by the smaller object at first. Then the question rises why this kind of opposite behavior is observed for such symmetry broken heterodimer sets. Its answer lies in the electrodynamic calculations and force distribution analysis instead of the quasi-static analysis; mainly due to the generation of multipoles. Based on the results demonstrated in Fig. 3.5 (a) - (h) we shall discuss the detail dynamics considering a specific case: φ =60 degree.

In Fig. 3.5 (d) and (h) we have plotted the difference of the bulk Lorentz force, which clearly suggests that the total binding force is dominated by the bulk part of Lorentz force [which is in contrast with the commonly observed dominance of surface [114]/ polarization charge induced force [109] for plasmonic objects]. This force can be considered as the scattering force part [114, 143] of the total force, which is physically originating from the multiple scattering between the smaller and the bigger object. Fig. 3.5 (c) and (g) suggest that during the anti-bonding resonance mode, the directive forward scattering of the bigger object is much higher than the smaller object. Surface charge plots in Fig. 3.6 suggest that for the parallel polarized illumination, during the wavelength spectrum around 350 nm to 470 nm, constructive interference occurs due to dipole quadrupole resonance. Though this is not super-scattering [40], it is recognized that the forward scattering of the bigger object increases during this spectra [cf. the extinction spectra in Fig. 3.4(g) where the magnitude of extinction co-efficient increases for higher rotation angles during this specific spectrum regime]. On the other hand, exactly opposite scenario takes place for the bonding mode resonance. For example- at higher wavelength regime, during bonding mode resonance, the smaller object even experiences optical pulling force [cf. Fig. 3.5(c) and (g)] because of: (i) very strong effective forward scattering along with (ii) more reflected light from the bigger object.

It is observed that the reversal wavelength of the optical binding type force $F_{Bind\,(y)}$ (BR)= ($F_{B\,(y)}$-$F_{S\,(y)}$) remains almost fixed along with the spectral dip position [cf. Fig. 3.4(c), (d) and (g), (h)], though the bonding mode resonance blue shifts gradually with the rotation of the bigger object. Moreover, very similar to ref [22], the reversal of the phase of the steady state current takes place near the spectral dip in our heterodimer set-ups as shown in Fig. 3.6 (m)-(r), though it is constructive dipole quadrupole resonance instead of destructive one.

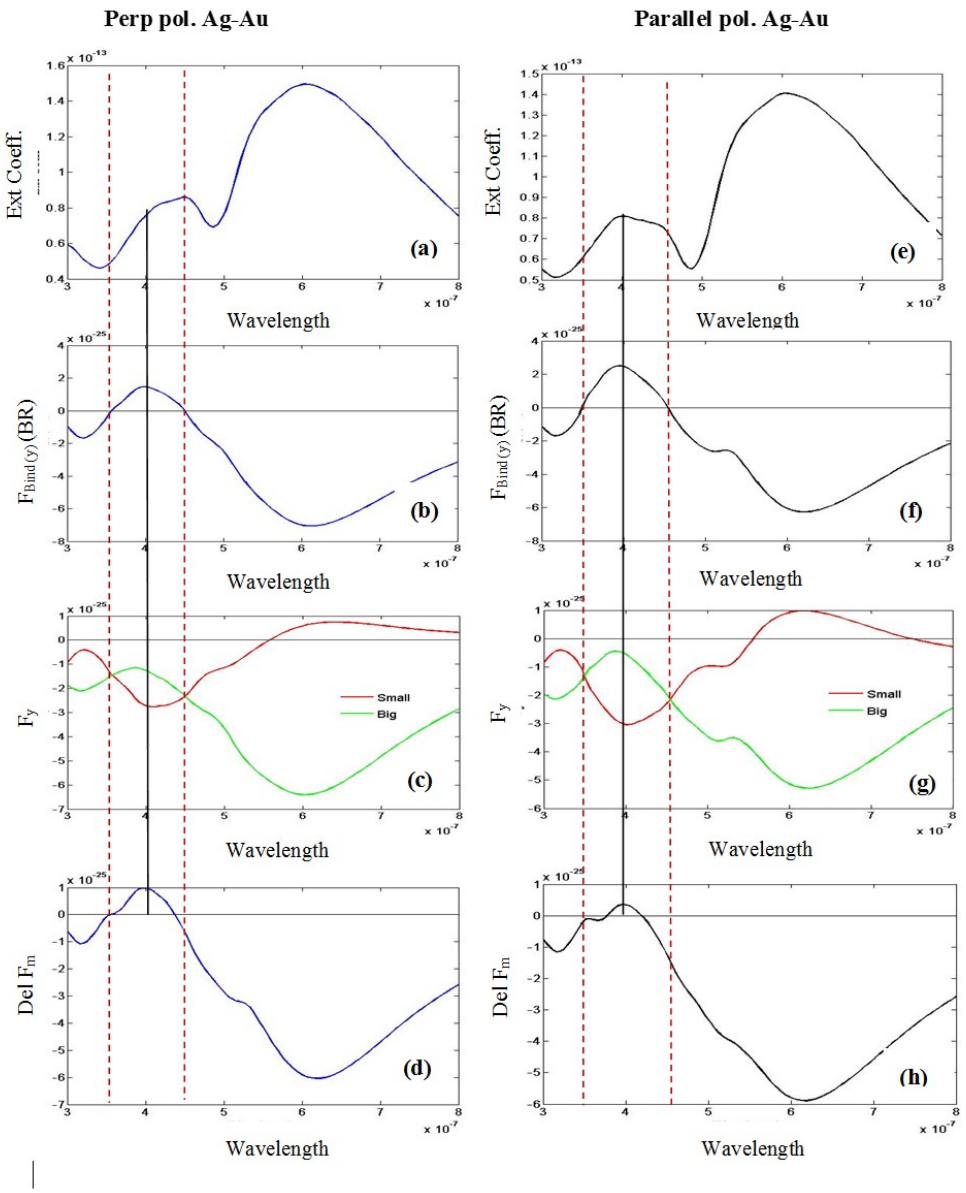

Fig. 3.5: SR and BR represent 'small rotate' and 'big rotate' respectively. For off axis Ag-Au and BR [the configuration of Fig.3.1 (d) and 'φ' = 60 degree]: Considering perpendicular polarized light (a) Extinction co-efficient (b) The binding force $F_{Bind\,(y)}$ (BR) (c) Time averaged force on each particle. (d) Difference of bulk Lorentz force. Considering parallel polarized light for same configuration (e) Extinction co-efficient (f) The binding force $F_{Bind\,(y)}$ (BR) (g) Time averaged force on each particle. (h) Difference of bulk Lorentz force for y components.

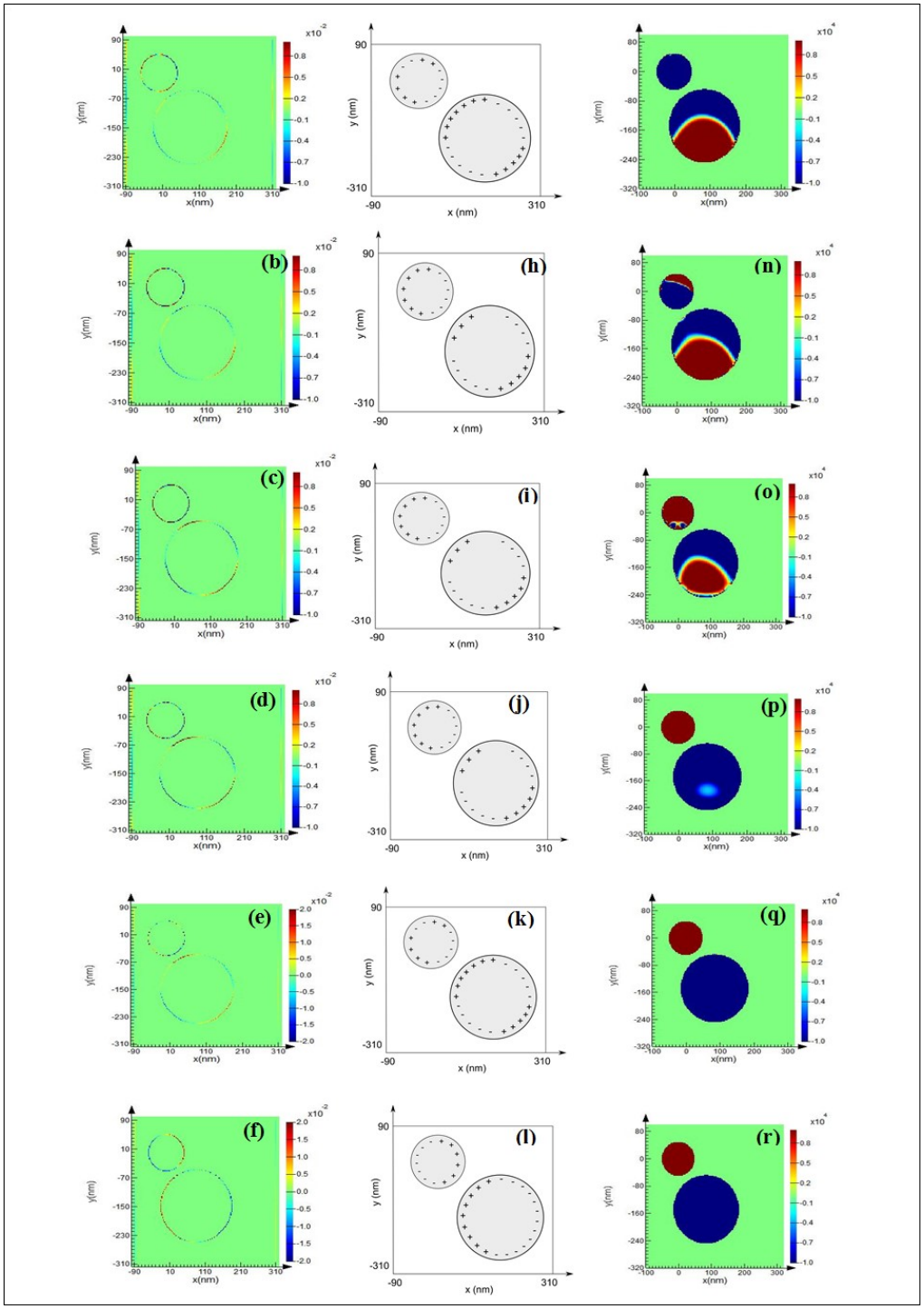

Fig. 3.6: For off axis Ag-Au and by rotating the big particle [the configuration of Fig.3.1 (d) and 'φ' = 60 degree]: Considering parallel polarized light, from left first two columns represent surface charges [(a)-(l)] and the third column represents steady state current [(m)-(r)]. We have chosen six wavelengths for six different rows (from top to bottom): 338, 354, 400, 457, 485 and 612 nm. Charge distributions: (a) QQ (b) DQ (c) DQ (d) DQ (e) QQ (f) DD; where Q and D mean quadrupole and dipole respectively.

3.5 Simplest procedure to reverse the longitudinal binding force for all the off-axis heterodimers

So far we have shown that: when the bigger object is rotated and the propagating light is perturbed by the smaller object at first, for only Ag-Au and Ag-Ag off-axis heterodimers reversal of longitudinal binding force occurs [i.e. the dynamics of Ag-Ag and Au-Au heterodimers has been shown in Fig. 3.7 and 3.8 respectively]. Especially after the anti-bonding resonance mode, the longitudinal binding force is observed always repulsive for such heterodimers. On the other hand, for Au-Au heterodimers this force is always repulsive for such configuration for the whole visible wavelength spectrum.

In contrast, when the smaller object is rotated and the propagating light is perturbed by the bigger object at first, for all the spherical heterodimers no reversal of longitudinal binding force occurs. Binding force is always attractive for such configuration.

So, (1) if we consider the higher wavelength regions and change the direction of propagating light manually by bringing the light source from one side of the dimers to another side, it will be easily possible to observe the mutual repulsion and attraction of all the heterodimer sets just due to the automatic change of the relative dimer position of smaller and bigger objects. Or (2) simply by changing the relative orientation of the heterodimers manually (not light propagation direction), it is also possible to observe such reversal at higher wavelength regions. Such simplest controls of force reversal due to ‘forced broken symmetry’ are certainly impossible with the plasmonic homo-dimers.

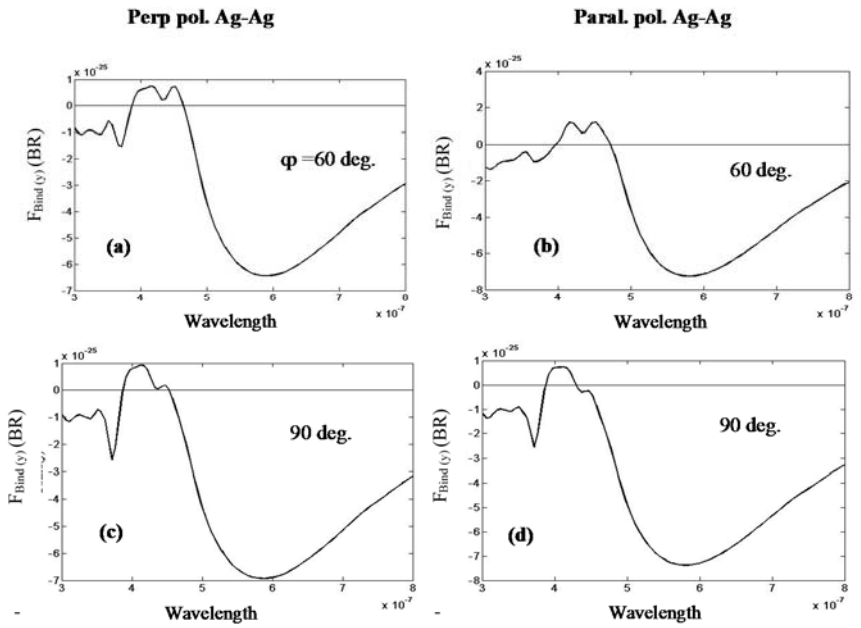

Fig 3.7: Reversal of longitudinal binding force for off-axis Ag-Ag heterodimers [cf. Fig. 3.1 (f)] for both polarizations.

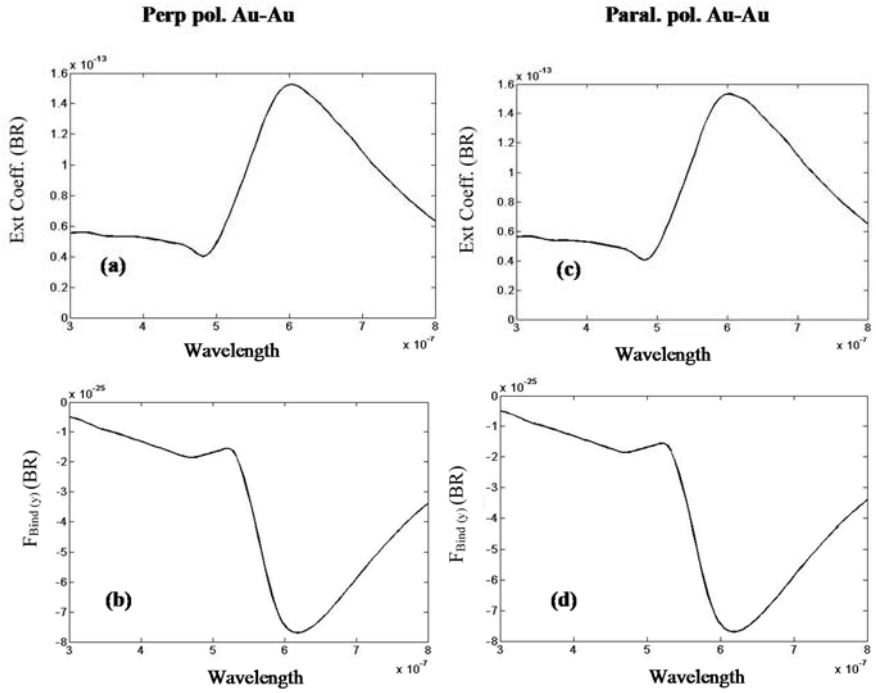

Fig. 3.8: (a) and (c): extinction coefficient of off-axis [only φ =90 degree case shown here] Au-Au hetero-dimers [cf. the configuration of Fig. 3.1(e)]. (b) and (d): Longitudinal binding force on off-axis [only φ =90 degree case shown here] Au-Au hetero-dimers.

3.6 CONCLUSIONS

In order to identify the conclusions of this chapter at a glance, we have listed our key observations in Table-3.1. It is expected that binding force reversal should occur almost for all the spherical heterodimer structures due to the presence of bonding and anti-bonding mode in the visible spectra. But our work suggests that reversal of lateral (for on-axis heterodimers) and longitudinal (for off-axis heterodimers) binding force of symmetry broken heterodimers follow fully different key parameters/mechanisms; i.e. later one depends on relative orientation and constructive dipole-quadrupole resonance but the former one on light polarization and the induced electric resonance. Most importantly, the reversal of longitudinal binding force can be easily controlled due to forced symmetry breaking just by changing the direction of wave propagation for a specific set-up of off-axis heterodimers or by changing their relative orientation.

In addition, though it is commonly believed that plasmonic forces mostly arise from the surface force and Fano resonance can be a promising way to achieve binding force reversal, our study based on Lorentz force dynamics suggests notably opposite proposals for the case of plasmonic spherical heterodimers. Notably, the longitudinal binding force of spherical heterodimers originates almost fully from the difference of the bulk part of Lorentz force, which strongly suggests the connection of bulk Lorentz force with the scattering force. As much study has not been done on the connection of Lorentz force with gradient and scattering forces, this work may open a new window for such investigations.

Chapter 4

Problem with Lorentz Force due to Material Background: Interfacial Tractor Beam

4.0 Summary of Chapter 4

In previous two chapters applications of Lorentz force have been demonstrated considering dielectric and plasmonic particles placed in air, where the well-known Lorentz force has led to accurate and consistent result. In this chapter, we consider a particle sub-merged into an *inhomogeneous* background composed of two different dielectric materials instead of air. Interestingly, the well-known Lorentz force leads to time averaged pushing force instead of the experimentally observed pulling force for the half immersed objects. As a result, two alternative approaches of force calculation other than commonly used external Minkowski stress tensor method have been implemented. For example- Ray tracing method is adopted to capture the direct process of momentum transfer from the complex background media, which is validated by the proposed modified Einstein-Laub method only employing *interior fields of the particle* in calculation. Our suggested interpretation supports the Minkowski approach only for the purpose of optical momentum transfer to the embedded scatterer rejecting Peierls' and Abraham's approach, although the momentum of photon in the continuous background medium should be considered as the type of Abraham for the calculation of the bulk part of Lorentz volumetric force distribution.

4.1 Introduction

Following the pioneering work of Marston in acoustics [144], optical "tractor beams" have attracted much interest due to their unusual mechanism in micromanipulation [16,25,30-33,36,59,62,90,145,146]. Generally speaking, a tractor beam is a customized light beam which exerts a negative scattering force (NSF) to a scatterer and pulling it opposite to the propagation direction of light, in contrast with to the conventional pushing forces [147]. Optical pulling force opens up a new way for gradientless optical manipulation technique distinct from optical tweezers [1,2,9], optical conveyor [33, 60,148], or nano-opto-mechanical systems [76, 149]. Recently, different types of tractor beam have been experimentally demonstrated using a Gaussian beam with an optical mirror (interfering incident and reflecting lights in certain limited regions) [36] and with dodecane droplets sitting on the dielectric interface [35]. However, in the presence of high power laser, the hydrodynamic effects (uneven heat dissipation, particle absorption, temperature gradient, liquid convection, surface energy well, etc.) may contribute too. Moreover, the stability criteria of the tractor beams have also not been investigated so far, which is very important for practical application purposes.

Though the mechanical effect has been demonstrated [35] as an overall consequence of all possible contributing factors, the mechanism of optical momentum transfer from a mixed bi-medium background (air and water) to a partially sub-merged particle is still unclear, particularly in the issue of what proper stress tensor and volumetric force law (i.e. Lorentz force) should be adopted for non-vacuum backgrounds. This motivates us to investigate the fundamental physics governing the momentum transfer from light to particle within an inhomogeneous (mixed) background matter, which leads to stimulating debates of Abraham-Minkowski controversy [27, 49,50, 58, 150-153]. In general, both Minkowskian [27, 50,153] and

non-Minkowskian [49, 90] formulations have been supported for the purpose of measuring the optical momentum transfer from homogenous background to an embedded particle. After a century of debate, it is not yet known hitherto which stress tensor (ST), volumetric force law (i.e. Lorentz force) and photon momentum scheme in matter should be the most appropriate one (e.g., Table 1 given in Ref. [27] and Table-1.1 in the introduction chapter of this thesis). It appears that since the identification of adequate 'particle momenta' is quite ambiguous and challenging [154], a recent resolution of the Abraham-Minkowski dilemma [58] still cannot address adequately the appropriate ST and volumetric Lorentz force law to be employed in complex (mixed) backgrounds [154, 155].

In this context, it is valuable to pursue a simplified optical configuration without those limitations or implications discussed above, in which we can discuss the mechanical light-matter interaction isolate. For this purpose, we investigate the light momentum transfer and related optical force on a transparent scatter floating on a dielectric liquid-gas interface [33-35], as shown in Fig. 4.1(a). Although Webb et al. [90, 155] have supported Abraham photon momentum (APM) as an appropriate one for the purpose of optical momentum transfer from *homogenous* background to an embedded particle, we have shown that optical momentum transfer for our case is more appropriate to consider as the transfer of Minkowski photon momentum (MPM). Interestingly, non-Minkowskian formulations such as external Chu stress tensor and the well-known Lorentz force show pushing force, which contradicts the experimental observation in [35]. As a result, two alternative approaches of force calculation other than external Minkowski stress tensor method have been implemented in this chapter. Detailed calculations by ray tracing method and modified Einstein-Laub equations (using the *interior fields only for the latter one*) show that negative pulling force and optical tractor beam is natural in our scheme.

However, our suggested interpretation supports the Minkowski approach only for the purpose of optical momentum transfer (or emission) to (from) the embedded scatterer (near the scatterer and the dielectric interface) rejecting Peierls' and Abraham's approach although the momentum of photon in the continuous background medium should be considered as the type of Abraham for the calculation of the bulk part of Lorentz volumetric force distribution. Since this scheme can be extended to any gas-liquid interface, we name our tractor beam "interfacial tractor beam" (ITB). The importance of this scheme is not only for that the tractor beam *per se* becomes practically realizable but also for that there is a clear-cut insight specially based on photon momentum for practical implementation [43].

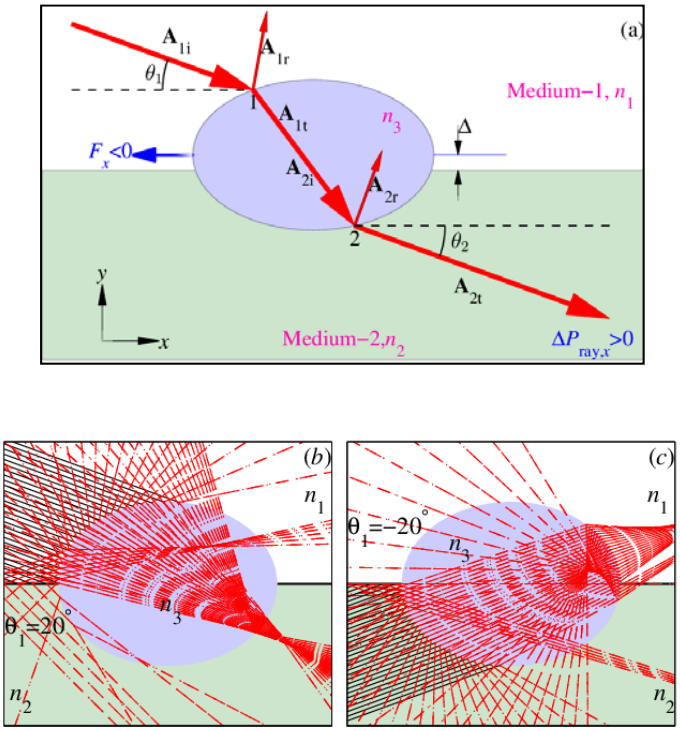

Fig. 4.1: (a) Schematic of photon momentum transfer in an inhomogeneous mixer background. $\mathbf{A}_{1i,1r,1t}$ and $\mathbf{A}_{2i,2r,2t}$ denote the propagation direction of the incident, reflection, and transmission at point 1 and 2, respectively [43] (lengths of the arrows indicating n_m, the refractive index of the associated medium). $\theta_{1,2}$ describe the angles of incident and transmission rays with $+x$ axis. (b) Ray tracing patterns of the system with an $\theta_1 = 20^\circ$ with $r_y = 0.75 r_x$ (r_x and r_y are the semi axes of the scatter along the x and y directions, respectively), $n_1 = 1$, $n_2 = 1.33$, and $n_3 = 1.45$. The black (solid) and red (dashed) lines show the incident and refractions rays,

respectively. (c) The same as (b) except for $\theta_1 = -20^\circ$. Figures adapted and reproduced with permission from ref. [43], © 2015, Nature publishing group.

4.2 Ray Tracing Method and Minkowski Stress Tensor by Employing Background Fields

The proposed background mixture is illustrated in Fig. 4.1(a). The scatterer (with refractive index of n_3) is suspended at the interface of a liquid (e.g., water, with a refractive index of n_2) and a gas (e.g., air, n_1). The incident and the scattered beams may lie in different mediums (also shown in the ray tracing patterns of Fig. 4.1(b) & (c)). Therefore, *not only the direction but also the amplitude* of the momentum of the light is changed. Without loss of generality, we restrict the calculation mostly in two dimensional structures for clarity.

In the ray tracing method [43], the momentum of a photon in each medium should be clearly defined first of all. Generally, the momentums $p_{1,2}$ carried by a photon in medium-1 and -2 respectively are

$$p_1 = \alpha_1 p_0 = \alpha_1 \frac{\hbar\omega}{c}, \quad p_2 = \alpha_2 p_0 = \alpha_2 \frac{\hbar\omega}{c} \tag{4.1}$$

Here $\hbar$, ω and c are reduced Planck constant, angular frequency, and light velocity in vacuum, respectively. $p_0 = \hbar\omega/c$ is the momentum of the photon in vacuum. For the material related constants $\alpha_{1,2}$, however, different values are proposed and there is also a long standing controversy on this point [24, 27, 29], such as $\alpha = n$ for

Minkowski formula [27, 50,152], $\alpha = n^{-1}$ for Abraham formula [27, 50,152], and $\alpha = \left(4n + 7n^2 - n^4\right)/(10n)$ for Peierls formula [158, 159].

In order to calculate the momentum transfer and corresponding forces quantitatively, we set the mediums of gas, liquid and scatterer to be air, water and silicon sphere with $n_1 = 1.0$, $n_2 = 1.33$, and $n_3 = 1.45$, respectively. Using the ray tracing method [43], all the rays illuminated on the scatter are traced (as illustrated in Fig. 4.1(b) and (c)), and momentum changes and in turn the optical force are calculated correspondingly.

Fig. 4.2(a) shows that the Minkowski and Abraham momentums are the upper and lower boundaries, respectively; while the Peierls momentum is about the average value of them. Using the above momentum formulations (Minkowski, Abraham and Pierels), the forces of F_x can be calculated by using the ray tracing method, and the results are shown in Fig. 4.2(b). It is seen that only the Minkowski momentum results in a negative pulling force in a wide range of incident angles while those of Abraham and Peierls momentums result in positive pushing forces regardless of the incident angles.

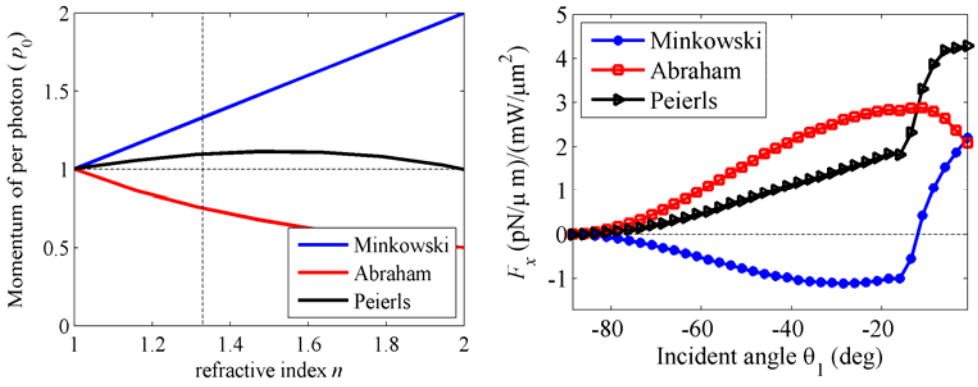

Fig. 4.2: (a) Changes of momentum per photon in materials with a refractive index n for Minkowski (blue), Abraham (red) and Peierls (black) formulations, respectively. (b) Optical forces (s-polarization) calculated by ray tracing simulations when Minkowski (blue), Abraham (red), and Peierls (black) momentums are used. Figures adapted and reproduced with permission from ref. [43], © 2015, Nature publishing group.

Fig. 4.3(a) shows the changes of F_x with the shape of the scatter at the case of $\theta_1 = 0^\circ$. When $0.425 < r_y / r_x < 0.775$, both p and s polarizations can produce negative force. Fig. 4.3(d) shows the force changes with incident angle on a circular scatter with $r_x = r_y$, and NSF are achieved within a broad incident direction.

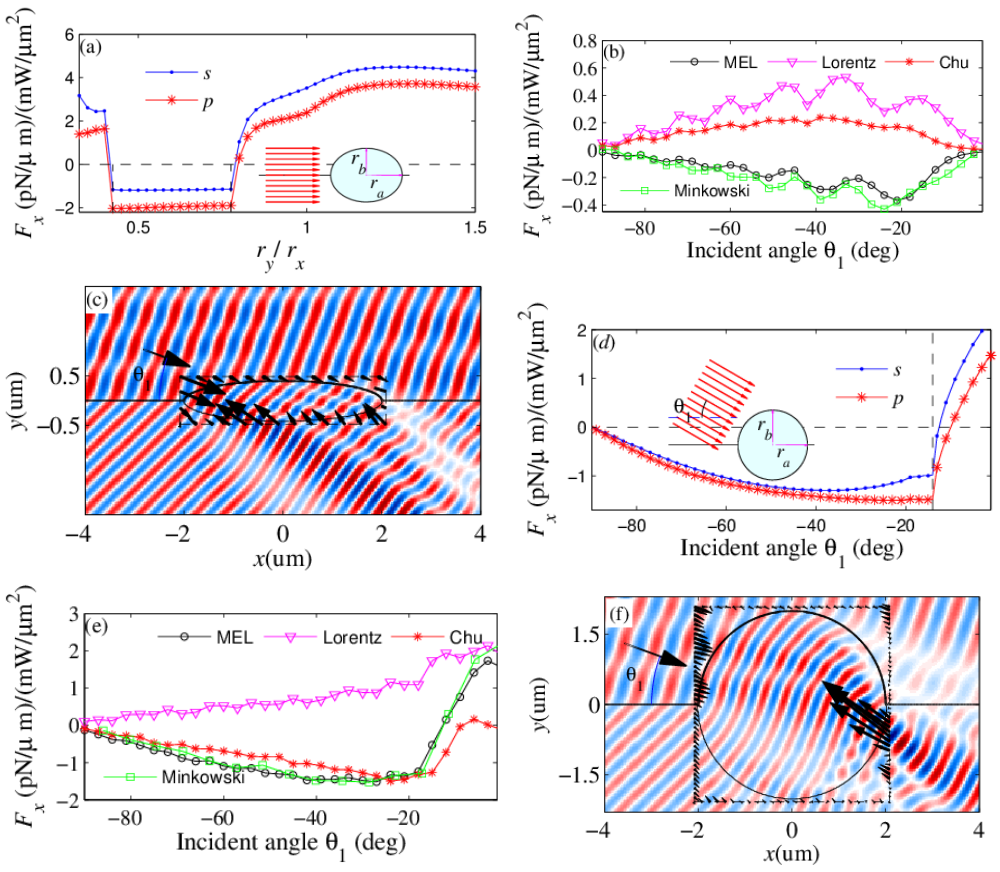

Fig. 4.3: Optical forces derived from different formulas. The parameters are $n_1 = 1.0$, $n_2 = 1.33$, $n_3 = 1.45$, and $\Delta = 0$, unless otherwise specified. (a) Optical forces change with the shape r_y / r_x at $\theta_1 = 0$. The forces are calculated using the ray tracing method, in which the Minkowski momentum approach of photon is adopted. (b) Optical forces changing with incident direction θ_1 for the p polarization calculated by the internal modified Einstein-Laub formula (MEL, circle line) proposed in this chapter, volume integration of Lorentz force density (Lorentz, triangle line), external Chu ST (Chu, asterisk line), as well as external Minkowski ST (Minkowski, square line). The size of the scatter is $r_x = 2.0$μm and $r_y = 0.4$μm (as shown in (c)). (c) Field pattern for the H_z at the case of $\theta_1 = -30^\circ$. (d) Optical forces changing with the incident direction θ_1 for a circular scatter of $r_x = r_y = 2.0$ μm. The forces are calculated by ray tracing method. (e, f) The same as (b, c) respectively, except force $r_y = 2.0$ μm. Figures adapted and reproduced with permission from ref. [43], © 2015, Nature publishing group.

These results agree with the analysis above. In order to calculate the force using ST's, we calculate the scattering using the finite difference in time domain (FDTD) method with a plane wave incidence for a circular scatter (with the semi axis along *x* direction of r_x, and *y* direction of r_y of $r_x = r_y = 2.0$ μm) and an ellipse scatter (with $r_x = 2\,\mu$m and $r_y = 0.4\,\mu$m). Then, the optical force experienced by the particles are calculated by the integration of time averaged external Minkowski stress tensor on a closed contour [see the dashed rectangles in Fig. 4.3© and 4.3(f)] surrounding the scatterer,

$$\left\langle \overline{\boldsymbol{T}} \right\rangle = \frac{1}{2}\mathrm{Re}[\boldsymbol{D}\boldsymbol{E}^* + \boldsymbol{B}\boldsymbol{H}^* - \frac{1}{2}\mathbf{I}(\boldsymbol{E}^* \cdot \boldsymbol{D} + \boldsymbol{H}^* \cdot \boldsymbol{B})] \tag{4.2}$$

The calculated forces for the elliptical and circular scatters are shown in Fig. 4.3(b) and 4.3(e) (square lines), respectively, and good agreements with ray tracing method are observed. Here, *s*-polarization results are not shown, since they are similar to those of *p*-polarization case. In the calculation, *local permittivity and permeability* are used along the integration paths (as shown in Fig. 4.3(c) and (f)). Fig. 4.3(c) and (f) show the field pattern of H_z scatterer at the case of $\theta_1 = -30^\circ$ for the circular and elliptical scatterers, respectively. The arrows show the element force vector on the closed contour, along which the total net force F_x is calculated by integration. One can find that most part of the pulling force is exerted when the photons left the scatterer, which agrees with our analysis.

4.3 Explanation of the Observations and the Two Photon Momenta

It is important to note that a previous analysis and the experimental observation in [35] cannot tell that the travelling momentum of the photon inside the continuous second background (water) is the Minkowski one. Previously for one same experiment (Jones and Leslie experiment [154, 155]), the optical force density formula based approaches have supported the transfer of both APM [155] and MPM [154]. Such ambiguities for the transfer of photon momentum from the background can only be overcome by direct photon momentum approach [27] such as the ray tracing method, which is the main purpose of our previous section. But surprisingly, for this ITB experiment [35], the force felt by the embedding water medium can also be calculated using Einstein-Laub formula employing the field inside water, which indeed supports APM (Cf. Eq (21) given in [155] and also ref. [161]). If the force of a lossless continuous medium is calculated via Minkowski ST (associated with MPM) employing interior fields, it gives zero experienced force. In the ITB experiment, at the interface of the scatterer and the water [35], MPM should arise due to the reduced impedance mismatch [162]. In fact, MPM generates a translation of the electromagnetic field [151]. This translation, relative to the host, is exactly the quantity required to represent the displacement of an embedded object [58]. As a result, MPM appears in almost all the major radiation pressure experiments that measure the displacement of an embedded object [58, 151].

In this discussion, it is important to mention the experimental observations of Ashkin and Dziedzic regarding the force density distribution in water [47], which support the Einstein–Laub force– density expression associated with the APM, according to Mansuripur et al. [161]. So, the connection of APM is related with the force distribution inside water medium, which suggests the role of APM as the pure electromagnetic part of photon momentum in a continuous medium. Therefore, the experimental observation of a pulling force on the scatterer in Ref. [35] indeed cannot prove that the MPM is the only correct photon momentum. In fact, both the MPM and the APM are probably correct, but their functionalities are quite different.

4.4 The Validity of Other Methods

Hereto, the transfer of optical momentum has been calculated based on Minkowski photon momentum approach, which is also in good agreement with the experimental observations reported in [35]. Surprisingly, any other photon momentum (Abraham or Peierls) does not predict optical pulling force (see Fig. 4.2(a) and (b)). In addition, force calculation results based on Lorentz vlumetric formula and external Chu ST shown in Fig. 4.3(b) and (e) do not guarantee negative forces, which are calculated by the force density integration of Lorentz force density (from the interior of the embedded particle) and external Chu's ST (from exterior of the embedded particle) [27] (external Nelson [163] ST leads to the same result). Although external Chu ST employing exterior fields shows optical pulling force for the 2D circle case (Fig. 4.3(e)), it shows pushing force for the 2D ellipse (Fig. 4.3(b)).

4.5 Modified Einstein-Laub Stress Tensor by Employing Interior Fields of the Scatterer

Another method to calculate the optical force unambiguously is using the force density inside the scatterer. Surprisingly, the time averaged Lorentz force [44] of the embedded particle also fails to provide the accurate result of total mechanical force, as shown in Fig. 4.3 (b) and (e). It appears that the Lorentz force reported in [44] (actually Chu force for nonmagnetic media [27]) is applicable *only when the background media is air*. If the background media is not air, Lorentz force [44] for the interior of the embedded particle should be modified (which will be discussed in details in the next chapter of this thesis). According to our point of view, the interior

mechanical force should be calculated via the proposed time averaged modified Einstein-Laub (MEL) stress tensor [164]:

$$\boldsymbol{F}_{\text{Total}} \approx \frac{1}{2}\text{Re}[\oint \left\langle \overline{\boldsymbol{T}}_{\text{MEL}}(\text{in}) \right\rangle \cdot d\mathbf{S}] \tag{4.3}$$

Where $\left\langle \overline{\boldsymbol{T}}_{\text{MEL}}(\text{in}) \right\rangle = \boldsymbol{D}_{in}\boldsymbol{E}_{in}^{*} + \boldsymbol{B}_{in}\boldsymbol{H}_{in}^{*} - \frac{1}{2}(\mu_b \boldsymbol{H}_{in}^{2} + \varepsilon_b \boldsymbol{E}_{in}^{2})\overline{\boldsymbol{I}}$, μ_b and ε_b are permeability and permittivity of the background medium of a particle, and $\overline{\boldsymbol{I}}$ is the unit tensor. In our setup, they are the local permeability and permittivity of air and water defined respectively in the specific 2D configuration of full wave simulation [Fig. 4.3(b) and (e)]. The quantities $\boldsymbol{E}_{\text{in}}$, $\boldsymbol{H}_{\text{in}}$, $\boldsymbol{D}_{\text{in}}$ & $\boldsymbol{B}_{\text{in}}$ are at the interior of the silica particle. The calculations via MEL stress tensor from the interior are fully in agreement with ray tracing method and Minkowski formulations from the exterior (see Fig.4.3(b), (e)). Detail discussion on MEL formulations [164] will be presented in next chapter, chapter 5.

4.6 Conclusions

In summary, our suggested interpretation supports the Minkowski approach only for the purpose of optical momentum transfer (or emission) to (from) the embedded scatterer (near the scatterer and the dielectric interface) rejecting Peierls' and Abraham's approach, although the momentum of photon in the continuous water background medium should be considered as the type of Abraham for the purpose of calculating the bulk part of Lorentz volumetric force. Interestingly, the well-known Lorentz force leads to time averaged pushing force instead of the experimentally observed pulling force for the half immersed objects. As a result, two alternative approaches of force calculation other than external Minkowski stress tensor method have been implemented. We believe that our proposal is very effective in order to

resolve not only the Abraham-Minkowski photon momentum dilemma but also the dilemma associated stress tensors and optical force including interfacial tractor beams.

Chapter 5

Modification of Lorentz Force for embedded chiral and achiral objects

5.0 Summary of Chapter 5

Although it is commonly believed that all the Lorentz volumetric force laws lead to the same total optical force for both chiral and achiral objects, this idea has been invalidated in the recent review by M.Bethune-Waddell and K. Chau [cf. *Rep. Prog. Phys.* 78, 122401 (2015)] discussing several previous experiments. In our previous chapter we have also shown one example of such cases. To identify the exact reason of such significant disagreements, we inspect in this chapter two tractor beam and one lateral force experiments on using distinct stress tensors (STs). In this chapter we have identified the exact reasons of such disagreements. We propose that it is possible to make different time-averaged force formulas equivalent based on the fulfilment of just two 'consistency conditions'. Finally, we demonstrate that by modifying the Einstein-Laub or Chu formulation, time-averaged STs and volume forces are obtainable those can overcome the aforementioned inconsistency for both chiral and achiral Mie objects embedded in even complex material backgrounds. Our work presented in this chapter also explains why such modification should be adopted for Chu or Einstein-Laub formulations in order to obtain an accurate and reliable time-averaged total force, both in magnitude and direction, on both chiral and achiral objects embedded in a generic material background.

5.1 Introduction

A tractor beam is a customized light beam which exerts negative force to a scatterer [24, 25, 32-36, 43, 59, 62,165] and pulling it opposite to the propagation direction of light, in contrast to the conventional pushing forces. Not only the counter intuitive idea of optical pulling (i.e. tractor beam effect) but also the idea of optical lateral force [166-169] is also growing famous in recent literature. Tractor beam and lateral force experiments, which involve the material background [35, 36, 24, 166], can also be investigated in details to understand the persistently debated roles of different STs, Lorentz/ volumetric forces and photon momenta such as Abraham-Minkowski controversy [27, 28, 57, 58]; as the employment of inappropriate approach may lead to pushing force (or inconsistent lateral force) instead of the experimentally observed pulling one (or consistent lateral force). Throughout this thesis we refer to 'exterior' or 'outside' magnitudes as those evaluated outside the volume of the embedded macroscopic object, while by ‘interior’ or 'intside' we shall refer to those quantities inside this object volume [cf. the force calculation process in Fig.5.1 (a) - (c)]. Although it is commonly believed all the volume force laws [27, 170] (i.e. Minkowski, Abraham, Chu, Einstein-Laub and Ampere/Nelson) should lead to the same time averaged total optical force, this idea has been invalidated in recent works [43, 28] considering several experimental set-ups [28] involving material background. In fact, if one involves the material background; several complexities arise:

(i) In order to calculate the total force on an embedded object, normally two conventions, i.e., GAP METHOD AND NO GAP METHOD, are applied [26, 78, 170-173] but which one is more accurate than the other is still not properly understood: (a) GAP METHOD [78,170,172,173]: By introducing a very small gap

between the scatterer and the background to yield the force as shown in Fig. 5.1(a). (b) NO GAP METHOD [26, 28, 35, 36, 43, 166, 171]: Without introducing any small gap outside the embedded scatterer as shown in Fig. 5.1(b) and (c). Between these two distinct methods, which one is more appropriate?

(ii) In addition, the involvement of chirality [19,20,77,174-181] can be a key factor to judge the consistency of the optical force calculation methods which are considered applicable for embedded achiral objects. Previous analyses of optical force in chiral objects are still restricted in these factors: (a) the dipolar limit of object [167,175,176], (b) air or vacuum background [77,174-181] and (c) internal force distribution inside a slab embedded in air [77,181]. But the stress tensor and force distribution inside any arbitrary generic embedded chiral object [i.e. more complex than Mie object which are used in real experiments [19, 20]] are still not investigated in details.

This chapter attempts to solve the aforementioned complexities. We demonstrate that even without introducing any artificial gap between the background and the embedded object, it is possible to make different time-averaged force formulas equivalent based on the fulfilment of just two 'consistency conditions' [denoted as C(I) and C(II) with details shown below]. This may also solve the reported problems [28, 35, 43] of total force calculation for almost all the real experiments conducted so far involving a material background. In addition, this work introduces the less time and memory consuming internal Modified Einstein-Laub (MEL) stress tensor method, (rather than the longer time consuming bulk volumetric force method [26, 183]) for both achiral [35,36,43,28] and chiral objects [19, 20] embedded in a generic background.

5.2 Proposal of Consistency Conditions

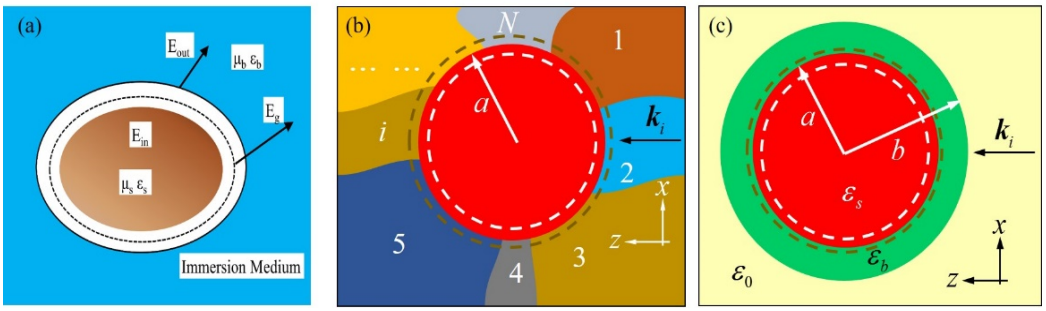

Fig. 5.1: Procedure of time averaged optical force calculation by employing stress tensors. (a) GAP METHOD: a small gap between the scatterer and the background should be considered. Time averaged total force on the scatterer should be calculated using the time-averaged ST $\langle \boldsymbol{F}_{\text{out}}^{\text{GAP}} \rangle$ evaluated *from fields strictly outside the object [i.e. gap field and background field]*, putting the integration boundary in the gap [170] (black dashed circle). However, the volume force calculation method is a little bit different, which is discussed in details in [78]. (b) and (c) NO GAP METHOD: In both examples the total force obtained by using the time-averaged ST is $\langle \boldsymbol{F}_{\text{out}} \rangle$ evaluated *from fields strictly outside the object considering no gap*, at $r = a^{+} = 1.001a$, (black circles); whereas this force is $\langle \boldsymbol{F}_{\text{in}} \rangle$ or bulk force when the ST is determined *from fields strictly inside the object* considering no gap at $r = a^{-} = 0.999a$ (white circles). In (b), a sphere or cylinder is immersed in an unbounded and heterogeneous background medium. In (c) a core-shell sphere or cylinder (i.e., the core is embedded in a bounded background).

One of the fundamental proposals of this chapter is: if $\overline{\overline{\boldsymbol{T}}}(\text{in})$ [applied at $r=a^{-}$ employing only the interior field of a scatterer, where a is the particle radius; cf. Fig. 5.1 (b) and (c)] is a valid internal stress tensor and $\boldsymbol{f}(\text{in})$ is its corresponding volume force; and $\overline{\overline{\boldsymbol{T}}}(\text{out})$ is a valid external stress tensor which is applied at $r=a^{+}$ using only exterior fields of an object; then the following 'validity condition' should be fulfilled: "On the boundary $r= a$ of any object, this equation: $[\overline{\overline{\boldsymbol{T}}}(\text{out}) - \overline{\overline{\boldsymbol{T}}}(\text{in})] \cdot \hat{\boldsymbol{n}} = \boldsymbol{f}^{\text{Surface}}$ should hold ($\hat{\boldsymbol{n}}$ being the local unit outward normal of the object surface). Also, the same surface force $\boldsymbol{f}^{\text{Surface}}$ should independently be found from the volume force

density $\boldsymbol{f}$ (in) by applying the appropriate boundary conditions at $r = a$. These two aforementioned conditions must be satisfied simultaneously."

For example- in [182], the process of obtaining $\boldsymbol{f}^{\text{Surface}}$ has been shown only from a volumetric force density stemming from the well-known Chu and Einstein-Laub force, and by considering only air as the background.

At the beginning of Appendix A (at the end of this thesis) it is shown that when the background is air, the difference of the external ST (notice that then all STs are same) and the internal ST of Chu (and of Einstein-Laub) at the object boundary is in complete agreement with the fully independently calculated surface force given by the volumetric formulation of Chu and Einstein-Laub. But when material background is involved: the first question should be: Q(I) which $\overline{\overline{\boldsymbol{T}}}(\text{out})$ should be appropriate? Then the second question is: Q(II) If

$$\left\langle \boldsymbol{F}^{\text{Bulk}} \right\rangle(\text{in}) = \int \left\langle \boldsymbol{f}^{\text{Bulk}} \right\rangle(\text{in}) \cdot d\boldsymbol{v} = \int \left\langle \overline{\overline{\boldsymbol{T}}}(\text{in}) \right\rangle \cdot d\boldsymbol{s} \neq 0$$

; which $\overline{\overline{\boldsymbol{T}}}(\text{in})$, along with its corresponding $\boldsymbol{f}$, will satisfy these two following 'consistency conditions' simultaneously: C(I) the aforementioned 'validity condition' and C(II) the consistent time-averaged force equation:

$\int \left\langle \overline{\overline{\boldsymbol{T}}}(\text{out}) \right\rangle \cdot d\boldsymbol{s} = \left\langle \boldsymbol{F}^{\text{Total}}(\text{Consistent}) \right\rangle = \left\langle \boldsymbol{F}^{\text{Bulk}} \right\rangle(\text{in}) + \left\langle \boldsymbol{F}^{\text{Surface}} \right\rangle$? In this chapter we show that when the background is a material medium instead of air, $\overline{\overline{\boldsymbol{T}}}(\text{out})$ and $\overline{\overline{\boldsymbol{T}}}(\text{in})$ cannot be arbitrary STs which satisfy C(I) and C(II) simultaneously.

Concerning Q(I), in order to sort out the appropriate ST $\overline{\overline{\boldsymbol{T}}}(\text{out})$, we investigate two major tractor beam experiments [35, 36] along with the recent set-up of a lateral force experiment [166]. We identify that the vacuum ST [170] of the GAP method leads to *inconsistent results* for tractor beams and lateral force experiments, especially when the symmetry is broken [35,166]. Both external Minkowski and

Abraham STs of a NO GAP METHOD lead to a consistent time-averaged total force for all those experiments, (and also for all previous experiments [28,46]). However, this does not mean external STs other than Minkowski (or Abraham) are incorrect. As a result, even to sort out appropriate $\bar{\bar{\boldsymbol{T}}}(\text{out})$, it is required to satisfy aforementioned consistency conditions C(I) and C(II) simultaneously. Now, we shall consider Q(II). As always $\left\langle \boldsymbol{F}^{\text{Bulk}} \right\rangle(\text{in}) = \int \left\langle \boldsymbol{f}^{\text{Bulk}} \right\rangle(\text{in}) \cdot d\boldsymbol{v} = \int \left\langle \bar{\bar{\boldsymbol{T}}}(\text{in}) \right\rangle \cdot d\boldsymbol{s} = 0$ for internal Minkowski ST for the transparent/non-absorbing objects, to sort out the appropriate $\bar{\bar{\boldsymbol{T}}}(\text{in})$ [and also $\bar{\bar{\boldsymbol{T}}}(\text{out})$ of Q(I)] we examine several cases for an object embedded in material background [19,20, 28,35,36,46, 84,97, 98, 183,184,185, 186].

For example- condition C(I) has been violated when: (i) $\bar{\bar{\boldsymbol{T}}}(\text{out})$ is considered $\bar{\bar{\boldsymbol{T}}}_{\text{Mink.}}(\text{out})$ and $\bar{\bar{\boldsymbol{T}}}(\text{in})$ is well known internal Chu or Einstein-Laub ST; and (ii) $\bar{\bar{\boldsymbol{T}}}(\text{out})$ and $\bar{\bar{\boldsymbol{T}}}(\text{in})$ both are considered $\bar{\bar{\boldsymbol{T}}}_{\text{EL}}$ respectively. More details will be discussed later. In contrast, C(II) is seriously violated when: (iii) $\bar{\bar{\boldsymbol{T}}}(\text{out})$ and $\bar{\bar{\boldsymbol{T}}}(\text{in})$ both are considered $\bar{\bar{\boldsymbol{T}}}_{\text{Chu}}$ respectively. More details will be discussed later. (iv) Already we have discussed very shortly that external vacuum ST of GAP METHOD violates the left hand side equation of C(II). These are identified as the main reasons of disagreements observed in [28] and [46] for different volumetric force laws.

Finally we demonstrate that when $\left\langle \boldsymbol{F}^{\text{Bulk}} \right\rangle(\text{in}) \neq 0$; to satisfy C(I) and C(II) simultaneously for a chiral or achiral Mie scatterer embedded in generic material backgrounds [i.e. homogeneous, heterogeneous, bounded or unbounded], $\bar{\bar{\boldsymbol{T}}}(\text{out})$ should be considered as Minkowski ST and $\bar{\bar{\boldsymbol{T}}}(\text{in})$ should be the modified version of Einstein-Laub (or Chu) formulation along with modified $\boldsymbol{f}(\text{in})$. So, in order to satisfy both C(I) and C(II) simultaneously, $\bar{\bar{\boldsymbol{T}}}(\text{out})$ and $\bar{\bar{\boldsymbol{T}}}(\text{in})$ cannot have the same form

for embedded transparent/non-absorbing scatterers. To explain the last observation for realistic situations [19,20, 28,35,36,46, 84,97, 98, 183- 186], we conclude at the end: though both the external Minkowski (and Abraham) ST and proposed internal MEL (and Modified Chu) methods lead to the same consistent time-averaged total force [i.e. they are mathematically equivalent], they should better be considered two fully different operations/process from the physical point of view.

5.3 The consistent external force with NO GAP METHOD

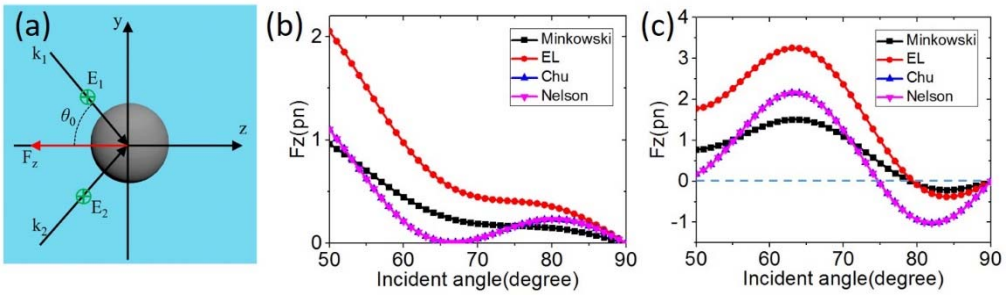

Fig. 5.2: (a) Optical sorting of a dielectric particle using two obliquely incident plane waves reported in [36]. The external force will be calculated based on NO GAP METHOD. Two TE-polarized plane waves (λ = 532 nm) incident at *varying angle* θ onto a polystyrene cylinder (n = 1.58) immersed in water (n = 1.33), shown: (b) For r = 320 nm, at steady state when the plane waves exert a pushing force in the $+x$ direction. Force on the bead calculated by external Minkowski, Einstein–Laub, Chu, and Ampere/Nelson ST for TE polarization as a function of incident angle θ. (c) For r = 410 nm, at steady state when the plane waves exert a pulling force in the $-x$ direction. Force on the bead calculated by external Minkowski, Einstein–Laub, Chu, and Ampere/Nelson ST for TE polarization as a function of incident angle θ. Pulling forces are only achieved for TE polarization within a short range of angles experimentally observed in [36].

In this section we investigate the consistency of the total force calculation for one tractor beam experiment [36] and one lateral force experiment [166] by the major

stress tensors namely: external Minkowski, Chu, Ampere and Einstein-Laub with NO GAP METHOD [cf. Fig.5.1(b) and (c)]. All the 3D simulations throughout this chapter are conducted using incident power of 0.57mW/μm^2. For example- the external time averaged total outside force by commonly applied Minkowski ST is written as [35,36,43,166]:

$$\left\langle \boldsymbol{F}_{\text{Total}} \right\rangle(\text{out}) = \int \left\langle \bar{\bar{\boldsymbol{T}}}^{\text{out}}_{\text{Mink}} \right\rangle \cdot d\boldsymbol{s}, \tag{5.1a}$$

$$\left\langle \bar{\bar{\boldsymbol{T}}}^{\text{out}}_{\text{Mink}} \right\rangle = \frac{1}{2}\text{Re}\left[\boldsymbol{D}_{\text{out}}\boldsymbol{E}^{*}_{\text{out}} + \boldsymbol{B}_{\text{out}}\boldsymbol{H}^{*}_{\text{out}} - \frac{1}{2}\left(\boldsymbol{B}_{\text{out}} \cdot \boldsymbol{H}^{*}_{\text{out}} + \boldsymbol{D}_{\text{out}} \cdot \boldsymbol{E}^{*}_{\text{out}} \right)\bar{\bar{\boldsymbol{I}}} \right]. \tag{5.1b}$$

'out' stands for fields outside the object, [e.g., on $r=a^{+}$, if it is a sphere or cylinder of radius *a,* cf. Fig. 5.1(b)] and $\bar{\bar{\boldsymbol{I}}}$ is the unity tensor. The electromagnetic vectors in Eq (5.1b) correspond to the total field, namely, incident plus field scattered by the body. For the force calculations with other stress tensors (i.e. external Chu, Ampere and Einstein-Laub), we shall also use this 'total' outside fields.

Without introducing any small gap (named as NO GAP METHOD in the introduction), total force has been calculated by different external stress tensors for two beam tractor configuration reported in [36] in Fig. 5.2(a) - (c) and also for lateral force experiment [166] configuration in Fig. 5.3(a)-(c). Though Minkowski's (or Abraham's) formulation leads to the most accurate time averaged force for some other experiments [2,35, 36, 47, 55,56] reported in [28]; for two tractor beam [36] and lateral force experiments [166] it may not be possible to recognize which one is the most consistent external ST. Due to the very big size of the object [166] considered in the real lateral force experiment [special technique has been applied in the first ref. of [166] due to the big size of particle: 4500 nm], we are modeling that same set-up with comparatively small sized object [cf. the second reference in [166], where a small object has been considered]. However, we are considering two cases: spherical and elliptical object to check the consistency of the lateral force considering the arbitrary

shape of the testing object. Previously for interfacial tractor beam experiment [35,43], only external Minkowski ST lead to the accurate prediction for arbitrary shaped objects [35,43] modelled as spherical and elliptical shaped objects. Though there is no difference among the signs of the total forces for the experiments reported in [36] and [166], their magnitudes are observed quite different in Fig. 5.2(b), (c) [two beam tractor] and in Fig. 5.3 (b), (c) [lateral force]. But the important fact is that: For the NO GAP METHOD: (A) The size based sorting of embedded particles by two beam method [cf. supplement of ref. [36]] is consistently predicted by all external STs. (B) The sign change of the force for two different handedness of polarizations observed for lateral force experiment [166] has also been correctly predicted by all external STs for spherical and elliptical objects respectively. In Fig. 3(a) given in the second ref. of [166], for 1500 nm sized object, a single direction of lateral force has been observed for a single handedness of circularly polarized light (consistent with our observation). These aforementioned observations will be imperative for our next investigation: the consistency of GAP METHOD for the tractor beam experiments [35,36] and the lateral force experiment [166].

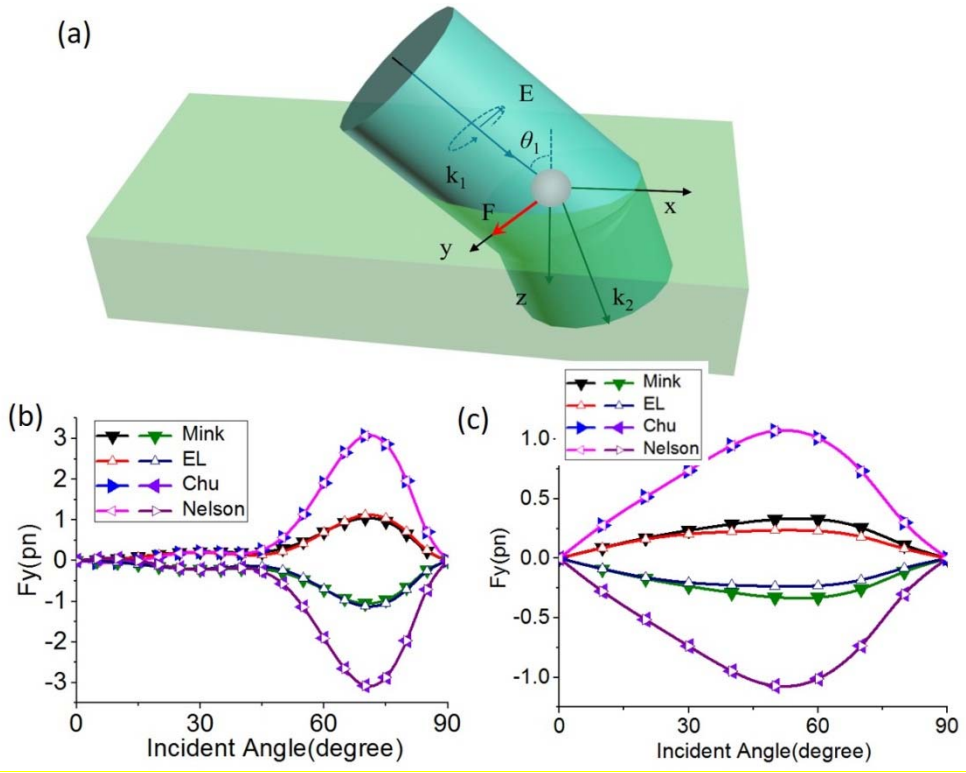

Fig. 5.3: (a) 3D Illumination geometry for a particle at the interface between two media to model the lateral force set-up in [166]. Either a right-handed or a left-handed circularly polarized (CP) beam of wavelength 1064 nm is incident along the *x*–*z* plane at angle θ_1 . $\mathbf{k_1}$ and $\mathbf{k_2}$ are wave vectors in media 1 and 2, respectively. The external force has been calculated based on the NO GAP METHOD. (b) Transversal force (negative for a left- handed CP and positive for right-handed CP) as a function of angle of incidence for a 500 nm (radius) spherical TiO_2 particle located at the water–air interface calculated by external Minkowski, Einstein–Laub, Chu, and Ampere/Nelson ST. The Minkowski and Einstein-Laub STs predict a smaller lateral force in comparison with the time-averaged force yield by the external Chu and Ampere ST. (c) Transversal force, (negative for left-handed CP and positive for right-handed CP) as a function of the angle of incidence for an elliptical polystyrene (PS) particle [r_x=800 nm and r_y=r_z=(800/3) nm] located at the water–air interface, calculated by external Minkowski, Einstein–Laub, Chu, and Ampere STs. The Minkowski and Einstein-Laub STs predict lower lateral force in comparison with the time-averaged force yielded by the external Chu and Ampere STs.

5.4 Inconsistency of the GAP METHOD and different other formulations

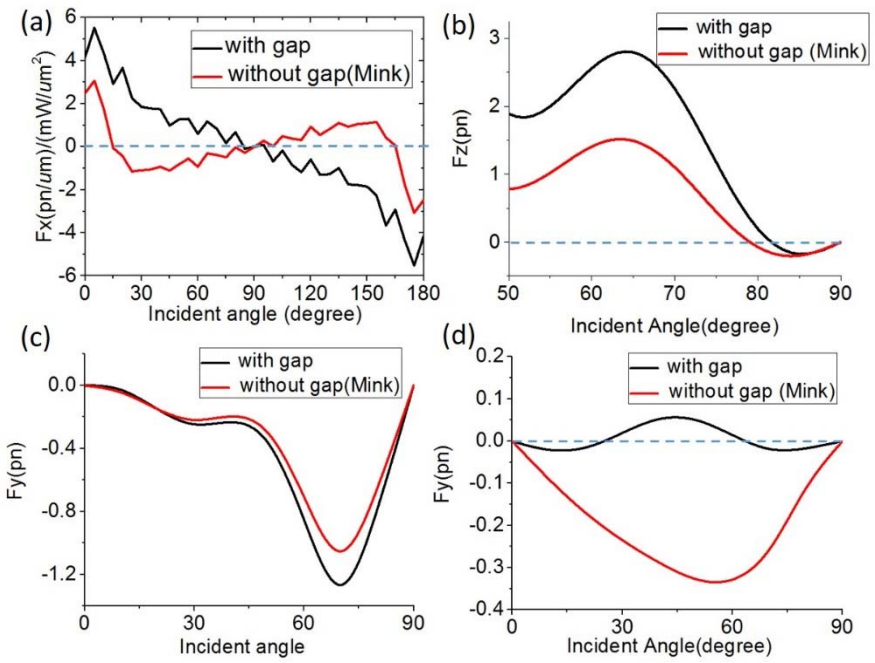

Fig. 5.4: Illustration of optical force with GAP METHOD. (a) Optical force for a 2D spherical shaped scatterer placed in air-water interface (cf. Fig. 2(d) and Fig. 2(e) given in [43]). The parameters are n_1=1.0, n_2=1.33, n_3=1.45. The variation in the optical forces with the incident angle [43] for the p-polarization case, as calculated via the external vacuum stress tensor considering a small gap of 2 nm [the possible smallest gap with 2D full wave simulation set-up; gap size << incident wavelength] between the scatterer and the water background. The size of the scatterer is defined by r_x = r_y =2.0 μm [3]. Instead of optical pulling [43], optical pushing is achieved based on GAP METHOD. We have also examined our results by varying the size of the artificial gap, (i.e. 6nm, 10 nm and 20 nm). The results are almost same for all those gaps. (b) Optical force (by vacuum ST) of a 3D dielectric particle given in Fig. 5.2(c) using two obliquely incident plane waves *but considering a small gap of 10 nm* [possible smallest gap with 3D full wave simulation set-up; gap size << incident wavelength] between water background and the embedded scatterer. Both GAP and NO GAP METHOD lead to consistent result. (c) For the 3D set-up of Fig. 5.3(b), the time averaged lateral force has been calculated by vacuum ST considering a small gap (10nm) between the scatterer and the water background for right hand CP wave. (d) For the 3D set-up of Fig. 5.3 (c), the time averaged lateral force has been calculated by vacuum ST considering a small gap (10 nm) between the scatterer and the water background for left hand CP wave. The sign of the lateral force is in complete disagreement with the time averaged force yield by NO GAP METHOD in Fig. 5.3(c).

One convention of calculating optical force is that if the background is material medium; the force should be calculated considering an extremely small gap [cf. Fig. 5.1(a)] between the embedded object and the background as discussed in ref. [78,170,172,173]. The main goal of this GAP METHOD approach is the idea that all

the optical force formulations should lead to the same time averaged total force [27, 170], as the total time averaged force is always the same for all the volume force formulations (when an object is placed in air). As a result, in this section we shall investigate the consistency of this GAP METHOD for the scatterers embedded in material media such as in [35], [36] and [166]. According to [170], if a small gap is introduced [cf. Fig. 5.1(a)], the external vacuum stress tensor (Chu type stress [170]) to yield the total outside force should be written in terms of gap fields ($\boldsymbol{E}_{\mathrm{g}}$, $\boldsymbol{H}_{\mathrm{g}}$) as:

$$\left\langle \boldsymbol{F}_{\mathrm{Total}} \right\rangle(\mathrm{out}) = \int \left\langle \overline{\overline{\boldsymbol{T}}}^{\mathrm{out}}_{\mathrm{Vacuum}} \right\rangle \cdot d\boldsymbol{s}, \tag{5.2a}$$

$$\left\langle \overline{\overline{\boldsymbol{T}}}^{\mathrm{out}}_{\mathrm{Vacuum}} \right\rangle = \frac{1}{2}\mathrm{Re}\left[\epsilon_0 \boldsymbol{E}_{\mathrm{g}} \boldsymbol{E}_{\mathrm{g}}^{*} + \mu_0 \boldsymbol{H}_{\mathrm{g}} \boldsymbol{H}_{\mathrm{g}}^{*} - \frac{1}{2}\left(\mu_0 \boldsymbol{H}_{\mathrm{g}} \cdot \boldsymbol{H}_{\mathrm{g}}^{*} + \epsilon_0 \boldsymbol{E}_{\mathrm{g}} \cdot \boldsymbol{E}_{\mathrm{g}}^{*} \right) \overline{\overline{\boldsymbol{I}}} \right]. \tag{5.2b}$$

In Fig. 5.3(a) we have calculated the external force considering such an extremely small gap [cf. Fig. 5.1(a)] between the half immersed scatterer and the water background and by employing the stress tensor of Eq (5.2b). Instead of the experimentally observed pulling force [35, 43], we obtain pushing force due to such an extremely small gap as shown in Fig. 5.4(a). In contrast, both GAP METHOD and NO GAP METHOD lead to consistent pulling force for two beam tractor experiment [36] as shown in Fig. 5.4(b).Then we have considered the lateral force experiment reported in [166]. Though for the spherical sized object the total force seems in good agreement (cf. Fig. 5.4(c)) with the previously calculated forces with NO GAP METHOD (cf. Fig. 5.3 (b)), for elliptical shaped object the sign significantly alters (cf. Fig. 5.4(d)) in comparison with NO GAP METHOD (cf. Fig. 5.3(c)). So, the problem of GAP METHOD mainly arises when the background is inhomogeneous/ symmetry broken case [35,43,166] (or in general heterogeneous type as shown in Fig. 5.1(b)) [serious violation of C(II)].

Another detail analysis has been done in favor of GAP METHOD in ref. [78] (and also in refs. [172] and [173]). Instead of the external ST Eq (5.2b), it is suggested in

[78] to yield the total force by an appropriate volume force for some specific cases (described as method II in [78]). However, in Appendix A (at the end of this thesis) we have discussed in details why method II reported in [78] may not be a general way to yield the total force and to explain the so far reported experiments, especially for the experiments with inhomogeneous (or heterogeneous) background due to the violation of C(I).

In fact, even considering no such gap, the well-known Einstein-Laub volume force [28] (but not Chu and Ampere/Nelson force) predicts consistent time averaged total force for almost all previous experiments as shown in details in [28]. However, the magnitude of the total force by EL law is not in full/exact agreement with the total force calculated by external Minkowski ST or Helmholtz force [28,46] for *all those experiments*. But still we cannot comment regarding the inconsistency of EL force for material background case. One needs to examine C(I) and C(II) at first. This issue is discussed next.

At the beginning of Appendix A (at the end of this thesis) it is shown that exactly at the object boundary, the difference of well-established external Minkowski ST and internal Chu ST (also similarly applicable for Einstein-Laub ST) is found in agreement with the surface force of Chu (or Einstein-Laub) when the background is air. But if the background is any material medium instead of air or vacuum, this conclusion does not remain true. For example- condition C(I) has been violated when: (i) $\bar{\bar{\boldsymbol{T}}}(\text{out})$ is considered $\bar{\bar{\boldsymbol{T}}}_{\text{Mink.}}(\text{out})$ and $\bar{\bar{\boldsymbol{T}}}(\text{in})$ is well known internal Chu or Einstein-Laub ST; and (ii) $\bar{\bar{\boldsymbol{T}}}(\text{out})$ and $\bar{\bar{\boldsymbol{T}}}(\text{in})$ both are considered $\bar{\bar{\boldsymbol{T}}}_{\text{EL}}$ respectively. It should also be noted that EL force leads to inconsistent result for few experiments [violation of C(II)]: Hakim-Higham experiment [46], Rasetti experiment [50], few cases of Jones' experiments according to [28] [cf. Fig. 9 (a)-(d) given in [28]] and some other notable cases reported in [188].

In contrast, C(II) is seriously violated when: (iii) $\bar{\bar{\boldsymbol{T}}}(\text{out})$ and $\bar{\bar{\boldsymbol{T}}}(\text{in})$ both are considered $\bar{\bar{\boldsymbol{T}}}_{\text{Chu}}$ respectively. For example- when $\langle \boldsymbol{F}^{\text{Total}} \rangle = \langle \boldsymbol{F}^{\text{Bulk}} \rangle (\text{in}) + \langle \boldsymbol{F}^{\text{Surface}} \rangle$ is calculated by employing internal volumetric force of Chu [or by Chu ST: $\langle \boldsymbol{F}^{\text{Bulk}} \rangle (\text{in}) = \int \langle \bar{\bar{\boldsymbol{T}}}_{\text{Chu}} (\text{in}) \rangle \cdot d\boldsymbol{s}$] for the several real experiments reported in [28], it does not lead to the correct time averaged total force, $\langle \boldsymbol{F}^{\text{Total}} (\text{Consistent}) \rangle$ [Violation of right hand side of the equation given in C(II)]. In addition, in [43] it is shown that left hand side of equation of C(II) has been violated for $\bar{\bar{\boldsymbol{T}}}_{\text{Chu}} (\text{out})$ based on NO GAP METHOD. These are identified as the main reasons of disagreements observed in [28] (and also in [46]) for different volumetric forces.

In the next section we shall demonstrate that not only the surface force but also the bulk force of the well-known Einstein-Laub (or Chu) force law is responsible for such disagreements those reported in [28] and [46] for the real experiments. It would be possible to overcome such inconsistencies if and only if the GAP METHOD were applicable where the external Minkowski ST turns into Vacuum ST [cf. Eq (5.2b)]. But in this section we have already demonstrated the problem/inconsistency of the GAP METHOD. Hence the possible solution of such problems will be addressed in the next three sections.

5.5 Consistency of the external Minkowski and internal MEL or modified Chu formulations

Though so far Minkowski's ST has led to consistent time-averaged result for real experiments [28,46] by employing the exterior field of an embedded scatterer

[fulfilment of the left side of the equation in C(II)], more complex configurations may arise where Minkowski's ST and the Helmholtz force may fail [i.e. cf. refs. [189-191]]. As a result, we shall now examine whether external Minkowski leads to the fulfilment of both C(I) and C(II) together with any other internal ST or not. To handle future situations, and to sort out new optical force laws, if they proceed, the validity conditions C(I) and C(II) together and the analysis to follow below should be very effective.

A modification on the well-known EL volume force (and also Chu force [26]) has been predicted in [171]. Interestingly that modified version of the EL force led to exactly the same time-averaged force predicted by the external Minkowski ST in [171] for a dielectric object embedded in another dielectric. Commercial software [183] applies this modified version of the Einstein-Laub [171] or the Chu volume force density [26] to yield the total volumetric force on dielectric objects embedded in another dielectric. In order to explain the interfacial tractor beam experiment [35], the achiral internal MEL ST [43] has been applied previously without any derivation and consistent description. So far no explanation is given in [43] and [171] why both Minkowski ST and the MEL volume force [171] (and also modified Chu force [26,183]) and the MEL ST [43] lead to same/consistent time averaged result for dielectric cases. This section (and the final conclusion of this chapter) explains the reason, even considering more general cases such as magnetodielectric objects embedded in a generic magnetodielectric background.

Achiral MEL ST (which should yield the bulk force of an embedded scatterer) inside an object embedded in a generic heterogeneous background should be written as:

$$\left\langle \overline{\overline{\boldsymbol{T}}}^{\text{Bulk}}_{\text{MEL}(j)} \right\rangle (\text{in}) = \boldsymbol{D}_{\text{in}} \boldsymbol{E}^{*}_{\text{in}} + \boldsymbol{B}_{\text{in}} \boldsymbol{H}^{*}_{\text{in}} - \frac{1}{2}\left((\frac{\mu_{\text{b}\,(j)}}{\mu_{\text{s}}}) \mu_{\text{s}} \boldsymbol{H}^{*}_{\text{in}} \cdot \boldsymbol{H}_{\text{in}} + (\frac{\varepsilon_{b(j)}}{\varepsilon_{s}}) \varepsilon_{s} \boldsymbol{E}^{*}_{\text{in}} \cdot \boldsymbol{E}_{\text{in}} \right) \overline{\overline{\boldsymbol{I}}}. \qquad (5.3)$$

Here $j=1,2,3,....,\ N$ represents the number of background regions sharing interface with the object, [cf. our Fig. 5.1(b), (c) and forthcoming Fig. 5.7(a)]. ε_{b} and μ_{b} are fixed background permittivity and permeability and ε_s and μ_s are fixed permittivity and permeability of the scatterer. A possible derivation of Eq (5.3) is given in Appendix B where we have shown that the achiral MEL ST should be written in the time averaged form along with its time averaged volume force density (i.e. MEL force law for magnetodielectric object embedded in a generic magnetodielectric heterogeneous background):

$$\left\langle \boldsymbol{f}_{\mathrm{MEL}(j)}^{\mathrm{Bulk}} \right\rangle(\mathrm{in}) = \frac{1}{2}\mathrm{Re}\left[\left(\boldsymbol{P}_{\mathrm{Eff}(j)} \cdot \nabla \right) \boldsymbol{E}_{\mathrm{in}}^{*} + \left(\boldsymbol{M}_{\mathrm{Eff}(j)} \cdot \nabla \right) \boldsymbol{H}_{\mathrm{in}}^{*} - \left(i\omega \boldsymbol{P}_{\mathrm{Eff}(j)} \times \boldsymbol{B}_{\mathrm{in}}^{*} \right) + \left(i\omega \boldsymbol{M}_{\mathrm{Eff}(j)} \times \boldsymbol{D}_{\mathrm{in}}^{*} \right) \right]. \tag{5.4}$$

Consistency of Eq (5.3) and (5.4) has been shown for surface force calculation in Appendix C, which satisfies the 'validity condition' described in the introduction [fulfilment of C(I)]. In Eq (5.4), the effective polarization and magnetization are defined as [26,171]: $\boldsymbol{P}_{\mathrm{Eff}} = \left(\varepsilon_S - \varepsilon_{\mathrm{b}} \right) \boldsymbol{E}_{\mathrm{in}}$ and $\boldsymbol{M}_{\mathrm{Eff}} = \left(\mu_S - \mu_{\mathrm{b}} \right) \boldsymbol{H}_{\mathrm{in}}$. The total time averaged Bulk force on the embedded object should be:

$$\left\langle \boldsymbol{F}_{\mathrm{MEL}}^{\mathrm{Bulk}} \right\rangle(\mathrm{in}) = \sum\nolimits_j \int \left\langle \bar{\bar{\boldsymbol{T}}}_{\mathrm{MEL}(j)}^{\mathrm{Bulk}} \right\rangle(\mathrm{in}) \cdot d\boldsymbol{s}_{(j)} = \sum\nolimits_j \int \left\langle \boldsymbol{f}_{\mathrm{MEL}(j)}^{\mathrm{Bulk}} \right\rangle(\mathrm{in}) \cdot dv_{(j)} . \tag{5.5}$$

Consistency of Eq (5.5) can be determined analytically considering the internal force on a magnetodielectric slab embedded in another magnetodielectric. Both the internal ST and volumetric force lead to the same result [164]. So, internal MEL method and external Minkowski method fulfil the condition C(II) analytically for this simple case. However, internal Chu, EL and Ampere method do not lead to that same force.In addition, the external force calculated by Minkowi's force also lead to the exactly same result [164].

Now, we consider the consistency condition C(I). By applying the proper boundary conditions [cf. Appendix C], the surface force of Modified Einstein-Laub method can be written from two different ways: (i) By the volume force method of Eq (5.4) [as shown in [182] only for volumetric force] and (ii) from the difference of external Minkowski ST and internal MEL ST in Eq (5.3) just at the boundary. These two different ways lead to exactly same result:

$$\begin{aligned} \boldsymbol{f}_{\mathrm{MEL}}^{\mathrm{Surface}} &= [\bar{\bar{\boldsymbol{T}}}_{\mathrm{Mink}}^{\mathrm{out}}(\mathrm{out}) - \bar{\bar{\boldsymbol{T}}}_{\mathrm{MEL}(j)}(\mathrm{in})]\cdot\hat{\boldsymbol{n}}_{r=a} \\ &= \left\{\epsilon_{b(j)}(\boldsymbol{E}_{\mathrm{out}} - \boldsymbol{E}_{\mathrm{in}})\cdot\hat{\boldsymbol{n}}\right\}\left(\frac{\boldsymbol{E}_{\mathrm{out}} - \boldsymbol{E}_{\mathrm{in}}}{2}\right)_{\mathrm{at}\ r=a} + \left\{\mu_{b(j)}(\boldsymbol{H}_{\mathrm{out}} - \boldsymbol{H}_{\mathrm{in}})\cdot\hat{\boldsymbol{n}}\right\}\left(\frac{\boldsymbol{H}_{\mathrm{out}} - \boldsymbol{H}_{\mathrm{in}}}{2}\right)_{\mathrm{at}\ r=a} \end{aligned} \tag{5.6}$$

Eq (5.6) clearly explains why in [171], the time averaged result of total force predicted by Minkowski ST is in exact agreement with the MEL volume force reported in [171]. According to Eq (5.6), the total time averaged force calculation by MEL force is equivalent with the total force calculation based on Minkowski ST or Helmholtz force for any generic case. So, the total time averaged force on an embedded achiral object according to MEL method should finally be written as:

$$\int\left\langle \bar{\bar{\boldsymbol{T}}}_{\mathrm{Mink}}^{\mathrm{out}} \right\rangle \cdot d\boldsymbol{s} = \left\langle \boldsymbol{F}_{\mathrm{MEL}}^{\mathrm{Bulk}} \right\rangle(\mathrm{in}) + \left\langle \boldsymbol{F}_{\mathrm{MEL}}^{\mathrm{Surface}} \right\rangle \tag{5.7}$$

Hence at least analytically we have arrived at the fulfillment of both C(I) and C(II). In the next part of this work, the validity of Eq (5.7) [our proposed C(II)] will be investigated mainly based on numerically [i.e. full wave simulations] calculated results.

5.6 A short discussion on previous tractor beam and lateral force experiments

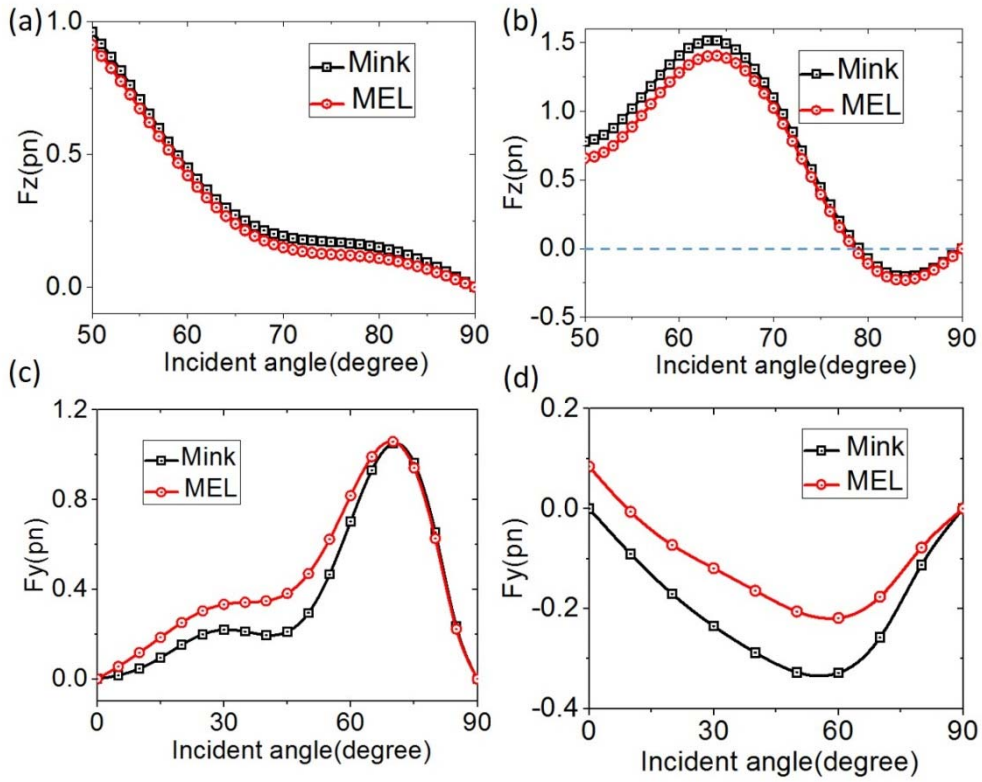

Fig. 5.5: Calculation of time averaged total optical force (NO GAP METHOD) by external Minkowski ST and the time averaged bulk force by internal MEL ST. These forces are always of same trend. By adding the surface force of achiral MEL with bulk force [cf. Eqs (5.6) and (5.7)], the magnitude exactly matches with external time averaged total force by Minkowski ST. (a) For the two beam tractor set-up in Fig. 5.2(b) with 320 nm object. (b) For the two beam tractor set-up in Fig. 5.2(c) with 410 nm object. (c) For the lateral force set-up in Fig. 5.3(b) [only left hand CP wave incident case] with spherical object. (d) For the lateral force set-up in Fig. 5.3(c) [only right hand CP case] with elliptical object. For all the cases the trend of the time-averaged bulk force, obtained by employing the internal field only, is very similar to the total outside force calculated by the external Minkowski ST, using fields exterior to the scatterer. The bulk force by modified Chu volume force or stress tensor does not follow the trend of the total force. Moreover, the internal force calculation by the MEL ST is very less-time and memory consuming in comparison with the modified volumetric force calculation method [cf. the detailed discussion in [26] and [183]]. These are the main computational advantages of MEL ST method.

The most probable reason of the success of Minkowski's theory lies on the fact that, in contrast with other force formulations, Minkowski's formulations, i.e. external Minkowski ST, Helmholtz force [35, 43, 28, 46, 192] and Minkowski photon momentum based ray tracing method [2,3] correctly account for the linear increase of transferred/emitted photon momentum at the boundary between the embedded object

and the background [35, 43]. Interestingly, when $[1-(\frac{\varepsilon_{b(j)}}{\varepsilon_s})]^2$ is very small for a dielectric object embedded in another dielectric (for example- most of the real experiments [35,36,166]), the surface force of MEL in Eq (5.6) almost vanishes, as $\left\langle \boldsymbol{f}_{\text{MEL}}^{\text{Surface}} \right\rangle \propto [1-(\frac{\varepsilon_{b(j)}}{\varepsilon_s})]^2$. Only for such special cases $\left\langle \boldsymbol{F}_{\text{Mink.}}^{\text{Total}} \right\rangle(\text{out}) \approx \left\langle \boldsymbol{F}_{\text{MEL}}^{\text{Bulk}} \right\rangle(\text{in})$ [as shown in [43] without any explanation]. In [43], the time averaged external force by Minkowski ST and the internal time averaged bulk force by MEL ST match well because the surface force almost vanishes. However, there must be a surface force part of MEL force. In [43], the time averaged external force by Minkowski ST and the internal time averaged bulk force by MEL ST match well because the surface force almost vanishes. But in general, for the exact total force formulation, that surface force should be added with the time averaged bulk force calculated by internal MEL ST [cf. Eq (5.7)] so that $\left\langle \boldsymbol{F}_{\text{Mink}}^{\text{Total}} \right\rangle(\text{out}) = \left\langle \boldsymbol{F}_{\text{MEL}}^{\text{Bulk}} \right\rangle(\text{in}) + \left\langle \boldsymbol{F}_{\text{MEL}}^{\text{Surface}} \right\rangle$. If the internal force for the tractor beam experiment in [35, 36] and the lateral force in [166] is calculated, our aforementioned conclusions still remain valid. It is shown in Fig.5.5 (a) and (b), total external time averaged force by Minkowski ST and the total internal bulk force by MEL ST are in almost full agreement for two beam tractor beam experiment in [36] due to very small value of $[1-(\frac{\varepsilon_{b(j)}}{\varepsilon_s})]^2$. However, the difference between the bulk force of MEL ST and the total force of external Minkowski ST is clearly observable for the lateral force experiment when $[1-(\frac{\varepsilon_{b(j)}}{\varepsilon_s})]^2$ is not very small [i.e. by considering a TiO_2 object embedded in air-water interface in Fig. 5.5(c)]. Also there is an effect of the size/shape change of the object on the bulk force of MEL ST as shown in Fig. 5.5(d). However, in Appendix D the bulk force calculation by MEL ST is shown for a Mie or more complex objects embedded in

homogeneous, heterogeneous and bounded background. As per we know, previously force calculation for heterogeneous medium has not been discussed in literature.

5.7 Chiral Modified Einstein-Laub and Chu formulations

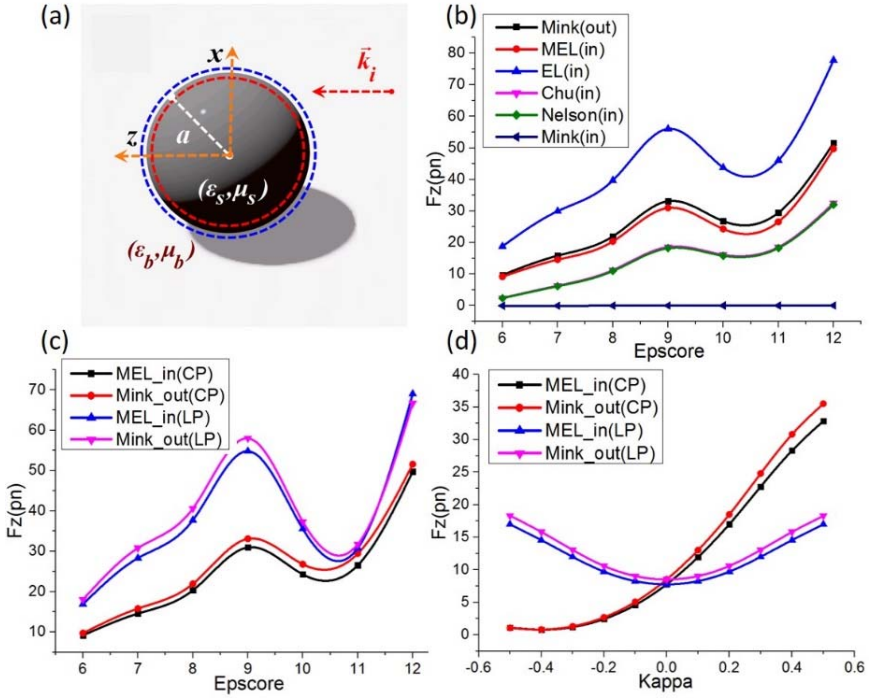

Fig. 5.6: Time-averaged forces: F_{out} at $r = a^{+} = 1.01a$ from Minkowski ST and F_{in} (bulk force) at $r = a^{-} = 0.999a$ from the Chiral MEL ST. These forces are always of same trend. By adding the surface force of Chiral MEL with bulk force, the magnitude exactly matches with external time averaged total force. (a) Calculation procedure of force on a dielectric sphere with a=500 nm (i.e., a Mie object) at $\lambda = 1064$ nm. The unbounded homogeneous dielectric background parameter: $\varepsilon_b = 4\varepsilon_0$. (b) Force on that chiral dielectric sphere (chirality parameter, $\kappa = 0.4$) by varying the permittivity of the sphere, illuminated by a linearly polarized plane wave $E_x = E_0 e^{i(kz-\omega t)}$. Notice that the internal forces (bulk forces) calculated by all other STs (i.e. EL, Chu, Nelson and Minkowski) are not so close to the total time averaged force. (c) Force on the same embedded chiral dielectric sphere by varying the permittivity of the sphere, illuminated by a linear polarized and a circularly polarized ($E_x + iE_y : E_x = E_0 e^{i(kz-\omega t)} = E_y$) wave. (d) Force on the embedded chiral dielectric ($\varepsilon_s = 4\varepsilon_0$) sphere by varying the chirality parameter of the sphere, illuminated by a linear polarized and a circularly polarized wave.

In this section we shall show the consistency of the proposed internal MEL method with the external Minkowski ST method [174]. Especially for chiral objects, no built in software [183] technique is available to yield the total volumetric force. The primary goal of this section is to set an efficient computational way for embedded chiral objects. The constitutive relations inside a chiral Mie object can be written as [77]:

$$\boldsymbol{D}_{\text{in}}^{\text{chiral}} = \varepsilon_{\text{s}} \boldsymbol{E}_{\text{in}} - j(\kappa / c)\boldsymbol{H}_{\text{in}}; \tag{5.8a}$$

$$\boldsymbol{B}_{\text{in}}^{\text{chiral}} = \mu_{\text{s}} \boldsymbol{H}_{\text{in}} + j(\kappa / c)\boldsymbol{E}_{\text{in}}. \tag{5.8b}$$

If a magneto-dielectric chiral object is embedded in a material background instead of air, the internal stress tensor that may yield the total force of the scatterer is the chiral MEL stress tensor for chiral object:

$$\left\langle \bar{\bar{\boldsymbol{T}}}_{\text{MEL}(j)}^{\text{chiral}} \right\rangle (\text{in}) = \boldsymbol{D}_{\text{in}}^{\text{chiral}} \boldsymbol{E}_{\text{in}}^{*} + \boldsymbol{B}_{\text{in}}^{\text{chiral}} \boldsymbol{H}_{\text{in}}^{*} - \frac{1}{2}\left((\frac{\mu_{\text{b}(j)}}{\mu_{\text{s}}})\mu_{\text{s}} \boldsymbol{H}_{\text{in}}^{*} \cdot \boldsymbol{H}_{\text{in}} + (\frac{\varepsilon_{b(j)}}{\varepsilon_{s}})\varepsilon_{s} \boldsymbol{E}_{\text{in}}^{*} \cdot \boldsymbol{E}_{\text{in}} \right) \bar{\bar{\boldsymbol{I}}}. \tag{5.9}$$

Where $j=1,2,3,....,\ N$ represents the number of background regions sharing interface with the chiral object. The total time averaged bulk force on the embedded object should be: $\left\langle \boldsymbol{F}_{\text{Bulk}} \right\rangle (\text{in}) = \sum_{j} \int \left\langle \bar{\bar{\boldsymbol{T}}}_{\text{MEL}(j)}^{\text{chiral}} \right\rangle (\text{in}) \cdot d\boldsymbol{s}_{(j)}$. A possible derivation of Eq (5.9) can be yielded very similar to our achiral MEL ST shown in Appendix B. The Bulk force of chiral MEL method can also be written as:

$$\left\langle \boldsymbol{f}_{\text{MEL}(j)}^{\text{Chiral}} \right\rangle (\text{Bulk}) = \frac{1}{2}\text{Re}\left[\left(\boldsymbol{P}_{\text{Chiral}(j)} \cdot \nabla \right) \boldsymbol{E}_{\text{in}}^{*} + \left(\boldsymbol{M}_{\text{Chiral}(j)} \cdot \nabla \right) \boldsymbol{H}_{\text{in}}^{*} - \left(i\omega \boldsymbol{P}_{\text{Chiral}(j)} \times \boldsymbol{B}_{\text{in}}^{*} \right) + \left(i\omega \boldsymbol{M}_{\text{Chiral}(j)} \times \boldsymbol{D}_{\text{in}}^{*} \right) \right]. \tag{5.10}$$

In Eq (5.10), the effective polarization and magnetization are defined as:

$$\boldsymbol{P}_{\text{chiral}} = \boldsymbol{P}_e + \boldsymbol{M}_c \,,\; \boldsymbol{P}_e = \left(\varepsilon_S - \varepsilon_{\text{b}}\right)\boldsymbol{E}_{\text{in}} \,,\; \boldsymbol{M}_c = -j(\kappa/c)\boldsymbol{H}_{\text{in}} \tag{5.11a}$$

$$\boldsymbol{M}_{\text{chiral}} = \boldsymbol{M}_{\text{n}} + \boldsymbol{P}_c \,,\; \boldsymbol{M}_{\text{n}} = \left(\mu_S - \mu_{\text{b}}\right)\boldsymbol{H}_{\text{in}} \,,\; \boldsymbol{P}_c = j(\kappa/c)\boldsymbol{E}_{\text{in}} \,. \tag{5.11b}$$

However, $\boldsymbol{D}_{\text{in}}^{\text{chiral}}$ and $\boldsymbol{B}_{\text{in}}^{\text{chiral}}$ in Eq (5.10) should be written from Eq (5.8a) and (5.8b) respectively. The surface force part has also been derived similar to achiral case discussed in previous section. The total time averaged force should be the surface force plus the bulk force. Consistency of chiral MEL ST for the unbounded homogeneous background is shown in Fig. 5.6 (a)-(d). In Fig. 5.7 (a)-(d), consistency of the chiral MEL ST has been shown considering a 2D infinite cylinder embedded in a heterogeneous background. Finally, the result shown in Fig. 5.8 [the bounded background case] bears some important physical insight. We have considered b=800 nm and a=600 nm. If b is made even much smaller and very close value of a (but b > a^{+}), still the conclusion presented in Fig. 5.8 (a)-(d) remains valid. Hence we can conclude that the boundary between the scatterer and background play a vital role to yield the total time averaged force, which may not be properly explained by GAP METHOD of force calculation.

The internal MEL ST (internal bulk force) leads to almost time averaged total force for several situations (or at least follows the trend of total time averaged force), which can be very useful from computational point of view for both embedded chiral and achiral objects. Finally, considering all the cases discussed in this work, probably we can assure the fulfilment of 'consistency conditions' C(I) and C(II) simultaneously by external Minkowski ST and the internal modified EL or Chu formulation both analytically and numerically.

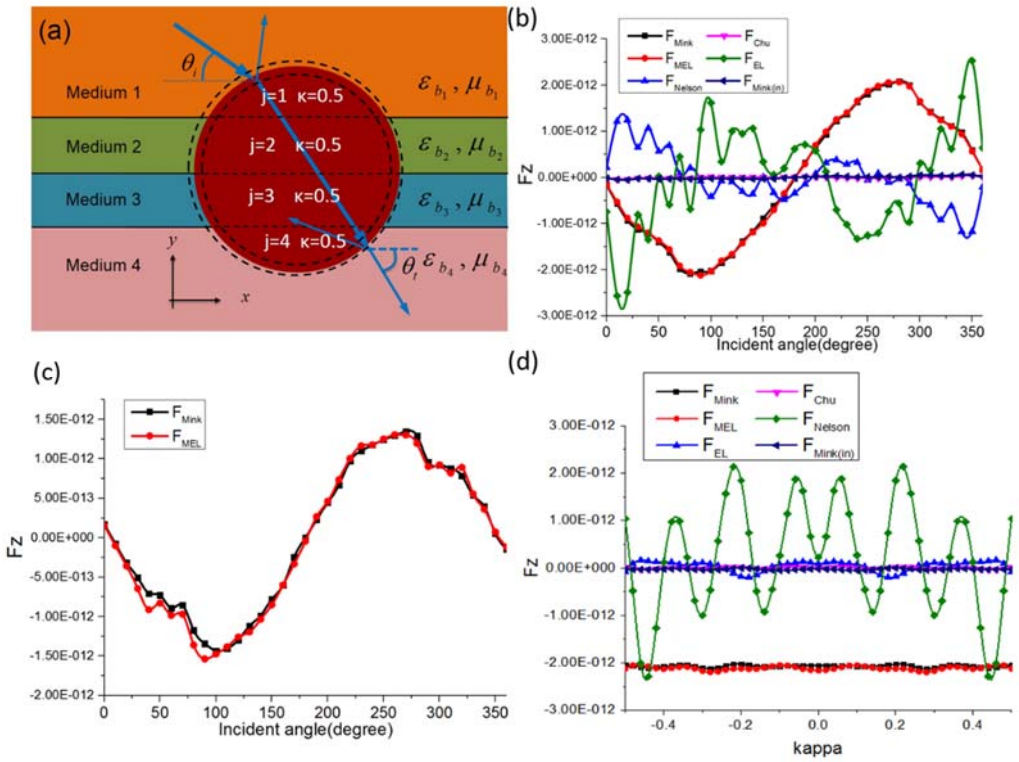

Fig. 5.7: Time-averaged forces: F_{out} at $r = a^{+} = 1.01a$ from Minkowski ST and F_{in} (bulk force) at $r = a^{-} = 0.999a$ from the Chiral MEL ST. These forces are always of same trend. By adding the surface force of Chiral MEL with bulk force, the magnitude exactly matches with external time averaged total force. (a) Calculation procedure of Force on a magneto-dielectric infinite chiral (chirality parameter, $\kappa = 0.5$) cylinder of $(\varepsilon_s, \mu_s) = (5\varepsilon_0, 4\mu_0)$ and radius 2000 nm embedded in heterogeneous unbounded background of four different magneto-dielectric layers: (ε_b, μ_b) = ($3\varepsilon_0$, $2\mu_0$); ($4\varepsilon_0$, $3\mu_0$);($5\varepsilon_0$, $4\mu_0$); ($6\varepsilon_0$, $5\mu_0$) at $\lambda = 1064$ nm. (b) Force on that cylinder when the plane wave $E_x = E_0 e^{i(kz-\omega t)}$ illuminates at varying angles. Notice that the internal force calculated by all other STs (i.e. EL, Chu, Nelson and Minkowski) are not in the same trend of the total external force. (c) Force on the same embedded cylinder when the illuminating circularly polarized wave: $E_x + iE_y$: $E_x = E_0 e^{i(kz-\omega t)} = E_y$ incidents at varying angles. (d) Force on the cylinder when the illuminating plane waves at angle 45 degree at varying chiral parameter κ.

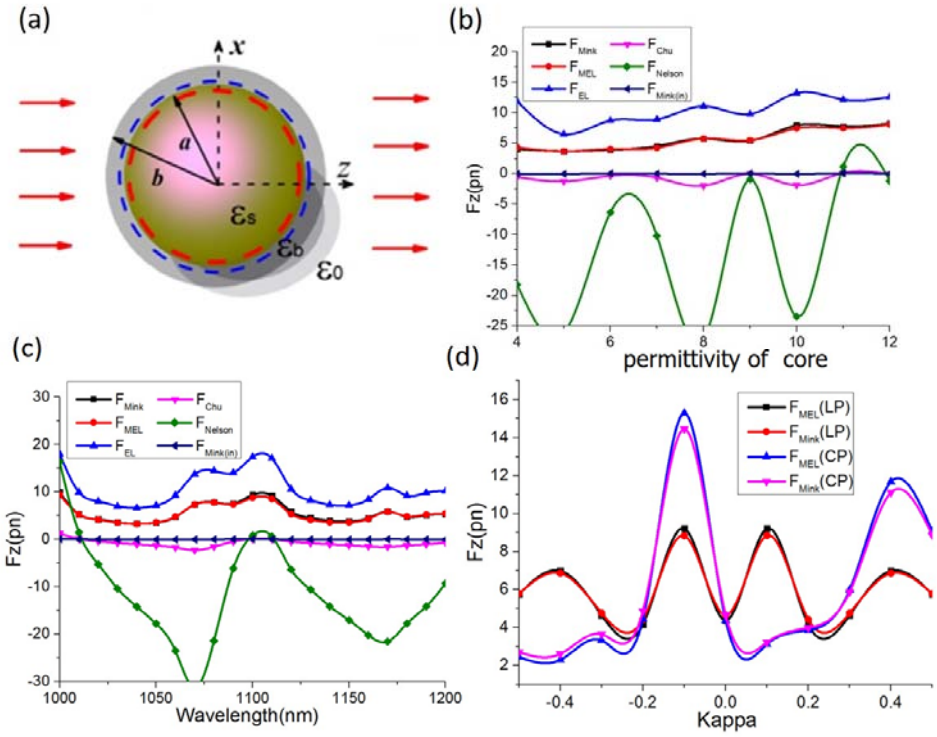

Fig. 5.8: Time-averaged forces: F_{out} at $r = a^{+} = 1.01a$ from Minkowski ST and F_{in} (bulk force) at $r = a^{-} = 0.999a$ from the Chiral MEL ST. These forces are always of same trend. By adding the surface force of Chiral MEL with bulk force, the magnitude exactly matches with external time averaged total force. (a) Calculation procedure of a 3D magneto-dielectric core where the whole core-shell sphere is embedded in air. Core radius, a=600 nm, $\varepsilon_s = 8\varepsilon_0$, $\mu_s = 4\mu_0$ Bounded local immediate background (i.e. the shell) parameters: radius, b=800 nm and $\varepsilon_s = 4\varepsilon_0$; $\mu_s = 2\mu_0$. This entire core-shell is illuminated at wavelength 1070 nm. (b) For plane wave illumination, $E_x = E_0 e^{i(kz-\omega t)}$: $\left\langle \boldsymbol{F}_{\text{out}}^{\text{Core}} \right\rangle$ at different chirality parameters obtained from Minkowski ST at $r=a^{+}$ using the fields in the shell. Force $\left\langle \boldsymbol{F}_{\text{in}}^{\text{Core}} \right\rangle$ based on the Chiral MEL ST at $r=a^{-}$ using core fields. The bulk force on the core by other STs do not follow the trend of the total external force. (c) For circularly polarized wave illumination ($E_x + iE_y : E_x = E_0 e^{i(kz-\omega t)} = E_y$): still the bulk force by Chiral MEL ST is of the same trend of the external time averaged total force for the variation of chirality parameter of the core. (d) For linear and circularly polarized wave illumination: again our conclusions remain valid for the variation of chirality parameter κ of the core.

5.8 Conclusion

In this chapter we have shown that: the 'validity condition' of $\overline{\overline{\boldsymbol{T}}}(\text{in})$ and $\boldsymbol{f}$ (in), defined at the beginning, plays a key role for the severe disagreement reported in [28, 46] of different force laws employed to describe real experimental results. We have proposed a solution to this problem based on the MEL ST, the MEL volume force [171] or alternatively by the modified Chu volume force [26, 183]. However, If $\left\langle \boldsymbol{F}^{\text{Bulk}} \right\rangle(\text{in}) = \int \left\langle \overline{\overline{\boldsymbol{T}}}(\text{in}) \right\rangle \cdot d\boldsymbol{s} \neq 0$; $\overline{\overline{\boldsymbol{T}}}(\text{out})$ and $\overline{\overline{\boldsymbol{T}}}(\text{in})$ cannot have the same form to satisfy both consistency conditions C(I) and C(II) simultaneously, when the background is a material medium rather than air. What is the physical reason behind that? A possible answer of this important question is discussed next.

Let us consider the total momentum conservation equation [17]: $\oint \overline{\overline{\mathbf{T}}}.ds = \int \boldsymbol{f}\, dv + \frac{\partial}{\partial t}\int \boldsymbol{G}\, dv$ and $\boldsymbol{p}_{\text{Total}} = \boldsymbol{p}_{\text{Mech.}} + \boldsymbol{p}_{\text{Non-Mech.}}$ where $\boldsymbol{p}$ represents momentum. Here $\boldsymbol{G}$ is the electromagnetic momentum density. Though the total momentum $\boldsymbol{p}_{\text{Total}}$ is always a conserved quantity, whenever one calculates/measures the photon momentum transfer from the background [58,151], it leads to Minkowski photon momentum where instead of simple mechanical and non-mechanical momentum part, the linear momentum equation can better be described as [58]: $\boldsymbol{p}_{\text{Total}} = \boldsymbol{p}^{\text{med}}_{\text{Cano.}} + \boldsymbol{p}_{\text{Mink}}$ where $\boldsymbol{p}_{\text{Mink}} = \int \boldsymbol{G}_{\text{Mink}} dv$ with $\boldsymbol{G}_{\text{Mink}} = \boldsymbol{D} \times \boldsymbol{B}$. On the other hand, Abraham photon momentum [P_{Abr} (in)] is considered as the travelling momentum of photon [151], which [P_{Abr} (in)] can also be considered as the remaining electromagnetic part of the photon momentum after delivering the mechanical momentum of photon inside an object setting that object in motion [hence kinetic momentum [58]: $\boldsymbol{p}_{\text{Total}} = \boldsymbol{p}^{\text{med}}_{\text{Kin}} + \boldsymbol{p}_{\text{Abr}}$, where $\boldsymbol{p}_{\text{Abr}} = \int \boldsymbol{G}_{\text{Abr}} dv$ with $\boldsymbol{G}_{\text{Abr}} = \frac{\boldsymbol{E} \times \boldsymbol{H}}{c^2}$]. So, the role of Minkowski and Abraham photon momenta are fully different [58, 151] and

hence in the aforementioned conservation equation, $\boldsymbol{G}$ should also be different when we describe two different process: transfer of momentum from background (i.e. transfer of $\boldsymbol{p}_{\text{Mink}}$ from background to an embedded object due to Doppler effect [58]) and delivery of momentum inside an object (i.e. $\boldsymbol{p}_{\text{Abr}}$ inside the Einstein-Balaz's box [58]). This suggests that: as total momentum is a conserved quantity, $\boldsymbol{f}$ can also be different due to different $\boldsymbol{G}$ and they should bear fully different physical meanings. Hence the proposed explanation is that: time averaged Minkowski's 'total' force describes how much mechanical momentum has already been transferred to an embedded object from the background medium, which can be calculated just by employing the external fields of the embedded object. In contrast, time averaged MEL 'bulk' force describes how much force (due to local fields) has been felt by the induced dipoles of an embedded object by which (dipoles) that object is made. Now, most importantly, though by adding the surface force of MEL with the time averaged bulk force we get exactly the same value of time averaged total force predicted by Minkowski's external force [$\left\langle \boldsymbol{F}_{\text{Mink}}^{\text{Total}} \right\rangle(\text{out}) = \left\langle \boldsymbol{F}_{\text{MEL}}^{\text{Bulk}} \right\rangle(\text{in}) + \left\langle \boldsymbol{F}_{\text{MEL}}^{\text{Surface}} \right\rangle$], they [left side and right side of aforementioned equation] are two fully different things from physical point of view. In fact, this issue has already been pointed regarding only photon momenta in refs. [58, 151]. But such dissimilarity may, in general, also be true for the role of distinct time averaged stress tensors, which has been overlooked so far. So, we suggest the distinct physical meanings of the left and right hand sides of this equation: $\left\langle \boldsymbol{F}_{\text{Mink}}^{\text{Total}} \right\rangle(\text{out}) = \left\langle \boldsymbol{F}_{\text{MEL}}^{\text{Bulk}} \right\rangle(\text{in}) + \left\langle \boldsymbol{F}_{\text{MEL}}^{\text{Surface}} \right\rangle$, which (distinct physical meanings) is also applicable for the modified Chu formulation [26]: $\left\langle \boldsymbol{F}_{\text{Mink}}^{\text{Total}} \right\rangle(\text{out}) = \left\langle \boldsymbol{F}_{\text{Chu}}^{\text{Bulk}} \right\rangle(\text{in}) + \left\langle \boldsymbol{F}_{\text{Chu}}^{\text{Surface}} \right\rangle$.

Last but not least, our work explains not only the reason of the inconsistency of different time averaged volumetric forces reported in [28], [46], but also provides an efficient alternative solution to calculate the time-averaged bulk force with the

modified Einstein-Laub (MEL) stress tensor method, saving much calculation time and memory with respect to the time-consuming bulk volumetric force method [183] for both embedded achiral [19,20, 28,35,36,46, 84,97, 98, 183- 186] and chiral objects [19,20]. Similar time-averaged modified formulations are also possible on employing modified Chu methods [26,183]. In fact, the main goal of this chapter is not to show superiority of one formula over another. Rather the main targets of this work were to make fully distinct formulas mathematically equivalent to yield accurate and consistent time-averaged total optical force, as well as explaining the exact reason of discrepancies of previous theories for real experimental observations.

Chapter 6

Modified Lorentz Force and Plasmonic Cube Dimers over Substrate: Binding Force Reversal

6.0 Summary of Chapter 6

In previous chapter it has been discussed in details why Lorentz force should be modified when the embedding background is material one instead of air. In this chapter we apply the modified Lorentz force (modified Chu force) to study the behavior of binding force for two cubes over different substrates fully immersed in water. The behavior of Fano resonance and the reversal of near field optical binding force of dimers over different substrates have not been studied so far. In this work, we observe that if the closely located plasmonic cube homodimers (over glass or high permittivity dielectric substrate) are illuminated with plane wave polarized parallel to dimer axis, no reversal of optical binding force occurs. But if we apply the same set-up over a plasmonic substrate, stable Fano resonance occurs along with the reversal of binding force. It is observed that during such Fano resonance stronger coupling occurs between the dimers and plasmonic substrate along with the strong enhancement of the substrate current even in presence of dielectric spacer. Interestingly, for both the strong quadrupole-quadrupole and dipole-dipole resonances of the dimers, the binding force is dominated by Coulombic surface charge induced modified surface Lorentz force ; whereas during the Fano resonance binding force reversal is dominated by polarization current induced modified bulk Lorentz force.

6.1 Introduction

Fano resonance and the Fano line shape [193] cannot be described by the Lorentz resonance formula [194]. In plasmonic nanostructures, Fano resonance can happen due to the resonant destructive interference between a super-radiant (bright) mode and subradiant (dark) modes [195]. The promising applications of plasmonic hybridization and Fano resonances [39,41] have been investigated in improved sensitivity of the resonance [196], bio sensing [119], surface-enhanced Raman scattering [197], photonic propagation and wave guiding [198], plasmon-induced transparency [124] and many others [127]. In contrast, much less attention is dedicated on near field optical force due to Fano resonance; especially for plasmonic dimers [39,41] as discussed only in [22,23]. Specially, plasmonic particle over substrate show remarkable properties: Fano resonances [199], Boradband tenability in plasmonic resonance [200], modification of energies of the plasmon modes [201], changing the localized density of states [202], radiative enhancement [203], frequency shift of an electric dipole resonance [204] and so on. But the behavior of near field optical force for plasmonic dimers over different types of substrate and the effect of substrate on the reversal of near filed optical binding force have not been studied in literature. In fact, only few works have been reported on the reversal of near field optical binding force due to Fano resonance, i.e. for nanobar structures [22], for disk along with a ring structure [23]. But reversal of near field binding force are highly dependent on inter-particle distance and particle size for those set-ups.

According to ref. [205]: “The inter particle separations are usually comparable to the wavelength of the illuminating laser beam and, therefore, mainly long-range interactions mediated by the far-field scattered field are considered while the near-

field coupling is usually omitted in the related studies." But with the recent technology, the inter particle distance between the nano particles can be precisely controlled [206]. More importantly, the size and shape of the gap between the nanoparticle and film can also be controlled to sub nanometer precision bottom-up fabrication approaches [206]. The film-coupled nanoparticle geometry has recently been applied to enhancing optical fields, accessing the quantum regime of plasmonics [207], and the design of surfaces with controlled reflectance [208]. Still no investigation has been carried out regarding the behavior of both Fano resonance and the reversal of near field optical binding force with respect to the inter particle distance of two dimers over different substrates.

In this work, it is observed that if two plasmonic cube homodimers are placed closely without any substrate or above glass or high refractive index substrate, no reversal of optical binding force occurs. But if we apply the same set-up over a plasmonic substrate, stable and stronger Fano resonance occurs along with the reversal of binding force. It is well known that usually Fano resonance is ultra-sensitive and previously reported reversal of optical binding force dies out very quickly if the inter particle gap of the heterodimers [22] increase even a little bit. Moreover, this [22] previously reported Fano resonance induced reversal of binding force is highly dependent on particle size, which has not been achieved in [22] and [23] by homodimers. In general, reversal of near field lateral optical binding force for the same polarization of light is quite uncommon with the homodimers placed without substrates [113, 134, 135, 209]. Even if the homodimers are placed over substrates, reversal of near field lateral optical binding force has not been observed in refs. [136, 210,211] for spherical shaped and rod shaped plasmonic homodimers.

As a result, we have investigated a fully alternative way to achieve strong and stable reversal of optical binding force based on cube homodimer and substrate system, where stable and much stronger Fano resonance can be achieved due to the

substrate coupling with larger area of the lower portions of cube dimers. Though nanoparticles of sphere is easy to synthesize in experiment, the substrate-induced hybridization of the plasmon modes can be much larger [199] for a planar metallic nanoparticle (i.e. a cube) deposited on a plasmonic substrate [206,208] than for a spherical particle [201]. This happens because the plasmon-induced steady state currents and surface charges will be located closer to the strong surface currents and plsmonic screening charges induced on the surface of the substrate over a large area.

We have demonstrated that from the interplay between localized surface plasmon and propagating surface plasmon polariton along with the strong coupling between the two particles with the plasmonic substrate, the reversal of the optical binding force occurs during the strong Fano resonance**.** The physical mechanisms of binding force reversal have been explained based on modified Lorentz force dynamics. This lateral binding force reversal for the homodimers may be more flexible than the previously reported cases in [22, 23] where the reversal of near field binding force of the heterodimers dies out with the change of: (i) inter particle distance and (ii) particle size. Our configuration provides much relaxation of those parameters and hence can be verified experimentally with simpler experimental set-ups.

6.2 Optical Force calculation

We again specify that throughout this thesis we refer to 'exterior' or 'outside' forces as those evaluated outside the volume of the macroscopic particles, while ‘interior’ or 'inside' refer to those quantities inside this object volume. In order to consider the realistic effects, we have done all the numerical calculations using full wave simulations [100] in three dimensional (3D) structures.

The proposed simple set-up is illustrated in Fig. 6.1(a). The Silver particles are placed near to each other above a silver substrate (whole set-up is embedded in water). Spacer of height 5 nm is always considered above all the substrates in this chapter. The real and imaginary part of the permittivity of silver is taken from the standard Palik data [100, 139]. Inter particle distance is '*d*'. The source is a simple *x*-polarized plane wave $E_x = E_0 e^{j\beta z}$ propagating towards –*z* direction. This set-up is a symmetry broken system which later plays a vital role for the force reversal. The 'outside optical force' [33] is calculated by the integration of time averaged Minkowski [43, 84] stress tensor at r=a^+ employing the background fields of the scatterer of radius *a*:

$$\begin{aligned} \left\langle \boldsymbol{F}_{\text{Total}}^{\text{Out}} \right\rangle &= \oint \left\langle \overline{\overline{\boldsymbol{T}}}^{\text{out}} \right\rangle \cdot d\boldsymbol{s} \\ \left\langle \overline{\overline{\boldsymbol{T}}}^{\text{out}} \right\rangle &= \frac{1}{2}\text{Re}[\boldsymbol{D}_{\text{out}}\boldsymbol{E}_{\text{out}}^{*} + \boldsymbol{B}_{\text{out}}\boldsymbol{H}_{\text{out}}^{*} - \frac{1}{2}\overline{\overline{\boldsymbol{I}}}(\boldsymbol{E}_{\text{out}}^{*}\cdot\boldsymbol{D}_{\text{out}} + \boldsymbol{H}_{\text{out}}^{*}\cdot\boldsymbol{B}_{\text{out}})] \end{aligned} . \tag{6.1}$$

Where 'out' represents the exterior total field of the scatterer; $\boldsymbol{E}$, $\boldsymbol{D}$, $\boldsymbol{H}$ and $\boldsymbol{B}$ are the electric field, displacement vector, magnetic field and induction vectors respectively, $\langle\ \rangle$ represents the time average and $\overline{\overline{\boldsymbol{I}}}$ is the unity tensor.

On the other hand, based on the modified Lorentz force (i.e. modified Chu force), the total force (surface force and the bulk force [26,171,183] part of modified Lorentz force) can be written as:

$$\left\langle \boldsymbol{F}_{\text{Total}} \right\rangle = \left\langle \boldsymbol{F}_{\text{Volume}} \right\rangle = \left\langle \boldsymbol{F}_{\text{Bulk}} \right\rangle + \left\langle \boldsymbol{F}_{\text{Surf}} \right\rangle = \int \left\langle \boldsymbol{f}_{\text{Bulk}} \right\rangle dv + \int \left\langle \boldsymbol{f}_{\text{Surface}} \right\rangle ds \tag{6.2}$$

Where

$$\begin{aligned} \left\langle \boldsymbol{f}_{\text{Surface}} \right\rangle &= [\sigma_e \boldsymbol{E}_{avg}^{*} + \sigma_m \boldsymbol{H}_{avg}^{*}\ ]_{\text{at } r=a} \\ &= \{\epsilon_b(\boldsymbol{E}_{\text{out}} - \boldsymbol{E}_{\text{in}})\cdot\hat{\boldsymbol{n}}\}\left(\frac{\boldsymbol{E}_{\text{out}} + \boldsymbol{E}_{\text{in}}}{2}\right)^{*}_{\text{at } r=a} + \{\mu_b(\boldsymbol{H}_{\text{out}} - \boldsymbol{H}_{\text{in}})\cdot\hat{\boldsymbol{n}}\}\left(\frac{\boldsymbol{H}_{\text{out}} + \boldsymbol{H}_{\text{in}}}{2}\right)^{*}_{\text{at } r=a}, \end{aligned} \tag{6.3}$$

$\boldsymbol{f}_{\text{Surface}}$ is the modified surface force density (the force which is felt by the induced bound electric and magnetic surface charges of a scatterer), which is calculated just at the boundary of a scatterer [26,171,183]. 'in' represents the interior fields of the scatterer; 'avg' represents the average of the field. σ_e and σ_m are the bound electric and magnetic surface charge densities of the scatterer respectively. The unit vector $\hat{\boldsymbol{n}}$ is an outward pointing normal to the surface. ε_b is permittivity and μ_b is permeability of the background (i.e. water).

$$\left\langle \boldsymbol{f}_{\text{Bulk}} \right\rangle = \frac{1}{2}\text{Re}[\varepsilon_0(\nabla\cdot\boldsymbol{E}_{\text{in}})\boldsymbol{E}_{\text{in}}^{*} + \mu_0(\nabla\cdot\boldsymbol{H}_{\text{in}})\boldsymbol{H}_{\text{in}}^{*}] - \frac{1}{2}\text{Re}[i\omega(\varepsilon_s-\varepsilon_b)\{\boldsymbol{E}_{\text{in}}\times\boldsymbol{B}_{\text{in}}^{*}\} + i\omega(\mu_s-\mu_b)\{\boldsymbol{D}_{\text{in}}^{*}\times\boldsymbol{H}_{\text{in}}\}] \tag{6.4}$$

$\boldsymbol{f}_{\text{Bulk}}$ is the modified bulk force density, which is calculated from the interior of the scatterer by employing the inside field [26,171,183]. ε_s is permittivity and μ_s is permeability of the scatterer. As per we know, the Lorentz force dynamics of plasmonic particles and specially dimers have not been discussed previously. It is notable that the 'external dipolar force' [34, 38] (which has also been described as Lorentz force in [38]) is quite different than the Lorentz force defined in our Eqs (2) - (4).

6.3 Plasmonic cubes over plasmonic substrate: a short discussion on resonance modes and reversal of binding force

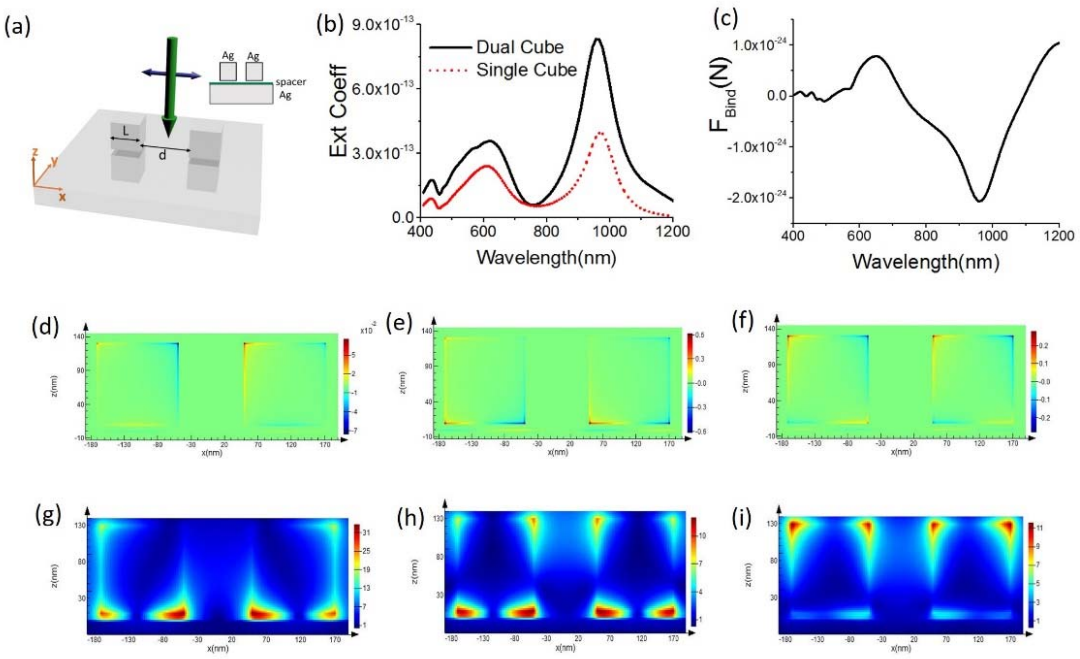

Fig. 6.1: (a) Two silver cubes (L=120 nm) are placed over silver substrate and their inter-particle gap, *d*, is 100 nm (spacer height 5 nm from the bare substrate and the cubes are placed 5 nm away from the spacer). (b) Comparison of the extinction coefficients of two silver cubes [set-up of Fig. (a)] and a single silver cube placed over silver substrate. (c) The binding force of set-up (a). (d)-(f): charge distribution at wavelengths: 966 (DD), 754 (Fano) and 627 (QQ) nm respectively. D and Q represent dipole and quadrupole respectively. (g)-(i): Electric field distribution for those same wavelengths respectively.

In Fig. 6.1(a) we have considered two silver cubes of length 120 nm each (100 nm apart). These cubes are placed in water above a silver substrate. A spacer of 5 nm height is considered between the cubes and the substrate and the cubes are placed 5 nm above the spacer. This set-up is shined by a plane wave described in previous section. The extinction spectra in Fig. 6.1(b) reveals that Fano dip takes place at around 754 nm and the strength of extinction coefficient increases two times than a single cube placed over silver substrate. The quadropolar resonance (at wavelength 627 nm), dipolar resonance (at 966 nm) and Fano dip (at around 754 nm) do not experience shifting due to the addition of the identical cube. It is demonstrated in Fig. 6.1(c) that reversal of optical binding force [i.e. positive value of $F_{\text{Bind }(x)}$ means

attractive force and negative value means repulsive force] takes place near the Fano dip at 754 nm wavelength. It should also be noted that if we decrease the inter particle distance of the cubes, the magnitude of the lateral binding force increases where lateral binding force, $F_{\text{Bind }(x)} = \left(F_{1\,(x)} - F_{2\,(x)}\right)$. Here subscript (x), (1) and (2) represent: +x direction, left cube and right cube respectively. It is also observed in our full wave simulations that the reversal of binding force occurs at the Fano dip position (around the wavelength 1000 nm) even if we change the length of the cube from 120 to 180 nm [cf. Fig. 6.2 (a)-(c)]. Such reversal of binding force is quite generic for plasmonic cubes of other sizes placed over plasmonic substrates. The only countable issue to achieve such force reversal is to achieve Fano type dip at first with the single cube. However, the force reversal wavelength and the Fano resonance both red shift with the increase of the cube dimension. The reason of Fano resonance for the dimers can be very easily explained based on the destructive interference of quadropolar and dipolar mode of the dimer as previously discussed considering high refractive index substrate in [199]. The distinct charge distributions of the plasmonic cubes have been shown in Figs 6.1(d) –6.2(f) for different resonance modes [i.e. dipole-dipole (DD), Fano and quadrupole-quadrupole (QQ) resonance respectively]. In addition, in Figs 6.1(g)-(i) the electric field magnitudes of different modes [i.e. DD, Fano and QQ resonance respectively] have been demonstrated. The field distributions are similar (but not identical) to ref. [199] where the substrate is considered as high refractive index dielectric. The strength of electric field magnitude increases due to the use of plasmonic substrate, which is a necessary condition for stronger coupling and resonance that leads to binding force reversal. However, the mixed nature of electric field at the Fano dip clearly supports the mixing of dipolar and quadrupolar resonance [199, 200].

But the question is whether Fano resonance is the only factor to achieve such force reversal. The answer is: strong Fano resonance induced by strong plasmonic coupling

is the key factor of such force reversal but it is not the only reason. For example- in the next section we shall demonstrate that Fano resonance also occurs for Silicon substrate with cube dimers but no reversal of binding force takes place for such case. In addition, more details on the physical mechanism of such optical force reversal will be discussed in the next sections.

At the DD resonance mode (i.e. 966 nm wavelength), field lines form closed loops around the separation between the particle and the metallic film [212]. Maximum value of the repulsive binding force occurs at this wavelength as shown in Fig. 6.1(c). This resonance mode corresponds to the localized surface plasmon (LSP) mode associated to the silver particle. According to another point of view [206], this resonance mode can be explained as a magnetic cavity mode that roughly satisfies the half wavelength criteria. In particular, the metal (silver)−insulator (spacer)−metal (silver) region supports a transmission line type of mode modified by the plasmonic dispersion of the metal. A large effective impedance mismatch occurs at the edges of the cube and most of the energy is reflected back under the cube [cf. the electric field distribution in Fig. 6.1(g)].

On the other hand, a resonance peak of extinction spectra occurs at around 627 nm as shown in Fig. 6.1 (c), which corresponds to QQ resonance. Local maxima of the attractive binding force occurs during this resonance. It corresponds to the surface plasmon polariton (SPP) mode propagating on the silver/air interface of the metallic film, which is excited near this wavelength [cf. ref. [212]]. The corresponding enhancement of the particle excitation field increases the intensity of field scattered at infinity [cf. the electric field distribution in Fig. 6.1(i)]. From another point of view [206], this higher order mode is an example of waveguide modes and occurs at shorter wavelengths such that the cavity is longer than a half wavelength of the mode.

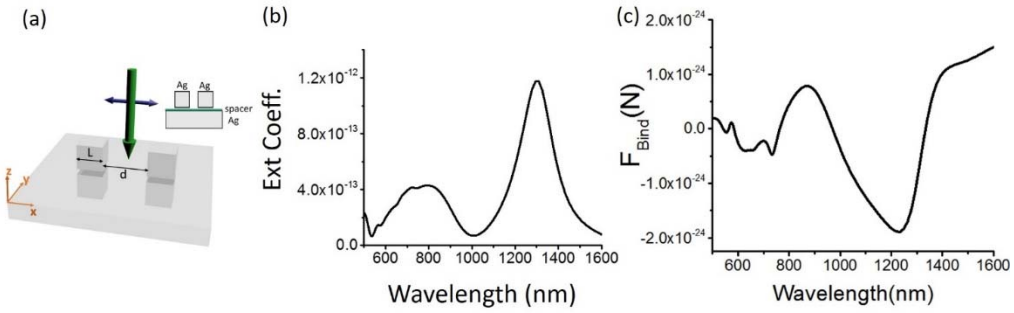

Fig. 6.2: (a) Two silver cubes (L=180 nm) are placed over silver substrate and their inter-particle gap,d, is 150 nm. The spacer (refractive index 1.4) height is 5nm for all the cases discussed in this work. Cubes are placed 5nm (h= 5nm) away from the spacer. *x*-polarized plane wave is propagating towards –*z*-direction. (b) Extinction co-efficient (c) Optical binding force.

6.4 Plasmonic cubes over different substrates: effect on binding force

So far we have discussed regarding single or double plasmonic cubes over plasmonic substrates. Now we shall compare the behavior of optical binding force considering two plasmonic cubes without substrate and over the glass or Silicon (high refractive index) or silver (plasmonic substrate) substrate fully immersed in water [cf. Fig. 6.3 (a) –(c)]. No reversal of optical binding force is observed in Fig. 6.3 (c). This same conclusion is true for the 2nd case [cf. Figs. 6.3(d)-(f)] when no reversal of optical binding force is observed. However, in Fig. 6.3(g)-(i), the substrate is Silicon (modelled as Palik data [100, 139]). Ultimately Fano dip spectral region is observed in Fig. 6.3(h) due to Fano resonance. But no reversal of optical binding force is observed in Fig. 6.3 (i). This is an important observation. This observation suggests that Fano resonance is not the only criteria to achieve the reversal of optical binding force [which occurs for silver slab in Fig. 6.3 (l)] rather some other factors (will be discussed next) significantly influence the origin of the reversal of optical binding force. Now we shall discuss the behavior of binding force distribution for these three resonances: (i) DD (ii) QQ and (iii) Fano resonance, when the substrate is silver one.

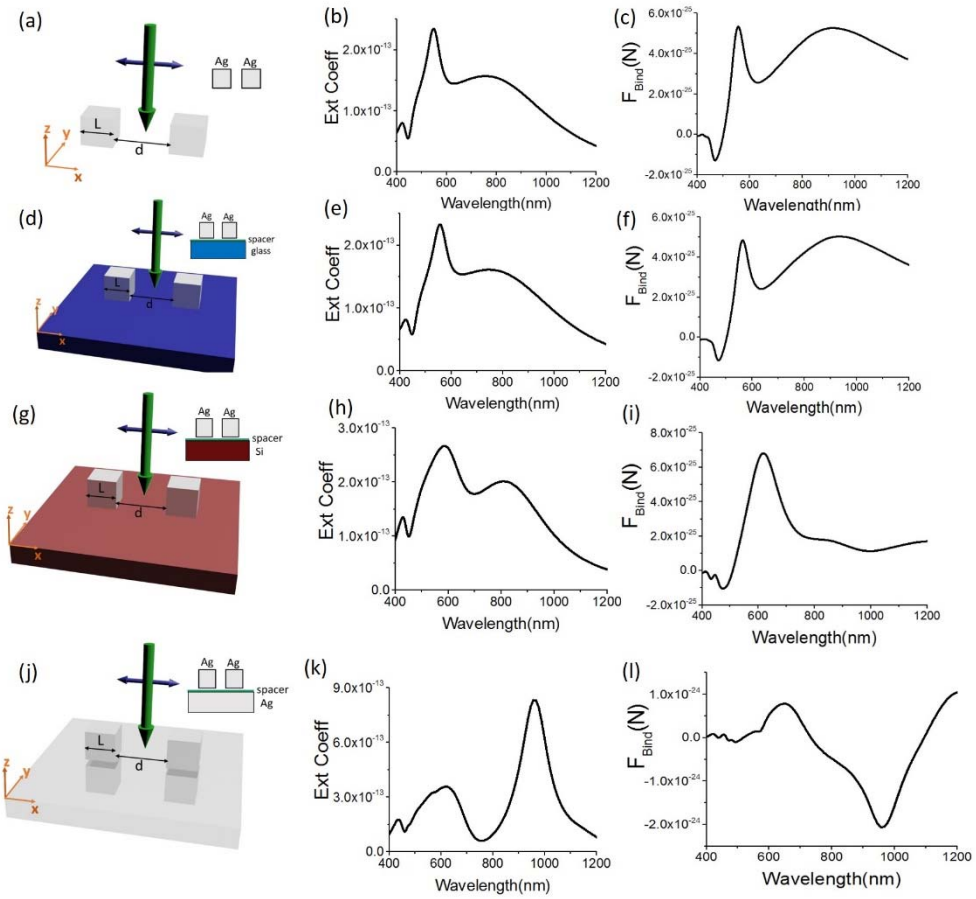

Fig.6.3: Two silver cubes (L=120 nm) are placed over different substrates and their inter-particle gap, *d*, is 150 nm. The spacer height is always 5nm. Cubes are placed 5nm (h= 5nm) away from the spacer. *x*-polarized plane wave is propagating towards –*z*-direction. (a)-(c): No substrate is placed; the extinction coefficient and binding force for that configuration. (d)-(f): Glass substrate (refractive index 1.5) is placed; the extinction coefficient and binding force for that configuration. (g)-(i): Silicon substrate is placed; the extinction coefficient and binding force for that configuration. (j)-(l): Silver substrate is placed; the extinction coefficient and binding force for that configuration.

For the DD resonance mode, the resonance process with the plasmonic substrate is quite different in comparison with the other substrates. During the DD resonance mode, the accumulated charges are strongly coupled with the plasmonic substrate and the total power is mostly concentrated between the cube and the plasmonic substrate. The charge distribution essentially results in a current loop between the nano cube and metal film inducing a strongly enhanced magnetic field. This resonance is then mainly of magnetic nature [206, 208, 212]. But the most interesting part is that: though the resonance is of magnetic nature, the difference of the scattering part

(which originates from magnetic induction: $\boldsymbol{J} \times \boldsymbol{B}_{\text{in}}$; where $\boldsymbol{J}$ is the polarization induced current) of the total Lorentz force vanishes during the peak of LSP or DD resonance mode [cf. Fig. 6.4 (a), (c) for both 120 and 180 nm lengthened cubes]:

$$\text{Del F}_{\text{Bulk}(x)} = \int[\langle \boldsymbol{f}_{\text{Bulk (1)}} \rangle dv_{(1)}] - \int[\langle \boldsymbol{f}_{\text{Bulk (2)}} \rangle dv_{(2)}] \tag{6.5}$$

So, the total binding force at LSP or DD resonance peak is fully due to the surface charges and the difference of surface force can be expressed as:

$$\text{Del F}_{\text{Surf (x)}} = \int[\langle \boldsymbol{f}_{\text{Surface}\,(B)} \rangle ds_{(1)}] - \int[\langle \boldsymbol{f}_{\text{Surface}\,(S)} \rangle ds_{(2)}] \tag{6.6}$$

It should be noted that: $F_{\text{Bind}\,(x)} = \left(F_{1\,(x)} - F_{2\,(x)}\right) = \text{Del F}_{\text{Bulk}(x)} + \text{Del F}_{\text{Surf (x)}}$. In Fig 6.5(i) it can be seen that the flipped $\int[\langle \boldsymbol{f}_{\text{Surface (1)}} \rangle ds_{(1)}]$ [and also $\text{Del F}_{\text{Surf (x)}}$; cf. Fig 6.4 (b) and (d)] reaches its maximum negative value near the DD resonance for plasmonic silver substrate [also cf. Fig 6.3(l)].

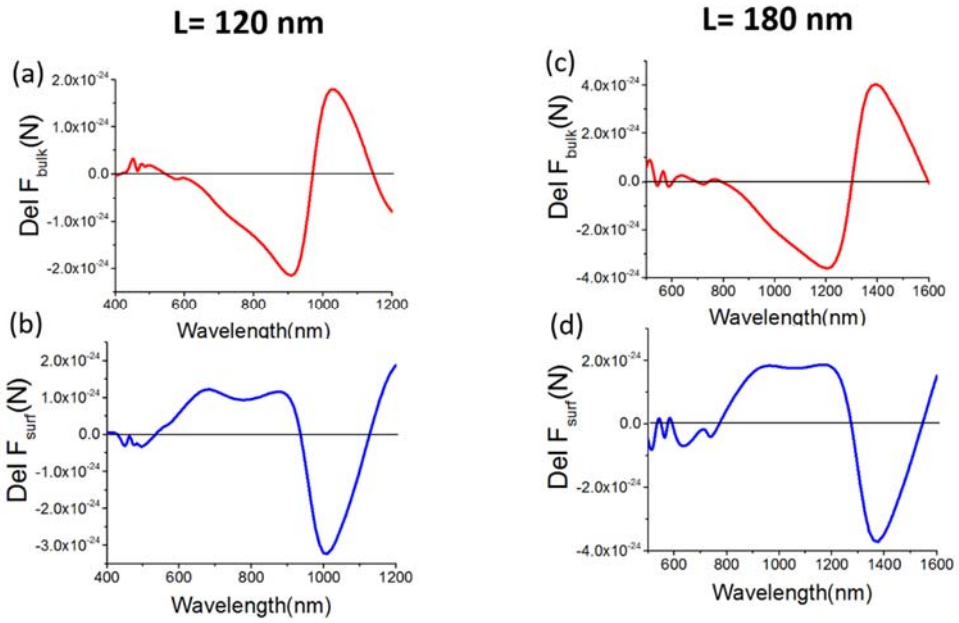

Fig. 6.4: For cube homodimers over silver substrate, plot of $\text{Del F}_{\text{Bulk}(x)}$ and $\text{Del F}_{\text{Surf (x)}}$ [cf. Eq (6.5) and (6.6)]. Spacer height is always 5 nm and height of the cubes from the spacer is fixed 5nm from the spacer. For first column: Length of each cube is 120 nm and they are placed 100 nm apart. For second column: Length of each cube is 180 nm and they are placed 150 nm apart.

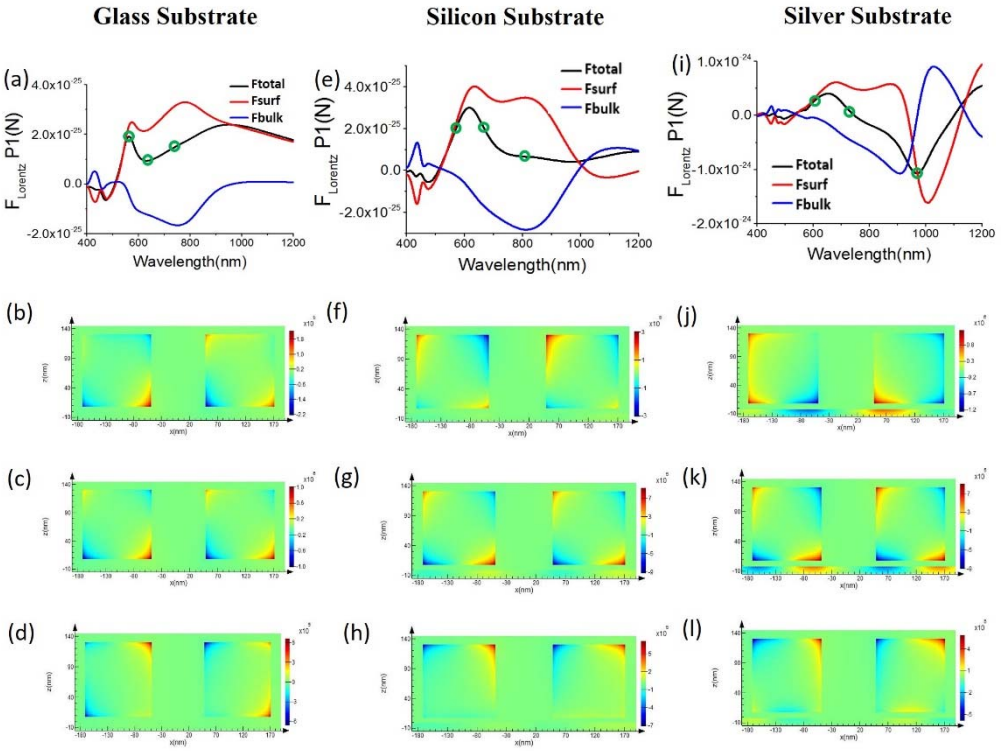

Fig. 6.5: For the cases of different substrates, Lorentz force components and the steady state current (J_y) of two 120 lengthened silver cubes along with the substrate. First row represents the Lorentz force components: surface force, bulk force and total force only on cube-1 (left cube, denoted as P1). '°' represents the chosen wavelengths for which the steady state current distributions are plotted later. Second, third and fourth row represent the steady state current (J_y) from front view [in xz plane; setting the window very close to the cube surfaces from front view] for three different wavelengths (marked as '°') respectively: (a)-(d): For glass substrate where wavelengths are chosen: 754, 622 and 550 nm respectively. (e)-(h): For Silicon substrate where resonance wavelengths are: 816 (DD), 679 (Fano) and 578 nm (QQ) respectively. (i)-(l): For Silver substrate where resonance wavelengths are: 966 (DD) ,754 (Fano) and 627 nm (QQ) respectively.

From the first row of Fig. 6.5, it can also be seen that such reversal of $\int[\langle \boldsymbol{f}_{\text{Surface (1)}} \rangle ds_{(1)}]$ does not happen for other substrates. This can be explained based on the electric field coupling between the cubes and also between cubes with plasmonic substrate. Electric field enhancement becomes much stronger for the case of plasmonic substrate in comparison with other substrates especially at this particular

resonance. The surface force in Eq (6.3) depends on the electric fields of the cube boundary/interface, which becomes much stronger during this DD resonance.

Though the maximum value of repulsive binding force for DD or LSP mode is just due to surface charges, the local maximum value of attractive binding force for QQ or SPP resonance at wavelength 627 nm [cf. Fig. 6.3(l)] is the combined effect of static (opposite surface charges as shown in Fig. 6.1 (f)) and dynamic (propagation of SPP) process. If we give a close look at Lorentz force in Fig. 6.4, it is clearly observable that at this QQ resonance: though the resultant binding force is due to the dominance of $\mathrm{Del\,F_{Surf\,(x)}}$, $\mathrm{Del\,F_{Bulk(}}_{x)}$ also exists. This fact can be verified from Fig. 6.5(i), where the dominance of $\int[\langle \boldsymbol{f}_{\mathrm{Surface}\,(B)} \rangle ds_{(1)}]$ on cube-1 is clearly observable. The opposite charges of the cubes create the attractive force between the cubes placed over any substrate such as plasmonic or glass or silicon substrate. At the same time, the propagating surface plasmon of the plasmonic substrate also create force on the cubes in the opposite direction of its propagation, which ultimately causes the local maximum value of attractive force at this QQ or SPP resonance [cf. Fig. 6.3(l)].

Now we shall consider the behavior of optical force for Fano resonance when the reversal of lateral binding force takes place [cf. Fig. 6.3(l)]. If we compare the extinction efficiency of the four cases [cf. the second column of Fig. 6.3], the magnitude is almost 2.5 times stronger for the plasmonic (silver) substrate case. In addition, if we consider the strength of induced current at resonant frequencies (i.e. Fano resonance and previously discussed DD resonance mode), the surface current for the case of silver slab is quite stronger in comparison with all other cases: no substrate, glass substrate and silicon substrate case. Now if we give a closer look to the individual cube (i.e. cube-1): it is clearly observable that the bulk force part turns into negative force only near the Fano resonance regime for the case of plasmonic substrate. However, this bulk force (which is mainly connected with the scattering

force of plasmonic objects [114, 143]) is never dominant, when the substrate is glass or silicon. The total force of cube-1 for glass and silicon substrate case is always dominated by surface force. In contrast, the scenario is fully reversed for the case of silver substrate especially during the Fano resonance. In Fig. 6.5(i) it can be observed that the reversal of optical binding force occurs due to the reversal of bulk Lorentz force. Our ultimate conclusions are: (i) the reversal starts to occur from strong multiple scattering. (ii) Though it is commonly believed that internal wave-field does not contribute much for optical force on plasmonic objects (cf. the dominance of surface force in [109, 114]), during the Fano resonance the scenario is quite different.

6.5 Effect of height, size and background material on binding force

In previous section we have discussed the effect of different substrates on lateral binding force. In this section we shall focus our discussion on lateral binding force due to the change of dimer heights from the plasmonic substrate.

In Fig. 6.6(a)-(f), it is shown that when the cubic silver dimers are far away (45 nm away from the spacer) from the plasmonic substrate, Fano resonance does not occur. For these dimers, placed 45 nm away from the spacer, the dominant resonance in Fig. 6.6(a) is the DD resonance [but for the isolated dimer case in Fig. 6.3(a) the dominant resonance is not DD mode [199]]. It should be noted that the binding force at DD resonance mode behaves quite differently for these two cases: (i) Far from the substrate- strong mutual attractive force occurs and (ii) very close [i.e. 5nm away from spacer as shown in Fig. 6.3 (j)-(l)] to the substrate- strong mutual repulsive force occurs [the reversal mainly occurs before this dipole resonance at the strong Fano resonance, when stronger coupling with the plasmonic substrate starts to occur].

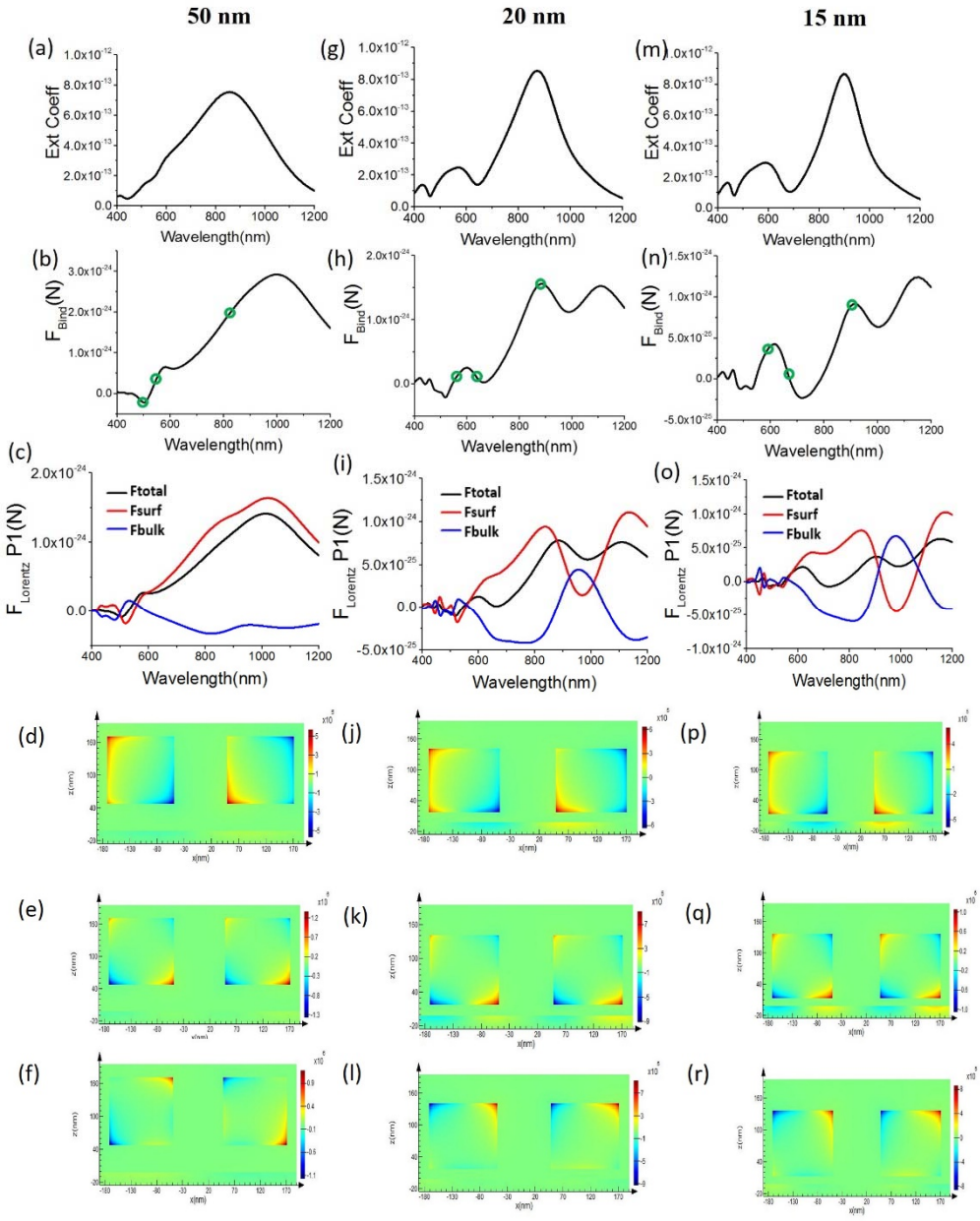

Fig. 6.6: Two silver cubes (L=120 nm) are placed at different heights from the silver substrates (three different columns represent the position of the cubes: 50, 20 and 15 nm away from the substrate) and their inter-particle gap, *d*, is fixed 100 nm. The spacer height is 5nm. *x*-polarized plane wave is propagating towards –*z*-direction. For different heights from the substrate: First row: extinction co-efficient; second row: binding force; '°' represents the chosen wavelengths for which the steady state current distributions are plotted later. Third row: Lorentz force components along with the total force only on cube-1 (left cube, denoted as P1); fourth, fifth and sixth row: steady state current (J_y) from front view [in xz plane; setting the window very close to the cube surfaces from front view] for two silver cubes along with the substrate in three different wavelengths (marked as '°'). For first column [50 nm height, (d)-(f)] wavelengths are chosen as: 855, 553 and 503 nm respectively. For second column [20 nm height, (j)-(l)] resonance wavelengths are: 872 (DD), 631 (Fano) and 567 nm (QQ) respectively. For third column [15 nm height, (p)-(r)] resonance wavelengths are: 890 (DD), 674 (Fano) and 590 nm (QQ) respectively.

Now, in Fig. 6.6(g)-(l), when the cubic silver dimers are closely placed (15 nm away from the spacer) from the plasmonic (silver) substrate, Fano resonance does not die out. However, such Fano resonance is not strong enough and optical binding force does not reverse. This configuration can better be comparable with the case: plasmonic homodimers (cube) over the previously discussed Si substrate. The current, electric fields and magnetic fields of such set-ups are also similar (but not identical) to that previously discussed case of dimers over Si substrate. Now, in Fig. 6.6 (m)- (r), when the cubic silver dimers are closely placed (10 nm away from the spacer) from the plasmonic substrate, strong Fano resonance just starts to occur along with strong coupling with the substrate. During this resonance, the bulk part of Lorentz force reverses and just starts to dominate the total force on each dimer [cf. Fig. 6.6(o)]. Ultimately these lead to the reversal of optical binding force as shown in Fig. 6.6 (n). The mechanism of binding force for this case is very similar to the case [5 nm away from the substrate] discussed previously in details in previous section.

The waveguide description [213] of resonance mode [206, 208] also aids in understanding the observed dependence of the resonance shift on both the size of the nano cube [as can be seen from the comparison of Fig. 6.1(b), (c) and Fig. 6.2 (b), (c)] and the gap between the silver cube and the silver substrate [as shown in Figs. 6.6]. (1) For larger cube, the length of the cavity increases and will therefore support a resonance at a longer wavelength. As a result, the resonance redshifts. (2) Similarly, when the gap between the substrate and the cube gets smaller, the effective refractive index of the cavity mode increases. This effectively lengthens the cavity [206] and results in a resonance condition at a longer wavelength. For case (1) and (2), when the second cube is placed closely to the first cube, the induced stable Fano resonance also

red shifts following the rapid red shift of DD resonance and hence the binding force reversal wavelength also red shifts following the Fano dip in figures of Fig. 6.6 and Fig. 6.1 (b), (c); Fig. 6.2 (b), (c).

Throughout this work, the background material has been considered water. The simplest way to blue shift all the resonances along with the wavelength of binding force reversal is to decrease the background refractive index. Last but not least, with the increase of the inter-particle gap, the binding force magnitude decreases slowly but still this overall set-up provides a very relaxed mechanism to verify the reversal of optical binding force.

6.6 Conclusions

In summary, we have investigated a very simple possible configuration to demonstrate the reversal of lateral optical binding force with plasmonic homodimers based on strong Fano resonance. Among all the substrates (i.e. glass, Si, Ag, Au etc.), the closely placed plasmonic particles should remain very close only to the plasmonic substrate so that the bulk part of the total Lorentz force dominates the total lateral force of each cube during the substrate mediated Fano resonance. The surface current (along with the strong electric and magnetic coupling) increases significantly only for the close presence of the plasmonic substrate, which bears significant influence on the reversal of binding force of the dimers. Though we have shown only the homodimer cases, our proposed idea should also work for the cube heterodimers providing more flexibility on particle size. We believe that our proposals can be verified experimentally due to the simplicity of the proposed set-ups; and thus the attractive

and repulsive forces between two plasmonic objects can be robustly adjusted based on the idea proposed in this chapter.

Chapter 7

Consistency of Minkowski's Theory: Some Final Proposals

7.1 Introduction and Summary of Chapter 7

In chapter 5, we have suggested the modification of Lorentz force for the embedded chiral and achiral objects. Later, in chapter 6, we have explained the dynamics of binding force reversal of plasmonic cubes based on the idea of modified Lorentz force discussed in chapter 5. In contrast, based on the proposed 'consistency conditions' of chapter 5, in this chapter we have proposed a new idea/hypothesis named as 'existence domain'. '*Existence domain*' is the region either outside a scattering body taking only its exterior fields into account, or in its interior considering only the inside fields. Though almost all the time averaged distinct STs and volumetric force laws are restricted to the idea of 'existence domain', we demonstrate that the time averaged stress tensor and volumetric force law of Minkowski are free from such restrictions. In addition, we have discussed in details the differences between time averaged and instantaneous force laws for different formulations in this chapter. Notably only Minkowski's theory remains valid for all circumstances without any modification. As a result, considering 'all' the proposals in this chapter, it appears that Minkowski formulations are most probably more accurate description of physical optical force along with photon momentum.

7.2 Time averaged Force: Proposal of 'existence domain' hypothesis

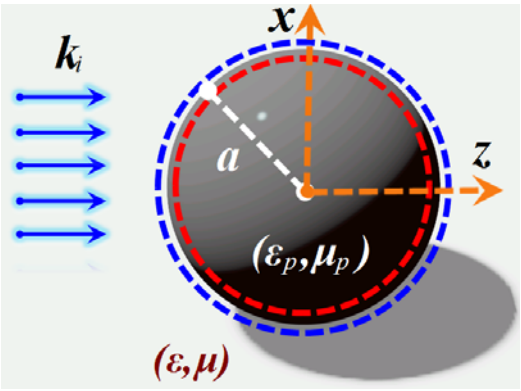

Fig. 7.1 Optical momentum transfers from an incident plane wave of propagating vector k_i to a spherical particle with permittivity ε_p and permeability μ_p. The total force calculated using the Stress Tensor (ST) is: F_{out} when the time-averaged ST is evaluated from fields outside the particle, through a surface of radius $r = a^+ = 1.001a$ (blue lines), and F_{in} when the time-averaged ST is evaluated from the inside of the particle through a surface of radius $r = a^- = 0.999a$ (red lines).

According to chapter 5, though the proposed modified Einstein-Laub (MEL) ST (and the bulk volume force of MEL or modified version [26] of the well-known Chu force [214]) leads to a consistent time-averaged 'bulk' force for embedded generic objects, it is applicable at $r=a^-$ employing *only the interior fields* of an embedded object [cf. Fig. 7.1]. On the other hand, Minkowski (and Abraham) ST leads to consistent time-averaged 'total' force when they are applied at $r=a^+$ [cf. Fig. 7.1] employing *only the exterior fields* of an embedded object (and zero force when applied at $r=a^-$ on employing interior fields). We have also explained the reason behind that in chapter 5, and suggested the distinct physical meanings of the left and right-hand sides of the equation: $\langle \boldsymbol{F}_{\text{Mink}}^{\text{Total}} \rangle(\text{out}) = \langle \boldsymbol{F}_{\text{MEL}}^{\text{Bulk}} \rangle(\text{in}) + \langle \boldsymbol{F}_{\text{MEL}}^{\text{Surface}} \rangle$ (also alternatively applicable for Chu formulations).

Ultimately above proposal leads to a very surprising but significant conclusion for the well-known distinct time averaged stress tensors. We henceforth characterize the idea of '*existence domain*' for the time averaged optical stress tensors (and volumetric forces) as the region either outside a scattering body taking only its exterior fields into account, or in its interior considering only the inside fields. The fundamental proposals [named as two consistency conditions] in favour of the idea of '*existence domain*' proposed in chapter 5.

In chapter 5, we have considered a special condition for non-absorbing objects:

$\left\langle \boldsymbol{F}^{\text{Bulk}} \right\rangle(\text{in}) = \int \left\langle \boldsymbol{f}^{\text{Bulk}} \right\rangle(\text{in}) \cdot d\boldsymbol{v} = \int \left\langle \overline{\overline{\boldsymbol{T}}}(\text{in}) \right\rangle \cdot d\boldsymbol{s} \neq 0$. But if we consider a more generic case where the existence of time averaged bulk force is not any big deal for a non-absorbing object, it is possible to arrive an optical force law (Minkowski force) which is not restricted to the idea of 'existence domain'.

To clarify the aforementioned proposal by a very simple example (more complex cases already discussed in chapter 5), let us consider a magnetodielectric slab embedded in another magnetodielectric. The surface force part of well-known Chu and Einstein-Laub force vanishes for the slab case. But the bulk part plays the main role to decide the time averaged total force [215]. The lossless embedded slab illuminated at normal incidence by a linearly polarized plane wave propagating along the z-direction with electric vector: $E_x = E_0 e^{i(kz-\omega t)}$. The 'outside force' can be calculated considering the transfer of $\boldsymbol{p}_{\text{Mink}}(\text{out}) = \hbar \boldsymbol{k}$ from the background to the embedded slab (cf. Eq (60) given in [215]). At the same time, the interior force on the embedded slab is calculated by internal bulk force of modified Einstein-Laub or modified Chu. All of them are in full agreement with each other:

$$\left[N_i\hbar k_i + N_r\hbar k_r - N_t\hbar k_t\right]^{\text{Transfer Process}}_{\text{From Background}} = \frac{1}{2}\frac{E_0^2}{\mu_s\left(\frac{\mu_b\varepsilon_S}{\mu_S\varepsilon_b}-1\right)}\left[\left(\varepsilon_s-\varepsilon_b\right)\mu_s-\left(\mu_s-\mu_b\right)\varepsilon_s\right]\left\{1+\left|R\right|^2-\left|T\right|^2\right\} \tag{7.1}$$

Here $\boldsymbol{R}$ and $\boldsymbol{T}$ denote the reflection and transmission coefficients of the slab, while *a* and *b* are constants determined from the boundary conditions. The quantity $N = \langle S \rangle / \hbar\omega$ denotes the photon flux and $\langle S \rangle$ is the time-averaged Poynting vector. '*i*', '*r*' and '*t*' mean incident, reflected and transmitted, respectively. Now, the important conclusions are:

(1) Thus the left side of Eq (7.1) describes the transfer of momentum to the embedded slab employing the incident, reflected, and transmitted $\boldsymbol{p}_{\text{Mink}}(\text{out}) = \hbar\boldsymbol{k}$, respectively. The left part of Eq (7.1) can be derived from the Minkowski's formulation as shown in [216]. In chapter 5, we have already discussed in details that except the external Minkowski ST, other formulations do not support the accurate calculation of time averaged total 'external force'.

(2) In contrast, the right side of Eq (7.1) represents the total internal MEL or Modified Chu force felt by the slab, obtained by employing only its internal field. Without modifying the well-known EL or Chu force, it is not possible to obtain the equivalent results [more details discussed in chapter 5]. Though, the time averaged internal Minkowski ST leads to zero bulk force, the surface force part (obtained by Helmholtz force) also leads to the total force value equal to the one shown in Eq (7.1) [for details on Helmholtz force based calculations cf. the examples given in Ref. [215]].

So, above simple example clearly points the fact that: in time averaged situation, the Minkowski force remains valid at least at (i) the surface of the object [i.e. Helmholtz force] and (ii) outside the object [i.e. the background medium]. (iii) For the last part:

the bulk force part of Minkowski's force, one needs to consider absorbing slab. Such an example has already been shown in the last section of Ref. [215].

All the above mentioned proposals can be verified in an implicit way: based on the 'validity condition' [denoted as C(I) in chapter 5] proposed in chapter 5. As a result, now, we shall show that in instantaneous and in time average case, Minkowski force remains valid everywhere in space. The detail calculations are given below. Even from the physical point of view, time averaged Minkowski ST can be applied both inside and outside the object [44] and hence free from the restriction of 'existence domain'. In fact, the calculations given below also suggest this same fact.

The surface force of Minkowski / Helmholtz volumetric formulation:

$$\boldsymbol{f}^{\text{Surface}}_{\text{Helmholtz}} = \left\{ -\frac{1}{2}\boldsymbol{E}^2 \Delta\varepsilon - \frac{1}{2}\boldsymbol{H}^2 \Delta\mu \right\}_{r=a} \tag{7.2}$$

Now, from the non-diagonal (ND) components of Minkowski ST we get:

$$\begin{aligned}[\bar{\bar{\boldsymbol{T}}}^{\text{MIX}}_{\text{Mink}}(\text{out}) - \bar{\bar{\boldsymbol{T}}}^{\text{MIX}}_{\text{Mink}}(\text{in})]\cdot\hat{\boldsymbol{n}}\ _{r=a} = &\left[\begin{array}{l}[\epsilon_b \boldsymbol{E}^{\perp}_{\text{out}}\cdot\boldsymbol{E}^{\perp}_{\text{out}} - \epsilon_s \boldsymbol{E}^{\perp}_{\text{in}}\cdot\boldsymbol{E}^{\perp}_{\text{in}}]\hat{\boldsymbol{n}} + [\epsilon_b \boldsymbol{E}^{\parallel}_{\text{m out}}\cdot\boldsymbol{E}^{\perp}_{\text{out}} - \epsilon_s \boldsymbol{E}^{\parallel}_{\text{m in}}\cdot\boldsymbol{E}^{\perp}_{\text{in}}]\hat{\boldsymbol{m}} \\ \quad + [\epsilon_b \boldsymbol{E}^{\parallel}_{\text{q out}}\cdot\boldsymbol{E}^{\perp}_{\text{out}} - \epsilon_s \boldsymbol{E}^{\parallel}_{\text{q in}}\cdot\boldsymbol{E}^{\perp}_{\text{in}}]\hat{\boldsymbol{q}}\end{array}\right]_{r=a} \\ + &\left[\begin{array}{l}[\mu_b \boldsymbol{H}^{\perp}_{\text{out}}\cdot\boldsymbol{H}^{\perp}_{\text{out}} - \mu_s \boldsymbol{H}^{\perp}_{\text{in}}\cdot\boldsymbol{H}^{\perp}_{\text{in}}]\hat{\boldsymbol{n}} + [\mu_b \boldsymbol{H}^{\parallel}_{\text{m out}}\cdot\boldsymbol{H}^{\perp}_{\text{out}} - \mu_s \boldsymbol{H}^{\parallel}_{\text{m in}}\cdot\boldsymbol{H}^{\perp}_{\text{in}}]\hat{\boldsymbol{m}} \\ \quad + [\mu_b \boldsymbol{H}^{\parallel}_{\text{q out}}\cdot\boldsymbol{H}^{\perp}_{\text{out}} - \mu_s \boldsymbol{H}^{\parallel}_{\text{q in}}\cdot\boldsymbol{H}^{\perp}_{\text{in}}]\hat{\boldsymbol{q}}\end{array}\right]_{r=a}\end{aligned} \tag{7.3}$$

'MIX' represents the mixed diagonal and non-diagonal elements of the stress tensor, which are not connected with the identity tensor, $\bar{\bar{\boldsymbol{I}}}$. ε_{b} and μ_{b} are fixed background permittivity and permeability, and ε_s and μ_s are fixed permittivity and permeability of the scatterer. 'out' represents the total fields (incident plus scattered field) outside a scatterer. 'in' represents the fields inside a scatterer. Electric field at the object and background boundary is defined as: $\boldsymbol{E} = \boldsymbol{E}^{\perp}_{n}\hat{\boldsymbol{n}} + \boldsymbol{E}^{\parallel}_{\text{m}}\hat{\boldsymbol{m}} + \boldsymbol{E}^{\parallel}_{\text{q}}\hat{\boldsymbol{q}}$ where $\hat{\boldsymbol{n}}$, $\hat{\boldsymbol{m}}$ and $\hat{\boldsymbol{q}}$ are mutually orthogonal arbitrary unit

vectors, which are applicable for different co-ordinate systems such as Cartesian or Spherical or Cylindrical. $\hat{\boldsymbol{n}}$ is the local unit normal of the object surface, which is considered aligned towards the direction of wave vector direction (for simplicity). $\boldsymbol{E}^{\parallel}$ and $\boldsymbol{E}^{\perp}$ are the parallel and perpendicular components of electric fields at the background and object boundary. In a very similar way, the magnetic field has also been defined.

Now, by employing the electromagnetic boundary conditions in above Eq (7.4):

$$[\bar{\bar{\boldsymbol{T}}}^{\mathrm{MIX}}_{\mathrm{Mink}}(\mathrm{out})-\bar{\bar{\boldsymbol{T}}}^{\mathrm{MIX}}_{\mathrm{Mink}}(\mathrm{in})]\cdot\hat{\boldsymbol{n}}_{r=a}=[\epsilon_b\boldsymbol{E}^{\perp}_{\mathrm{out}}\cdot\boldsymbol{E}^{\perp}_{\mathrm{out}}-\epsilon_s\boldsymbol{E}^{\perp}_{\mathrm{in}}\cdot\boldsymbol{E}^{\perp}_{\mathrm{in}}]\hat{\boldsymbol{n}}+[\mu_b\boldsymbol{H}^{\perp}_{\mathrm{out}}\cdot\boldsymbol{H}^{\perp}_{\mathrm{out}}-\mu_s\boldsymbol{H}^{\perp}_{\mathrm{in}}\cdot\boldsymbol{H}^{\perp}_{\mathrm{in}}]\hat{\boldsymbol{n}} \tag{7.4}$$

In contrast, from the pure diagonal (D) components we get [after employing the electromagnetic boundary conditions]:

$$\begin{aligned}[\bar{\bar{\boldsymbol{T}}}^{\mathrm{D}}_{\mathrm{Mink}}(\mathrm{out})-\bar{\bar{\boldsymbol{T}}}^{\mathrm{D}}_{\mathrm{Mink}}(\mathrm{in})]\cdot\hat{\boldsymbol{n}}_{r=a}=&\\ -\frac{1}{2}\Big[&\left(\epsilon_b\boldsymbol{E}^{\perp}_{\mathrm{out}}\cdot\boldsymbol{E}^{\perp}_{\mathrm{out}}-\epsilon_s\boldsymbol{E}^{\perp}_{\mathrm{in}}\cdot\boldsymbol{E}^{\perp}_{\mathrm{in}}\right)\hat{\boldsymbol{n}}+\left(\epsilon_b\boldsymbol{E}^{\parallel}_{\mathrm{m\,out}}\cdot\boldsymbol{E}^{\parallel}_{\mathrm{m\,out}}-\epsilon_s\boldsymbol{E}^{\parallel}_{\mathrm{m\,in}}\cdot\boldsymbol{E}^{\parallel}_{\mathrm{m\,in}}\right)]\hat{\boldsymbol{m}}\\ &+\left(\epsilon_b\boldsymbol{E}^{\parallel}_{\mathrm{q\,out}}\cdot\boldsymbol{E}^{\parallel}_{\mathrm{q\,out}}-\epsilon_s\boldsymbol{E}^{\parallel}_{\mathrm{q\,in}}\cdot\boldsymbol{E}^{\parallel}_{\mathrm{q\,in}}\right)\hat{\boldsymbol{q}}\Big]_{r=a}\\ -\frac{1}{2}\Big[&\left(\mu_b\boldsymbol{H}^{\perp}_{\mathrm{out}}\cdot\boldsymbol{H}^{\perp}_{\mathrm{out}}-\mu_s\boldsymbol{H}^{\perp}_{\mathrm{in}}\cdot\boldsymbol{H}^{\perp}_{\mathrm{in}}\right)\hat{\boldsymbol{n}}+\left(\mu_b\boldsymbol{H}^{\parallel}_{\mathrm{m\,out}}\cdot\boldsymbol{H}^{\parallel}_{\mathrm{m\,out}}-\mu_s\boldsymbol{H}^{\parallel}_{\mathrm{m\,in}}\cdot\boldsymbol{H}^{\parallel}_{\mathrm{m\,in}}\right)\hat{\boldsymbol{m}}\\ &+\left(\mu_b\boldsymbol{H}^{\parallel}_{\mathrm{q\,out}}\cdot\boldsymbol{H}^{\parallel}_{\mathrm{q\,out}}-\mu_s\boldsymbol{H}^{\parallel}_{\mathrm{q\,in}}\cdot\boldsymbol{H}^{\parallel}_{\mathrm{q\,in}}\right)\hat{\boldsymbol{q}}\Big]_{r=a}\end{aligned} \tag{7.5}$$

Now, by adding Eq (7.4) and (7.5) and after doing some calculations, we get exactly Eq (7.2) at the object boundary.

Our final conclusions on time averaged forces are shown at a glance in Fig. 7.2. To get a clear view of the operations physically involved with the different time averaged STs and volumetric force laws, we list them in Table-7.1.

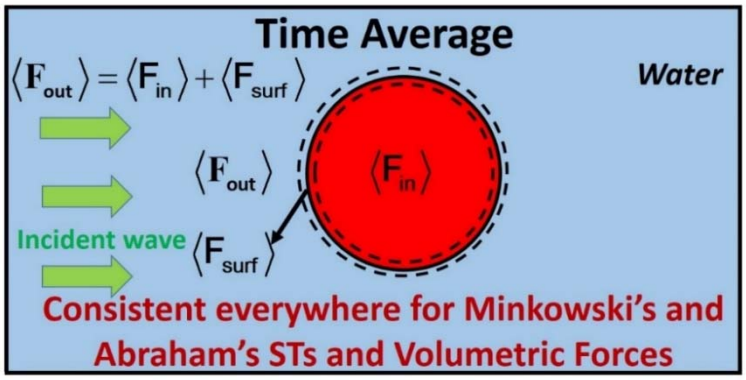

Fig. 7.2: The consistency of Minkowski's and Abraham's theory everywhere in space for time averaged cases. Our discussions in section 7.2 and later in Table-7.1 suggest that: for time averaged scenario, almost all stress tensors and volumetric force laws are restricted to the idea of 'existence domain' except Minkowski and Abraham STs and their corresponding volumetric force laws.

Table- 7.1: Time averaged macroscopic stress tensors and volume forces: proposal of 'existence domain' (not applicable for Minkowski and Abraham formulations)

	Time averaged force	Comment
Minkowski	$\langle \boldsymbol{F}_{\text{Mink}}(\text{out}) \rangle = \frac{1}{2}\text{Re} \int_{at\ r=a^+} \langle \bar{\bar{\boldsymbol{T}}}_{\text{Mink}}(\text{out}) \rangle . \mathbf{ds}$ $\langle \bar{\bar{\boldsymbol{T}}}_{\text{Mink}}(\text{out}) \rangle = \boldsymbol{D}_{\text{out}} \boldsymbol{E}^*_{\text{out}} + \boldsymbol{B}_{\text{out}} \boldsymbol{H}^*_{\text{out}} - \frac{1}{2}\left(\boldsymbol{B}_{\text{out}} \cdot \boldsymbol{H}^*_{\text{out}} + \boldsymbol{D}_{\text{out}} \cdot \boldsymbol{E}^*_{\text{out}} \right) \bar{\bar{\boldsymbol{I}}}$ $\langle \boldsymbol{F}_{\text{Mink}}(\text{in}) \rangle = \frac{1}{2}\text{Re} \int_{at\ r=a^-} \langle \bar{\bar{\boldsymbol{T}}}_{\text{Mink}}(\text{in}) \rangle . \mathbf{ds}$ $\langle \bar{\bar{\boldsymbol{T}}}_{\text{Mink}}(\text{in}) \rangle = \boldsymbol{D}_{\text{in}} \boldsymbol{E}^*_{\text{in}} + \boldsymbol{B}_{\text{in}} \boldsymbol{H}^*_{\text{in}} - \frac{1}{2}\left(\boldsymbol{B}_{\text{in}} \cdot \boldsymbol{H}^*_{\text{in}} + \boldsymbol{D}_{\text{in}} \cdot \boldsymbol{E}^*_{\text{in}} \right) \bar{\bar{\boldsymbol{I}}}$	The time averaged external Minkowski ST characterizes the transfer of momentum transported by the field from any background medium to an embedded scatterer. The time averaged external Minkowski ST yields the correct (so far for almost all real experiments) total 'outside force' only from fields outside the embedded object with the integration at $r=a^+$. The correct total 'outside force' can also be obtained directly from calculations employing $\boldsymbol{P}_{\text{Mink}}$ (i.e. by ray tracing method). Though the time averaged internal Minkowski ST yields a zero mechanical force ('felt force') at the interior of a lossless object, it leads to the correct internal force (bulk part of Helmholtz force) felt by the free charges for an absorbing objects. Exactly at the boundary of a generic object, the difference between the external and internal Minkowski stress tensor leads to the Helmholtz surface force. Hence, time averaged Minkowski ST (and Helmholtz

		force) should be considered valid as both external and internal ST (and force), which is fully opposite case of time averaged EL, Chu or Ampere/Nelson STs and force laws.
Abraham	$\langle \boldsymbol{F}_{\text{Abr}}(\text{out})\rangle = \frac{1}{2}\text{Re}\int_{at\ r=a^+} \langle \overline{\overline{\boldsymbol{T}}}_{\text{Abr}}(\text{out})\rangle.\mathbf{ds}$ $\langle \overline{\overline{\boldsymbol{T}}}_{\text{Abr}}(\text{out})\rangle = \frac{1}{2}[\boldsymbol{D}_{\text{out}}\boldsymbol{E}^*_{\text{out}} + \boldsymbol{E}_{\text{out}}\boldsymbol{D}^*_{\text{out}} + \boldsymbol{B}_{\text{out}}\boldsymbol{H}^*_{\text{out}} + \boldsymbol{H}_{\text{out}}\boldsymbol{B}^*_{\text{out}} - (\boldsymbol{B}_{\text{out}}\cdot\boldsymbol{H}^*_{\text{out}} + \boldsymbol{D}_{\text{out}}\cdot\boldsymbol{E}^*_{\text{out}})\overline{\overline{\boldsymbol{I}}}]$ $\langle \boldsymbol{F}_{\text{Abr}}(\text{in})\rangle = \frac{1}{2}\text{Re}\int_{at\ r=a^-} \langle \overline{\overline{\boldsymbol{T}}}_{\text{Abr}}(\text{in})\rangle.\mathbf{ds}$ $\langle \overline{\overline{\boldsymbol{T}}}_{\text{Abr}}(\text{in})\rangle = \frac{1}{2}[\boldsymbol{D}_{\text{in}}\boldsymbol{E}^*_{\text{in}} + \boldsymbol{E}_{\text{in}}\boldsymbol{D}^*_{\text{in}} + \boldsymbol{B}_{\text{in}}\boldsymbol{H}^*_{\text{in}} + \boldsymbol{H}_{\text{in}}\boldsymbol{B}^*_{\text{in}} - (\boldsymbol{B}_{\text{in}}\cdot\boldsymbol{H}^*_{\text{in}} + \boldsymbol{D}_{\text{in}}\cdot\boldsymbol{E}^*_{\text{in}})\overline{\overline{\boldsymbol{I}}}]$	The time averaged Abraham ST yields the same force as Minkowski ST. But the correct total 'outside force' cannot be directly obtained from the $\boldsymbol{P}_{\text{Abr}}$ (i.e. by ray tracing method). The difference between Minkowski's force and Abraham's force arises only in instantaneous force. However, Abraham formulations are not relativistically invariant.
Einstein-Laub	$\langle \boldsymbol{F}_{\text{EL}}(\text{in})\rangle = \frac{1}{2}\text{Re}\int_{at\ r=a^-} \langle \overline{\overline{\boldsymbol{T}}}_{\text{EL}}\rangle.\mathbf{ds}$ $\langle \overline{\overline{\boldsymbol{T}}}_{\text{EL}}\rangle = \boldsymbol{D}_{\text{in}}\boldsymbol{E}^*_{\text{in}} + \boldsymbol{B}_{\text{in}}\boldsymbol{H}^*_{\text{in}} - \frac{1}{2}(\mu_o\boldsymbol{H}_{\text{in}}\cdot\boldsymbol{H}^*_{\text{in}} + \varepsilon_0\boldsymbol{E}_{\text{in}}\cdot\boldsymbol{E}^*_{\text{in}})\overline{\overline{\boldsymbol{I}}}$	The time averaged EL ST yields the 'bulk force' felt by the induced dipoles or 'inside force' from fields just inside the object embedded in air or vacuum. This ST does not characterize the flow of momentum transported by the field from the background medium to an embedded scatterer. Hence it is not applicable to get the 'outside force'. For an object embedded in air or vacuum, the difference of external vacuum ST and the internal EL ST at the object boundary leads to a surface force $\boldsymbol{f}^{\text{surface}}$ which exactly matches with the surface force fully independently calculated by the EL volumetric force [cf. Appendix A and C]. But when an object is embedded in a material medium, the difference of the external EL ST and internal EL ST does not lead to the surface force of EL. As a result, MEL ST should be applied to yield the internal time averaged total force and to satisfy the two consistency conditions [C(I) and C(II)] presented in chapter 5.
Chu	$\langle \boldsymbol{F}_{\text{Chu}}(\text{in})\rangle = \frac{1}{2}\text{Re}\int_{at\ r=a^-} \langle \overline{\overline{\boldsymbol{T}}}_{\text{Chu}}(\text{in})\rangle.\mathbf{ds}$ $\langle \overline{\overline{\boldsymbol{T}}}_{\text{Chu}}(\text{in})\rangle = \varepsilon_0\boldsymbol{E}_{\text{in}}\boldsymbol{E}^*_{\text{in}} + \mu_o\boldsymbol{H}_{\text{in}}\boldsymbol{H}^*_{\text{in}} - \frac{1}{2}(\mu_o\boldsymbol{H}_{\text{in}}\cdot\boldsymbol{H}^*_{\text{in}} + \varepsilon_0\boldsymbol{E}_{\text{in}}\cdot\boldsymbol{E}^*_{\text{in}})\overline{\overline{\boldsymbol{I}}}$	Time averaged Chu ST yields the 'bulk force' felt by the induced charges and currents or 'inside force' from fields just inside the object embedded in air or vacuum. This ST does not characterize the flow of momentum transported by the field from the background medium to an embedded scatterer. Hence it is not applicable to get the 'outside force'. For an object embedded in any material medium, the difference of external vacuum ST and the internal Chu ST at the object boundary leads to a $\boldsymbol{f}^{\text{surface}}$ which exactly matches with the surface force fully independently calculated by the Chu volume

		force [cf. next section, section 7.3, of this conclusion and Appendix A]. But both the internal and external Chu ST do not lead to the time averaged consistent force for an embedded object. Only by modifying the internal Chu formulations along with its surface force, it is possible to yield the time averaged total force on an embedded object.
Ampere/ Nelson	$\langle \boldsymbol{F}(\text{in}) \rangle = \frac{1}{2}\text{Re} \int\limits_{at\ r=a^-} \langle \overline{\overline{\boldsymbol{T}}}_{\text{Amp}}(\text{in}) \rangle . \mathbf{ds}$ $\langle \overline{\overline{\boldsymbol{T}}}_{\text{Amp}}(\text{in}) \rangle = \varepsilon_0 \boldsymbol{E}_{\text{in}} \boldsymbol{E}_{\text{in}}^* + \mu_0^{-1} \boldsymbol{B}_{\text{in}} \boldsymbol{B}_{\text{in}}^* - \frac{1}{2}\left(\mu_0^{-1} \boldsymbol{B}_{\text{in}}^2 + \varepsilon_0 \boldsymbol{E}_{\text{in}}^2\right) \overline{\overline{\boldsymbol{I}}}$	The Nelson ST and force law behave exactly same as the Chu formulation for a dielectric object placed in air. For magneto-dielectric objects, it behaves differently. This ST does not characterize the flow of momentum transported by the field from the background medium to an embedded scatterer. Hence it is not applicable to get the 'outside force' very similar to EL and Chu ST.
Modified Einstein-Laub	$\langle \boldsymbol{F}_{\text{MEL}}(\text{in}) \rangle = \frac{1}{2}\text{Re} \int\limits_{at\ r=a^-} \langle \overline{\overline{\boldsymbol{T}}}_{\text{MEL}}(\text{in}) \rangle . \mathbf{ds}$ $\langle \overline{\overline{\boldsymbol{T}}}_{\text{MEL}}(\text{in}) \rangle = \boldsymbol{D}_{\text{in}} \boldsymbol{E}_{\text{in}}^* + \boldsymbol{B}_{\text{in}} \boldsymbol{H}_{\text{in}}^* - \frac{1}{2}\left(\mu_b \boldsymbol{H}_{\text{in}} \cdot \boldsymbol{H}_{\text{in}}^* + \varepsilon_b \boldsymbol{E}_{\text{in}} \cdot \boldsymbol{E}_{\text{in}}^*\right) \overline{\overline{\boldsymbol{I}}}$	MEL ST is similar to time averaged EL ST but when the background is material medium instead of air. For Air background, the MEL ST turns into EL ST. The time averaged MEL ST yields the 'bulk force' felt by the induced dipoles or 'inside force' from fields just inside the object embedded in material medium. This ST is also not applicable to get the 'outside force'. For an object embedded in material medium, the difference of external Minkowski ST and the internal MEL ST at the boundary of that embedded object leads to a version of $\boldsymbol{f}^{\text{Surface}}$ which exactly matches with the surface force fully independently calculated by the MEL volumetric force [cf. Appendix C]. Also note that: similar arguments are applicable for internal modified version of Chu ST for objects embedded in material medium [cf. our discussion in chapter 5].

7.3 Instantaneous and Time averaged Optical Force:

Accuracy of Minkowski's theory

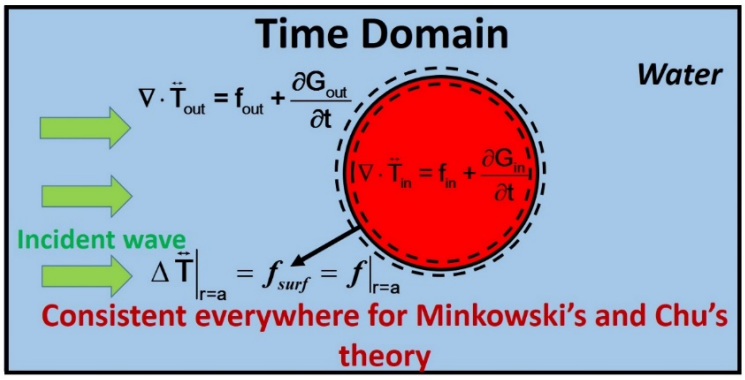

Fig. 7.3: Consistency of Minkowski's and Chu's theory for instantaneous and Time averaged force. Our discussions in section 7.3 and later in Table-7.2 suggest that: for instantaneous scenario, the consistency of only Minkowski's and Chu's theory remain everywhere in space based on: (i) consistent surface force calculation [described as 'validity condition' C(I) in chapter 5] and (ii) Relativistic invariance.

In previous section we have discussed that except Minkowski's and Abraham's stress tensors and volumetric force laws, all other force formulations are restricted with the idea of 'existence domain' for the case of time averaged force calculation. In addition, to yield the time averaged total force on an embedded object, we require to modify the Einstein-Laub, Chu and Ampere formulations. However, though the time averaged form of the Einstein-Laub and Chu formulations require modifications inside any embedded object, for the instantaneous case, well-known form of Chu force remains consistent everywhere (i.e. inside the embedded object, at the surface of the object and also at the background) among these two forces.

When we consider an object embedded in a material medium, the surface force of Chu can be determined from the well-known volumetric force of Chu by appropriate boundary conditions [182]:

$$\boldsymbol{f}_{\text{Chu}}^{\text{Surface}} = \left\{\epsilon_0 (\boldsymbol{E}_{\text{out}} - \boldsymbol{E}_{\text{in}}) \cdot \hat{\boldsymbol{n}}\right\} \left(\frac{\boldsymbol{E}_{\text{out}} + \boldsymbol{E}_{\text{in}}}{2} \right)_{r=a} + \left\{\mu_0 (\boldsymbol{H}_{\text{out}} - \boldsymbol{H}_{\text{in}}) \cdot \hat{\boldsymbol{n}}\right\} \left(\frac{\boldsymbol{H}_{\text{out}} + \boldsymbol{H}_{\text{in}}}{2} \right)_{r=a} \tag{7.6}$$

Now, from the non-diagonal (ND) components of Chu ST we get:

$$[\bar{\bar{\boldsymbol{T}}}^{\mathrm{MIX}}_{\mathrm{Vacuum}}(\mathrm{out})-\bar{\bar{\boldsymbol{T}}}^{\mathrm{MIX}}_{\mathrm{Chu}}(\mathrm{in})]\cdot\hat{\boldsymbol{n}}\ _{r=a}=$$
$$\left[\begin{array}{l}[\epsilon_0\boldsymbol{E}^{\perp}_{\mathrm{out}}\cdot\boldsymbol{E}^{\perp}_{\mathrm{out}}-\epsilon_0\boldsymbol{E}^{\perp}_{\mathrm{in}}\cdot\boldsymbol{E}^{\perp}_{\mathrm{in}}]\hat{\boldsymbol{n}}+[\epsilon_0\boldsymbol{E}^{\parallel}_{\mathrm{m\,out}}\cdot\boldsymbol{E}^{\perp}_{\mathrm{out}}-\epsilon_0\boldsymbol{E}^{\parallel}_{\mathrm{m\,in}}\cdot\boldsymbol{E}^{\perp}_{\mathrm{in}}]\hat{\boldsymbol{m}}\\ \qquad\qquad+[\epsilon_0\boldsymbol{E}^{\parallel}_{\mathrm{q\,out}}\cdot\boldsymbol{E}^{\perp}_{\mathrm{out}}-\epsilon_0\boldsymbol{E}^{\parallel}_{\mathrm{q\,in}}\cdot\boldsymbol{E}^{\perp}_{\mathrm{in}}]\hat{\boldsymbol{q}}\end{array}\right]_{r=a}$$
$$+\left[\begin{array}{l}[\mu_0\boldsymbol{H}^{\perp}_{\mathrm{out}}\cdot\boldsymbol{H}^{\perp}_{\mathrm{out}}-\mu_0\boldsymbol{H}^{\perp}_{\mathrm{in}}\cdot\boldsymbol{H}^{\perp}_{\mathrm{in}}]\hat{\boldsymbol{n}}+[\mu_0\boldsymbol{H}^{\parallel}_{\mathrm{m\,out}}\cdot\boldsymbol{H}^{\perp}_{\mathrm{out}}-\mu_0\boldsymbol{H}^{\parallel}_{\mathrm{m\,in}}\cdot\boldsymbol{H}^{\perp}_{\mathrm{in}}]\hat{\boldsymbol{m}}\\ \qquad\qquad+[\mu_0\boldsymbol{H}^{\parallel}_{\mathrm{q\,out}}\cdot\boldsymbol{H}^{\perp}_{\mathrm{out}}-\mu_0\boldsymbol{H}^{\parallel}_{\mathrm{q\,in}}\cdot\boldsymbol{H}^{\perp}_{\mathrm{in}}]\hat{\boldsymbol{q}}\end{array}\right]_{r=a}$$
(7.7)

Now, by applying the electromagnetic boundary conditions, we finally arrive for non-diagonal components:

$$[\bar{\bar{\boldsymbol{T}}}^{\mathrm{MIX}}_{\mathrm{Vacuum}}(\mathrm{out})-\bar{\bar{\boldsymbol{T}}}^{\mathrm{MIX}}_{\mathrm{Chu}}(\mathrm{in})]\cdot\hat{\boldsymbol{n}}\ _{r=a}=$$
$$\left[\begin{array}{l}[\epsilon_0\boldsymbol{E}^{\perp}_{\mathrm{out}}\cdot\boldsymbol{E}^{\perp}_{\mathrm{out}}-\epsilon_0\boldsymbol{E}^{\perp}_{\mathrm{in}}\cdot\boldsymbol{E}^{\perp}_{\mathrm{in}}]\hat{\boldsymbol{n}}+\frac{\epsilon_0}{2}\left(\boldsymbol{E}^{\parallel}_{\mathrm{m\,out}}+\boldsymbol{E}^{\parallel}_{\mathrm{m\,in}}\right)[\boldsymbol{E}^{\perp}_{\mathrm{out}}-\boldsymbol{E}^{\perp}_{\mathrm{in}}]\hat{\boldsymbol{m}}\\ \qquad\qquad+\frac{\epsilon_0}{2}\left(\boldsymbol{E}^{\parallel}_{\mathrm{q\,out}}+\boldsymbol{E}^{\parallel}_{\mathrm{q\,in}}\right)[\boldsymbol{E}^{\perp}_{\mathrm{out}}-\boldsymbol{E}^{\perp}_{\mathrm{in}}]\hat{\boldsymbol{q}}\end{array}\right]_{r=a}$$
$$+\left[\begin{array}{l}[\mu_0\boldsymbol{H}^{\perp}_{\mathrm{out}}\cdot\boldsymbol{H}^{\perp}_{\mathrm{out}}-\mu_0\boldsymbol{H}^{\perp}_{\mathrm{in}}\cdot\boldsymbol{H}^{\perp}_{\mathrm{in}}]\hat{\boldsymbol{n}}+\frac{\mu_0}{2}\left(\boldsymbol{H}^{\parallel}_{\mathrm{m\,out}}+\boldsymbol{H}^{\parallel}_{\mathrm{m\,in}}\right)[\boldsymbol{H}^{\perp}_{\mathrm{out}}-\boldsymbol{H}^{\perp}_{\mathrm{in}}]\hat{\boldsymbol{m}}\\ \qquad\qquad+\frac{\mu_0}{2}\left(\boldsymbol{H}^{\parallel}_{\mathrm{q\,out}}+\boldsymbol{H}^{\parallel}_{\mathrm{q\,in}}\right)[\boldsymbol{H}^{\perp}_{\mathrm{out}}-\boldsymbol{H}^{\perp}_{\mathrm{in}}]\hat{\boldsymbol{q}}\end{array}\right]_{r=a}$$
(7.8)

Now, we can also write for diagonal components:

$$[\bar{\bar{\boldsymbol{T}}}^{\mathrm{D}}_{\mathrm{Vacuum}}(\mathrm{out})-\bar{\bar{\boldsymbol{T}}}^{\mathrm{D}}_{\mathrm{Chu}}(\mathrm{in})]\cdot\hat{\boldsymbol{n}}\ _{r=a}=-\frac{1}{2}\left\{\left[\epsilon_0\boldsymbol{E}^{\perp}_{\mathrm{out}}\cdot\boldsymbol{E}^{\perp}_{\mathrm{out}}-\epsilon_0\boldsymbol{E}^{\perp}_{\mathrm{in}}\cdot\boldsymbol{E}^{\perp}_{\mathrm{in}}\right]\hat{\boldsymbol{n}}+\left[\mu_0\boldsymbol{H}^{\perp}_{\mathrm{out}}\cdot\boldsymbol{H}^{\perp}_{\mathrm{out}}-\mu_0\boldsymbol{H}^{\perp}_{\mathrm{in}}\cdot\boldsymbol{H}^{\perp}_{\mathrm{in}}\right]\hat{\boldsymbol{n}}\right\}_{r=a}$$
(7.9)

'D' represents pure diagonal elements of the stress tensor. Now, by adding Eqs (7.8) and (7.9), after some calculations we get exactly Eq (7.6), the surface force of well-known Chu force. But this type of matching does not happen for the Einstein-Laub volumetric force considering embedded object.

It is also notable that both Chu and Minkowski stress tensor and their volumetric force laws are relativistically invariant as shown in [217, 218]. On the other hand,

Abraham's and Einstein-Laub's force laws are not relativistically invariant [217-219].

Now, our final conclusions on instantaneous forces are shown at a glance in Fig. 7.3.

In the Table-7.2, we have discussed in details the differences between time averaged forces and instantaneous force formulations.

Table -7.2: Optical force laws: difference between instantaneous forces and their corresponding time averaged forces

	Stress tensor $\overline{\overline{\boldsymbol{T}}}$ and Force density, $\boldsymbol{f}$	Electromagnetic momentum density, $\boldsymbol{G}$	Comment
Minkowski	$\overline{\overline{\boldsymbol{T}}} = \boldsymbol{DE} + \boldsymbol{BH} - \frac{1}{2}(\boldsymbol{B}\cdot\boldsymbol{H} + \boldsymbol{D}\cdot\boldsymbol{E})\overline{\overline{\boldsymbol{I}}}$ $\boldsymbol{f} = -\frac{1}{2}\boldsymbol{E}^2\Delta\varepsilon - \frac{1}{2}\boldsymbol{H}^2\Delta\mu$	$\boldsymbol{D}\times\boldsymbol{B}$	(1) Let us consider at first that a lossless glass object is embedded in water. Helmholtz/Minkowski's volumetric force distribution is applicable at each point of space. But in continuous medium (if lossless), it vanishes even in instantaneous scenario and appears only at the boundary of the object. But this does not mean Minkowski force is not applicable everywhere. For example- Now, we consider the glass object is absorbing. Then a local/bulk force part exists for Minkowski force along with the Helmholtz's surface force. This bulk force describes how much momentum is transferring 'only' to the free carries due to local bulk fields of that glass object, which can also be obtained from internal Minkowski ST at $r=a^-$. Now, the interesting point is that: the time averaged external Minkowski ST at $r=a^+$ yields the time averaged total force [Helmholtz surface force plus the bulk force on free carriers] on that embedded absorbing glass object just by employing the external fields of the scatterer (fields from water background). In addition, exactly at the object boundary, the difference of internal Minkowski ST and the external Minkowski ST leads to that surface force of Helmholtz. (2) When absorption takes place in background, a local/bulk force arises in Minkowski's force connected with the local fields in the background;

			which represents how much momentum is transferring 'only' to the free carriers of the background (but not to the embedded glass object). - Hence Minkowski force has different physical operations in different spatial regions such as inside the absorbing embedded object; at the interface of the background and embedded object; and at the absorbing water background. But still it is applicable everywhere in space without any modification and also continuous for the case of instantaneous force (also relativistically form invariant). Hence Minkowski ST/ force is consistent everywhere in space for both cases.
Abraham	$\overline{\overline{\boldsymbol{T}}} = \frac{1}{2}\begin{bmatrix} \boldsymbol{DE}+\boldsymbol{ED} \\ +\boldsymbol{BH}+\boldsymbol{HB} \\ -(\boldsymbol{B}\cdot\boldsymbol{H}+\boldsymbol{D}\cdot\boldsymbol{E})\overline{\overline{\boldsymbol{I}}} \end{bmatrix}$ $\boldsymbol{f} = -\left(\frac{1}{2}\boldsymbol{E}^2\Delta\varepsilon + \frac{1}{2}\boldsymbol{H}^2\Delta\mu\right) + \boldsymbol{f}_A;$ $\boldsymbol{f}_A = \left(n^2-1\right)\frac{\partial}{\partial t}\left(\frac{\boldsymbol{E}\times\boldsymbol{H}}{c^2}\right)$	$\frac{\boldsymbol{E}\times\boldsymbol{H}}{c^2}$	The difference between Minkowski's force and Abraham's force arises only for instantaneous force due to $\boldsymbol{f}_A$ term in Abraham's force. Though in time averaged case Abraham force law is consistent everywhere in space, it is not relativistically invariant. Hence for instantaneous force, it cannot be considered consistent.
Einstein- Laub	$\overline{\overline{\boldsymbol{T}}} = \boldsymbol{DE}+\boldsymbol{BH} - \frac{1}{2}(\mu_o \boldsymbol{H}\cdot\boldsymbol{H} + \varepsilon_0 \boldsymbol{E}\cdot\boldsymbol{E})\overline{\overline{\boldsymbol{I}}}$ $\boldsymbol{f} = (\boldsymbol{P}\cdot\nabla)\boldsymbol{E} + (\boldsymbol{M}\cdot\nabla)\boldsymbol{H} + \frac{\partial \boldsymbol{P}}{\partial t}\times\mu_o\boldsymbol{H} - \frac{\partial \boldsymbol{M}}{\partial t}\times\varepsilon_0\boldsymbol{E}$	$\frac{\boldsymbol{E}\times\boldsymbol{H}}{c^2}$	(1) If Einstein-Laub force is applied to a lossless glass object (embedded in water background) employing the local field of the object, the EL force inside the object does not represent the 'correct' magnitude of bulk force felt by the object [cf. the discussion after Eq (7.1) in section 7.2 of this conclusion]. It is the modified Einstein-Laub volumetric force [or MEL ST; cf. chapter 5] which should be applied to yield the time averaged bulk force of an embedded object. But it should be noted that the MEL version of volumetric force may not the correct form of the force distribution for instantaneous force, as it creates some important problems with Einstein-Balazs thought experiment [220]. (2) For an object embedded in air or vacuum, the difference of external vacuum ST and the internal EL ST at the object boundary leads to a $\boldsymbol{f}^{\text{surface}}$ which exactly matches with the surface force fully independently calculated by the EL volumetric force. But the difference of external and internal EL ST does not lead to the consistent $\boldsymbol{f}^{\text{surface}}$ for an object embedded in material medium. For such an object, the difference of external Minkowski ST and the internal MEL ST at the boundary of that embedded object leads to a version of $\boldsymbol{f}^{\text{surface}}$ which exactly matches with the surface force fully independently calculated by the MEL volumetric

			force [cf. Appendix A and C]. (3) On the other hand, the well-known Einstein-Laub force in the water background employing the local field of the water represents the bulk force felt by the water background itself. It does not represent how much momentum has been transferred from the water background to the embedded object. - So, based on (1)-(3), we conclude that: in time averaged scenario: the MEL force should be applied inside the embedded scatterer [cf. chapter 5]. On the other hand, the well-known time averaged EL force should be applied in the background medium to determine the force felt by the background water medium. For the case of instantaneous force: EL force is not relativistically invariant. Hence EL ST/force is not consistent everywhere in space for both cases.
Chu	$\overline{\overline{\boldsymbol{T}}} = \varepsilon_0 \boldsymbol{EE} + \mu_0 \boldsymbol{HH} - \frac{1}{2}(\mu_o \boldsymbol{H}\cdot\boldsymbol{H} + \varepsilon_0 \boldsymbol{E}\cdot\boldsymbol{E})\overline{\overline{\boldsymbol{I}}}$ $\boldsymbol{f} = -(\nabla\cdot\boldsymbol{P})\boldsymbol{E} - (\nabla\cdot\boldsymbol{M})\boldsymbol{H} + \frac{\partial \boldsymbol{P}}{\partial t}\times\mu_0\boldsymbol{H} - \frac{\partial \boldsymbol{M}}{\partial t}\times\varepsilon_0\boldsymbol{E}$	$\frac{\boldsymbol{E}\times\boldsymbol{H}}{c^2}$	The conclusions for Chu force are very similar to the Einstein-Laub force except one difference: the instantaneous force behavior. Instantaneous Chu force is more physical than the instantaneous EL force due to its nature of relativistic invariance. So, from the physical point of view, it can be suggested that the instantaneous volumetric force distribution based on the bound charges and currents of Chu formulation is more accurate than the induced dipole based EL formulation. In chapter 5 we have highlighted the importance of both the time averaged modified EL and modified Chu force laws. Though instantaneous Chu force remains consistent everywhere, in time averaged scenario it does not remain consistent everywhere. For example- though the time averaged force felt by the water background should be calculated by well-known Chu force, the time averaged force on the embedded scatterer should be calculated by its modified version (very similar behavior of time averaged scenario of EL/MEL force).
Ampere/ Nelson	$\overline{\overline{\boldsymbol{T}}} = \varepsilon_0 \boldsymbol{EE} + \mu_0^{-1} \boldsymbol{BB} - \frac{1}{2}\left(\mu_0^{-1}\boldsymbol{B}^2 + \varepsilon_0 \boldsymbol{E}^2\right)\overline{\overline{\boldsymbol{I}}}$ $\boldsymbol{f} = -(\nabla\cdot\boldsymbol{P})\boldsymbol{E} + \frac{\partial \boldsymbol{P}}{\partial t}\times\boldsymbol{B} + (\nabla\times\boldsymbol{M})\times\boldsymbol{B}$	$\varepsilon_0 \boldsymbol{E}\times\boldsymbol{B}$	The Nelson/Ampere ST (or its modified version) and force law behaves exactly same as the Chu formulation (or its modified version) for a dielectric scatterer.

7.4 Photon Momentum for instantaneous and Time averaged cases: Accuracy of Minkowski's theory

Based on the discussions in the previous sections [sections 7.2 and 7.3], finally, a question arises: can we model the momentum of photon as the one of Minkowski everywhere in the space? It is so far understood that the travelling momentum of photon (i.e. at the background) can better be modelled as Abraham/kinetic photon momentum [151] and the transferred momentum from the background to the embedded object should be considered as Minkowski/canonical photon momentum [43,151]. Classically Minkowski photon momentum arises just at the interface of the background and the embedded object [162]. Also the well-known Snell's law at the interface of two different mediums can be derived only from the conservation of the tangential component of Minkowski photon momentum. So far almost all the real experiments [43,58] have strongly supported the Minkowski photon momentum as the physical momentum of photon. Our analysis throughout the thesis suggests that either in instantaneous or in time average case, Minkowskian formulations remain valid everywhere in space and so far all the major radiation pressure experiments have unambiguously supported Minkowski's force formulations [28,46] and photon momentum [43,58]. One of the main arguments in favor of Abraham photon momentum mainly arises from the validity of Einstein-Laub's volumetric force distribution, which is connected with Abraham photon momentum, in case of Ashkin's experiment on water surface [161] (in other words: from the volumetric force calculations those support Abraham momentum density [28,151]). But Einstein-Laub formulation may not be appropriate to describe the physical reality considering both instantaneous [218] and time averaged analysis [cf. our discussion in previous two sections and chapter 5]. At the same time, such experiments [28,161] can also be explained better based on the Minkowskian force and Minkowski photon momentum

[28,221]. On the other hand, the well-known Chu force (that also supports Abraham photon momentum), which remains valid everywhere in instantaneous scenario [but not in time averaged case], does not lead to the correct force distribution for Ashkin's experiment on water surface [28]. One recent study has also invalided the idea of Abraham photon momentum even in instantaneous scenario [222]. Our final conclusions on photon momentum are shown at a glance in Fig. 7.4.

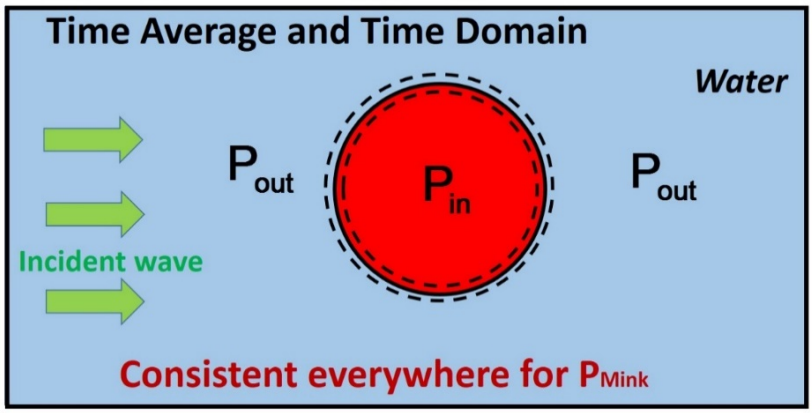

Fig. 7.4: Consistency of Minkowski photon momentum. Based on our discussions in this conclusion chapter [specially cf. Fig. 7.2 and 7.3], it can be understood that Minkowski's force formulations remain consistent everywhere in space. This fact implicitly suggests that: for both time averaged and instantaneous cases, Minkowski photon momentum can also be considered as the consistent photon momentum everywhere in space. Ray tracing method, Snell's law, almost all real experiments on radiation pressure directly support only the Minkowski photon momentum as the observable physical momentum of photon. On the other hand, even if it can be considered that Abraham photon momentum is the travelling momentum of photon in a continuous medium, most probably there is no way to reject the idea that: Minkowski photon momentum arises at the boundary of the embedded objects [cf. chapter 4 of this thesis and in chapter 5 it is also shown that the GAP METHOD, which is modelled to support Abraham's photon momentum everywhere in space, leads to inconsistent result of time averaged total force]. One recent study has invalided the idea of Abraham photon momentum even in instantaneous scenario [222]. As a result, for a unified consistent theory of optical force and photon momentum, either in instantaneous or in time averaged case, most probably Minkowski photon momentum is the strongest candidate for appropriate photon momentum as shown in above figure.

7.5 Conclusion

This chapter and Chapter 5 of this thesis partially answer the question after almost 100 years of Einstein's prediction [223] why Minkowski's theory is more accurate than Einstein-Laub theory to obtain the time averaged total force [due to: (i) 'existence domain' and (ii) modification issues]. Based on the proposals in chapter 5, we have proposed the idea/hypothesis of 'existence domain' in this chapter [section 7.2]. Though almost all the time averaged distinct STs and volumetric force laws are restricted to the idea of 'existence domain', we demonstrate that the time averaged stress tensor and volumetric force law of Minkowski are free from such restrictions. In addition, we have discussed in details the differences between time averaged and instantaneous force laws for different formulations in this chapter [section 7.3]. Notably only Minkowski's theory remains valid for all circumstances without any modification. So, after almost 100 years of Einstein's prediction [223], this chapter, most probably finally answers why Minkowski's theory is more accurate for all circumstances.

Considering 'all' the proposals in this chapter, it appears that Minkowski formulations are most probably more accurate description of physical optical force along with photon momentum. So, according to our proposals in this chapter, it may also be possible to consider the presence of Minkowski photon momentum everywhere in space along with the interface of the two different medium. However, if it would be possible to experimentally measure the presence of bulk force distribution of any ideal non-absorbing medium by any future experiment, it would certainly prove our proposals in this chapter physically a little bit inaccurate (as no bulk force should take place for Minkowski formulations in case of non-absorbing medium). However, whatever the experimental observation in future, from physical point of view: Minkowski's force most probably always describes the transfer of

optical momentum from background to an embedded object (external Minkowski ST) or to the embedded free charges (internal Minkowski ST).

Chapter 8

Conclusion and Future Works

8.1 Summary of the Thesis

Radiation pressure, in conjunction with photon momentum, has always constituted an intriguing phenomenon in physics. An accurate prediction of the electromagnetic force is important for complex biological systems, stable optical manipulation, tractor beams, MEMs and nano-opto-mechanical systems, among many applications. Most experiments in those areas need determinations of these optical forces on objects immersed in a non-vacuum environment. However, inside matter different definitions and descriptions of the macroscopic optical force and the photon momentum have been put forward, among others by Minkowski, Abraham, Ampere/Nelson, Einstein-Laub, Chu or Peierls. Even after extensive debates spanning over a century, there are still several unsolved problems regarding exactitudes of stress tensors or force laws, and on their individual validities or limitations inside matter.

One of the main goals of this thesis was to investigate the problems/dilemmas of optical volumetric/Lorentz forces specially observed in real radiation pressure experiments performed up to date. Moreover, Lorentz force dynamics was previously restricted to simple cases. In literature, Lorentz force analysis for optical pulling force (tractor beams) and the reversal of near field optical binding force (i.e. for plasmonic objects) have not been investigated in details so far. As a result, in this thesis, physics and applications of Lorentz force have been investigated in details with special

interest in tractor beam effect, plasmonic objects, chiral objects and the objects embedded in a generic material medium.

At the beginning part of this thesis, in chapters 2 and 3, we have considered the Lorentz force dynamics for comparatively simple cases such as objects placed in air. Time averaged total force calculated by well-known Lorentz force and the external stress tensor method are found in full agreement for those two chapters without any modification in Lorentz force. More specifically, as the stimulating connection between the Lorentz force and optical pulling force has not been investigated in details previously, chapter 2 demonstrates the Lorentz force analysis and its applications for tractor beam like effect [214]. It is shown based on Lorentz force analysis that the bound surface charges of Rayleigh scatterer experience backward force, which overcomes the positive bulk force and ultimately results in the net pulling of the scatterer for several spatial regions outside two dielectric hollow core cylindrical waveguide. Later, this idea of dielectric waveguide tractor beam has been extended for dielectric coupler set-ups for stable transverse equilibrium and long distance operation. On the other hand, Chapter 3 demonstrates the Lorentz force analysis for plasmonic off-axis and on-axis spherical heterodimers. It is shown based on Lorentz force analysis that the reversal of longitudinal binding force can be easily controlled through forced symmetry breaking: (i) just by changing the direction of light/wave propagation for a specific set-up of off-axis heterodimers or (ii) just by changing their relative orientation while keeping the light/wave propagation in a fixed direction. Notably, the longitudinal binding force of spherical heterodimers originates almost fully from the difference of the bulk part of Lorentz force, which strongly suggests the connection of bulk Lorentz force with the scattering force. As much study has not been performed on the connection of Lorentz force with gradient and scattering forces, the work presented in chapter 3 may open a new window for such investigations.

In contrast, in chapters 4, 5, 6 and 7, we have considered much complicated cases such as chiral and achiral objects embedded in material medium. Specially chapters 4 and 5 of this thesis deal with very fundamental topics of optical force: consistency of stress tensors, volumetric forces and photon momenta inside matter. In chapter 4 it is shown that the well-known Lorentz force leads to inconsistent result (pushing force) instead of the experimentally observed optical pulling force for interfacial tractor beam experiment [43]. Our suggested interpretation in chapter 4 supports the Minkowski approach only for the purpose of optical momentum transfer to the embedded scatterer for the interfacial tractor beam experiment [35], although the momentum of photon in the continuous water background can be considered as the type of Abraham for the calculation of the bulk part of Lorentz volumetric force distribution. Later chapter 5 discusses in detail why the well-known Lorentz/volumetric forces fail not only in interfacial tractor beam experiment but also for several other real experiments. Exactly at the boundary of an object, the difference of the external Minkowski ST and internal ST of Chu (and Einstein-Laub) is found in agreement with the surface force yielded by Chu (and Einstein-Laub) force only when the background is air or vacuum rather than a material. We identify this as one of the main reasons of the disagreements observed in the major radiation pressure experiments which include material medium as background. Some other notable reasons of such disagreements have also been identified and discussed in that same chapter. We also demonstrate that it is still possible to establish different equivalent time-averaged Lorentz / volumetric force formulas based on the fulfilment of just two ‘consistency conditions’. Based on those proposed ‘consistency conditions’, finally, we propose that by modifying the Einstein-Laub (EL) or Chu formulation, time-averaged STs and volume forces are obtained those can overcome the aforementioned inconsistency for almost all previous experiments. Specially, our proposed modified Einstein-Laub ST can be considered as an efficient mathematical toolkit, an

alternative of time and memory consuming volumetric forces, to yield the internal bulk force of a chiral or achiral object embedded in complex material backgrounds (i.e. homogeneous, heterogeneous, bounded etc.).

In chapter 6, we have shown an interesting application of modified Lorentz force, i.e. modified Chu force. We have observed that if the closely located plasmonic cube homodimers (over glass or high permittivity dielectric substrate) are illuminated with plane wave polarized parallel to dimer axis, no reversal of optical binding force occurs. But if we apply the same set-up over a plasmonic substrate, stable and stronger Fano resonance occurs along with the reversal of binding force. Interestingly, for both the strong quadrupole-quadrupole and dipole-dipole resonances of the dimers, the binding force is dominated by Coulombic surface charge induced force; whereas during the Fano resonance binding force reversal is dominated by polarization current induced modified bulk Lorentz force (which is unconventional in comparison with the usual idea of optical force on plasmonic objects).

Finally in chapter 7 (the chapter before conclusion), we have proposed the hypothesis of 'existence domain' inspired by the idea presented in chapter 5. Though almost all the time averaged distinct STs and volumetric force laws are restricted to the idea of 'existence domain', we demonstrate that the time averaged stress tensor and volumetric force law of Minkowski are free from such restrictions. In addition, we have discussed in details the differences between time averaged and instantaneous force laws for different formulations in chapter 7. Notably only Minkowski's theory (stress tensor, force law and photon momentum) remains valid for all circumstances without any modification.

The main contributions of this thesis are the following: Firstly, to identify the exact reasons of the failure of distinct time averaged optical force formulas in real radiation pressure experiments performed up to date and to settle them. Secondly, the consistency conditions [C(I) and C(II) in chapter 5] of optical forces , which lead to

the equivalent formulations of several distinct time averaged optical forces applicable for objects embedded in generic backgrounds [i.e. homogeneous, heterogeneous, bounded and so on]. Thirdly, the hypothesis of 'existence domain' in chapter 7, which along with aforementioned consistency conditions lead to sort out the most probable consistent theory of optical force and photon momentum applicable everywhere in space (i.e. Minkowski's theory) both in instantaneous and time averaged scenario. Fourthly, the applications of Lorentz force and modified Lorentz force dynamics for tractor beam effect and plasmonic dimers, which lead so several unconventional conclusions not presented before in literature.

8.2 Final Remarks and Future Works

In 1918 Albert Einstein wrote against his own theory of optical force to Walter Dällenbach [223]: *"It has long been known that the values I had derived with Laub at the time are wrong; Abraham, in particular, was the one who presented this in a thorough paper. The correct strain tensor has incidentally already been pointed out by Minkowski"*. Unfortunately, even after almost 100 years, it is not clear why Einstein predicted so regarding the theory of optical force generally known as optical stress tensor associated with optical Lorentz force.

This thesis (especially chapters 5 and 7), most probably, finally answers why Minkowski's theory is scientifically more accurate for all circumstances. Hence, it appears that Minkowski formulations are most probably more appropriate description of physical optical force along with photon momentum. It may also be possible to consider the presence of Minkowski photon momentum everywhere in space along with the interface of the two different medium according to previous chapter (chapter 7). However, if it would be possible to experimentally measure the presence of bulk

force distribution of any ideal non-absorbing medium by any future experiment, it would certainly prove our proposals in favor of Minkowski's theory a little bit inaccurate physically (as no bulk force should take place for Minkowski formulations in case of non-absorbing medium). However, whatever the experimental observation in future, from physical point of view: Minkowski's force always describes the transfer of optical momentum from background to an embedded object (external Minkowski ST) or to the embedded free charges (internal Minkowski ST). According to the conclusion of chapter 5, if time averaged bulk force is found not zero for a non-absorbing medium (i.e. in any future experiment), then it should better be considered that: (i) both time averaged external Minkowski force and time averaged internal modified Chu (or modified Einstein-Laub) force are physical entities but (ii) their physical operations should be considered quite distinct from each other [for details cf. the conclusion of chapter 5]. And hence the forms of the optical force law can be fully different to describe these fully different physical process/physical operations. In addition, if bulk force distribution for non-absorbing medium will be experimentally observed in real time analysis, then the idea of travelling momentum of photon as the one of Abraham [cf. our discussion in chapter 4] may not be neglected. As a result, such a future experiment on bulk force (especially in real time analysis), if properly proceeds, will probably resolve many misconceptions and dilemmas in the area of distinct optical forces along with photon momenta. This may be possible by introducing much modifications in the recent experiments of 'Ashkin-Dziedzic type' [47] as discussed in ref. [221, 224, 225] and by measuring the state of bulk part of water (or any ideal non-absorbing liquid) instead of the water surface.

Proposals presented in this thesis can be very effective to resolve not only the dilemma of distinct stress tensors and optical Lorentz forces but also the controversy of Abraham-Minkowski photon momenta. In addition, so far the idea of tractor beams are mostly restricted with highly sophisticated structured beams or exotic artificial

materials [226]. This thesis may also open a new window of optical pulling force/tractor beams due to the exclusion of conventional structured tractor beams along with the artificial exotic matters. Last but not least, the proposed ideas for the reversal of near field optical binding force may also be useful for the future applications of plasmonic dimers in the areas of improved plasmonic sensors, particle clustering and aggregation.

APPENDICES

Appendix A

Detail analysis on GAP METHOD of optical force calculation

Before discussing the volume force method of GAP METHOD (defined in the introduction of chapter 5 and also cf. Fig. 1A below), we highlight the surface force determination of Chu force.

It is already shown in [182] that when we consider an object placed in air, the surface force of Chu can be determined from the appropriate boundary conditions [78, 173, 182] of Chu volumetric force:

$$\boldsymbol{f}_{\text{Chu}}^{\text{Surface}} = \left\{\epsilon_0 (\boldsymbol{E}_{\text{out}} - \boldsymbol{E}_{\text{in}}) \cdot \hat{\boldsymbol{n}}\right\} \left(\frac{\boldsymbol{E}_{\text{out}} + \boldsymbol{E}_{\text{in}}}{2} \right)_{\text{at r=a}} + \left\{\mu_0 (\boldsymbol{H}_{\text{out}} - \boldsymbol{H}_{\text{in}}) \cdot \hat{\boldsymbol{n}}\right\} \left(\frac{\boldsymbol{H}_{\text{out}} + \boldsymbol{H}_{\text{in}}}{2} \right)_{\text{at r=a}} \quad \text{(A1)}$$

However, in [182] the surface force has not been calculated by employing the stress tensors. We shall show the process of surface force calculation by employing the stress tensor method in this section. The internal Chu stress tensor (ST) can be written as:

$\bar{\bar{\boldsymbol{T}}}_{\text{Chu}}^{\text{in}} = \left[\epsilon_0 \boldsymbol{E}_{\text{in}} \boldsymbol{E}_{\text{in}}^* + \mu_0 \boldsymbol{H}_{\text{in}} \boldsymbol{H}_{\text{in}}^* - \frac{1}{2} \left(\mu_0 \boldsymbol{H}_{\text{in}} \cdot \boldsymbol{H}_{\text{in}}^* + \epsilon_0 \boldsymbol{E}_{\text{in}} \cdot \boldsymbol{E}_{\text{in}}^* \right) \bar{\bar{\boldsymbol{I}}} \right]$. Here 'in' represents the fields inside a scatterer. Now, we shall show that the surface force of Chu in Eq (A1) can be yielded from the difference of external vacuum stress tensor $\bar{\bar{\boldsymbol{T}}}_{\text{Vacuum}}(\text{out})$ and

the internal Chu ST [cf. Eq (5.2b) in chapter 5 for vacuum ST; for the case of air background: the gap field ($\boldsymbol{E}_{\mathrm{g}}$) itself is the outside field ($\boldsymbol{E}_{\mathrm{out}}$) in Fig. 1A given below]:

$$[\bar{\bar{\boldsymbol{T}}}^{\mathrm{MIX}}_{\mathrm{Vacuum}}(\mathrm{out})-\bar{\bar{\boldsymbol{T}}}^{\mathrm{MIX}}_{\mathrm{Chu}}(\mathrm{in})]\cdot\hat{\boldsymbol{n}}\,_{r=a}=[\epsilon_0\boldsymbol{E}^{\perp}_{\mathrm{out}}\cdot\boldsymbol{E}^{\perp}_{\mathrm{out}}-\epsilon_0\boldsymbol{E}^{\perp}_{\mathrm{in}}\cdot\boldsymbol{E}^{\perp}_{\mathrm{in}}]\hat{\boldsymbol{n}}+[\epsilon_0\boldsymbol{E}^{\parallel}_{\mathrm{m\,out}}\cdot\boldsymbol{E}^{\perp}_{\mathrm{out}}-\epsilon_0\boldsymbol{E}^{\parallel}_{\mathrm{m\,in}}\cdot\boldsymbol{E}^{\perp}_{\mathrm{in}}]\hat{\boldsymbol{m}}$$
$$+[\epsilon_0\boldsymbol{E}^{\parallel}_{\mathrm{q\,out}}\cdot\boldsymbol{E}^{\perp}_{\mathrm{out}}-\epsilon_0\boldsymbol{E}^{\parallel}_{\mathrm{q\,in}}\cdot\boldsymbol{E}^{\perp}_{\mathrm{in}}]\hat{\boldsymbol{q}}$$
$$+[\mu_0\boldsymbol{H}^{\perp}_{\mathrm{out}}\cdot\boldsymbol{H}^{\perp}_{\mathrm{out}}-\mu_0\boldsymbol{H}^{\perp}_{\mathrm{in}}\cdot\boldsymbol{H}^{\perp}_{\mathrm{in}}]\hat{\boldsymbol{n}}+[\mu_0\boldsymbol{H}^{\parallel}_{\mathrm{m\,out}}\cdot\boldsymbol{H}^{\perp}_{\mathrm{out}}-\mu_0\boldsymbol{H}^{\parallel}_{\mathrm{m\,in}}\cdot\boldsymbol{H}^{\perp}_{\mathrm{in}}]\hat{\boldsymbol{m}}$$
$$+[\mu_0\boldsymbol{H}^{\parallel}_{\mathrm{q\,out}}\cdot\boldsymbol{H}^{\perp}_{\mathrm{out}}-\mu_0\boldsymbol{H}^{\parallel}_{\mathrm{q\,in}}\cdot\boldsymbol{H}^{\perp}_{\mathrm{in}}]\hat{\boldsymbol{q}}$$

'MIX' represents the mixed diagonal and non-diagonal elements of the stress tensor, which are not connected with the identity tensor, $\bar{\bar{\boldsymbol{I}}}$. 'out' represents the total fields (incident plus scattered field) outside a scatterer. Electric field at the object and background boundary is defined as: $\boldsymbol{E}=\boldsymbol{E}^{\perp}\hat{\boldsymbol{n}}+\boldsymbol{E}^{\parallel}_{\mathrm{m}}\hat{\boldsymbol{m}}+\boldsymbol{E}^{\parallel}_{\mathrm{q}}\hat{\boldsymbol{q}}$ where $\hat{\boldsymbol{n}}$, $\hat{\boldsymbol{m}}$ and $\hat{\boldsymbol{q}}$ are mutually orthogonal arbitrary unit vectors, which are applicable for different co-ordinate systems such as Cartesian or Spherical or Cylindrical. $\hat{\boldsymbol{n}}$ is the unit normal of the object surface. $\boldsymbol{E}^{\parallel}$ and $\boldsymbol{E}^{\perp}$ are the parallel and perpendicular components of electric fields at the background and object boundary. In a very similar way, the magnetic field has also been defined. Now, by applying the electromagnetic boundary conditions, we finally arrive for mix components:

$$[\bar{\bar{\boldsymbol{T}}}^{\mathrm{MIX}}_{\mathrm{Vacuum}}(\mathrm{out})-\bar{\bar{\boldsymbol{T}}}^{\mathrm{MIX}}_{\mathrm{Chu}}(\mathrm{in})]\cdot\hat{\boldsymbol{n}}\,_{r=a}=\left[\begin{array}{r}[\epsilon_0\boldsymbol{E}^{\perp}_{\mathrm{out}}\cdot\boldsymbol{E}^{\perp}_{\mathrm{out}}-\epsilon_0\boldsymbol{E}^{\perp}_{\mathrm{in}}\cdot\boldsymbol{E}^{\perp}_{\mathrm{in}}]\hat{\boldsymbol{n}}+\frac{\epsilon_0}{2}\left(\boldsymbol{E}^{\parallel}_{\mathrm{mout}}+\boldsymbol{E}^{\parallel}_{\mathrm{min}}\right)[\boldsymbol{E}^{\perp}_{\mathrm{out}}-\boldsymbol{E}^{\perp}_{\mathrm{in}}]\hat{\boldsymbol{m}}\\ +\frac{\epsilon_0}{2}\left(\boldsymbol{E}^{\parallel}_{\mathrm{qout}}+\boldsymbol{E}^{\parallel}_{\mathrm{qin}}\right)[\boldsymbol{E}^{\perp}_{\mathrm{out}}-\boldsymbol{E}^{\perp}_{\mathrm{in}}]\hat{\boldsymbol{q}}\end{array}\right]_{r=a}$$
$$+\left[\begin{array}{r}[\mu_0\boldsymbol{H}^{\perp}_{\mathrm{out}}\cdot\boldsymbol{H}^{\perp}_{\mathrm{out}}-\mu_0\boldsymbol{H}^{\perp}_{\mathrm{in}}\cdot\boldsymbol{H}^{\perp}_{\mathrm{in}}]\hat{\boldsymbol{n}}+\frac{\mu_0}{2}\left(\boldsymbol{H}^{\parallel}_{\mathrm{mout}}+\boldsymbol{H}^{\parallel}_{\mathrm{min}}\right)[\boldsymbol{H}^{\perp}_{\mathrm{out}}-\boldsymbol{H}^{\perp}_{\mathrm{in}}]\hat{\boldsymbol{m}}\\ +\frac{\mu_0}{2}\left(\boldsymbol{H}^{\parallel}_{\mathrm{qout}}+\boldsymbol{H}^{\parallel}_{\mathrm{qin}}\right)[\boldsymbol{H}^{\perp}_{\mathrm{out}}-\boldsymbol{H}^{\perp}_{\mathrm{in}}]\hat{\boldsymbol{q}}\end{array}\right]_{r=a}$$

(A2)

Now, we can also write:

Appendices

$$[\bar{\bar{T}}^{D}_{\text{Vacuum}}(\text{out})-\bar{\bar{T}}^{D}_{\text{Chu}}(\text{in})]\cdot\hat{\boldsymbol{n}}_{r=a}=[\epsilon_0\boldsymbol{E}^{\perp}_{\text{out}}\cdot\boldsymbol{E}^{\perp}_{\text{out}}-\epsilon_0\boldsymbol{E}^{\perp}_{\text{in}}\cdot\boldsymbol{E}^{\perp}_{\text{in}}]\hat{\boldsymbol{n}}+[\mu_0\boldsymbol{H}^{\perp}_{\text{out}}\cdot\boldsymbol{H}^{\perp}_{\text{out}}-\mu_0\boldsymbol{H}^{\perp}_{\text{in}}\cdot\boldsymbol{H}^{\perp}_{\text{in}}]\hat{\boldsymbol{n}}_{r=a} \quad \text{(A3)}$$

'D' represents pure diagonal elements of the stress tensor. Now, by adding Eqs (A2) and (A3), after some calculations we get exactly Eq (A1), the surface force of Chu:

$$[\bar{\bar{T}}_{\text{Vacuum}}(\text{out})-\bar{\bar{T}}_{\text{Chu}}(\text{in})]\cdot\hat{\boldsymbol{n}}_{r=a}=[\{\epsilon_0(\boldsymbol{E}_{\text{out}}-\boldsymbol{E}_{\text{in}})\cdot\hat{\boldsymbol{n}}\}\left(\frac{\boldsymbol{E}_{\text{out}}+\boldsymbol{E}_{\text{in}}}{2}\right)_{\text{at r=a}}+\{\mu_0(\boldsymbol{H}_{\text{out}}-\boldsymbol{H}_{\text{in}})\cdot\hat{\boldsymbol{n}}\}\left(\frac{\boldsymbol{H}_{\text{out}}+\boldsymbol{H}_{\text{in}}}{2}\right)_{\text{at r=a}}] \quad \text{(A4)}$$

So, when the object is placed in air: (i) internal Chu stress tensor yields the time averaged bulk force of Chu volume force and (ii) the external vacuum ST leads to the total time averaged force (bulk force plus the additional surface force). This is also true for the Einstein-Laub volumetric force. We have found analytically that the difference of external vacuum ST and the internal Einstein-Laub ST leads to a surface force of Einstein-Laub [173,182], which exactly matches with the independently calculated surface force from the volumetric force of Einstein-Laub [182].

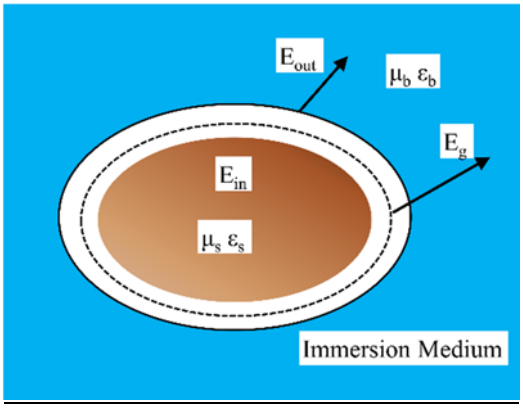

Fig. 1A: When the object is surrounded by a medium other than the free space, a narrow gap may be imagined to exist between the object and its surroundings according to refs. [170, 78,172,173]. The integration boundary is then placed within the gap. $\boldsymbol{E}_g$ represents the electric field in that narrow gap.

Now, we can go back to our discussion on the topic of GAP METHOD [170, 78,172,173] as illustrated in Fig. 1A. In [78] considering the consistency of the

volume force, finally it has been concluded that: When such a gap is given between the scatterer and the surrounding background, the total force of the embedded scatterer should be calculated based on (described as method II in [78] and cf. Fig. 1A):

$$\left\langle \boldsymbol{F}_{\text{Gap Method}}^{\text{Total}} \right\rangle = \left\langle \boldsymbol{F}_{\text{Gap Method}}^{\text{Bulk}} \right\rangle(\text{in}) + \left\langle \boldsymbol{F}_{\text{Gap Method}}^{\text{Surface}} \right\rangle \tag{A5}$$

$$\left\langle \boldsymbol{f}_{\text{Gap Method}}^{\text{Surface}} \right\rangle = \frac{1}{2}\text{Re}[\left\{\epsilon_0(\boldsymbol{E}_{\text{g}} - \boldsymbol{E}_{\text{in}})\cdot\hat{\boldsymbol{n}}\right\}\left(\frac{\boldsymbol{E}_{\text{out}}^{\perp} + \boldsymbol{E}_{\text{in}}^{\perp}}{2}\right)_{\text{at r=a}} + \left\{\mu_0(\boldsymbol{H}_{\text{g}} - \boldsymbol{H}_{\text{in}})\cdot\hat{\boldsymbol{n}}\right\}\left(\frac{\boldsymbol{H}_{\text{out}}^{\perp} + \boldsymbol{H}_{\text{in}}^{\perp}}{2}\right)_{\text{at r=a}}^{*}] \tag{A6}$$

$$\left\langle \boldsymbol{f}_{\text{Gap Method}}^{\text{Bulk}} \right\rangle(\text{in}) = \frac{1}{2}\text{Re}\left[-\left(i\omega\boldsymbol{P}\times\boldsymbol{B}_{\text{in}}^{*}\right) + \left(i\omega\boldsymbol{M}\times\boldsymbol{D}_{\text{in}}^{*}\right)\right]. \tag{A7}$$

Here $\boldsymbol{P} = \left(\varepsilon_S - \varepsilon_0\right)\boldsymbol{E}_{\text{in}}$, $\boldsymbol{M} = \left(\mu_S - \mu_0\right)\boldsymbol{H}_{\text{in}}$, $\boldsymbol{B}_{\text{in}} = \mu_S\boldsymbol{H}_{\text{in}}$ and $\boldsymbol{D}_{\text{in}} = \varepsilon_S\boldsymbol{E}_{\text{in}}$. But the bulk and surface force calculation based on the above method may not be a general procedure due to these reasons:

(1) Though above Eq (A5) is successful for small object only for few specific cases [78], it may lead to inconsistent result for embedded Mie or more complex objects according to the same ref. [78].

(2) The surface force of Chu force calculated in [182] from the direct volume force method. It is also shown in Eqs (A1-A4) that the same surface force can also be calculated for a dielectric object (placed in air) from the difference of the external ST, $\bar{\bar{\boldsymbol{T}}}_{\text{Vacuum}}(\text{out})$, and the internal ST of Chu, $\bar{\bar{\boldsymbol{T}}}_{\text{Chu}}(\text{in})$, just at the boundary of the scatterer. So, the total force of a scatterer placed in air calculated by volume force method is nothing but the force calculated by the external ST.

Now, we again consider the work of Barnett et al. [182] where the procedure of surface force calculation has been illustrated by properly applying the boundary conditions. If we apply those boundary conditions and at the same time consider that there is a small gap between the scatterer and the surrounding background, the consistent equation leads to the force equation where the average field at the boundary of the scatterer should be calculated with gap fields ($\boldsymbol{E}_{\mathrm{g}}$, $\boldsymbol{H}_{\mathrm{g}}$) instead of the real fields ($\boldsymbol{E}_{\mathrm{out}}$, $\boldsymbol{H}_{\mathrm{out}}$) of the background medium (described as method III in [78] and cf. Fig. 1A):

$$\left\langle \boldsymbol{f}_{\text{Gap Method}}^{\text{Surface}} \right\rangle = \frac{1}{2}\mathrm{Re}\left[\left\{ \epsilon_0 (\boldsymbol{E}_{\mathrm{g}} - \boldsymbol{E}_{\mathrm{in}}) \cdot \hat{\boldsymbol{n}} \right\} \left(\frac{\boldsymbol{E}_{\mathrm{g}}^{\perp} + \boldsymbol{E}_{\mathrm{in}}^{\perp}}{2} \right)_{\text{at r=a}} + \left\{ \mu_0 (\boldsymbol{H}_{\mathrm{g}} - \boldsymbol{H}_{\mathrm{in}}) \cdot \hat{\boldsymbol{n}} \right\} \left(\frac{\boldsymbol{H}_{\mathrm{g}}^{\perp} + \boldsymbol{H}_{\mathrm{in}}^{\perp}}{2} \right)_{\text{at r=a}}^{*} \right] \tag{A7}$$

It is also interesting that if we consider a vacuum stress tensor at the gap [170] shown between the scatterer and the background, the difference between the external vacuum stress tensor and the internal Chu stress tensor leads to the same surface force of Eq (A7):

$$[\bar{\bar{\boldsymbol{T}}}_{\text{Vacuum}}^{\text{GAP}}(\text{out}) - \bar{\bar{\boldsymbol{T}}}_{\text{Chu}}(\text{in})] \cdot \hat{\boldsymbol{n}}_{r=a} = \left[\left\{ \epsilon_0 (\boldsymbol{E}_{\mathrm{g}} - \boldsymbol{E}_{\mathrm{in}}) \cdot \hat{\boldsymbol{n}} \right\} \left(\frac{\boldsymbol{E}_{\mathrm{g}}^{\perp} + \boldsymbol{E}_{\mathrm{in}}^{\perp}}{2} \right)_{\text{at r=a}} + \left\{ \mu_0 (\boldsymbol{H}_{\mathrm{g}} - \boldsymbol{H}_{\mathrm{in}}) \cdot \hat{\boldsymbol{n}} \right\} \left(\frac{\boldsymbol{H}_{\mathrm{g}}^{\perp} + \boldsymbol{H}_{\mathrm{in}}^{\perp}}{2} \right)_{\text{at r=a}} \right] \tag{A8}$$

But that equation (method III in [78]) does not lead to the consistent result according to that same ref. [78]. In addition, we have already shown in chapter 5 that the total force calculated by external ST $\bar{\bar{\boldsymbol{T}}}_{\text{Vacuum}}^{\text{GAP}}(\text{out})$ in Eq (A8) [method III in [78] should also lead to the same force of Eq (5.2a) given in chapter 5] leads to wrong result for experiments which include inhomogeneous background (or in general heterogeneous background).

So, Eq (A5) above is an independent equation (described as method II in [78] which is a more accurate formulation than method I and III according to ref. [78]) which cannot be derived from the volume force of Chu [182] by employing the proper boundary conditions to the static force part shown in [182]. At the same time, there is no such external (and also internal) ST which leads to the surface force yielded by Eq (A6) above from the difference of external ST and the internal Chu ST just at the object boundary.

(3) Last but not least, the difference of any external ST and the internal Chu ST does not lead to the surface force given in Eq (A6). So, Eq (A5) above (described as method II in [78]) is a fully independent equation to yield the time averaged total force, which may not be a generic way to yield the total time averaged force of the embedded objects.

However, an alternative way to yield the time averaged total force (by volume force method) for the embedded objects can be well-known Einstein-Laub force [28] as shown for several previous experiments [28] but without considering any small gap between the scatterer and the background. However, the problems of EL force for real experiments, those involve material background, have been discussed shortly in chapter 5.

Appendix B

Possible derivation of the internal Modified Einstein-Laub stress tensor

Previously the Eisntein-Laub (EL) stress tensor was derived in [227] from the well-known EL force density method. In this section we shall derive the modified EL ST from the modified EL (MEL) force in the same way as described in [227] but in the time averaged form. For an embedded achiral dielectric object embedded in another homogeneous dielectric, the EL force density takes a modified form [171]:

$$\left\langle \boldsymbol{f}_{\mathrm{MEL}} \right\rangle = \frac{1}{2}\mathrm{Re}\left[\left(\boldsymbol{P}_{\mathrm{Eff}} \cdot \nabla \right) \boldsymbol{E}_{\mathrm{in}}^{*} - i\omega \left(\boldsymbol{P}_{\mathrm{Eff}} \times \boldsymbol{B}_{\mathrm{in}}^{*} \right) \right]. \tag{B1}$$

In Eq (B1), it is interesting to note that the polarization have been written as effective polarization as [26,171,183]:

$$\boldsymbol{D}_{\mathrm{in}} = \boldsymbol{D}_{\mathrm{Eff}} = \varepsilon_{\mathrm{b}} \boldsymbol{E}_{\mathrm{in}} + \boldsymbol{P}_{\mathrm{Eff}}; \quad \boldsymbol{P}_{\mathrm{Eff}} = \left(\varepsilon_{S} - \varepsilon_{\mathrm{b}} \right) \boldsymbol{E}_{\mathrm{in}}, \tag{B2}$$

In the same way, the effective magnetization can also be written as [26]:

$$\boldsymbol{B}_{\mathrm{in}} = \boldsymbol{B}_{\mathrm{Eff}} = \mu_{\mathrm{b}} \boldsymbol{H}_{\mathrm{in}} + \boldsymbol{M}_{\mathrm{Eff}}; \; \boldsymbol{M}_{\mathrm{Eff}} = \left(\mu_{S} - \mu_{\mathrm{b}} \right) \boldsymbol{H}_{\mathrm{in}}. \tag{B3}$$

It should be noted that ε_{b} and μ_{b} are fixed constant parameters [For example- they do not vary with respect to time]. In [183] it is argued in favor of Eq (B2): "*Note that the equation for net force without rescaling with the background permittivity will give the total force on the volume including force on the background material which*

does not result in motion of the particle." The idea of effective induced electric (and magnetic) dipole moment has been also applied previously to yield the 'outside force' of dipolar objects in [16, 97, 186] in a very similar way of the idea of effective polarization and magnetization given in Eq (B2) and (B3). For example- the induced effective dipole moment has been derived in Eq (22) given in ref. [97] from the effective polarization model of Eq (B2) but with the exterior field of an embedded scatterer for external dipolar force.

However, in [26], it is shown that for a magneto-dielectric object embedded in another magneto-dielectric, the external force by Minkowski ST matches with the time averaged force via Modified Chu (MCHU) volume force expressed in terms of effective polarization and magnetization as:

$$\left\langle \boldsymbol{f}_{\text{Total}}^{\text{MCHU}} \right\rangle = \left\langle \boldsymbol{f}_{\text{Surface}}^{\text{MCHU}} \right\rangle + \left\langle \boldsymbol{f}_{\text{Bulk}}^{\text{MCHU}} \right\rangle \tag{B4}$$

$$\left\langle \boldsymbol{f}_{\text{Surface}}^{\text{MCHU}} \right\rangle = \frac{1}{2}\text{Re}[\left\{\epsilon_b(\boldsymbol{E}_{\text{out}} - \boldsymbol{E}_{\text{in}})\cdot\hat{\boldsymbol{n}}\right\}\left(\frac{\boldsymbol{E}_{\text{out}} + \boldsymbol{E}_{\text{in}}}{2}\right)^*_{\text{at r=a}} + \left\{\mu_b(\boldsymbol{H}_{\text{out}} - \boldsymbol{H}_{\text{in}})\cdot\hat{\boldsymbol{n}}\right\}\left(\frac{\boldsymbol{H}_{\text{out}} + \boldsymbol{H}_{\text{in}}}{2}\right)^*_{\text{at r=a}}] \tag{B5}$$

$$\left\langle \boldsymbol{f}_{\text{Bulk}}^{\text{MCHU}} \right\rangle = \frac{1}{2}\text{Re}[-i\omega\left(\boldsymbol{P}_{\text{Eff}} \times \boldsymbol{B}_{\text{in}}^*\right) + i\omega\left(\boldsymbol{M}_{\text{Eff}} \times \boldsymbol{D}_{\text{in}}^*\right)]. \tag{B6}$$

For several cases [26,183, 228, 229], this volume force method has been applied to yield the total force. For example- the effect of background permittivity has been described in [229] for the cases of binding forces. Considering the consistency of Eqs (B4-B6) [26], [183], the modified EL force law in [171] can be written in a generic form for a magneto-dielectric object embedded in another magneto-dielectric in accordance with [161] as:

$$\left\langle \boldsymbol{f}_{\text{MEL}}^{\text{Bulk}} \right\rangle(\text{in}) = \frac{1}{2}\text{Re}\left[\left(\boldsymbol{P}_{\text{Eff}}\cdot\nabla\right)\boldsymbol{E}_{\text{in}}^* + \left(\boldsymbol{M}_{\text{Eff}}\cdot\nabla\right)\boldsymbol{H}_{\text{in}}^* - i\omega\boldsymbol{P}_{\text{Eff}} \times \left(\boldsymbol{B}_{\text{in}}^* - \boldsymbol{M}_{\text{Eff}}^*\right) + i\omega\boldsymbol{M}_{\text{Eff}} \times \left(\boldsymbol{D}_{\text{in}}^* - \boldsymbol{P}_{\text{Eff}}\right)\right].$$

(B7)

In Eq (B7), the $i\omega \boldsymbol{P}_{\mathrm{Eff}} \times \boldsymbol{M}^{*}_{\mathrm{Eff}}$ terms cancel out finally. As it is shown in [188] that the application of EL formulation may lead to misleading results for very simple situations, the final time averaged form of MEL force should be written in terms of $\boldsymbol{B}$ instead of $\mu_0 \mathbf{H}$ according to [161] (also cf. reference [230] where the difference between the time varying and the time averaged force has been argued):

$$\left\langle \boldsymbol{f}_{\mathrm{MEL}}^{\mathrm{Bulk}} \right\rangle (\mathrm{in}) = \frac{1}{2} \mathrm{Re}\left[\left(\boldsymbol{P}_{\mathrm{Eff}} \cdot \nabla \right) \boldsymbol{E}_{\mathrm{in}}^{*} + \left(\boldsymbol{M}_{\mathrm{Eff}} \cdot \nabla \right) \boldsymbol{H}_{\mathrm{in}}^{*} - \left(i\omega \boldsymbol{P}_{\mathrm{Eff}} \times \boldsymbol{B}_{\mathrm{in}}^{*} \right) + \left(i\omega \boldsymbol{M}_{\mathrm{Eff}} \times \boldsymbol{D}_{\mathrm{in}}^{*} \right) \right]. \quad \text{(B8)}$$

Now, in order to yield the final form of the MEL stress tensor, the intermediate step of the MEL force [not the final time averaged form given in Eq (B8)] can be written from Eq (B7) as:

$$\left\langle \boldsymbol{f}_{\mathrm{MEL}}^{\mathrm{Bulk}} \right\rangle (\mathrm{in}) = \frac{1}{2} \mathrm{Re}[(\boldsymbol{P}_{\mathrm{Eff}} \cdot \nabla)\boldsymbol{E}_{\mathrm{in}} + (\boldsymbol{M}_{\mathrm{Eff}} \cdot \nabla)\boldsymbol{H}_{\mathrm{in}} - i\omega \boldsymbol{P}_{\mathrm{Eff}} \times \mu_{\mathrm{b}} \boldsymbol{H}_{\mathrm{in}} + i\omega \boldsymbol{M}_{\mathrm{Eff}} \times \varepsilon_{\mathrm{b}} \boldsymbol{E}_{\mathrm{in}}] \quad \text{(B9)}$$

Eq (B9) ,which represents only an intermediate step of final MEL force in Eq (B8), turns into the EL force equation if the background is air. It should be noted that the Maxwell equations remain unique everywhere in terms of $\boldsymbol{D}$ and $\boldsymbol{B}$ only. However, as the internal induced polarization and magnetization are affected/influenced by the background permittivity and permeability specially due to the effect of the boundary/interface, the division of $\boldsymbol{D}$ and $\boldsymbol{B}$ can be expressed based on Eq (B2) and (B3).As a result, considering $\mathbf{P}_{\mathrm{Eff}}$ and $\mathbf{M}_{\mathrm{Eff}}$ in Eq (B2) and (B3) as a consistent mathematical description, the Maxwell-Chu [155] equations can be written for the embedded object as:

$$\nabla \times \boldsymbol{E}_{\mathrm{in}} = i\omega \boldsymbol{B}_{\mathrm{in}} = i\omega(\mu_{\mathrm{b}} \boldsymbol{H}_{\mathrm{in}} + \boldsymbol{M}_{\mathrm{Eff}}), \quad \text{(B10)}$$

$$\nabla \times \boldsymbol{H}_{\mathrm{in}} = -i\omega \boldsymbol{D}_{\mathrm{in}} = -i\omega(\varepsilon_{\mathrm{b}} \boldsymbol{E}_{\mathrm{in}} + \boldsymbol{P}_{\mathrm{Eff}}), \quad \text{(B11)}$$

$$\nabla \cdot \boldsymbol{D}_{\mathrm{in}} = \nabla \cdot (\varepsilon_{\mathrm{b}} \boldsymbol{E}_{\mathrm{in}} + \boldsymbol{P}_{\mathrm{Eff}}) = 0 \quad \text{(B12)}$$

$$\nabla \cdot \boldsymbol{B}_{\text{in}} = \nabla \cdot (\mu_{\text{b}} \boldsymbol{H}_{\text{in}} + \boldsymbol{M}_{\text{Eff}}) = 0 \tag{B13}$$

In order to determine the final form of the stress tensor, let us consider the $\text{Re}[\varepsilon_{\text{b}}\mu_{\text{b}}\boldsymbol{E}_{\text{in}} \times (-i\omega \boldsymbol{H}_{\text{in}}^{*}) - \varepsilon_{\text{b}}\mu_{\text{b}}\boldsymbol{H}_{\text{in}} \times (-i\omega \boldsymbol{E}_{\text{in}}^{*})]$ term which is zero. By adding this $\text{Re}[\varepsilon_{\text{b}}\mu_{\text{b}}\boldsymbol{E}_{\text{in}} \times (-i\omega \boldsymbol{H}_{\text{in}}^{*}) - \varepsilon_{\text{b}}\mu_{\text{b}}\boldsymbol{H}_{\text{in}} \times (-i\omega \boldsymbol{E}_{\text{in}}^{*})]$ term with previous Eq (B9), we finally obtain:

$$\left\langle \nabla \cdot \overline{\overline{\boldsymbol{T}}} \right\rangle = \left\langle \boldsymbol{f}_{\text{MEL}}^{\text{Bulk}} \right\rangle (\text{in}) + \left\langle \frac{\partial}{\partial t} \boldsymbol{G} \right\rangle = \frac{1}{2} \text{Re}[[(\boldsymbol{P}_{\text{Eff}} \cdot \nabla)\boldsymbol{E}_{\text{in}}^{*} + (\boldsymbol{M}_{\text{Eff}} \cdot \nabla)\boldsymbol{H}_{\text{in}}^{*} - i\omega \boldsymbol{P}_{\text{Eff}} \times \mu_{\text{b}} \boldsymbol{H}_{\text{in}}^{*} + i\omega \boldsymbol{M}_{\text{Eff}} \times \varepsilon_{\text{b}} \boldsymbol{E}_{\text{in}}^{*}] + [\varepsilon_{\text{b}}\mu_{\text{b}}\boldsymbol{E}_{\text{in}} \times (-i\omega \boldsymbol{H}_{\text{in}}^{*}) - \varepsilon_{\text{b}}\mu_{\text{b}}\boldsymbol{H}_{\text{in}} \times (-i\omega \boldsymbol{E}_{\text{in}}^{*})]] \tag{B14}$$

In above equation $\left\langle \frac{\partial}{\partial t} \boldsymbol{G} \right\rangle$ is zero where $\boldsymbol{G}$ is a non-mechanical momentum density. After some calculations, we get from Eq (B14):

$$\left\langle \nabla \cdot \overline{\overline{\boldsymbol{T}}} \right\rangle = \left\langle \boldsymbol{f}_{\text{MEL}}^{\text{Bulk}} \right\rangle (\text{in}) = \frac{1}{2} \text{Re}[(\boldsymbol{P}_{\text{Eff}} \cdot \nabla)\boldsymbol{E}_{\text{in}}^{*} + (\boldsymbol{M}_{\text{Eff}} \cdot \nabla)\boldsymbol{H}_{\text{in}}^{*} - \varepsilon_{\text{b}} \boldsymbol{E}_{\text{in}}^{*} \times (\nabla \times \boldsymbol{E}_{\text{in}}) - \mu_{\text{b}} \boldsymbol{H}_{\text{in}}^{*} \times (\nabla \times \boldsymbol{H}_{\text{in}})] \tag{B15}$$

By applying Eqs (B2) and (B3), we can write from Eq (B15):

$$\left\langle \nabla \cdot \overline{\overline{\boldsymbol{T}}} \right\rangle = \left\langle \boldsymbol{f}_{\text{MEL}}^{\text{Bulk}} \right\rangle (\text{in}) = \frac{1}{2} \text{Re}[\nabla (\boldsymbol{D}_{\text{in}} \boldsymbol{E}_{\text{in}}^{*} + \boldsymbol{B}_{\text{in}} \boldsymbol{H}_{\text{in}}^{*}) - \frac{1}{2} \nabla (\varepsilon_{\text{b}} \boldsymbol{E}_{\text{in}}^{*} . \boldsymbol{E}_{\text{in}}) - \frac{1}{2} \nabla (\mu_{\text{b}} \boldsymbol{H}_{\text{in}}^{*} . \boldsymbol{H}_{\text{in}})] \tag{B16}$$

Hence the time averaged MEL ST inside an object embedded in a homogeneous background can be written as:

$$\left\langle \overline{\overline{\boldsymbol{T}}}_{\text{MEL}}^{\text{Bulk}} \right\rangle (\text{in}) = \frac{1}{2} \text{Re}[\boldsymbol{D}_{\text{in}} \boldsymbol{E}_{\text{in}}^{*} + \boldsymbol{B}_{\text{in}} \boldsymbol{H}_{\text{in}}^{*} - \frac{1}{2} \left((\frac{\mu_{\text{b}}}{\mu_{\text{s}}}) \mu_{\text{s}} \boldsymbol{H}_{\text{in}}^{*} \cdot \boldsymbol{H}_{\text{in}} + (\frac{\varepsilon_{\text{b}}}{\varepsilon_{s}}) \varepsilon_{s} \boldsymbol{E}_{\text{in}}^{*} \cdot \boldsymbol{E}_{\text{in}} \right) \overline{\overline{\boldsymbol{I}}}]. \tag{B17}$$

Eq (B17) turns into EL Stress tensor [227] when the embedding background is air instead of material medium. However, still one important issue remains unsolved:

Are Eqs (B1) [171], (B8) and (B17) consistent equations, which lead to the same surface force from two different ways of calculations (as shown at the beginning of Appendix A): (i) from direct volume force [183] and (ii) from the difference of external and internal ST. This issue is answered in the next appendix.

Appendix C

Derivation of the MEL surface force in two fully different ways

At first we consider the surface force calculation process shown in [183] (which applied in [183] to yield the surface force: (i) only from volumetric force and (ii) only for air background) and apply that process for the static part of Eq (B8) at the boundary of the embedded object (at r=a) [considering there is no artificial gap between the scatterer and the background]:

$$\boldsymbol{f}_{\mathrm{MEL}}^{\mathrm{Surface}}=[\left\{\epsilon_b(\boldsymbol{E}_{\mathrm{out}}-\boldsymbol{E}_{\mathrm{in}})\cdot\hat{\boldsymbol{n}}\right\}\left(\frac{\boldsymbol{E}_{\mathrm{out}}-\boldsymbol{E}_{\mathrm{in}}}{2}\right)_{\text{at r=a}}+\left\{\mu_b(\boldsymbol{H}_{\mathrm{out}}-\boldsymbol{H}_{\mathrm{in}})\cdot\hat{\boldsymbol{n}}\right\}\left(\frac{\boldsymbol{H}_{\mathrm{out}}-\boldsymbol{H}_{\mathrm{in}}}{2}\right)_{\text{at r=a}}] \tag{C1}$$

At the object boundary, the average polarization requires to be considered as $\boldsymbol{P}_{\mathrm{Eff}}/2$ to arrive at Eq (C1) and; Eq (C1) turns into the surface force of well-known Einstein-Laub force when background is considered air. Now considering the difference between the external Minkowski ST and the internal MEL ST just at the boundary of an embedded scatterer:

$$[\bar{\bar{\boldsymbol{T}}}_{\mathrm{Mink}}^{\mathrm{MIX}}(\mathrm{out})-\bar{\bar{\boldsymbol{T}}}_{\mathrm{MEL}}^{\mathrm{MIX}}(\mathrm{in})]\cdot\hat{\boldsymbol{n}}_{\,r=a}=[\epsilon_b\boldsymbol{E}_{\mathrm{out}}^{\perp}\cdot\boldsymbol{E}_{\mathrm{out}}^{\perp}-\epsilon_s\boldsymbol{E}_{\mathrm{in}}^{\perp}\cdot\boldsymbol{E}_{\mathrm{in}}^{\perp}]\hat{\boldsymbol{n}}+[\mu_b\boldsymbol{H}_{\mathrm{out}}^{\perp}\cdot\boldsymbol{H}_{\mathrm{out}}^{\perp}-\mu_s\boldsymbol{H}_{\mathrm{in}}^{\perp}\cdot\boldsymbol{H}_{\mathrm{in}}^{\perp}]\hat{\boldsymbol{n}}_{\,r=a} \tag{C2}$$

$$[\bar{\bar{\boldsymbol{T}}}_{\mathrm{Mink}}^{\mathrm{D}}(\mathrm{out})-\bar{\bar{\boldsymbol{T}}}_{\mathrm{MEL}}^{\mathrm{D}}(\mathrm{in})]\cdot\hat{\boldsymbol{n}}_{\,r=a}=-\frac{1}{2}[[\epsilon_b\boldsymbol{E}_{\mathrm{out}}^{\perp}\cdot\boldsymbol{E}_{\mathrm{out}}^{\perp}-\epsilon_b\boldsymbol{E}_{\mathrm{in}}^{\perp}\cdot\boldsymbol{E}_{\mathrm{in}}^{\perp}]+[\mu_b\boldsymbol{H}_{\mathrm{out}}^{\perp}\cdot\boldsymbol{H}_{\mathrm{out}}^{\perp}-\mu_b\boldsymbol{H}_{\mathrm{in}}^{\perp}\cdot\boldsymbol{H}_{\mathrm{in}}^{\perp}]]\hat{\boldsymbol{n}}_{r=a} \tag{C3}$$

Now, adding Eq (C2) and (C3) together, after some calculations we get:

$$[\bar{\bar{T}}^{out}_{Mink}(out)-\bar{\bar{T}}_{MEL}(in)]\cdot\hat{\boldsymbol{n}}_{r=a}=[\{\epsilon_b(\boldsymbol{E}_{out}-\boldsymbol{E}_{in})\cdot\hat{\boldsymbol{n}}\}\left(\frac{\boldsymbol{E}_{out}-\boldsymbol{E}_{in}}{2}\right)_{at\ r=a}+\{\mu_b(\boldsymbol{H}_{out}-\boldsymbol{H}_{in})\cdot\hat{\boldsymbol{n}}\}\left(\frac{\boldsymbol{H}_{out}-\boldsymbol{H}_{in}}{2}\right)_{at\ r=a}] \quad \text{(C4)}$$

-Which exactly matches with Eq (C1).

Appendix D

Time averaged external (total force) and internal force (bulk force) for an embedded achiral object:

All the 3D simulations throughout chapter 5 and this appendix are conducted using incident power of 0.57mW/μm^2.

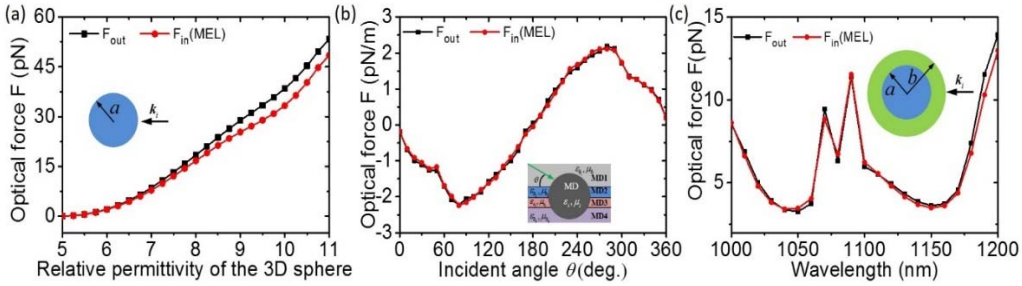

Fig. 1D: Time-averaged forces: F_{out} at $r = a^{+} = 1.01a$ from Minkowski ST [231,232] and F_{in} (bulk force) at $r = a^{-} = 0.999a$ from the modified Einstein-Laub (MEL) ST [232]. These forces are always of same trend. By adding the surface force of MEL with the bulk force, the magnitude exactly matches with external time averaged total force. (a) Homogeneous background: Force on a non-absorbing dielectric sphere by varying its permittivity (with a=500 nm, illuminated by a linearly polarized plane wave $E_x = E_0 e^{i(kz-\omega t)}$ at $\lambda = 1064$ nm). The unbounded homogeneous dielectric background parameter is: $\varepsilon_b = 5\varepsilon_0$. (b) Heterogeneous background: Force on a magneto-dielectric infinite cylinder of $(\varepsilon_s, \mu_s) = (5\varepsilon_0, 4\mu_0)$ and radius 2000 nm embedded in an heterogeneous unbounded background of four different magneto-dielectric layers: $(\varepsilon_b, \mu_b) = (3\varepsilon_0, 2\mu_0)$; $(4\varepsilon_0, 3\mu_0)$;$(5\varepsilon_0, 4\mu_0)$; $(6\varepsilon_0, 5\mu_0)$. The illuminating plane wave with $\lambda = 1064$nm indices at varying angles. (c) A 3D core-shell magneto-dielectric sphere embedded in air is illuminated by a linearly polarized plane wave with varying wavelengths. Core radius, a=500 nm, $\varepsilon_s = 8\varepsilon_0$, $\mu_s = 3\mu_0$. Bounded local immediate background (i.e. the shell) parameters: radius, b=600 nm and $\varepsilon_b = 4\varepsilon_0$; $\mu_s = 2\mu_0$. $\boldsymbol{F}_{\text{out}} = \left\langle \boldsymbol{F}_{\text{out}}^{\text{Core}} \right\rangle$, at different illumination wavelengths λ obtained from Minkowski ST at r=a^{+} using the fields in the shell. $\boldsymbol{F}_{\text{in}} = \left\langle \boldsymbol{F}_{\text{in}}^{\text{Core}} \right\rangle$ based on MEL ST at r=a^{-} using core fields.

Bibliography

[1] A. Ashkin, J. M. Dziedzic, J. E. Bjorkholm, and S. Chu, Observation of a single-beam gradient force optical trap for dielectric particles. Opt. Lett. 11, 288 (1986).

[2] A. Ashkin, Acceleration and trapping of particles by radiation pressure. Phys. Rev. Lett. 24, 156 (1970).

[3] K. Dholakia and P. Zemánek, Colloquium: Gripped by light: Optical binding. Reviews of Modern Physics 82, 1767 (2010).

[4] M. M. Burns, J.-M. Fournier, and J. A. Golovchenko, Optical binding. Phys. Rev. Lett. 63, 1233 (1989).

[5] P. C. Chaumet and M. Nieto-Vesperinas, Optical binding of particles with or without the presence of a flat dielectric surface. Phys. Rev. B 64, 035422 (2001).

[6] E. Almaas and I. Brevik, Possible sorting mechanism for microparticles in an evanescent field. Phys. Rev. A 87, 063826 (2013).

[7] A. Jonáš and P. Zemánek, Light at work: The use of optical forces for particle manipulation. sorting, and analysis. Electrophoresis 29, 4813 (2008).

[8] M. M. Wang, E. Tu, D. E. Raymond, J. M. Yang, H. Zhang, N. Hagen, B. Dees, E. M. Mercer, A. H. Forster, I. Kariv, P. J. Marchand, and W. F. Butler, Microfluidic sorting of mammalian cells by optical force switching. Nat. Biotechnol. 23, 83 (2004).

[9] J. R. Moffitt, Y. R. Chemla, S. B. Smith, and C. Bustamante, Recent advances in optical tweezers. Annu. Rev. Biochem. 77, 205 (2008).

[10] D. G. Grier, A revolution in optical manipulation. Nature 424, 810 (2003).

[11] K. G. Dholakia and T. Čižmár, Shaping the future of manipulation. Nat. Photonics 5, 335 (2011).

[12] D. Chang, J. Thompson, H. Park, V. Vuletić, A. Zibrov, P. Zoller, and M. Lukin, Trapping and manipulation of isolated atoms using nanoscale plasmonic structures. Phys. Rev. Lett. 103, 123004 (2009).

[13] A. Reiserer, C. Nölleke, S. Ritter, and G. Rempe, Ground-state cooling of a single atom at the center of an optical cavity. Phys. Rev. Lett. 110, 223003 (2013).

[14] F. M. Fazal and S. M. Block, Optical tweezers study life under tension. Nature Photon. 5, 318 (2011).

[15] H. Li, D. Zhou, H. Browne, and D. Klenerman, Evidence for resonance optical trapping of individual fluorophore-labeled antibodies using single molecule fluorescence spectroscopy. J. Am. Chem. Soc. 128, 5711 (2006).

[16] M. Nieto-Vesperinas, J. J. Sáenz, R. Gómez-Medina, and L. Chantada, Optical forces on small magnetodielectric particles. Opt. Express 18, 11428 (2010).

[17] M. Nieto-Vesperinas, P. C. Chaumet, and A. Rahmani, Near-field photonic forces. Philos. Trans. A Math Phys Eng. Sci 362, 719 (2004).

[18] M. L. Juan, M. Righini, and R. Quidant, Plasmon nano-optical tweezer. Nat. Photonics 5, 349 (2011).

[19] G. Tkachenko and E. Brasselet, Optofluidic sorting of material chirality by chiral light. Nat.comm. 5, 3577 (2014).

[20] G. Tkachenko and E. Brasselet, Helicity-dependent three-dimensional optical trapping of chiral microparticles. Nat.comm. 5, 4491 (2014).

[21] A. Hayat, J. P. B. Mueller, and F. Capasso, Lateral chirality-sorting optical forces. Proc. Nat. Acad. Sci. 112, 13190 (2015).

[22] Q. Zhang, J. J. Xiao, X. M. Zhang, Y. Yao, and H. Liu, Reversal of optical binding force by Fano resonance in plasmonic nanorod heterodimer. Opt. Express 21, 6601 (2013).

[23] Q. Zhang and J. J. Xiao, Multiple reversals of optical binding force in plasmonic disk-ring nanostructures with dipole-multipole Fano resonances. Opt. letters 38, 4240 (2013).

[24] V. Shvedov, A. Davoyan, C.R. Hnatovsky, N. Engheta, and W.A Krolikowski, Long-range polarization-controlled optical tractor beam. Nat. Photonics 8, 846 (2014).

[25] A. Novitsky, C.-W. Qiu, and H. Wang, Single gradientless light beam drags particles as tractor beams. Phys. Rev. Lett. 107, 203601 (2011).

[26] B. A. Kemp, T. M. Grzegorczyk, and J. A. Kong, Lorentz Force on Dielectric and Magnetic Particles. Journal of Electromag. Wave Appl. 20, 827 (2006).

[27] B. A. Kemp, Resolution of the Abraham-Minkowski debate: Implications for the electromagnetic wave theory of light in matter. J. Appl. Phys. 109, 111101 (2011).

[28] M. Bethune-Waddell and K. J. Chau, Simulations of radiation pressure experiments narrow down the energy and momentum of light in matter.

Reports on Progress in Physics 78, 122401 (2015).

[29] K. Dholakia, P. Reece, and M. Gu, Optical micromanipulation. Chem. Soc. Rev. 37, 42 (2008).

[30] A. Novitsky, C.-W. Qiu, and A. Lavrinenko, Material-independent and size-independent tractor beams for dipole objects. Phys. Rev. Lett. 109, 023902 (2012).

[31] S. Sukhov and A. Dogariu, Negative nonconservative forces: Optical “tractor beams” for arbitrary objects. Phys. Rev. Lett. 107, 203602 (2011).

[32] S. Sukhov and A. Dogariu, On the concept of "tractor beams". Opt. Lett. 35, 3847 (2010).

[33] D. B. Ruffner and D. G. Grier, Optical conveyors: A class of active tractor beams. Phys. Rev. Lett. 109, 163903 (2012).

[34] M. M. Rahman, A. A. Sayem, M. R. C. Mahdy, M. E. Haque, R. Islam, S. T. R. Chowdhury, and M. A. Matin, Tractor beam for fully immersed multiple objects: Long distance pulling, trapping, and rotation with a single optical set-up. Annalen der Physik 527, 777 (2015).

[35] V. Kajorndejnukul, W. Q. Ding, S. Sukhov, C. W. Qiu, and A. Dogariu, Linear momentum increase and negative optical forces at dielectric interface. Nat. Photonics 7, 787 (2013).

[36] O. Brzobohatý, V. Karásek, M. Šiler, L. Chvátal, T. Čižmár, and P. Zemánek, Experimental demonstration of optical transport, sorting and self-arrangement using a ‘tractor beam’. Nat. Photonics 7, 123 (2013).

[37] A. Dogariu, S. Sukhov, and J. Sáenz, Optically induced 'negative forces'. Nat. Photonics 7, 24 (2013).

[38] V. D. Miljkovic, T. Pakizeh, B. Sepulveda, P. Johansson, and M. Kall, Optical Forces in Plasmonic Nanoparticle Dimers. The Journal of Physical Chemistry C 114, 7472 (2010).

[39] O. Peña-Rodríguez, U. Pal, M. Campoy-Quiles, L. Rodríguez-Fernández, M. Garriga, and M. I. Alonso, Enhanced Fano resonance in asymmetrical Au: Ag heterodimers. The Journal of Physical Chemistry C 115, 6410 (2011).

[40] W. Wan, W. Zheng, Y. Chen, and Z. Liu, From Fano-like interference to superscattering with a single metallic nanodisk. Nanoscale 6, 9093 (2014).

[41] L. V. Brown, H. Sobhani, J. B. Lassiter, P. Nordlander, and N. J. Halas, Heterodimers: plasmonic properties of mismatched nanoparticle pairs. Acs Nano 4, 819 (2010).

[42] M. I. Petrov, S. V. Sukhov, A. A. Bogdanov, A. S. Shalin, and A. Dogariu, Surface plasmon polariton assisted optical pulling force. Laser and Photonics Reviews 10, 116 (2016).

[43] C.-W. Qiu, W. Ding, M.R.C. Mahdy, D. Gao, T. Zhang, F.C. Cheong, A. Dogariu, Z. Wang, and C.T. Lim, Photon momentum transfer in inhomogeneous dielectric mixtures and induced tractor beams. Light: Science and Applications 4, e278 (2015).

[44] B. A. Kemp, T. M. Grzegorczyk, and J. A. Kong, Optical momentum transfer to absorbing Mie particles. Phys. Rev. Lett. 97, 133902 (2006).

[45] M. Mansuripur, Resolution of the Abraham–Minkowski controversy. Optics Communications 283, 1997 (2010).

[46] I. Brevik, Experiments in phenomenological electrodynamics and the electromagnetic energy-momentum tensor. Phys Rep. 52, 133 (1979).

[47] A. Ashkin and J. M. Dziedzic, Radiation pressure on a free liquid surface. Phys. Rev. Lett. 30 139 (1973).

[48] H. Minkowski, Die grundgleichungen für die elektromagnetischen vorgänge in bewegten körpern. Math. Ann. 68, 472 (1910) and H. Minkowski, The basic equations for electromagnetic processes in moving bodies. Nachr. Ges. Wiss. Gottingen, Math. Phys. Kl. 53 (1908).

[49] R. Pfeifer, T. Nieminen, N. Heckenberg, and H. Rubinsztein-Dunlop, Colloquium: Momentum of an electromagnetic wave in dielectric media. Rev. Mod. Phys. 79, 1197 (2007).

[50] P. W. Milonni and R. W. Boyd, Momentum of light in a dielectric medium. Adv. Opt. Photonics 2, 519 (2010).

[51] M. Abraham and R. C. Circ., Mat. Palermo 28, 1 (1909).

[52] M. Abraham and R. C. Circ., Mat. Palermo 30, 33 (1910).

[53] B. A. Kemp and T. M. Grzegorczyk, The observable pressure of light in dielectric fluids. Optics letters 36, 493 (2011).

[54] S. S. Hakim and J. B. Higham, Proc. Roy. Soc. 80, 190 (1962).

[55] R. V. Jones and J. C. S. Richards, The pressure of radiation in a refracting medium. Proc. R. Soc. Lond. 221, 480 (1954).

[56] R. V. Jones and B. Leslie, The measurement of optical radiation pressure in dispersive media. Proc. R. Soc. Lond. A 360, 347 (1978).

[57] K. T. McDonald, Bibliography on the Abraham-Minkowski Debate: http://www.physics.princeton.edu/~mcdonald/examples/ambib.pdf (2015).

[58] S.M. Barnett, Resolution of the Abraham-Minkowski Dilemma. Phys. Rev. Lett. 104, 070401 (2010).

[59] J. Chen, J. Ng, Z. Lin, and C. T. Chan, Optical pulling force. Nat. Photon. 5, 531 (2011).

[60] CizmarT et al. Appl. Phys. Lett. 86, 174101 (2005).

[61] CizmarT, Siler M, Zemánek. Appl. Phys. B 84, 197 (2006).

[62] Mizrahi A and Fainman, Opt. Lett. 35, 3405 (2010).

[63] B.A. Kemp, J.A. Kong, and T.M. Grzegorczyk, Reversal of wave momentum in isotropic left-handed media. Phys. Rev. A 75, 053810 (2007).

[64] C. Wang, Z. Gong, Y. L. Pan, and G. Videen, Laser pushing or pulling of absorbing airborne particles. Applied Physics Letters 109, 011905 (2016).

[65] H. Chen, B. Zhang, Y. Luo, B. A. Kemp, J. Zhang, L. Ran, and B.I. Wu, Lorentz force and radiation pressure on a spherical cloak. Phys. Rev. A 80, 011808 (2009).

[66] T. Čižmár, L. C. D. Romero, K. Dholakia, and D. L. Andrews, Multiple optical trapping and binding: New routes to self-assembly. J. Phys. B: At., Mol. Opt. Phys. 43, 102001 (2010).

[67] S. K. Mohanty, J. T. Andrews, and P. K. Gupta, Optical binding between dielectric particles. Opt. Express 12, 2746 (2004).

[68] B. N. Slama-Eliau, and G. Raithel, Three-dimensional arrays of submicron particles generated by a four-beam optical lattice. Physical Review E 83, 051406 (2011).

[69] Z. Yan, R. A. Shah, G. Chado, S. K. Gray, M. Pelton, and N. F. Scherer, Guiding spatial arrangements of silver nanoparticles by optical binding interactions in shaped light fields. ACS Nano 7, 1790 (2013).

[70] Z. Yan, U. Manna, W. Qin, A. Camire, P. Guyot-Sionnest, and N. F. Scherer, Hierarchical photonic synthesis of hybrid nanoparticle assemblies. The Journal of Physical Chemistry Letters 4, 2630 (2013).

[71] F. C. Cheong, B. J. Krishnatreya, and D. G. Grier, Strategies for three-dimensional particle tracking with holographic video microscopy. Opt. Express 18, 13563 (2010).

[72] M. Polin, Y. Roichman, and D. G. Grier, Autocalibrated colloidal interaction measurements with extended optical traps. Physical Review E 77, 051401 (2008).

[73] V. Demergis and E. L. Florin, Ultrastrong optical binding of metallic nanoparticles. Nano Lett. 12, 5756 (2012).

[74] D. S. Bradshaw and D. L. Andrews, Optically induced forces and torques: Interactions between nanoparticles in a laser beam. Phys. Rev. A 72, 033816 (2005).

[75] R. Zhao, P. Tassin, T. Koschny, and C. M. Soukoulis, Optical forces in nanowire pairs and metamaterials. Opt. Express 18, 25665 (2010).

[76] M. Li, W. H. P. Pernice, and H. X. Tang, Tunable bipolar optical interactions between guided lightwaves. Nat. Photonics 3, 464 (2009).

[77] M. Li. H. Wang, D. Gao, L. Gao, J. Xu, and C. W. Qiu, Radiation pressure of active dispersive chiral slabs. Opt. Express. 23, 16546 (2015).

[78] A. R. Zakharian, P. Polynkin, M. Mansuripur, and J. V. Moloney, Single-beam trapping of micro-beads in polarized light: Numerical simulations. Opt. express 14, 3660 (2006).

[79] A. Akbarzadeh, M. Danesh, C. W. Qiu, and A. J. Danner, Tracing optical force fields within graded-index media. New Journal of Physics 16, 053035 (2014).

[80] M. Mansuripur, Optical manipulation: Momentum exchange effect. Nat. Photonics 7, 765 (2013).

[81] A. Ashkin and J. M. Dziedzic, Optical trapping and manipulation of viruses and bacteria. Science 235, 1517 (1987).

[82] H. Yin , M. D. Wang, K. Svoboda, R. Landick, S. M. Block, and J. Gelles, Transcripting against an applied force. Science 270, 1653 (1995).

[83] L. N. Ng, B. J. Luff, M. N. Zervas, and J. S. Wilkinson, Forces on a Rayleigh Particle in the Cover Region of a Planar Waveguide. J. Lightwave Technol. 18, 388 (2000).

[84] T. Zhu, M. R. C. Mahdy, Y. Cao, H. Lv, F. Sun, Z. Jiang, and W. Ding, Optical pulling using evanescent mode in sub-wavelength channels. Opt. Express. 24, 18436 (2016).

[85] V. R. Almeida, Q. C. Xu, A. Barrios, and M. Lipson, Guiding and confining light in void nanostructure. Opt. Lett. 29, 1209 (2004).

[86] A. H. J. Yang, S. D. Moore, B. S. Schmidt, M. Klug, M. Lipson, and D. Erickson, Optical manipulation of nano particles and biomolecules in sub-wavelength slot waveguides. Nature 457, 71 (2009).

[87] L. Tong, R. R. Gattass, J. B. Ashcom, S. He, J. Lou, M. Shen, I. Maxwell, and E. Mazur, Sub-wavelength diameter silica wires for low-loss optical wave guiding. Nature 426, 816 (2003).

[88] C. Xu, H. Lei, Y. Zhang, and B. Li, Backward transport of nano particles in fluidic flow. Opt. Express 20, 3 (2012).

[89] L. Zhao, Y. Li, J. Qi, J. Xu, and Q. Sun, Quasi three-dimensional optical trapping by two counter-propagating beams in nano-fiber. Opt. Express. 18, 6 (2010).

[90] K. J. Webb and Shivanand, Negative electromagnetic plane-wave force in gain media. Phys. Rev. E 84, 057602 (2011).

[91] A. V. Maslov, Resonant Pulling of a Microparticle Using a Backward Surface Wave. Phys. Rev. Lett. 112, 113903 (2014).

[92] D. Gao, A. Novitsky, T. Zhang, F. C. Cheong, L. Gao, C. T. Lim, B. Luk'yanchuk, and C.-W. Qiu, Unveiling the correlation between non-diffracting tractor beam and its singularity in Poynting vector. Laser Photon. Rev 9, 75 (2014).

[93] Y. Pang and R. Gordon, Optical Trapping of 12 nm Dielectric Spheres Using Double-Nanoholes in a Gold Film. Nano Lett. 11, 3763 (2011).

[94] Wikipedia link: http://en.wikipedia.org/wiki/100_nanometres and S. M. Grist, S. A. Schmidt, J. Flueckiger, V. Donzella, W. Shi, S. T. Fard, J.T. Kirk, D. M. Ratner, K. C. Cheung, and L. Chrostowski, Silicon photonic micro-disk resonators for label-free biosensing. Opt. Express 21, 7994 (2013).

[95] M. Mansuripur and A. R. Zakharian, Maxwell's macroscopic equations, the energy-momentum postulates, and the Lorentz law of force. Phys. Rev. E 79,

026608 (2009).

[96] A. Akbarzadeh, J. A. Crosse, M. Danesh, C. W. Qiu, A. J. Danner, and C. M. Soukoulis, Interplay of optical force and ray-optic behavior between Luneburg lenses. ACS Photonics 2, 1384 (2015).

[97] M. L. Juan, R. Gordon, Y. Pang, F. Eftekhari, and R. Quidant, Self-induced back-action optical trapping of dielectric nano particles. Nat. Phys. 5, 915 (2009).

[98] J. T. Rubin, and L. Deych, On optical forces in spherical whispering gallery mode resonators. Opt. Express 19, 22337 (2011).

[99] J. T. Rubin and L. I. Deych, Optical forces due to spherical microresonators and their manifestation in optically induced orbital motion of nanoparticles. Phys. Rev. A 84, 023844 (2011).

[100] Lumerical FDTD: https://www.lumerical.com/tcad-products/fdtd/

[101] P. Yeh, A. Yariv, and E. Marom, Theory of Bragg fiber. J. Opt. Soc. Am. 68, 1196 (1978) and

H. Munir, D.K. Soumitra, M.R.C. Mahdy, H. Dihan, and Md. Matin, Robust Optical Fiber Using Single Negative Metamaterial, IEEE Phot. Tech. Letter 25, 1043 (2013).

[102] S. Gou, S. Albin, and R.S. Rogowski, Comparative analysis of Bragg fibers. Opt. Express 12, 198 (2004).

[103] V. Intaraprasonk and S. Fan, Optical pulling force and conveyor belt effect in resonator–waveguide system. Opt. letters 38, 3264 (2013).

[104] H. Ren, A. Salandrino, G. A. Siviloglou, and D. N. Christodoulides, Anomalous Optical Force Fields around High-Contrast Subwavelength

Nanowaveguides. Quantum Electronics and Laser Science Conference, 1-2, (2010) and F. L. Kien, and A. Rauschenbeutel, Negative azimuthal force of nanofiber-guided light on a particle. Phys. Rev. A 88, 063845 (2013).

[105] D. Haefner, S. Sukhov, and A. Dogariu, Spin hall effect of light in spherical geometry. Phys.rev.lett. 102, 123903 (2009) and S. Sukhov, V. Kajorndejnukul, and A. Dogariu, Dynamic Consequences of Optical Spin-Orbit Interaction. Nat. Photonics 9, 809 (2015).

[106] S. Mokhov, R. El-Ganainy, and D. N. Christodoulides, Power circulation via negative energy-flux wormholes in optical nano waveguides. Opt. Express 14, 3255 (2006).

[107] F. J. Rodríguez-Fortuño, G. Marino, P. Ginzburg, D. O'Connor, A. Martínez, G. A. Wurtz, and A. V. Zayats, Near-field interference for the unidirectional excitation of electromagnetic guided modes. Science 340, 328 (2013).

[108] J. D. Jackson, Classical electrodynamics, 3rd edition, New York: Wiley (1999).

[109] T. V. Raziman and O. J. Martin, Internal optical forces in plasmonic nanostructures. Opt. Express 23, 20143 (2015).

[110] A. Herczyński, Bound charges and currents. Am. J. Phys. 81, 202 (2013).

[111] D. J. Griffiths, Introduction to Electrodynamics, 3rd edition Upper Saddle River, NJ: prentice Hall (1999).

[112] T. M. Grzegorczyk, B. A. Kemp, and J. A. Kong, Stable Optical Trapping Based on Optical Binding Forces. Phys. Rev. Lett. 96, 113903 (2006).

[113] J. Ng, R. Tang, and C. T. Chan, Electrodynamics study of plasmonic bonding and anti-bonding forces in a bisphere. Phys. Revi. B 77, 195407(2008).

[114] C. Min, Z. Shen, J. Shen, Y. Zhang, H. Fang, G. Yuan, L. Du, S. Zhu, T. Lei, and X. Yuan, Focused plasmonic trapping of metallic particles. Nat. comm. 4, 2891 (2013).

[115] M. Zeisberger, A. Tuniz, and M. A. Schmidt, Analytic model for the complex effective index dispersion of metamaterial-cladding large-area hollow core fibers. Opt. express 24, 20515 (2016).

[116] M. J. Shawon, G. A. Mahdiraji, M. M. Hasan, B. H. Shakibaei, S. Y. Gang, M. R. C. Mahdy, and F. R. M. Adikan, Single Negative Metamaterial-Based Hollow-Core Bandgap Fiber With Multilayer Cladding. IEEE Photonics J. 7, 4600812 (2015).

[117] S. Sheikholeslami, Y. W. Jun, P. K. Jain, and A. P. Alivisatos, Coupling of optical resonances in a compositionally asymmetric plasmonic nanoparticle dimer. Nano Lett. 10, 2655 (2010).

[118] P. K. Jain and M. A. El-Sayed, Noble metal nanoparticle pairs: effect of medium for enhanced nanosensing. Nano Lett. 8, 4347 (2008).

[119] N. Verellen, P. Van Dorpe, C. J. Huang, K. Lodewijks, G. A. E. Vandenbosch, L. Lagae, and V. V. Moshchalkov, Plasmon Line Shaping Using Nanocrosses for High Sensitivity Localized Surface Plasmon Resonance Sensing. Nano Lett. 11, 391 (2011).

[120] P. L. Stiles, J. A. Dieringer, N. C. Shah, and R. R. Van Duyne, Annu. Rev. Anal. Chem. 1, 601 (2008).

[121] A. M. Michaels, J. Jiang, and L. Brus, Ag nano-crystal junctions as the site for surface-enhanced Raman scattering of single rhodamine 6G molecules. The Journal of Physical Chemistry B 104, 11965 (2000).

[122] K. Li, M. I. Stockman, and D. J. Bergman, Self-similar chain of metal nanospheres as an efficient nanolens. Phys. Rev. Lett. 91, 227402 (2003).

[123] S. A. Maier, P. G. Kik, and H. A. Atwater, Optical pulse propagation in metal nanoparticle chain waveguides. Phys. Rev. B 67, 205402 (2003).

[124] S. Zhang, D. A. Genov, Y. Wang, M. Liu, and X. Zhang, Plasmon-Induced Transparency in Metamaterials. Phys. Rev. Lett. 101, 047401(2008).

[125] L. Verslegers, Z. Yu, Z. Ruan, P. B. Catrysse, and S. Fan, From electromagnetically induced transparency to superscattering with a single structure: a coupled-mode theory for doubly resonant structures. Phys. Rev. Lett. 108, 083902 (2012).

[126] A. J. Pasquale, B. M. Reinhard, and L. Dal Negro, Engineering Photonic-Plasmonic Coupling in Metal Nanoparticle Necklaces. ACS Nano 5, 6578 (2011).

[127] T. Shegai, S. Chen, V. D. Miljkovi_c, G. Zengin, P. Johansson, Käll, and M., A Bimetallic Nanoantenna for Directional Colour Routing. Nat. Comm. 2, 481(2011).

[128] P. Nordlander, C. Oubre, E. Prodan, K. Li, and M. I. Stockman, Plasmon hybridization in nanoparticle dimers. Nano Lett. 4, 899 (2004).

[129] Z. J. Yang, Z. S. Zhang, L. H. Zhang, Q. Q. Li, Z. H. Hao, and Q. Q. Wang, Fano resonances in dipole-quadrupole plasmon coupling nanorod dimers. Optics letters 36, 1542 (2011).

[130] J. N. Li, T. Z. Liu, H. R. Zheng, F. Gao, J. Dong, Z. L. Zhang, and Z. Y. Zhang, Plasmon resonances and strong electric field enhancements in side-by-side tangent nanospheroid homodimers. Opt. Express. 21, 17176 (2013).

[131] L. Shao, C. Fang, H. Chen, Y. C. Man, J. Wang, and H. Q. Lin, Distinct plasmonic manifestation on gold nanorods induced by the spatial perturbation of small gold nanospheres. Nano Lett. 12, 1424 (2012).

[132] S. Marhaba, G. Bachelier, C. Bonnet, M. Broyer, E. Cottancin, N. Grillet, and M. Pellarin, Surface plasmon resonance of single gold nanodimers near the conductive contact limit. The Journal of Physical Chemistry C 113, 4349 (2009).

[133] P. Chu and D. L. Mills, Electromagnetic response of nanosphere pairs: Collective plasmon resonances, enhanced fields, and laser-induced forces. Phys. Rev. B 77, 045416 (2008).

[134] A. J. Hallock, P. L. Redmond, and L. E. Brus, Optical forces between metallic particles. Proc Natl Acad Sci U S A 102, 1280 (2005).

[135] P. Chu and D. L. Mills, Laser-induced forces in metallic nanosystems: The role of plasmon resonances. Phys. Rev. Lett. 99, 127401(2007).

[136] H. Liu, J. Ng, S. B. Wang, Z. H. Hang, C. T. Chan, and S. N. Zhu, Strong plasmon coupling between two gold nanospheres on a gold slab. New Journal of Physics 13, 073040 (2011).

[137] C. Van Vlack, P. Yao, and S. Hughes, Optical forces between coupled plasmonic nanoparticles near metal surfaces and negative index material waveguides. Phys. Rev. B 83, 245404 (2011).

[138] R. C. Weast, M. J. Astle, and W. H. Beyer, CRC handbook of chemistry and physics (Vol. 69). Boca Raton, FL: CRC press (1988).

[139] Edward D. Palik, Handbook of optical constants of solids. Vol. 3. Academic press, 1998.

[140] L. S. Slaughter, Y. Wu, B. A. Willingham, P. Nordlander, and S. Link, Effects of symmetry breaking and conductive contact on the plasmon coupling in gold nanorod dimers. Acs Nano 4, 4657 (2010).

[141] C. Tabor, D. Van Haute, and M. A. El-Sayed, Effect of orientation on plasmonic coupling between gold nanorods. ACS Nano 3, 3670 (2009).

[142] P. K. Jain, W. Huang, and M. A. El-Sayed, On the universal scaling behavior of the distance decay of plasmon coupling in metal nanoparticle pairs. Nano Lett. 7, 2080 (2007).

[143] R. Quidant and C. Girard, Surface-plasmon-based optical manipulation. Laser Photonics Rev. 2, 47 (2008).

[144] P. L.Marston, Axial radiation force of a bessel beam on a sphere and direction reversal of the force. J. Acoust. Soc. Am. 120, 3518 (2006).

[145] S.-H. Lee, Y. Roichman, and D. G. Grier, Optical solenoid beams. Opt. Express 18, 6988 (2010).

[146] A. Salandrino and D. N. Christodoulides, Reverse optical forces in negative index dielectric waveguide arrays. Opt. Lett. 36, 3103 (2011).

[147] G. A. Swartzlander, Jr, T. J. Peterson, A. B. Artusio-Glimpse, and A. D. Raisanen, Stable optical lift. Nat. Photon. 5, 48 (2011).

[148] P. D. Miller, N. N. Akhmediev, and A. Ankiewicz, Optical conveyor belts: a new scheme for fiber communications. Opt. Lett. 21, 1132 (1996).

[149] G. S. Wiederhecker, L. Chen, A. Gondarenko, and M. Lipson, Controlling photonic structures using optical forces. Nature 462, 633 (2009).

[150] M. Mansuripur, Trouble with the Lorentz law of force: Incompatibility with special relativity and momentum conservation. Phys. Rev. Lett. 108, 193901 (2012).

[151] S. M. Barnett and R. Loudon, The enigma of optical momentum in a medium. Phil. Trans. R. Soc. A 368, 927 (2010).

[152] C. Baxter and R. Loudon, Radiation pressure and photon momentum in dielectrics. J. Mod. Opt. 57, 830 (2010).

[153] R. Loudon, Radiation pressure and momentum transfer in dielectrics: The photon drag effect. Phys. Rev. A 71, 063802 (2005).

[154] D. J. Griffiths, Resource Letter EM-1: Electromagnetic Momentum. Am. J. Phys. 80, 7 (2012).

[155] K. J. Webb, Dependence of the radiation pressure on the background refractive index. Phys. Rev. Lett. 111, 043602 (2013).

[156] E. Brasselet, R. Wunenburger, and J.-P. Delville, Liquid optical fibers with a multistable core actuated by light radiation pressure. Phys. Rev. Lett. 101, 014501 (2008).

[157] O. Emile and J. Emile, Low-power laser deformation of an air-liquid interface. Phys. Rev. Lett. 106, 183904 (2011).

[158] R. Peierls, The momentum of light in a refracting medium. Proc. R. Soc. London Ser. A 347, 475 (1976).

[159] R. Peierls, The momentum of light in a refracting medium. II. Generalization. Application to oblique reflexion. Proc. R. Soc. London Ser. A 355, 141 (1977).

[160] E. R. Tkaczyk, Vectorial laws of refraction and reflection using the cross product and dot product. Opt. Lett. 37, 972 (2012).

[161] M. Mansuripur, A. R. Zakharian, and E. M. Wright, Electromagnetic force distribution inside matter. Phys. Rev. A 88, 023826 (2013).

[162] M. Mansuripur and A. R. Zakharian, Whence the Minkowski momentum? Opt. Commun. 283, 3557 (2010).

[163] R. Loudon, L. Allen, and D. F. Nelson, Propagation of electromagnetic energy and momentum through an absorbing dielectric. Phys. Rev. E 55, 1071 (1997).

[164] Mahdy, M. R. C., Dongliang Gao, Weiqiang Ding, M. Q. Mehmood, Manuel Nieto-Vesperinas, and Cheng-Wei Qiu, A unified theory correcting Einstein-Laub electrodynamics solves dilemmas in the photon momenta and electromagnetic stress tensors. arXiv:1509.06971 (2015).

[165] A. Novitsky and C.-W. Qiu, Pulling extremely anisotropic lossy particles using light without intensity gradient. Phys. Rev. A 90, 053815 (2014).

[166] S. Sukhov, V. Kajorndejnukul, R. R. Naraghi, and A. Dogariu, Dynamic Consequences of Optical Spin-Orbit Interaction. Nat. Photonics 9, 809 (2015) and S. Sukhov, V. Kajorndejnukul, and A. Dogariu, Dynamic Consequences of Optical Spin-Orbit Interaction. ArXiv:1504.01766 (2015).

[167] S. B. Wang and C. T. Chan, Lateral optical force on chiral particles near a surface. Nat. comm. 5, 3307 (2014).

[168] R. Fortuño, J. Francisco, N. Engheta, A. Martínez, and A. V. Zayats, Lateral forces on circularly polarizable particles near a surface. Nat. comm. 6, 8799 (2015).

[169] C. Huajin, Y. Jiang, N. Wang, W. Lu, S. Liu, and Z. Lin, Lateral optical force on paired chiral nanoparticles in linearly polarized plane waves. Opt. Lett. 40, 5530 (2015).

[170] B. A. Kemp, Macroscopic Theory of Optical Momentum. Prog. in Opt. 60, chapter 5 (2015).

[171] M. Dienerowitz, M. Mazilu, and K. Dholakia, Optical manipulation of nanoparticles: a review. J. Nanophoton. 2, 021875 (2008).

[172] M. Mansuripur, A. R. Zakharian, and J. V. Moloney, Radiation pressure on a dielectric wedge. Opt. Express 13, 2064 (2005).

[173] M. Mansuripur, A. R. Zakharian, and J. V. Moloney, Equivalence of total force (and torque) for two formulations of the Lorentz law. Proc. of the SPIE Conf., 6326 (2006).

[174] Q. C. Shang, Z. S. Wu, T. Qu, Z.J. Li, L. Bai, and L. Gong, Analysis of the radiation force and torque exerted on a chiral sphere by a Gaussian beam. Opt. Express 21, 8677 (2013).

[175] A. Canaguier-Durand, J. A. Hutchison, C. Genet, and T. W. Ebbesen, Mechanical separation of chiral dipoles by chiral light. New J. of Phys. 15, 123037 (2013).

[176] K. Ding , J. Ng, L. Zhou, and C. T.Chan, Realization of optical pulling forces using chirality. Phys. Rev. A 89, 063825 (2014).

[177] G. Tkachenko and E. Brasselet, Spin controlled optical radiation pressure. Phys. Rev. Lett. 111, 033605 (2013).

[178] R. J. Hernandez, A. Mazzulla, A. Pane, K. V. Sepúlveda, and G. Cipparrone , Attractive-repulsive dynamics on light-responsive chiral microparticles induced by polarized tweezers. Lab on a chip 13, 459 (2013).

[179] M. G. Donato, J. Hernandez, A. Mazzulla, C. Provenzano, R. Saija, R. Sayed, S. Vasi, A. Magazzù, P. Pagliusi, R. Bartolino, PG.Gucciardi, O. M. Maragò, and G. Cipparrone, Polarization-dependent optomechanics mediated by chiral microresonators. Nat. Comm. 5, 3656 (2014).

[180] D. E. Fernandes and M. G. Silveirinha, Optical tractor beam with chiral light. Phys. Rev. A 9, 061801(R) (2015).

[181] G. Li, M. Wang, H. Li, M. Yu, Y. Dong, and J. Xu, Wave propagation and Lorentz force density in gain chiral structures. Opt. Mat. Express 6, 388 (2016).

[182] S. M. Barnett and R. Loudon, On the electromagnetic force on a dielectric medium. J. Phys. B: At. Mol. Opt. Phys. 39, S671 (2006).

[183] Volumetric Technique of Lumerical Software:

https://kb.lumerical.com/en/nanophotonic_applications_optical_tweezers_volumetric_technique.html

and

https://kb.lumerical.com/en/index.html?nanophotonic_applications_optical_tweezers_volumetric_technique.html

[184] A. Rohrbach, Stiffness of optical traps: Quantitative agreement between experiment and electromagnetic theory. Phys. Rev. Lett. 95, 168102 (2005).

[185] J. Guck, R. Ananthakrishnan, T. J. Moon, C. C. Cunningham, and J. Kas, Optical Deformability of Soft Biological Dielectrics. Phys. Rev. Lett. 84,

5451 (2000).

[186] M. Hoeb, J.O. Radler, S. Klein, M. Stutzmann, and M.S. Brandt, Light-induced dielectrophoretic manipulation of DNA. Biophys J. 93, 1032 (2007).

[187] F. Rasetti, Deflection of mesons in magnetized iron, Phys. Rev. 66, 1 (1944).

[188] K. T. Mcdonald, Biot-Savart vs. Einstein-Laub Force Law. Joseph Henry Laboratories, Princeton University, Princeton, NJ 08544, (2013),

http://www.physics.princeton.edu/~mcdonald/examples/laub.pdf.

[189] J. Hu, S. Lin, L. fC. Kimerling, and K. Crozier, Optical trapping of dielectric nanoparticles in resonant cavities. Phys. Rev. A 82, 053819 (2010).

[190] V. V. Datsyuk and O. R. Pavlyniuk, Maxwell stress on a small dielectric sphere in a dielectric. Phys. Rev. A 91, 023826 (2015).

[191] R. Saija, P.Denti, F.Borghese, O. M. Marago, and M.A. Iati, Optical trapping calculations for metal nanoparticles. Comparison with experimental data for Au and Ag spheres. Opt. Express **17**, 10231 (2009).

[192] I. Brevik and S. A. Ellingsen, Comment on “Casimir force acting on magnetodielectric bodies embedded in media”. Phys. Rev. A 79, 027801 (2009).

[193] U. Fano, Effects of Configuration Interaction on Intensities and Phase Shifts. Phys. Rev. 124, 1866 (1961).

[194] Y. S. Joe, A. M. Satanin, and C. S. Kim, Classical analogy of Fano resonances. Phys. Scr. 74, 259 (2006).

[195] A. E. Miroshnichenko, S. Flach, and Y. S. Kivshar, Fano resonances in nanoscale structures. Rev. Mod. Phys. 82, 2257 (2010).

[196] S. S. Acimovic, M. P. Kreuzer, M. U. Gonzalez, R. Quidant, Plasmon near-field coupling in metal dimers as a step toward single-molecule sensing. ACS Nano 3, 1231(2009).

[197] A. M. Michaels, J. Jiang, L. Brus, Ag nanocrystal junctions as the site for surface-enhanced Raman scattering of single rhodamine 6G molecules. J. Phys. Chem. B 104, 11965 (2000).

[198] K. R. Li, M. I. Stockman, D. J. Bergman, Self-similar chain of metal nanospheres as an efficient nanolens. Phys. Rev. Lett. 91, 227402 (2003).

[199] S. Zhang, K. Bao, N. J. Halas, H. Xu, and P. Nordlander, Substrate-induced Fano resonances of a plasmonic nanocube: a route to increased-sensitivity localized surface plasmon resonance sensors revealed. Nano Letters 11, 1657 (2011).

[200] D. Sikdar, W. Zhu, W. Cheng, and M. Premaratne, Substrate-Mediated Broadband Tunability in Plasmonic Resonances of Metal Nanoantennas on Finite High-Permittivity Dielectric Substrate. Plasmonics 10, 1663(2015).

[201] M. W. Knight, Y. Wu, J. B. Lassiter, P. Nordlander, and N. J. Halas, Substrates matter: influence of an adjacent dielectric on an individual plasmonic nanoparticle. Nano Letters 9, 2188 (2009).

[202] K. Joulain, R. Carminati, J. P. Mulet, and J. J. Greffet, Definition and measurement of the local density of electromagnetic states close to an interface. Phys. Rev. B 68, 245405 (2003).

[203] Z. Wu, and Y. Zheng, Radiative Enhancement of Plasmonic Nanopatch Antennas. Plasmonics 11, 213 (2016).

[204] W. R. Holland, and D. G. Hall, Frequency shifts of an electric-dipole resonance near a conducting surface. Phys. Rev. Lett. 52, 1041(1984).

[205] O. Brzobohatý, T. Čižmár, V. Karásek, M. Šiler, K. Dholakia, and P. Zemánek, Experimental and theoretical determination of optical binding forces. Opt. Express 18, 25389 (2010).

[206] J. B. Lassiter, F. McGuire, J. J. Mock, C. Ciracì, R. T. Hill, B. J. Wiley, and D. R. Smith, Plasmonic waveguide modes of film-coupled metallic nanocubes. Nano Letters 13, 5866 (2013).

[207] C. Manolatou and F. Rana, Subwavelengthnanopatch cavities for semiconductor plasmon lasers. IEEE Journal of Quantum Electronics 44, 435(2008).

[208] A. Moreau, C. Ciracì, J. J. Mock, R. T. Hill, Q. Wang, B. J. Wiley, and D. R. Smith, Controlled-reflectance surfaces with film-coupled colloidal nanoantennas. Nature 492, 86 (2012).

[209] Z. Xiao-Ming, X. Jun-Jun, and Z. Qiang, Optical binding forces between plasmonicnanocubes: A numerical study based on discrete-dipole approximation. Chinese Phys. B 23, 017302 (2013).

[210] Q. Zhang, J. J. Xiao, X. M. Zhang, and Y. Yao, Optical binding force of gold nanorod dimers coupled to a metallic slab. Optics Communications 301, 121 (2013).

[211] A. S. Zelenina, R. Quidant, and M. Nieto-Vesperinas, Enhanced optical forces between coupled resonant metal nanoparticles. Opt. Lett. 32, 1156 (2007).

[212] G. L. Úvŕque and O. J. Martin, Optical interactions in a plasmonic particle coupled to a metallic film. Opt. Express 14, 9971(2006).

[213] P. T. Bowen and D. R. Smith, Coupled-mode theory for film-coupled plasmonic nanocubes. Phys. Rev. B 90, 195402 (2014).

[214] M. R. C. Mahdy, M. Q. Mehmood, Weiqiang Ding, Tianhang Zhang, and Zhi Ning Chen, Lorentz force and the optical pulling of multiple rayleigh particles outside the dielectric cylindrical waveguides. Annalen der Physik 529 (2017).

[215] W. Frias and A. I. Smolyakov, Electromagnetic forces and internal stresses in dielectric media. Phys. Rev. E 85, 046606 (2012).

[216] B. Kemp, T. Grzegorczyk, and J. Kong, Ab initio study of the radiation pressure on dielectric and magnetic media. Opt. Express 13, 9280 (2005).

[217] V. B. Veselago, Energy, linear momentum and mass transfer by an electromagnetic wave in a negative-refraction medium. Phys. Usp. 52, 649 (2009).

[218] C. J. Sheppard, and B. A. Kemp, Kinetic-energy-momentum tensor in electrodynamics. Phys. Rev. A 93, 013855 (2016).

[219] V. B. Veselago and V. V. Shchavlev, On the relativistic invariance of the Minkowski and Abraham energy-momentum tensors. Phys. Usp. 53, 317 (2010).

[220] K. J. Chau and H. J. Lezec, Revisiting the Balazs thought experiment in the presence of loss: electromagnetic-pulse-induced displacement of a positive-index slab having arbitrary complex permittivity and permeability. Applied Phys. A 105, 267 (2011).

[221] O. A. Capeloto V. S. Zanuto, L. C. Malacarne, M. L. Baesso, G. V. B. Lukasievicz, S. E. Bialkowski, and N. G. C. Astrath, Quantitative assessment of radiation force effect at the dielectric air-liquid interface. Scientific reports 6, 20515 (2016).

[222] C. Wang, Can the Abraham Light Momentum and Energy in a Medium Constitute a Lorentz Four-Vector? Journal of Modern Physics 4, 1123 (2013).

[223] A. Einstein, The Collected Papers of Albert Einstein. Vol. 8, Princeton University Press, Princeton, NJ (1998).

[224] L. Zhang, W. She, N. Peng, and U. Leonhardt, Experimental evidence for Abraham pressure of light. New Journal of Physics 17, 053035 (2015).

[225] G. Verma and K. P. Singh, Universal Long-Range Nanometric Bending of Water by Light. Phys. Rev. Lett. 115, 143902 (2015) and

N. G. Astrath, L. C. Malacarne, M. L. Baesso, G. V. Lukasievicz, and S. E. Bialkowski, Unravelling the effects of radiation forces in water. Nat. Comm. 5, 4363 (2014).

[226] Dongliang Gao, Weiqiang Ding, Manuel Nieto-Vesperinas, Xumin Ding, Mahdy Rahman, Tianhang Zhang, Chwee Teck Lim and Cheng-Wei Qiu, Optical Manipulation from Microscale to Nanoscale: Fundamentals, Advances, and Prospects. Light: Science and Applications 6, e17039 (2017).

[227] K. J. Chau and H. J. Lezec, Revisiting the Balazs thought experiment in the case of a left-handed material: electromagnetic-pulse-induced displacement of a dispersive, dissipative negative-index slab. Opt. Express 20, 10138 (2012).

[228] T. M. Grzegorczyk and J. A. Kong, Analytical expression of the force due to multiple TM plane-wave incidences on an infinite lossless dielectric circular cylinder of arbitrary size. JOSA B 24, 644 (2007).

[229] T. M. Grzegorczyk, B. A. Kemp, and J. A. Kong, Trapping and binding of an arbitrary number of cylindrical particles in an in-plane electromagnetic field. JOSA A 23, 2324 (2006).

[230] B. A. Kemp, Comment on "Revisiting the Balazs thought experiment in the presence of loss: electromagnetic-pulse-induced displacement of a positive-index slab having arbitrary complex permittivity and permeability". Applied Phys. A 110, 517 (2013).

[231] Tianhang Zhang, Mahdy Rahman Chowdhury Mahdy, Yongmin Liu, Jing hua Teng, Lim Chwee Teck, Zheng Wang and Cheng-Wei Qiu, All-Optical Chirality-sensitive Sorting via Reversible Lateral Forces in Interference Fields. ACS Nano (2017).

[232] M.R.C. Mahdy, Tianhang Zhang, Weiqiang Ding, Amin Kianinejad, Manuel Nieto-Vesperinas, Consistency of time averaged optical force laws for embedded chiral and achiral objects. *arXiv:1704.00334* (2017).